Report to the Texas Coastal Management Program:
CMP Cycle 23 Final Report:

Development of Galveston Bay 3D Hydrodynamic and Sediment Transport Models to Support Oyster Reefs

A report funded by a Texas Coastal Management Program Grant approved by the Texas Land Commissioner pursuant to National Oceanic and Atmospheric Administration Award No. NA18NOS4190153

Dr. Timothy M. Dellapenna[1&2]
Dr. Kyeong Park[1&2]
Dr. Jiabi Du,[3]
Nicole Schmidt[2]

[1]Department of Marine and Coastal Environmental Sciences, Texas A&M University at Galveston, Galveston, TX
[2]Oceanography Department, Texas A&M University, Galveston, TX
[3]Department of Applied Ocean Physics and Engineering, Woods Hole Oceanographic Institute, Woods Hole, MA

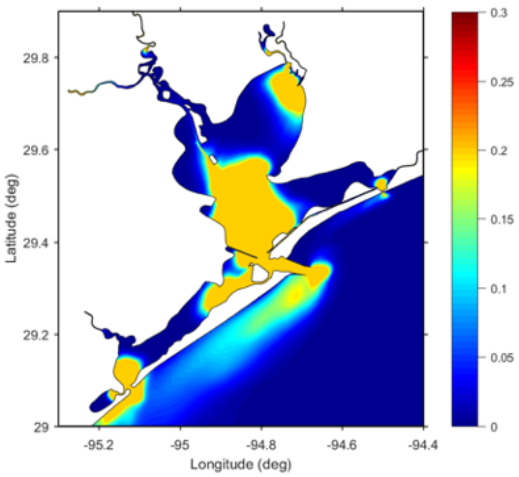

1. Introduction

This is a report of our CMP Cycle 23 project. The purpose of the original grant was to develop a high-resolution 3D Hydrodynamic model which could be used as a foundation to develop a 3D Hydrodynamic model to support various end uses, including the design of oyster reef restoration, as well as the modeling of particle bound contaminant transport and sediment transport in general. Reporting of results from a supplemental grant, which supported field sampling and data acquisition for the outcomes of this project are also included. This report has two parts, 1) a reporting of how each task was accomplished, and 2) appendices of all of the manuscripts that have either been published or the current state of the nearly finalized manuscript that is about to be submitted for publication.

2. Tasks

The following is a discussion of the project tasks from the original proposal as well as the supplemental task and what products were generated from them.

2.1. Task 1. Description: Field data collection

Conduct search of all available published and non-published data on sediment distributions within the study area, including accessing the TexSed database. Collect sediment field data and analyze data in the laboratory to fill in data holes.

Appendix A contains a report titled:

Dellapenna, T.M. and Schmidt, N., (unpublished) Surficial Sediment Data for Galveston Bay for Sediment Transport Model Input.

This document contains both the maps used for the development of the model as well as a bibliography of the sources of the data. Note, this data was also used in the development of Dellapenna, Schmidt and Park (unpublished) as well as Park and Du (2020-unpublished).

2.2. Task 2 Description: Build Models. Build the numerical 3D Hydrodynamic and Sediment transport models.

A description of the 3D Hydrodynamic model is provided in Appendix B in:

Du, J., Park, K., Shen, J., Zhang, Y.J., Yu, X., Ye, F., Wang, Z., Rabalais, N.N., 2019c. A hydrodynamic model for Galveston Bay and the shelf in the northern Gulf of Mexico. Ocean Sci. 15, 951–966. https://doi.org/10.5194/os-15-951-2019.

A description of the completed sediment transport model follows in Appendix B in a document titled:

Park, K., and Du, J., (unpublished) Galveston Bay Sediment transport model

We are planning on turning this document into a viable manuscript later this year.

Task 3 Description: Hurricane Harvey Model simulations. Run model simulations of Hurricane Harvey to determine where sediment from the Hurricane Harvey went, on various time steps from days to weeks to months to years.

These simulations were achieved through a series of four published papers (Appendix C) titled:

Du, J. and Park, K., 2019. Estuarine salinity recovery from an extreme precipitation event: Hurricane Harvey in Galveston Bay. Science of the total environment, 670, pp.1049-1059.

Du, J., Park, K., Dellapenna, T.M. and Clay, J.M., 2019. Dramatic hydrodynamic and sedimentary responses in Galveston Bay and adjacent inner shelf to Hurricane Harvey. Science of the Total Environment, 653, pp.554-564.

Du J., Park K., Dellapenna T.M., Clay J.M., 2019. Corrigendum to ''Dramatic hydrodynamic and sedimentary responses in Galveston Bay and adjacent inner shelf to Hurricane Harvey" [Sci. Total Environ. 653 (2019b), 554–564]. Sci. Total Environ. 697, 134219. https://doi.org/10.1016/j.scitotenv.2019.134219.

Du, J., Park, K., Yu, X., Zhang, Y.J. and Ye, F., 2020. Massive pollutants released to Galveston Bay during Hurricane Harvey: Understanding their retention and pathway using Lagrangian numerical simulations. Science of The Total Environment, 704, p.135364.

It should be noted Du et al. (2020) is the reporting of the Hydrodynamic model to simulate the transport of suspended sediment as a result of the Hurricane Harvey flood event. The development of the sediment transport model took longer than anticipated and at the writing of this report, simulations of sediment transport due to Hurricane Harvey have yet to be run on the model. We anticipate publishing the results of the sediment transport model presented here in the coming months. Once the simulation of Hurricane Harvey is performed, we also anticipate publishing the results as well, probably in 2021. Note, the simulation presented in this report is for non-Hurricane conditions, it would be anticipated that the Harvey simulation would have different results.

2.3. Task 4: Project Reporting

Quarterly reports were submitted timely, throughout the entire project and this document is the final project report.

2.4. Task S1: Instrumental Monitoring of suspended sediment dynamics in Galveston Bay- in support of the development of the sediment transport model for Galveston Bay. Deploy an instrumented mooring in lower Trinity Bay to monitoring suspended sediment concentrations in the bay. Instruments will include a CTD Sensor, which contains: 1) a conductivity sensor that provides salinity; 2) Pressure sensor that provides depth fluctuations (i.e. tides and waves); 3) Temperature; 4) Optical Backscatter Sensor (OBS)- there will be two of these placed near the bottom and 1 m off of the bottom to profile suspended sediment concentrations.

A deployment of an instrumented pod was conducted from January 29 through February 20, 2020. The results of the deployment, including a work up and presentation of the associated data is provided in Appendix D in the unpublished manuscript:

Dellapenna, T. M., Schmidt, N., and Park, K. (unpublished). Cold Front Sediment Resuspension, Age, and Residence times of suspended sediment using $^{7}Be/^{210}Pb_{xs}$ Ratio in Galveston Bay.

Note, this manuscript is based off of Nicole Schmidt's MS Thesis, which was supported by this project.

2.5. Task S2: Estimation of residence times of suspended sediment. A series of at least three samples of suspended sediments from within the bay, one from Trinity Bay, one from East Bay and one from West Bay, will be collected and the ratio of ^{7}Be and ^{210}Pb will be performed both during the lower energy summer conditions as well as the higher energy late fall/early winter conditions. ^{7}Be has a 53-day half-life and ^{210}Pb has a 22-year half-life. These ratios will allow for an estimation of the residence time of the suspended sediments within each portion of the bay, i.e., is the sediment being suspended newly eroded sediment or sediment that has been in the water column for a long time.

Along with the pod deployment, the results of this task, including a work up and presentation of the associated data is provided in Appendix D in the unpublished manuscript titled:

Schmidt, N., Dellapenna, T. M., and Park, K. (unpublished). Cold Front Sediment Resuspension, Age, and Residence times of suspended sediment using $^{7}Be/^{210}Pb_{xs}$ Ratio in Galveston Bay.

Note, this manuscript is based off of Nicole Schmidt's MS Thesis, which was supported by this project.

2.6. Task S3: Delineation of Hurricane Harvey deposits in the San Jacinto River and West Galveston Bay. Collect a series of at least four (4) cores (either vibra or pushcores) in the San Jacinto River and one (1) vibra core within Buffalo Bayou. Collect a series of at least fifteen (15) cores (either vibra or pushcores) in a combination of West Galveston Bay, Chocolate Bayou, Christmas Bay. Each core will be x-rayed and subsampled for grain size, water content and mercury (Hg) content.

The Hurricane Harvey deposit and the distribution of Hg in the San Jacinto Estuary is presented in Appendix E in the manuscript titled*:*

Dellapenna, T. M., Hoelscher, C., Hill, L., Al Mukaimi, M., and Knap, A. H., in review (accepted with revisions). How tropical cyclone flooding caused erosion and dispersal of mercury contaminated sediment in an urban estuary: the impact of Hurricane Harvey on Buffalo Bayou and the San Jacinto Estuary, Galveston Bay, USA, Science of the Total Environment (submitted, 4/22/20).

The reporting of the deliver and dispersal of Hg and sediment in Galveston Bay is presented in the manuscript titled:

Dellapenna, T. M., Hill, L., Hoelscher, C., Critides, L., Bartlett, V. Bell, M., Al Mukaimi, M., Du, J., Park, K., and Knap, A. H. (in prep to be submitted). Hurricane Harvey Delivered a Massive Load of Mercury Rich Sediment to Galveston Bay, Texas. To be submitted to Science of the Total Environment in Oct. 2020.

An additional manuscript is included, which has been submitted for publication and is currently in review. Although this research was not explicitly proposed for this project, the data is based off of samples collected from the cores collected for this project

Camargo, K. Sericano, J., Bhandari, S., Hoelscher, C., McDonald, T. J., Chiu, W. A., Wade, T. L., Dellapenna, T. M., Liu, Y., Knap, A. H., in review. Polycyclic aromatic hydrocarbons in Galveston Bay and the Houston Ship Channel: Post Hurricane Harvey baseline comparison to historical data. Submitted to Marine Pollution Bulletin (6/16/20).

It should be noted, we were not able to collect cores in West Galveston Bay on this project. Due to limited vessel access and weather conditions, this work had been delayed until late Spring 2020, but then the campus and our vessel operations were shut down due to the Covid 19 crisis and did not resume until such a time that there was not enough time left on the project to process the data.

3. Project Publications

This project has resulted in presentation of various aspect of this project both through research conference presentations as well as a series of five (5) published peer review papers, one paper currently in review and three (3) manuscripts in final stages of preparation for publication, as well as a document created to describe the sediment transport model, which will be turned into a manuscript later in the year.

Appendix A

Dellapenna, T.M. and Schmidt, N., (unpublished) Surficial Sediment Data for Galveston Bay for Sediment Transport Model Input.

Appendix B

Du, J., Park, K., Shen, J., Zhang, Y.J., Yu, X., Ye, F., Wang, Z., Rabalais, N.N., 2019c. A hydrodynamic model for Galveston Bay and the shelf in the northern Gulf of Mexico. Ocean Sci. 15, 951–966. https://doi.org/10.5194/os-15-951-2019.

Park, K., and Du, J., (unpublished) ***Galveston Bay Sediment transport model***

Appendix C

Du, J. and Park, K., 2019. Estuarine salinity recovery from an extreme precipitation event: Hurricane Harvey in Galveston Bay. *Science of the total environment*, *670*, pp.1049-1059.

Du, J., Park, K., Dellapenna, T.M. and Clay, J.M., 2019. Dramatic hydrodynamic and sedimentary responses in Galveston Bay and adjacent inner shelf to Hurricane Harvey. *Science of the Total Environment*, *653*, pp.554-564.

Du J., Park K., Dellapenna T.M., Clay J.M., 2019. Corrigendum to ‘‘Dramatic hydrodynamic and sedimentary responses in Galveston Bay and adjacent inner shelf to Hurricane Harvey” [Sci. Total Environ. 653 (2019b), 554–564]. Sci. Total Environ. 697, 134219. https://doi.org/10.1016/j.scitotenv.2019.134219.

Du, J., Park, K., Yu, X., Zhang, Y.J. and Ye, F., 2020. Massive pollutants released to Galveston Bay during Hurricane Harvey: Understanding their retention and pathway using Lagrangian numerical simulations. *Science of The Total Environment*, *704*, p.135364.

Appendix D

Schmidt, N., Dellapenna, T. M., and Park, K. (unpublished). Cold Front Sediment Resuspension, Age, and Residence times of suspended sediment using $^{7}Be/^{210}Pb_{xs}$ Ratio in Galveston Bay.

Appendix E

Dellapenna, T. M., Hoelscher, C., Hill, L., Al Mukaimi, M., and Knap, A. H., in review (accepted with revisions). How tropical cyclone flooding caused erosion and dispersal of mercury contaminated sediment in an urban estuary: the impact of Hurricane Harvey on Buffalo Bayou and the San Jacinto Estuary, Galveston Bay, USA, Science of the Total Environment (submitted, 4/22/20).

Dellapenna, T. M., Hill, L., Hoelscher, C., Critides, L., Bartlett, V. Bell, M., Al Mukaimi, M., Du, J., Park, K., and Knap, A. H. (in prep to be submitted). Hurricane Harvey Delivered a Massive Load of Mercury Rich Sediment to Galveston Bay, Texas. To be submitted to Science of the Total Environment in Oct. 2020.

Camargo, K. Sericano, J., Bhandari, S., Hoelscher, C., McDonald, T. J., Chiu, W. A., Wade, T. L., Dellapenna, T. M., Liu, Y., Knap, A. H., in review. Polycyclic aromatic hydrocarbons in Galveston Bay and the Houston Ship Channel: Post Hurricane Harvey baseline comparison to historical data. Submitted to Marine Polution Bulletin (6/16/20).

APPENDICES

Appendix A

Surficial Sediment Data For Galveston Bay For Sediment Transport Model Input

Dr. Timothy Dellapenna and Nicole Schmidt

1.0 Introduction

In order to develop a sediment transport model for Galveston Bay, a data base of surficial sediment was required to determine both the distribution and size classes for the model. To generate these data sets, a series of GIS layers were developed and are enclosed and discussed in this chapter.

2.0 Datasets

2.1 GIS Layers

The sources for all of the online maps and sediment sources are provided below in References and Data Sources. The GIS data layers which provided the basis for the maps were collected online from Texas Natural Resources Information System (TNRIS), including Geographic Names, Bathymetry Contours, Basemaps. All maps are in the WGS 1984 projection. Unpublished oyster reef GIS layers were generously provided by colleagues with the Texas Parks and Wildlife Division Dickinson Marine Laboratory. Additional GIS layers were obtained from NOAA's online portals. Additionally, the maps from the Submerged lands of Texas, Galveston-Houston area (White et al., 1985) were digitized to form a GIS for Sediment classification of polygons represented as polygons transcribed from Submerged Lands of Galveston-Houston area physical map shown in Fig. 1. This map provides a generalized view of both the dominate sediment type as well as the associated environments.

2.2 Grainsize Data

The grain size data used in this study was acquired from the archives of the TAMUG Coastal Geology Laboratory (TAMU-CGL) and from the Texas General Land Office (TGLO-TXSed) Texas Sediment Geodatabase (TxSed Geodatabase). The TAMUG-CGL grain size data is from 21 cores that were averaged to become condensed to seven sections within Galveston Bay (i.e. East Bay, West Bay, Lower Galveston Bay, Upper Galveston Bay, and Trinity Bay). The grain size data was generated using output from a Malvern Mastersizer 2000, which is an instrument that uses laser diffraction to determine grainsize distributions. The Malvern outputs a Simpson grain size distribution curve. The Simpson Curve is used to obtain an average clay, silt, and sand size of each sample analyzed. These analyses were performed on all of the samples analyzed through the TAMUG Coastal Geology Laboratory. The peaks on the Simpson curve were identified to find the average size of each size fraction (sand, silt, and clay, in microns) as well as the size of the 50th percentile (D50) of the sample. These values were recorded in an

excel file, along with the sample locations, and imported into ArcGIS and converted to a raster layer using the natural neighbors contouring tool. Pie charts of grain size distribution (Figure 4), D50 values were displayed (Figure 5), and a raster (using the natural neighbors tool) of the D50 values were created in ArcGIS.

To compliment the TAMUG Coastal Geology Laboratory data set, the Texas General Land Office (TXGLO) Texas Coastal Sediments Geodatabase (http://gisweb.glo.texas.gov/txsed/index.html) was used. Every sample with Galveston Bay was viewed and if the data was in the proper format, the grain size distribution percentages and sample locations were obtained and recorded in an excel file to display in ArcGIS. The percentages of sand, silt, and clay were converted to a raster file and contoured using the natural neighbors tool. The combined datasets were used to create a more thorough representation of the average grain size distributions within Galveston Bay (Figures 9,10, and 11).

2.3 Sediment Maps

A series of maps showing various aspects of sediment distributions were generated to both support the model and also to reach generalized conclusions on the controls and nature of sediment distributions.

2.3.1 Sediment Classification of Galveston Bay By Environment

Figure 1 shows the distribution of the dominant environments and their associated dominant sediment classes, which are: 1) River Influence (mud domininated); 2) Open Bay (Mud Dominated); and 3) Inlet Influence (Sand/Shell Dominated); Bay Margin (Sand Dominated). The polygons showing these distributions were digitized from *Plate V: Sediments, Geochemistry, Benthic Macroinvertebrates, and Associated Wetlands,* contained within the University of Texas Bureau of Economic Geology: *Submerged Lands of Texas, Galveston-Houston Area* (White et al, 1985) which contains the polygons of Inlet and River influence, in addition to Open Bay and Bay margin.

2.3.2 D50 Size Class Map- from Archived TAMUG-CGL Data

Figure 2 shows the spatial variability of the D50 size class map, contoured in microns. The D50, as noted above, is the size of the 50th percentile of sediment and provides a good proxy for the average grainsize, but provides no details about the range of variability of the sediment. The coarsest D50 is found at the head of Galveston Bay directly below the mouth of the San Jacinto estuary, along the eastern side of the Houston Ship Channel. The finest D50's are found within upper Trinity Bay and proximal to the mouth of Clear Lake. The mainstem of Galveston Bay and East Bay have intermediate D50's. Note, at this point, this is an incomplete data set and will be supplemented prior to final report.

2.3.3 Grain Size Distribution from TAMUG-CGL data

Figure 3 shows pie charts showing the grain size distributions of select sediment samples from the TAMUG-CGL archives. Note, at this point, this is an incomplete data set and will be supplemented prior to final report.

2.3.3 Grain Size Distribution from TAMUG-CGL data

Figure 3 shows pie charts showing the grain size distributions of select sediment samples from the TAMUG-CGL archives. Note, at this point, this is an incomplete data set and will be supplemented prior to final report.

2.3.4 Averaged D50 values

Figure 4 shows the posted D50 values of select sediment samples from the TAMUG-CGL archives. Note, at this point, this is an incomplete data set and will be supplemented prior to final report.

2.3.5 Average Sand Size for Galveston Bay from TAMUG-CGL data

Figure 5 shows the peaks Sand size of select sediment samples from the TAMUG-CGL archives. Note, at this point, this is an incomplete data set and will be supplemented prior to final report.

2.3.6 Average Silt Size for Galveston Bay from TAMUG-CGL data

Figure 5 shows the peaks Silt size of select sediment samples from the TAMUG-CGL archives. Note, at this point, this is an incomplete data set and will be supplemented prior to final report.

2.3.7 Average Clay Size for Galveston Bay from TAMUG-CGL data

Figure 7 shows the peaks Clay size of select sediment samples from the TAMUG-CGL archives. Note, at this point, this is an incomplete data set and will be supplemented prior to final report.

2.3.8 Location of the TexSeds Samples

Figure 8 shows the location of the samples used from the GLO TexSeds database.

2.3.9 %Sand Map from GLO Tex Seds database

Figure 9 Percentage of Sand when compared to Silt and Clay, from the GLO TexSeds database.

2.3.10 %Silt Map from GLO Tex Seds database

Figure 9 Percentage of Silt when compared to Sand and Clay, from the GLO TexSeds database.

2.3.10 %Clay Map from GLO Tex Seds database

Figure 9 Percentage of Clay when compared to Sand and Silt, from the GLO TexSeds database.

References/Data Sources

Grain Size Data-

- Texas General Land Office (GLO) Texas Sediment Geodatabase (TxSed Geodatabase) Retrieved from https://cgis.glo.texas.gov/txsed/index.html
  - Sand, silt, clay percentages

- Texas A&M University-Galveston Campus (TAMUG) Coastal Geology Laboratory Data Archives (Unpublished)

  -Malvern Mastersizer: Grain Size data of Galveston Bay and Trinity Bay

  -Created D50, Grain Size Distribution (Percentage)

GIS Layers

- NOAA: Galveston Bay DEM Raster Layer

  NOAA (2018, November 18). Coastal Digital Elevation Models (DEMs). Retrieved from https://catalog.data.gov/dataset/digital-elevation-models-from-noaa-ngdc

- Texas Natural Resources Information System (TNRIS)

  https://tnris.org

  -Coastal Bathymetery 2004

  https://data.tnris.org/collection/8fe992d8-1019-492a-b36b-9cfc3293ac6b

- Geographic Names, Bathymetry Contours, Basemap, Shoreline

- Texas Parks and Wildlife Division (TPWD) Oyster GIS Layers- unpublished oyster GIS layers provided by the TPWD-Dickinson Marine Laboratory, Dickinson, TX.

- White, W. A., Calnan, T. R., Morton, R. A., Kimble, R. S., Littleton, T. G., McGowen, J. H.,Nance, H. S., & Schmedes, K. E. (1985). *Submerged lands of Texas, Galveston-Houston area: Plate V: Sediments, Geochemistry, Benthic Macroinvertebrates, and associated Wetlands*. University of Texas at Austin, Bureau of Economic Geology.

  - Polygons of Open Bay Center Assemblage, Bay Margin Assemblage, River-Influence Assemblage, Inlet-Influence Assemblage

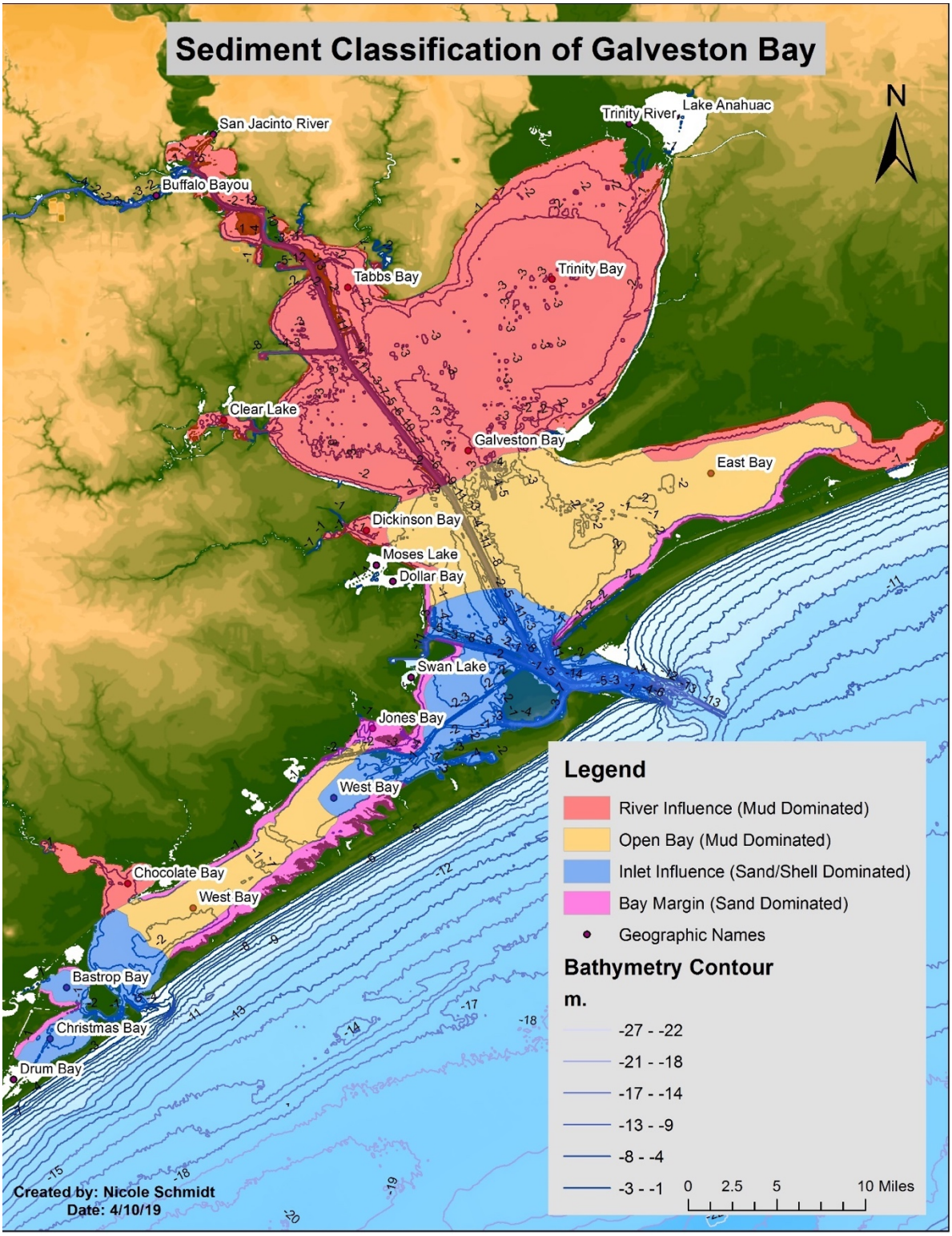

Figure 1. Sediment classification of polygons represented as polygons transcribed from Submerged Lands of Galveston-Houston area physical map.

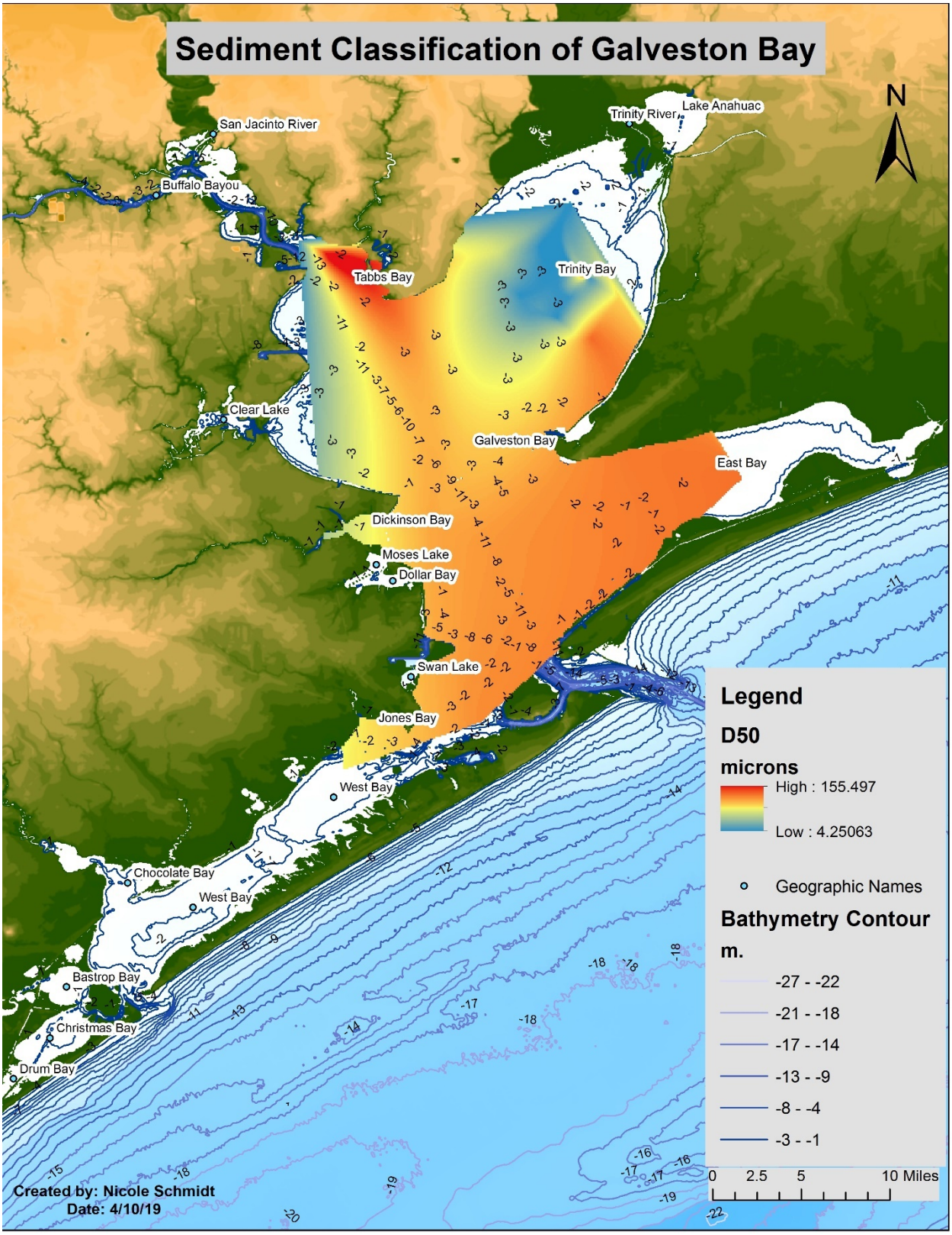

Figure 2. D50 values represented as Natural Neighbors Raster obtained from the Coastal Geology Lab including 21core locations (reduced to 7 total after averaging locations in close proximity) throughout Galveston Bay.

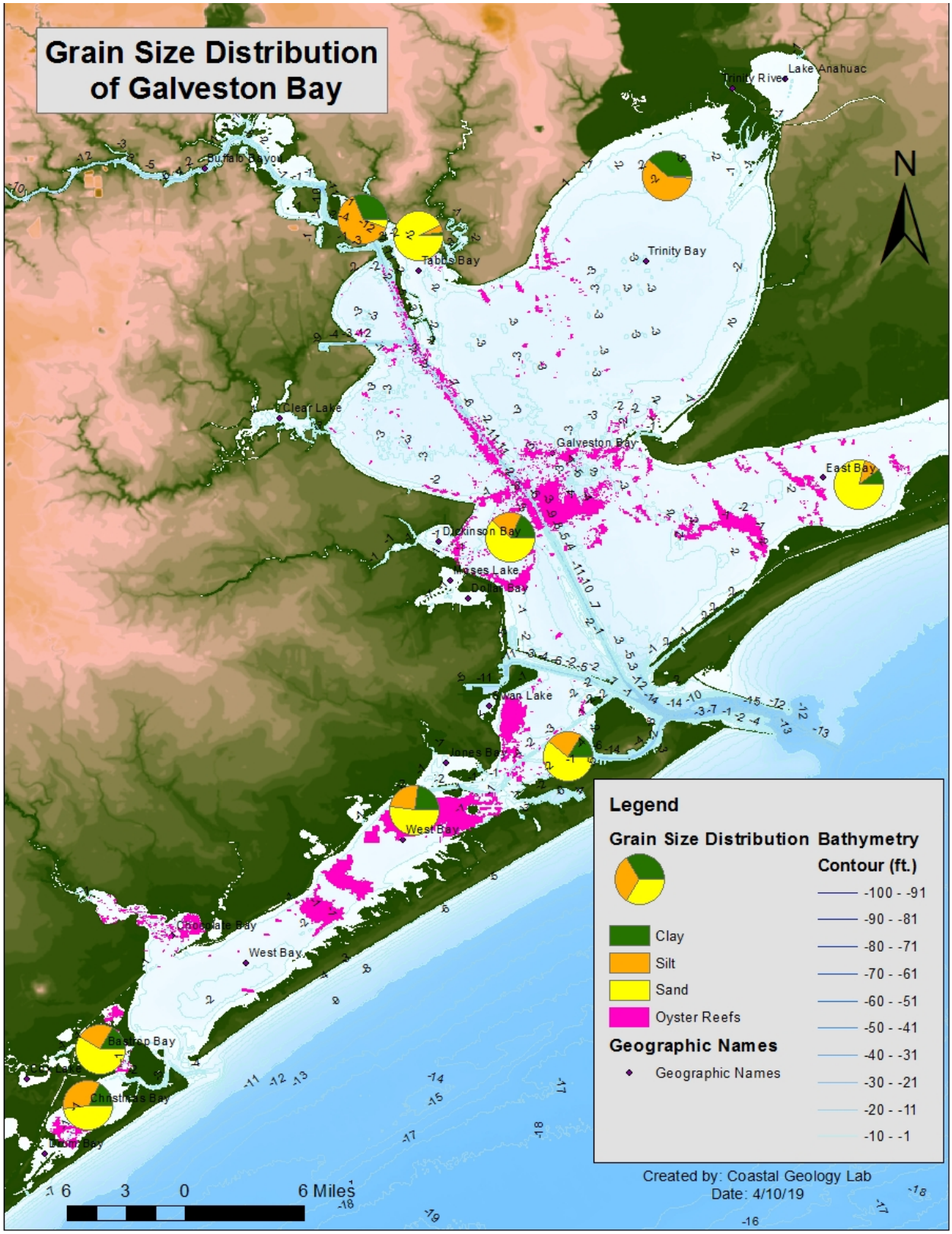

Figure 3. Percentage of Sand, Silt, and Clay obtained from the Coastal Geology Lab.

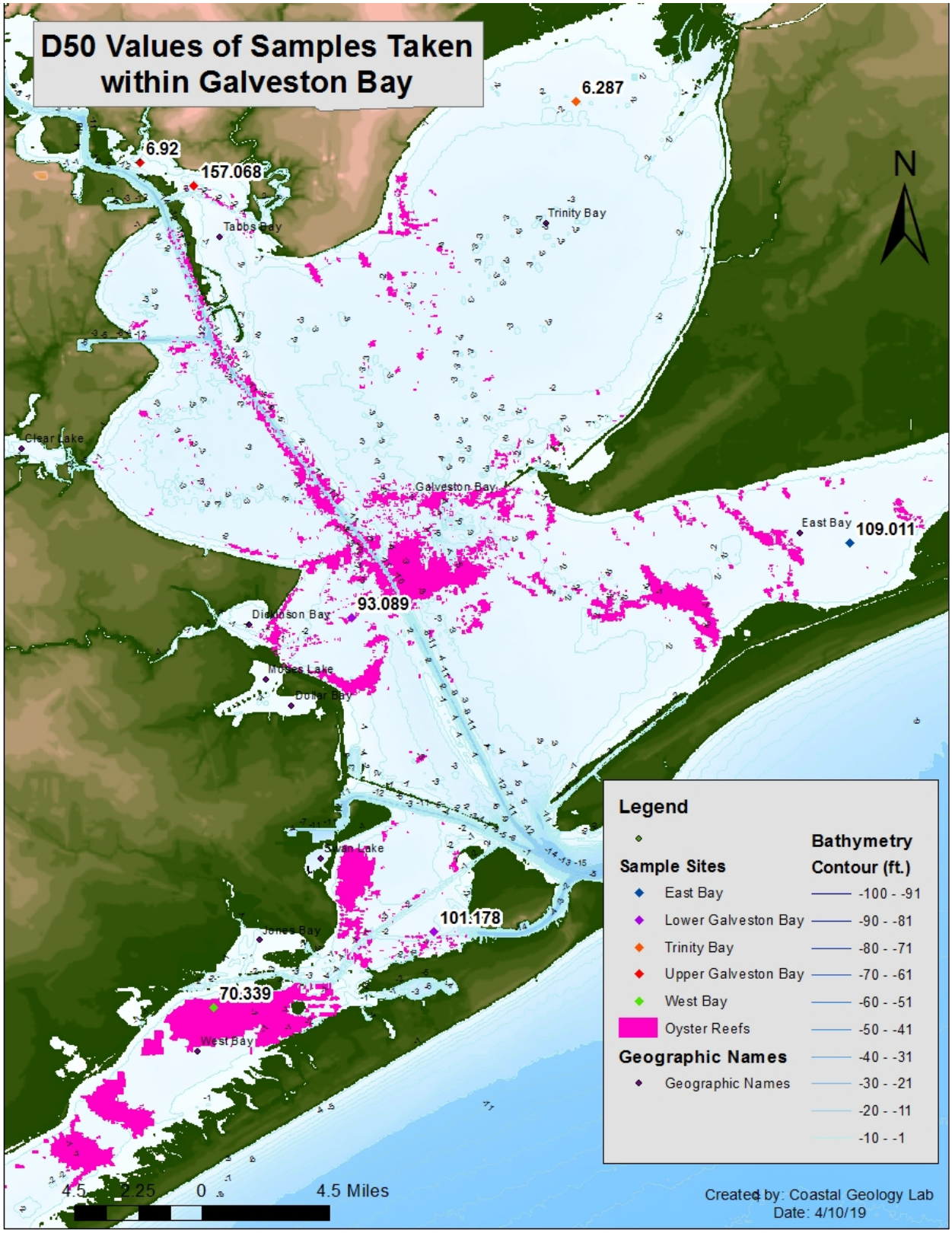

Figure 4. Actual D50 Values obtained from the Coastal Geology Lab divided into sections of Galveston Bay. Including 21 core locations that were averaged to the 7 sections of Galveston Bay based on proximity.

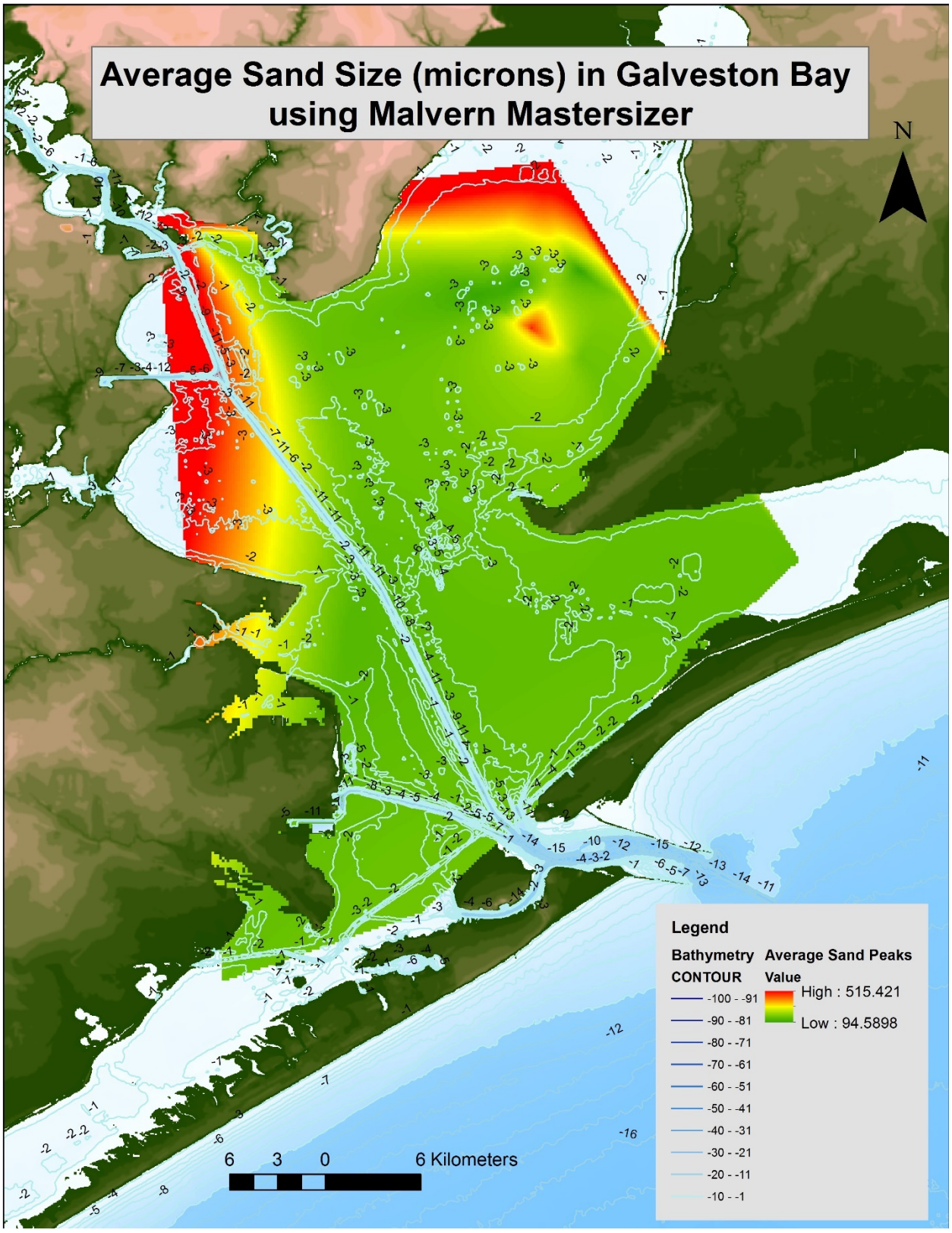

Figure 5. Average sand size of Galveston Bay using peaks from Simpsons Curve calculated in Malvern Mastersizer.

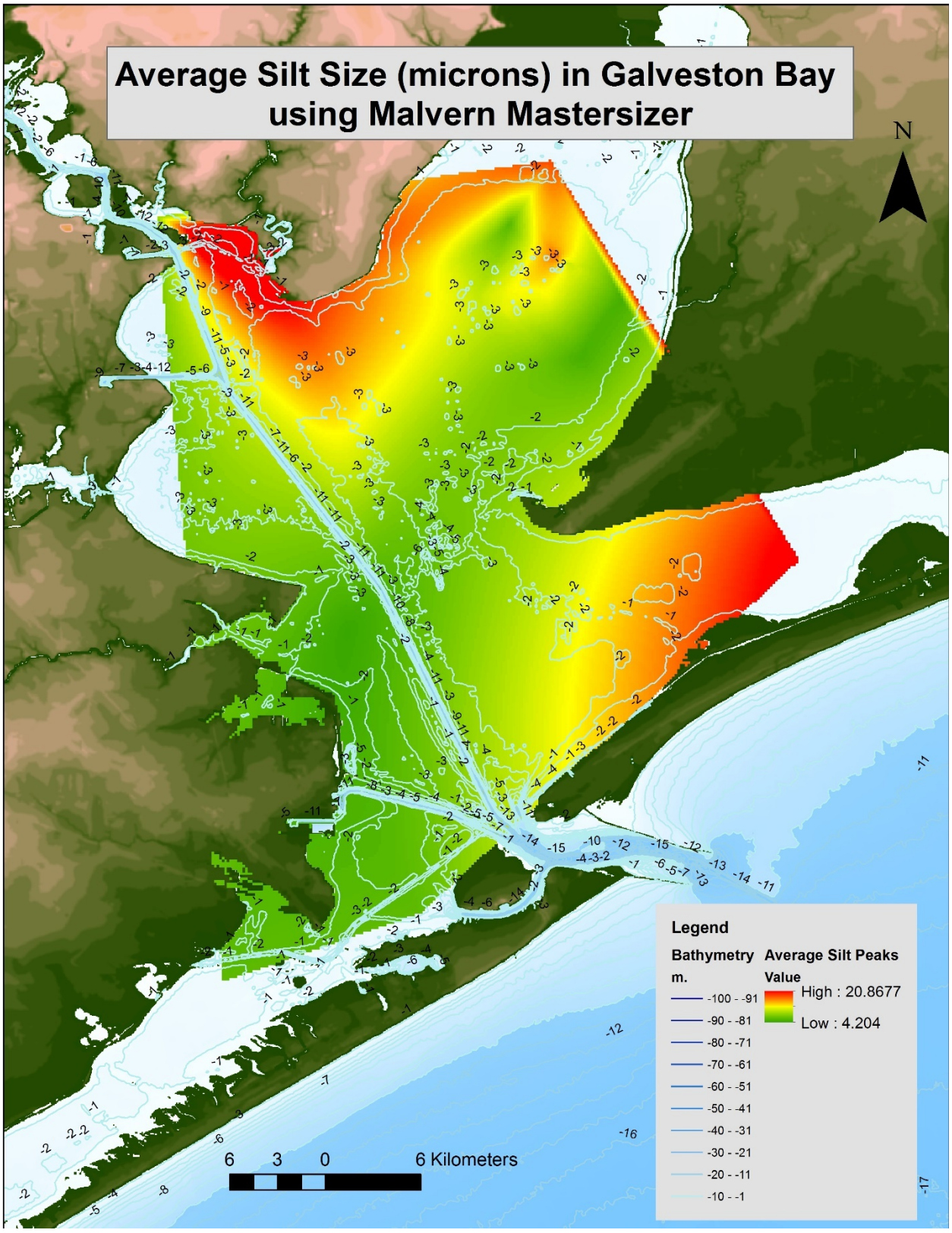

Figure 6. Average silt size of Galveston Bay using peaks from Simpson Curve calculated in Malvern Mastersizer.

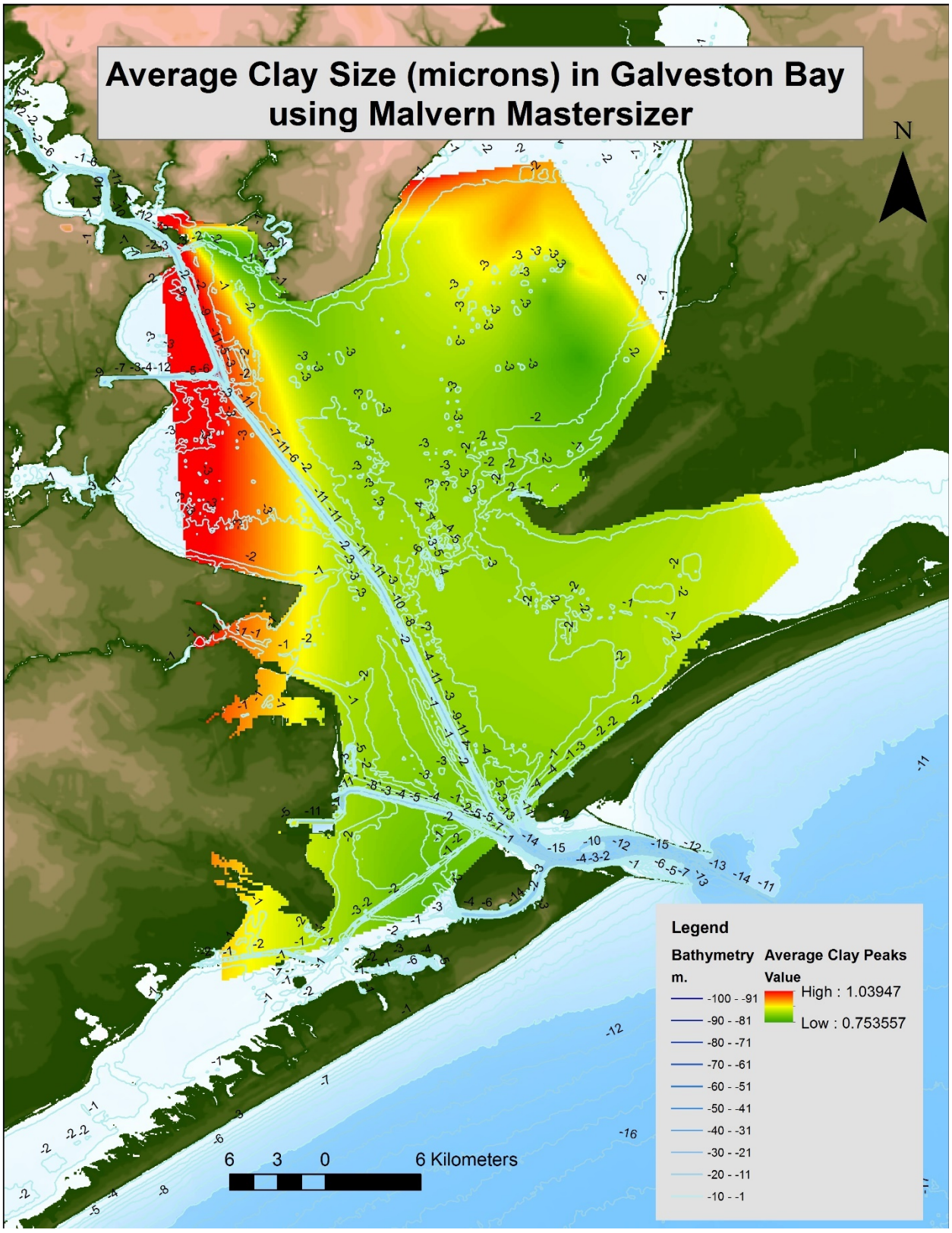

Figure 7. Average clay size of Galveston Bay using peaks from Simpsons Curve calculated in Malvern Mastersizer.

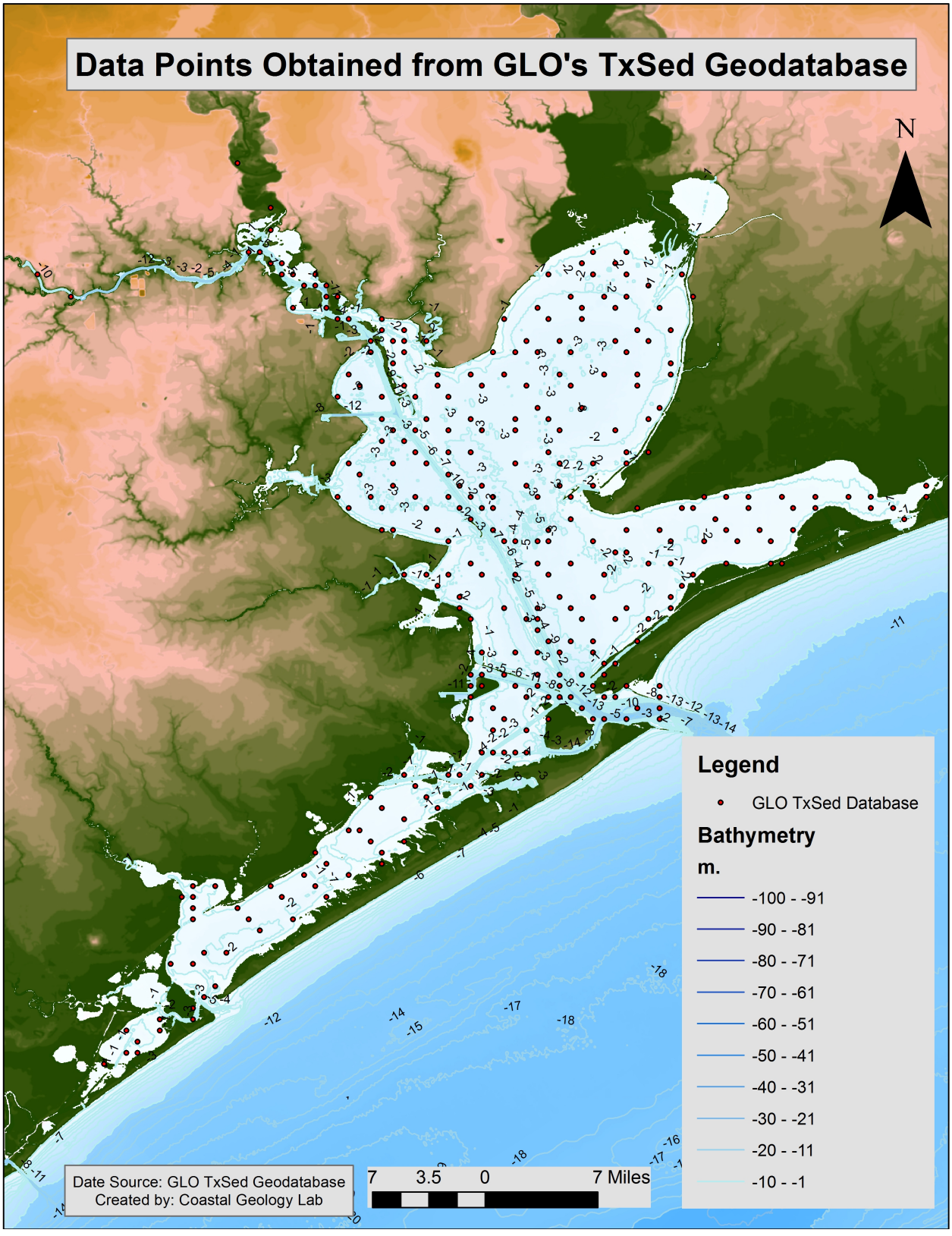

Figure 8. Sample Locations used for the %Sand (Fig. 9), %Silt (Fig. 10), %Clay (Fig. 11) for Galveston Bay using GLO's Texas Sediment Geodatabase.

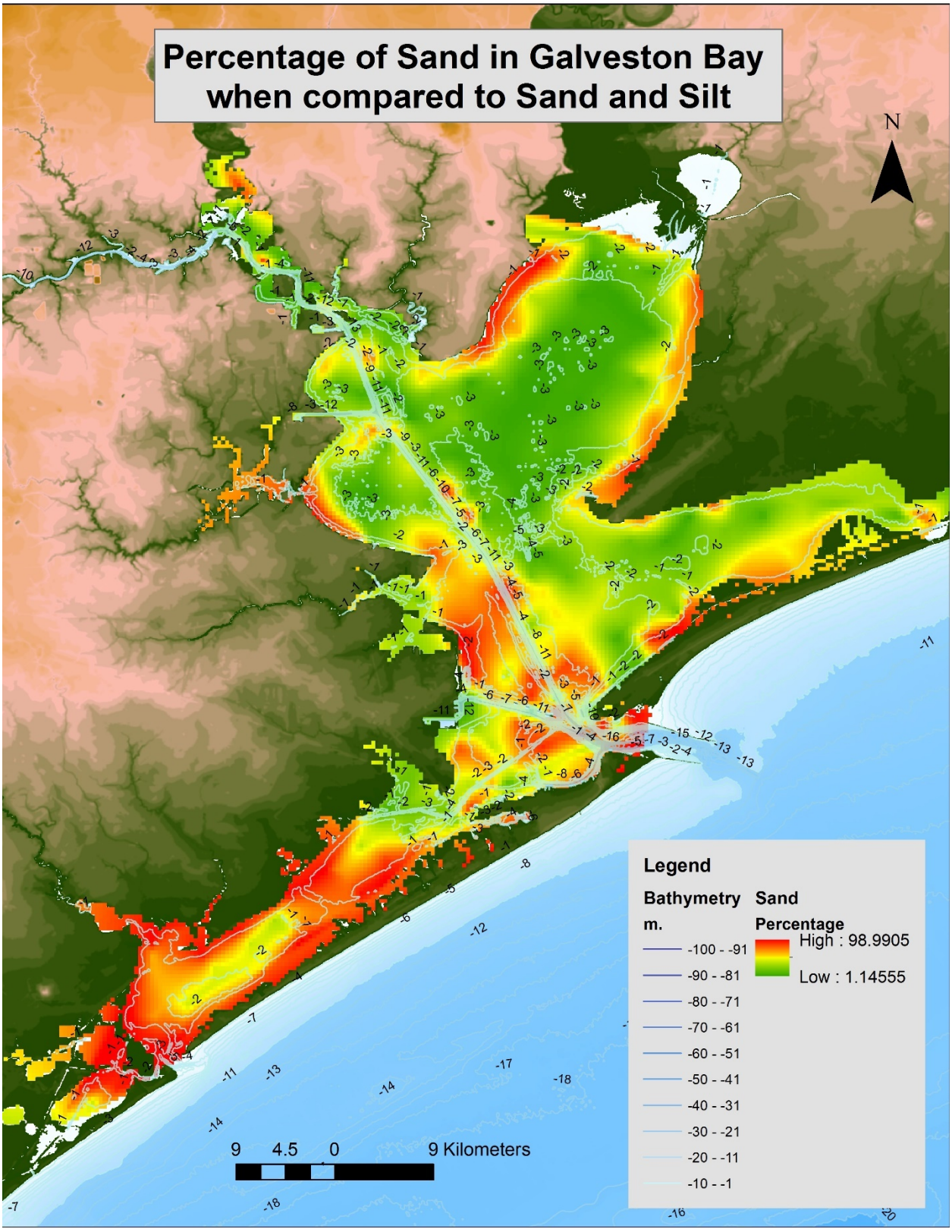

Figure 9. % sand (out of 100%, including clay and silt) in Galveston Bay using GLO's Texas Sediment Geodatabase.

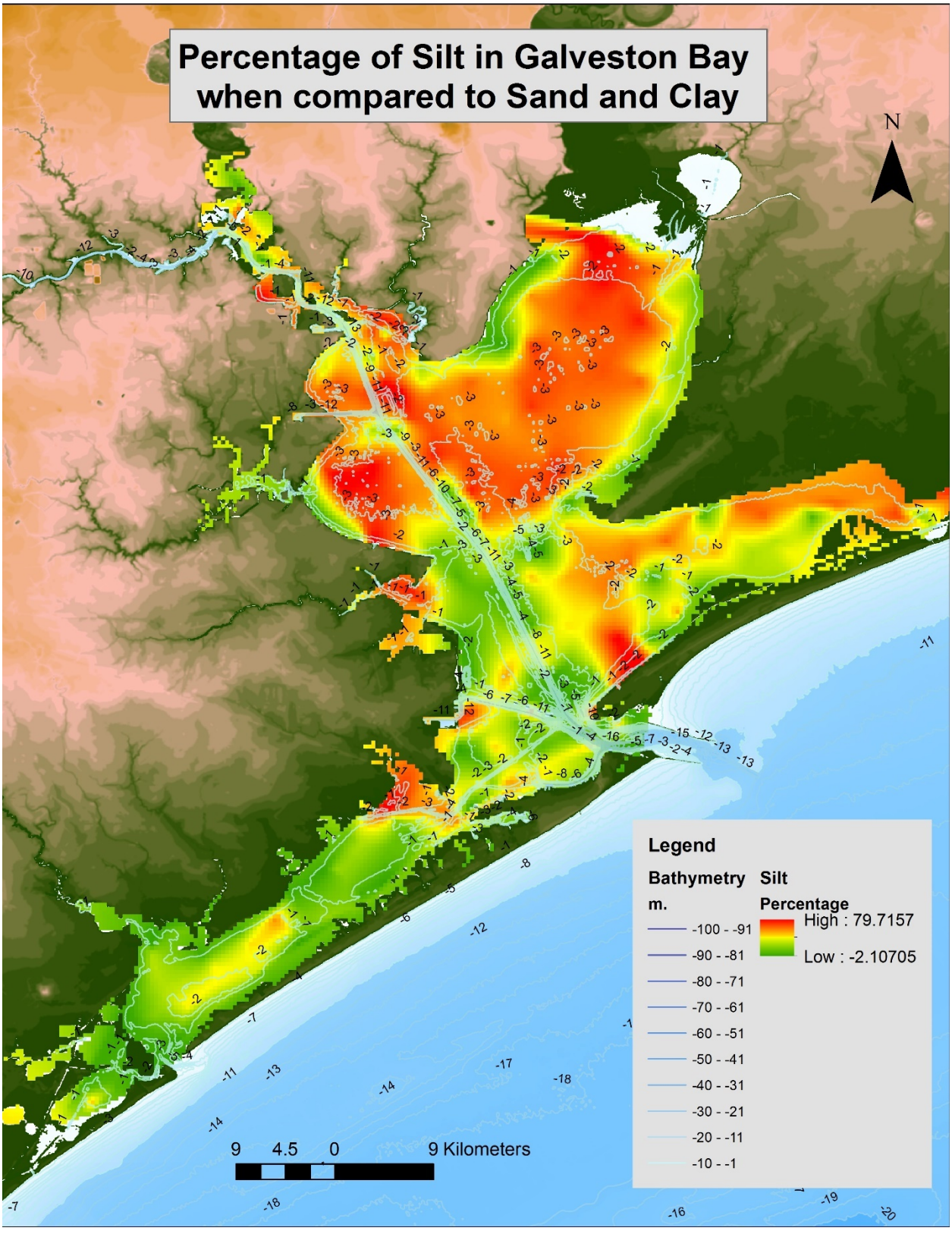

Figure 10. % silt (out of 100% including sand and clay) in Galveston Bay using GLO's Texas Sediment Geodatabase.

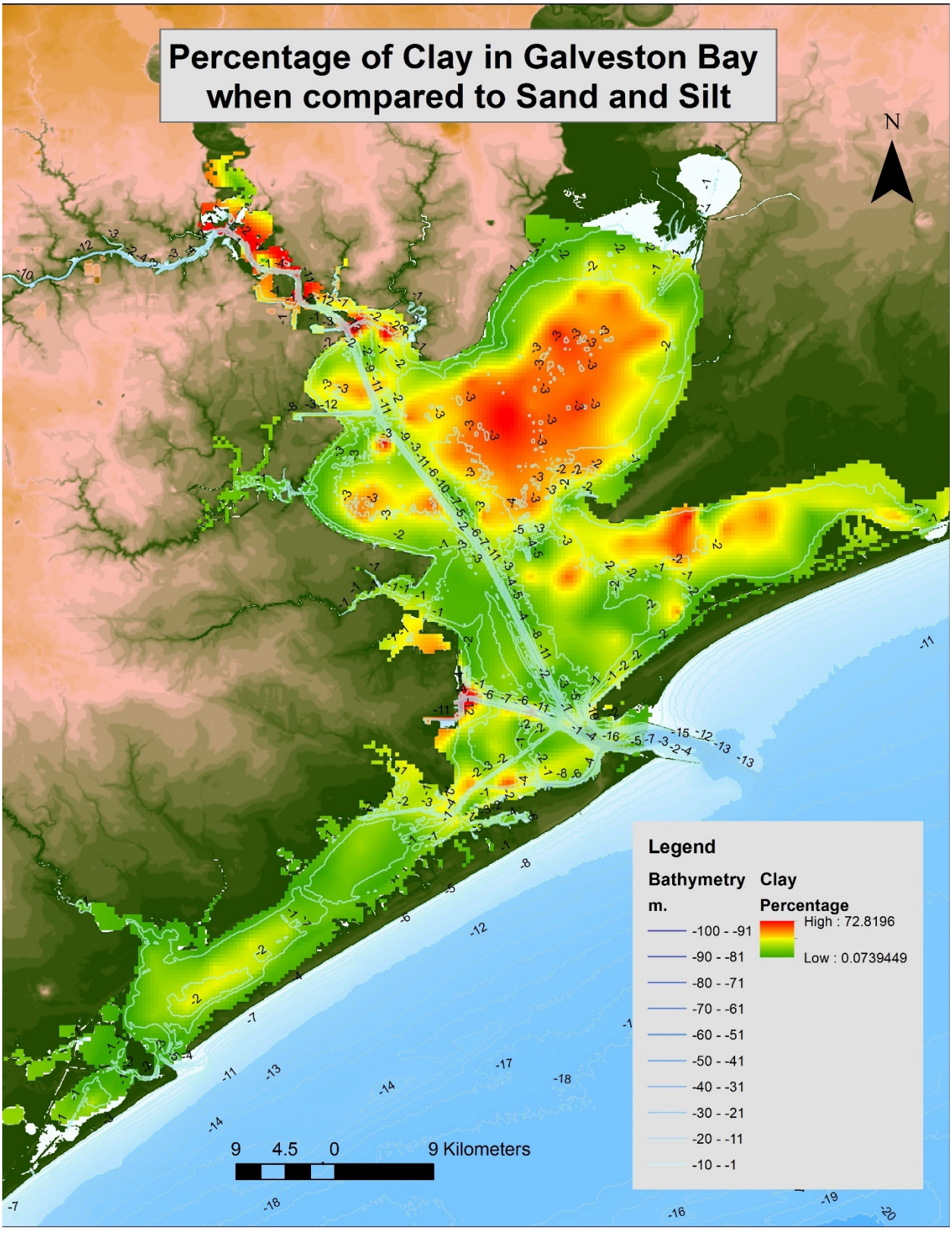

Figure 10. % clay (out of 100% including silt and sand) in Galveston Bay using GLO's Texas Sediment Geodatabase.

Appendix B

Ocean Sci., 15, 951–966, 2019
https://doi.org/10.5194/os-15-951-2019

Ocean Science Open Access EGU

A hydrodynamic model for Galveston Bay and the shelf in the northern Gulf of Mexico

Jiabi Du[1], Kyeong Park[1], Jian Shen[2], Yinglong J. Zhang[2], Xin Yu[2], Fei Ye[2], Zhengui Wang[3], and Nancy N. Rabalais[4]

[1]Department of Marine Sciences, Texas A&M University at Galveston, Galveston, TX 77554, USA
[2]Virginia Institute of Marine Science, College of William and Mary, Gloucester, VA 23062, USA
[3]School of Marine Sciences, University of Maine, Orono, ME 04469, USA
[4]Louisiana State University, Baton Rouge, LA 70803, USA

Correspondence: Jiabi Du (jdu@tamug.edu)

Received: 9 February 2019 – Discussion started: 4 March 2019
Revised: 15 May 2019 – Accepted: 27 June 2019 – Published: 17 July 2019

Abstract. A 3-D unstructured-grid hydrodynamic model for the northern Gulf of Mexico was developed, with a hybrid s–z vertical grid and high-resolution horizontal grid for the main estuarine systems along the Texas–Louisiana coast. This model, based on the Semi-implicit Cross-scale Hydroscience Integrated System Model (SCHISM), is driven by the observed river discharge, reanalysis atmospheric forcing, and open boundary conditions from global HYCOM output. The model reproduces the temporal and spatial variation of observed water level, salinity, temperature, and current velocity in Galveston Bay and on the shelf. The validated model was applied to examine the remote influence of neighboring large rivers, specifically the Mississippi–Atchafalaya River (MAR) system, on salinity, stratification, vertical mixing, and longshore transport along the Texas coast. Numerical experiments reveal that the MAR discharge could significantly decrease the salinity and change the stratification and vertical mixing on the inner Texas shelf. It would take about 25 and 50 d for the MAR discharge to reach the mouth of Galveston Bay and Port Aransas, respectively. The influence of the MAR discharge is sensitive to the wind field. Winter wind constrains the MAR freshwater to form a narrow lower-salinity band against the shore from the Mississippi Delta all the way to the southwestern Texas coast, while summer wind reduces the downcoast longshore transport significantly, weakening the influence of the MAR discharge on surface salinity along Texas coast. However, summer wind causes a much stronger stratification on the Texas shelf, leading to a weaker vertical mixing. The decrease in salinity of up to 10 psu at the mouth of Galveston Bay due to the MAR discharge results in a decrease in horizontal density gradient, a decrease in the salt flux, and a weakened estuarine circulation and estuarine–ocean exchange. We highlight the flexibility of the model and its capability to simulate not only estuarine dynamics and shelf-wide transport, but also the interactions between them.

1 Introduction

The northern Gulf of Mexico (GoM) is characterized by complicated shelf and coastal processes including multiple river plumes with varying spatial scales, a highly energetic deep current due to steep slopes, upwelling in response to alongshore wind, and mesoscale eddies derived from the Loop Current in the Gulf Stream (Oey et al., 2005; Dukhovskoy et al., 2009; Dzwonkowski et al., 2015; Barkan et al., 2017). Freshwater from the Mississippi–Atchafalaya River (MAR) basin introduces excess nutrients and terminates amidst one of the United States' most productive fishery regions and the location of the largest zone of hypoxia in the western Atlantic Ocean (Rabalais et al., 1996, 2002; Bianchi et al., 2010). The physical, biological, and ecological processes in the region have been attracting increasing attention, given its sensitive response to large-scale climate variation, accelerated sea-level rise, and extensive anthropogenic interventions (Justić et al., 1996; Rabalais et al., 2007).

Understanding the interaction and coupling between regional-scale ocean dynamics and local-scale estuarine processes is of great interest. Many observational (in situ and

satellite) (e.g., Cochrane and Kelly, 1986; DiMarco et al., 2000; Chu et al., 2005) and numerical modeling (e.g., Zavala-Hidalgo et al., 2003, 2006; Hetland and Dimarco, 2008; Fennel et al., 2011; Gierach et al., 2013; Huang et al., 2013) studies have been conducted for the shelf of the GoM. Hetland and Dimarco (2008) configured a hydrodynamic model based on the Regional Ocean Modelling System (ROMS; Shchepetkin and McWilliams, 2005) for the Texas–Louisiana shelf, which has been used for subsequent physical and/or biological studies (Fennel et al., 2011; Laurent et al., 2012; Rong et al., 2014). Zhang et al. (2012) extended the model domain westward to cover the entire Texas coast. Wang and Justić (2009) applied the Finite-Volume Coast Ocean Model (FVCOM; Chen et al., 2006) over a similar domain to that of Hetland and Dimarco (2008). Lehrter et al. (2013) applied the Navy Coastal Ocean Model (NCOM; Martin, 2000) over the inner Louisiana shelf with a focus on Mississippi River plumes. In addition, there were modeling studies for larger domains such as the entire GoM (Oey and Lee, 2002; Wang et al., 2003; Zavala-Hidalgo et al., 2003). For example, Zavala-Hidalgo (2003) used the NCOM to investigate the seasonally varying shelf circulation in the western shelf of the GoM. Bracco et al. (2016) used the ROMS to examine the mesoscale and sub-mesoscale circulation in the northern GoM.

Other hydrodynamic modeling studies focused on specific estuarine systems such as Galveston Bay (Rayson et al., 2015; Rego and Li, 2010; Sebastian et al., 2014), Mobile Bay (Kim and Park, 2012; Du et al., 2018a), and Choctawhatchee Bay (Kuitenbrouwer et al., 2018). These models tend to have smaller domains, including the target estuary and the inner shelf just outside the estuary. The dynamics in these coastal bays are affected by both large-scale shelf conditions and localized small-scale geometric and bathymetric features such as narrow but deep ship channels, seaward-extending jetties, and offshore sandbars, which are typically on the order of 10 to 100 m. Including both the estuarine and shelf processes and their interactions is critically important for a more comprehensive understanding of regional physical oceanography in the northern GoM. For this purpose, cross-scale models with unstructured grids have become an attractive option.

The hydrodynamic conditions (e.g., salinity, stratification, and vertical mixing) over the Louisiana shelf are known to be dominated by the influence of MAR plumes (Lehrter et al., 2013; Rong et al., 2014; Androulidakis et al., 2015). However, their effect on the salinity on the Texas shelf has not been well documented. Measurements at Port Aransas (600 km to the west of Atchafalaya River) show an evident seasonal cycle, with higher salinity during the summer and lower salinity during the winter (Bauer, 2002). Is this seasonality related to the seasonal variation of the MAR discharge and/or to the seasonality of the shelf transport? A broader question may be how the MAR discharge affects the salinity along the Texas coast. Furthermore, it is also important to understand the temporal and spatial scales with which the salinity at or near the mouth of an estuarine system respond to river plumes from neighboring river systems. For example, how long will it take for the salinity at the Texas coast to respond to a pulse of freshwater input from the MAR? This timescale in comparison to the timescales of estuarine processes (e.g., recovery timescale from storm disturbance) will allow one to determine whether the remote influence of neighboring major rivers is necessary to consider.

Here, we present a model for the northern GoM with a domain including all the major estuaries, as well as the shelf, and a fine-resolution grid for local estuaries to resolve small-scale bathymetric or geometric features such as ship channels and dikes. Using Galveston Bay as an example, we highlight the flexibility and capability of the model to simulate both estuarine and shelf dynamics. We demonstrate the importance of the interactions among estuaries and the shelf by investigating the remote influence of the MAR discharge on the hydrodynamics along the Texas coast.

2 Methodology

2.1 Model description

We employed the Semi-implicit Cross-scale Hydroscience Integrated System Model (SCHISM; Zhang et al., 2015, 2016), an open-source community-supported modeling system derived from the early SELFE model (Zhang and Baptista, 2008). SCHISM uses a highly efficient semi-implicit finite-element and finite-volume method with a Eulerian–Lagrangian algorithm to solve the turbulence-averaged Navier–Stokes equations under the hydrostatic approximation. It uses the generic length-scale model of Umlauf and Burchard (2003) with the stability function of Kantha and Clayson (1994) for turbulence closure. One of the major advantages of the model is that it has the capability of employing a very flexible vertical grid system, robustly and faithfully resolving the complex topography in estuarine and oceanic systems without any smoothing (Zhang et al., 2016; Stanev et al., 2017; Du et al., 2018b; Ye et al., 2018). A more detailed description of the SCHISM, including the governing equations, horizontal and vertical grids, numerical solution methods, and boundary conditions, can be found in Zhang et al. (2015, 2016).

2.2 Model domain and grid system

The model domain covers the Texas, Louisiana, Mississippi, and Alabama coasts, including the shelf as well as major estuaries (e.g., Mobile Bay, Mississippi River, Atchafalaya River, Sabine Lake, Galveston Bay, Matagorda Bay, and Corpus Christi Bay) (Fig. 1). The domain also includes part of the deep ocean to set the open boundary far away from the shelf to avoid imposing boundary conditions at topographically complex locations. The horizontal grid contains 142 972 surface elements (triangular and quadrangular), with

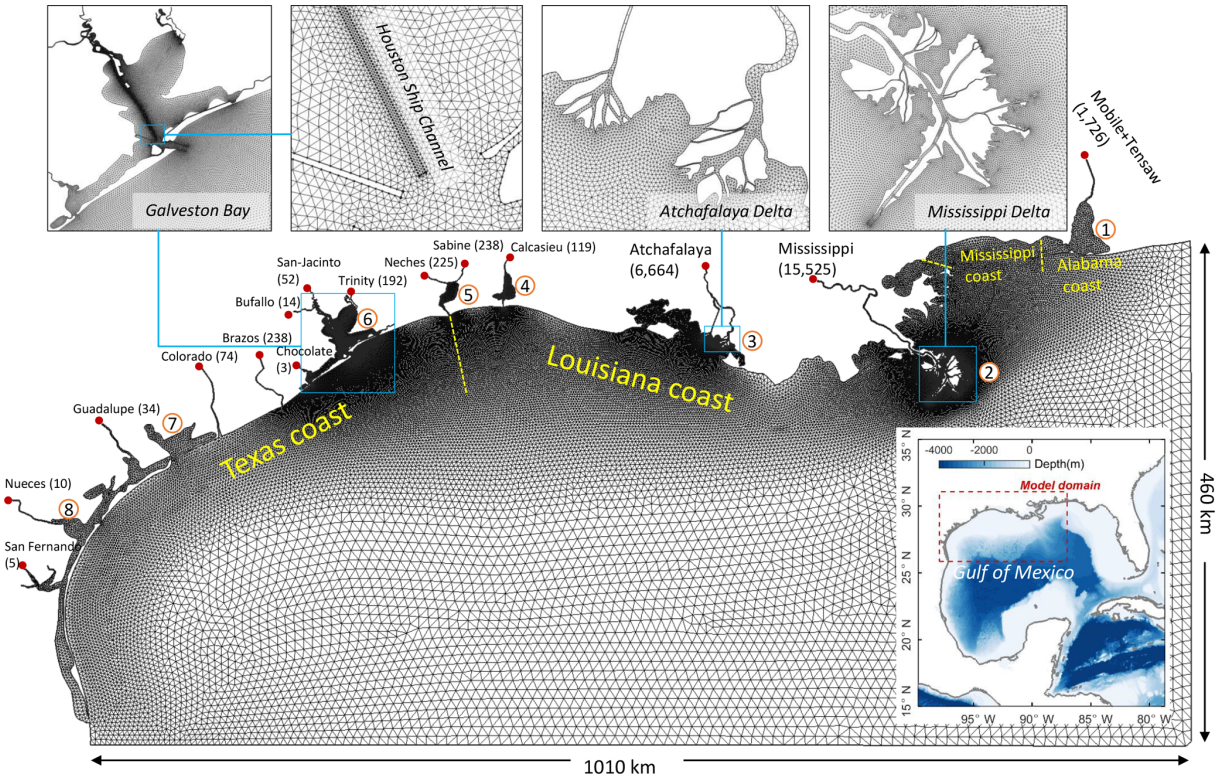

Figure 1. The model domain and the horizontal grid, with the upper panels showing zoomed-in views of selected coastal systems. Locations of major river inputs are indicated with red dots, with the associated mean river discharges ($m^3\ s^{-1}$) shown in parentheses. Major estuarine bay systems in the model domain include Mobile Bay (1), Mississippi River (2), Atchafalaya River (3), Calcasieu Lake (4), Sabine Lake (5), Galveston Bay (6), Matagorda Bay (7), and Corpus Christi Bay (8).

the resolution ranging from 10 km in the open ocean to 2.5 km on average on the shelf (shallower than 200 m) to 40 m at the Houston Ship Channel, a narrow but deep channel along the longitudinal axis of Galveston Bay. The fine grid for the ship channel is carefully aligned with the channel orientation in order to accurately simulate the salt intrusion process (Ye et al., 2018). Vertically, a hybrid s–z grid is used, with 10 sigma layers for depths less than 20 m and another 30 z layers for depths from 20 to 4000 m (20, 25, 30, 35, 40, 50, 60, 70, 80, 90, 100, 125, 150, 200, 250, 300, 350, 400, 500, 600, 700, 800, 900, 1000, 1250, 1500, 2000, 2500, 3000, 4000 m); shaved cells are automatically added near the bottom in order to faithfully represent the bathymetry and thus the bottom-controlled processes. This hybrid s–z vertical grid enables the model to better capture the stratification in the upper surface layer while keeping the computational cost reasonable for simulations of the deep waters. With a time step of 120 s and the second-order finite-volume implicit total variation diminishing (TVD^2) scheme for mass transport, it takes about 24 h for a 1-year simulation with 120 processors (Intel Xeon E5-2640 v4).

The bathymetry used in the model is based on the coastal relief model (3 arcsec resolution; https://www.ngdc.noaa.gov, last access: 7 November 2019). The local bathymetry in Galveston Bay is augmented by 10 m resolution digital elevation model (DEM) bathymetric data to resolve the narrow ship channel (150 m wide, 10–15 m deep) that extends from the bay entrance all the way to the Port of Houston. The bathymetry of the ship channels in other rivers, such as the Mississippi, Atchafalaya, and Sabine, is manually set following National Oceanic and Atmospheric Administration (NOAA) navigational charts. The depth in the model domain ranges from 3400 m in the deep ocean to less than 1 m in Galveston Bay (Fig. 2).

2.3 Forcing conditions

The model was validated for the 2-year conditions in 2007–2008 and was forced by the observed river discharge, reanalysis atmospheric forcing, and open boundary conditions from global HYCOM output. Daily freshwater inputs from United States Geological Survey (USGS) gauging stations were specified at 15 river boundaries (Fig. 1). For the Mississippi River, the largest in the study area, river discharge at Baton Rouge, LA (USGS 07374000), was used. For the Atchafalaya River, the second largest, the discharge data at the upper river station (USGS 07381490 at Simmesport, LA) were used, but the data before 2009 at this station are not

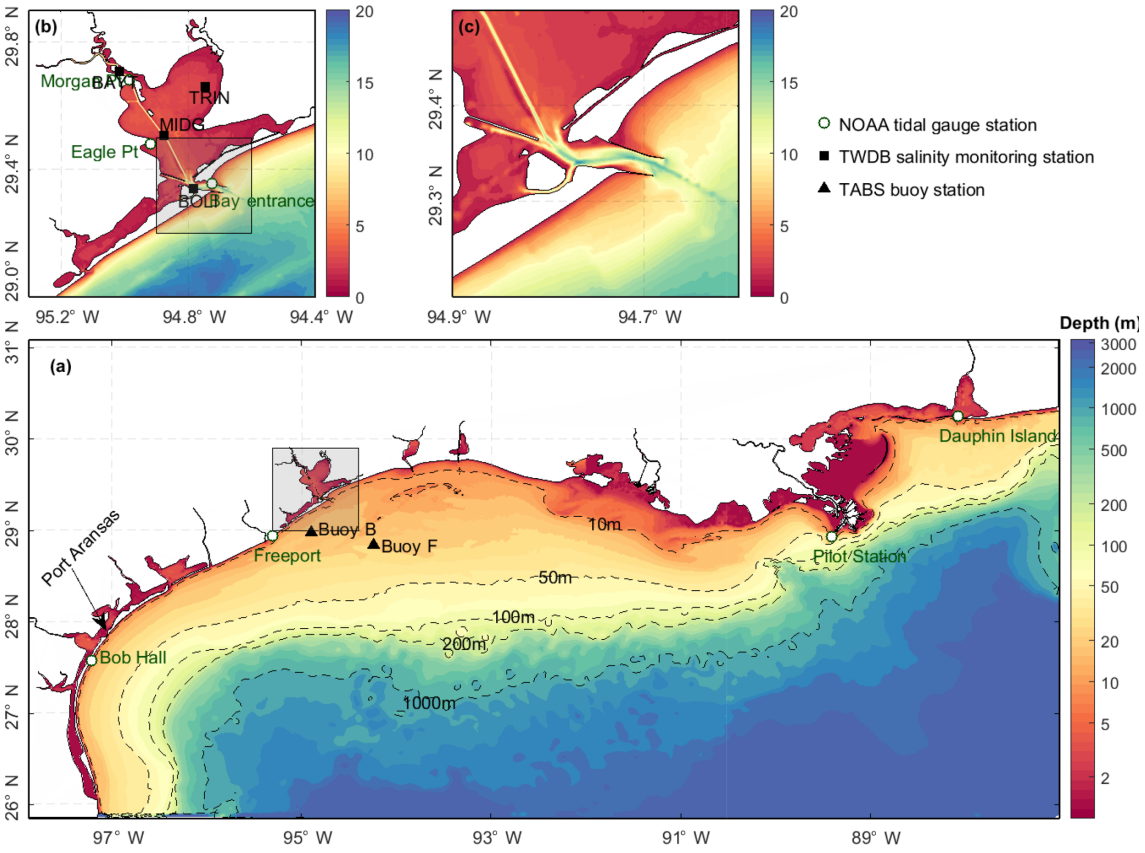

Figure 2. Bathymetry in the model domain showing zoomed-in views **(b–c)** of Galveston Bay and its main entrance. Note the log scale **(a)** for depth because of a very wide range of depth over the entire model domain. Also shown are the NOAA tidal gauge stations (open green circles), TWDB (Texas Water Development Board) salinity monitoring stations (solid black circles), and TABS (Texas Automated Buoy System) buoy stations (black solid triangles).

available. However, we found a significant linear relationship between this station and the one near the river mouth (USGS 07381600 at Morgan City, LA) with a 2 d time lag (r^2 of 0.92) based on the data from 2009 to 2017. The freshwater discharge estimated at Simmesport using this relationship for 2007–2008 was used to specify the Atchafalaya River freshwater input into the Atchafalaya Bay. For the Trinity River, the major river input for Galveston Bay, river discharge at the lower reach station at Wallisville (USGS 08067252) was used, where the mean river discharge (averaged over April 2014 and April 2018) is about 56 % of that at an upper reach station at Romayor (USGS 08066500). This is because the water from Romayor likely flows into wetlands and water bodies surrounding the main channel of the Trinity River before reaching Wallisville (Lucena and Lee, 2017). The river discharge data before April 2014 at the Wallisville station are not available. Similar to the case for the Atchafalaya River, there is a significant linear relationship between these two stations (r^2 of 0.89 with a 4 d time lag based on the data from 2014 to 2018). The freshwater discharge for 2007–2008 estimated using this relationship was used to specify the Trinity River freshwater input into Galveston Bay. River flows from other rivers were prescribed using the data at the closest USGS stations. Water temperatures at the river boundaries were also based on the data at these USGS stations.

Reanalyzed 0.25° resolution, 6-hourly atmospheric forcing data, including air temperature, solar radiation, wind, humidity, and pressure at mean sea level, were extracted from the European Centre for Medium-Range Weather Forecasts (ECMWF; https://www.ecmwf.int, last access: 7 November 2019). SCHISM uses the bulk aerodynamic module of Zeng et al. (1998) to estimate heat flux at the air–sea interface. Both harmonic tide and subtidal water level were used to define the ocean boundary condition, with the harmonic tide (M2, S2, K2, N2, O1, Q1, K1, and P1) from the global tidal model FES2014 (Carrere et al., 2015) and the subtidal water level from the low-pass-filtered (cutoff period of 15 d) daily global HYCOM output. The model was relaxed during inflow to the HYCOM output at the ocean boundary in terms of salinity, temperature, and velocity.

2.4 Numerical experiments

To investigate the remote influence of the MAR discharge, we conducted three numerical experiments that use the same model configuration as in the realistic 2007–2008 model run except for freshwater discharge, wind forcing, initial salinity condition, and salinity boundary condition. To isolate the influence of the MAR discharge, we considered freshwater discharges (constant long-term means) only for the Mississippi River, Atchafalaya River, and Galveston Bay, with no discharge from other coastal systems. To examine the effect of seasonal wind, we chose the January 2008 and July 2008 winds as representative of winter and summer winds, respectively. The January wind was dominated by northeast–east wind and expected to induce a stronger downcoast (from Louisiana toward Texas) longshore current compared to the predominantly south wind in July (Fig. S1). The initial salinity condition is set to 36 psu throughout the entire domain and for all vertical layers. Salinity at the ocean boundary is set to 36 psu throughout the simulation period.

Differences among the three experiment settings include the following: (1) experiment Jan-G includes only the river discharges into Galveston Bay ($259\,m^3\,s^{-1}$) and uses the January 2008 wind; (2) experiment Jan-GAM includes Galveston discharge as well as the MAR discharges ($22\,189\,m^3\,s^{-1}$) and uses the January 2008 wind; and (3) experiment Jul-GAM has the same discharges as Jan-GAM but uses the July 2008 wind. In each simulation, the January or July wind was repeated every month, rather than using monthly mean steady wind, in order to take into account the wind variability, which is known to play an important role in shelf circulation (Ohlmann and Niiler, 2005).

3 Model validation

The model results for 2007–2008 were compared with observations for water level at seven NOAA tidal gauge stations, salinity at four Texas Water Development Board (TWDB) stations, temperature at three NOAA stations, and current velocity at two Texas Automated Buoy System (TABS) buoys (see Fig. 2 for station locations). Comparisons were made for both total and subtidal (48 h low-pass-filtered) components. For quantitative assessment of the model performance, two indexes were used, model skill (Willmott, 1981) and mean absolute error (MAE):

$$\text{Skill} = 1 - \frac{\sum_{i=1}^{N} |X_{\text{mod}} - X_{\text{obs}}|^2}{\sum_{i=1}^{N} (|X_{\text{mod}} - \overline{X_{\text{obs}}}| + |X_{\text{obs}} - \overline{X_{\text{obs}}}|)^2}, \quad (1)$$

$$\text{MAE} = \frac{1}{N} \sum_{i=1}^{N} |X_{\text{mod}} - X_{\text{obs}}|, \quad (2)$$

where X_{obs} and X_{mod} are the observed and modeled values, respectively, with the overbar indicating the temporal average over the number of observations (N). The model skill provides an index of model–observation agreement, with a skill of 1 indicating perfect agreement and a skill of 0 indicating complete disagreement. The magnitude of the MAE indicates the average deviation between the model and observations.

3.1 Water level

Model–observation comparisons were made for water level at stations along the coast and inside Galveston Bay. Manning's friction coefficient, which is converted to the bottom drag coefficient for the 3-D simulation in the model, was used as a calibration parameter. The model results with a spatially uniform Manning's coefficient of $0.016\,m^{1/3}\,s^{-1}$ show good agreement with the observational data. Overall, the model reproduces both the tidal and subtidal components of water level at tidal gauge stations along the coast as well as inside Galveston Bay (Fig. 3, Table 1, and Fig. S2). The MAE is in the range of 7–8 and 5–7 cm for the total and subtidal components, respectively. The model skill varies spatially, with relatively low skills (0.88) at Pilot Station and Dauphin Island for the subtidal component and high skills (≥ 0.94) at the stations on the Texas coast, including Galveston Bay, for both the total and subtidal components. It is interesting to note that the model has also simulated the storm surge well during Hurricane Ike (around day 625), one of the most severe hurricanes to hit the Houston–Galveston area in recent years. When applied to investigate the dramatic estuarine response to Hurricane Harvey (2017) in Galveston Bay, this model successfully reproduced the long-lasting elevated water level inside the bay (Du and Park, 2019a; Du et al., 2019b). Simulation of surface elevation is sensitive to topography, bottom friction, boundary conditions, and atmospheric forcings. Some discrepancies are expected due to the assumption of a spatially uniform Manning's coefficient. Further improvement might be achieved by using spatially varying coefficients, but we did not deem it worth trying, considering the current satisfactory performance of the model. Additional discrepancies may come from the limited spatial and temporal resolution of atmospheric forcings, the accuracy of the bathymetric data, and the reliability of the open boundary conditions from the global HYCOM output.

3.2 Salinity

The model reasonably reproduces the observed variation in salinity at stations inside Galveston Bay (Fig. 4 and Table 1). The MAEs are no larger than 3 psu and the model skills range between 0.81–0.93 and 0.75–0.93 for the total and subtidal components, respectively. It is important to note that the salinity at the bay mouth under normal (i.e., non-flooding) conditions is sensitive to the longshore transport

Table 1. Error estimates for model–data comparison for 2007–2008.

Variables	Station	Total		Subtidal	
		MAE	Skill	MAE	Skill
Water level (cm)	Morgan's Point	7.61	0.96	6.65	0.95
	Eagle's Point	6.87	0.96	6.13	0.96
	Bay Entrance	7.98	0.96	6.17	0.94
	Freeport	7.62	0.96	6.37	0.94
	Bob Hall	6.65	0.97	5.41	0.94
	Pilot Station	6.23	0.95	5.36	0.88
	Dauphin Island	7.29	0.94	6.61	0.88
Salinity (psu)	TRIN (1.5 m)[a]	2.06	0.93	2.03	0.93
	BAYT (2.0 m)[a]	2.69	0.87	2.59	0.87
	MIDG (3.1 m)[a]	2.56	0.86	2.43	0.85
	BOLI (2.9 m)[a]	3.04	0.81	2.92	0.75
Surface temperature (°C)	Morgan's Point	0.93	0.99	0.92	0.99
	Eagle's Point	1.27	0.99	1.26	0.99
	Bay Entrance	0.91	0.99	0.86	0.99
Surface velocity ($m\,s^{-1}$)	Buoy B	0.14	0.88	0.11	0.82
	Buoy F	0.10	0.79	0.08	0.67

[a] The value within parentheses indicates the mean depth of the sensor below the surface.

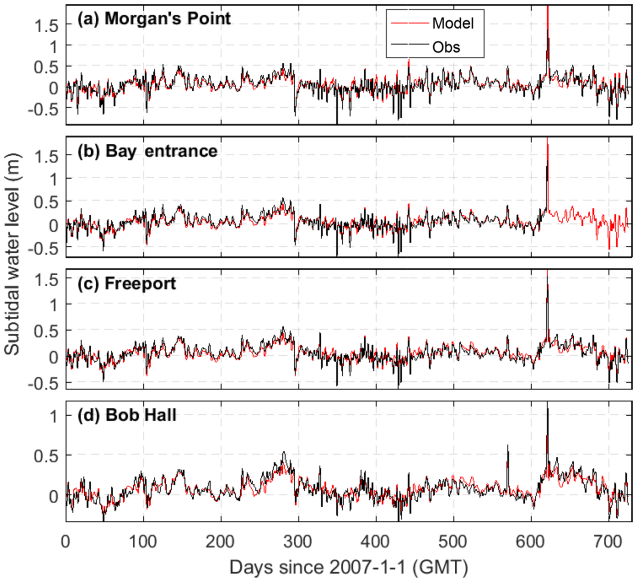

Figure 3. Subtidal surface elevation comparison between the model (red line) and observations (black line) at NOAA tidal gauge stations (see Fig. 2 for their locations).

of low-salinity water from neighboring estuaries, such as the nearby Sabine–Neches River, Atchafalaya River, and Mississippi River. Successful simulation of salinity at the bay mouth requires an accurate simulation of not only the bay-wide transport, but also the longshore transport. Errors in the modeled salinity at the bay mouth can propagate to the upper bay. For example, salinity during days 60–100 is overestimated at the mouth (station BOLI) and this error propagated into the middle bay station (station MIDG) (Fig. 4). Discrepancies as large as 10 psu are not likely caused by inaccurate discharge from the Trinity River, as this river has a very limited influence on the salinity on the shelf (further discussed in Sect. 4.3). Unfortunately, with no data available for the vertical salinity profile, the model performance for vertical mass transport cannot be evaluated. However, accurate simulation of the observed salinity at the mid-bay station provides alternative evidence supporting the model's validity in horizontal mass transport and salt intrusion.

The model also captures the sharp change in salinity during Hurricane Ike (around day 620). The salinity at the upper bay (Fig. 4b) decreased from 26 psu to 0 within 2 d, which was caused by a pulse of freshwater discharge from Lake Houston (see reservoir storage at USGS 08072000). In addition, the model reproduces the spatial difference well in the amplitude of the tidal signal in salinity. Salinity in Trinity Bay (Fig. 4a) shows a very weak tidal signal, while salinity at the bay mouth (Fig. 4d) has a much stronger tidal signal. Galveston Bay, in general, has micro-tidal ranges with a mean tidal range of 0.3 m at the mid-bay station (Eagle Point in Fig. 2). The tidal signal, however, becomes stronger at the narrow bay mouth (2.5 km wide), with the tidal current being as strong as $1\,m\,s^{-1}$ (see station g06010 at http://pong.tamu.edu/tabswebsite/, last access: 7 November 2019).

The modeled salinity was also compared to the observed salinity structure over the Texas–Louisiana shelf using the

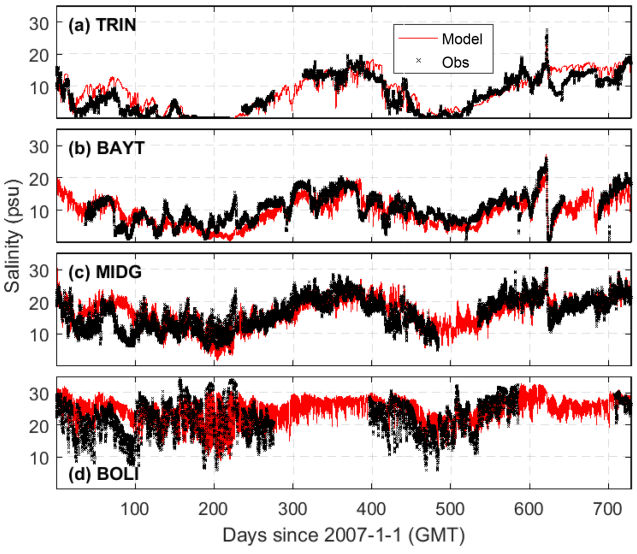

Figure 4. Salinity comparison between the model (red line) and observations (black cross) at four TWDB stations (see Fig. 2 for their locations).

data from a shelf-wide summer survey in July 2008 as an example (Fig. 5). Both the horizontal and vertical structures of salinity on the shelf are well reproduced by the model, with an MAE over 65 stations of 1 and 2 psu for the surface and bottom salinity, respectively. Data and the model consistently show a relatively shallow halocline at section A (west of Mississippi Delta) and a deeper halocline at section F (off Atchafalaya Bay). The upper layer off Atchafalaya Bay was nearly well mixed, which is also reproduced by the model, although the model somewhat underestimates the bottom salinity at section F. In addition, the model also shows that there was little tidal variability of the vertical salinity profile on the shelf (e.g., stations F4 and A7 in Fig. 5), which can be attributed to the small tidal range in the northern GoM.

3.3 Temperature

The model reproduces the observed temperatures well at three NOAA stations located from the Galveston Bay mouth to the upper bay (Fig. 6). Both the seasonal and diurnal cycles are well captured, with MAEs of about 1 °C and model skills of 0.99. Even within a relatively small region inside Galveston Bay, temperature can vary significantly. During days 300–350, for example, large fluctuations in temperature occurred at the mid-bay station (Fig. 6b), while the fluctuations were smaller at the bay entrance (Fig. 6a) and the upper bay (Fig. 6c). These spatiotemporal variations are reproduced well by the model, demonstrating not only the good performance of the model, but also the reliability of the atmospheric forcing data.

The model performance in reproducing temperature over the Texas–Louisiana shelf was further examined with satellite data for sea surface temperature (SST). Seasonality of the SST extracted from MODIS over the northern GoM is overall reproduced well (Fig. 7). It is worth noting that the model also reproduces the relatively low temperatures on the southern Texas coast during summer, which is a well-known upwelling zone during the summertime when upcoast (from Texas toward Louisiana) winds drive an offshore surface transport (Zavala-Hidalgo et al., 2003).

3.4 Shelf current

The shelf current plays a key role in transporting low-salinity water originating from MAR, and it can be affected by not only the wind field, but also the mesoscale eddies in the northern GoM. One of the important features of the Texas–Louisiana shelf is the quasi-annual pattern of the shelf current, which is predominantly westward most of the time except during summer (Cochrane and Kelly, 1986; Li et al., 1997; Cho et al., 1998). The prominent downcoast shelf current is driven by along-shelf wind and enhanced by the MAR discharge (Oey, 1995; Li et al., 1997; Nowlin et al., 2005). Under summer wind that usually has an upcoast component, the nearshore current is reversed to the upcoast direction (Li et al., 1997). Such seasonality also occurred during 2007–2008. The model reproduces the observed subtidal component of the surface longshore current at two TABS buoy stations outside Galveston Bay, buoy B ($\sim$ 20 km offshore) and buoy F ($\sim$ 80 km offshore) (Fig. 8), with MAEs of 8–14 cm s^{-1} and model skills of 0.67–0.88 (Table 1).

4 Remote influence of the MAR discharge

The conditions in Texas coastal waters are impacted by several remote sources, including mesoscale eddies (Oey et al., 2005; Ohlmann and Niiler, 2005), longshore transport of low-salinity water from major rivers (Li et al., 1997; Nowlin et al., 2005), and Ekman transport induced by longshore wind and the resulting upwelling–downwelling (Li et al., 1997; Zhang et al., 2012). Here, based on the realistic model results and numerical experiments, we discuss the remote influence of major river discharge and shelf dynamics on the longshore transport, salinity, stratification, and vertical mixing at the Texas coast, as well as the water exchange between the coastal ocean and local coastal system.

4.1 Variation in shelf current and salinity

The strength and direction of the shelf current are sensitive to the wind field. Comparison of the model results on day 150 (31 May 2007) and day 160 (10 June 2007) clearly shows the different distribution of lower-salinity water along the coast in response to wind field and the resulting shelf current (Fig. 9). The river discharge differences between these two days are negligible, and thus the differences in lower-salinity water distribution can be mainly attributed to the dif-

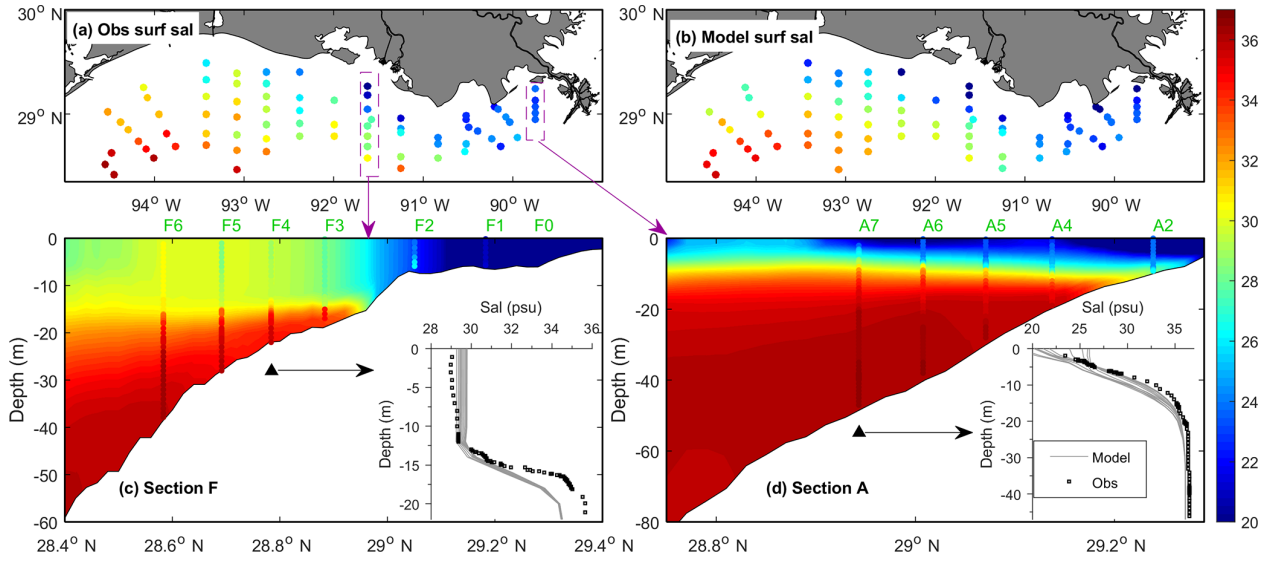

Figure 5. Salinity distribution at the Texas–Louisiana shelf from the shelf-wide survey on 22–27 July 2018: comparison of **(a)** observed and **(b)** modeled surface salinity and of the vertical profiles at two cross-shelf sections, **(c)** F and **(d)** A. In **(c)** and **(d)**, the colored dots indicate observed salinity, while the filled colors indicate modeled salinity, and the insets compare the vertical profiles of salinity at the selected stations of F4 and A7, respectively. The grey lines in the insets show the 12 modeled profiles over 1 d (observation time ±0.5 d).

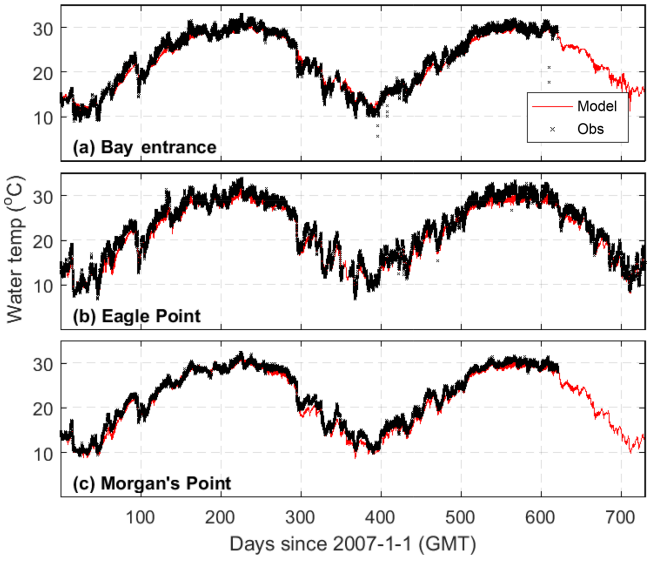

Figure 6. Temperature comparison between the model (red line) and observations (black line) at three NOAA stations (see Fig. 2 for their locations).

ferences in shelf current. Day 150 was characterized by a significant downcoast shelf current in the inner shelf, with a current speed exceeding 0.5 m s^{-1}, while day 160 was characterized by a rather weak shelf current with a speed of less than 0.1 m s^{-1}. The pattern of the surface residual current is related to the wind field. On day 150, a downcoast component of the wind induced an onshore Ekman transport, which in turn resulted in a downcoast geostrophic flow (Li et al., 1997). This downcoast flow transported low-salinity water from MAR toward Texas while constraining it to a narrow band against the shoreline (Fig. 9e). Under a weak or upcoast shelf current, in contrast, this constraining was weakened, leading to the offshore displacement of low-salinity water (Fig. 9f). As a result, salinity on the Texas inner shelf was higher on day 160 than on day 150.

Regulated by the shelf current, salinity distribution over the shelf exhibits evident seasonality. The model results show that a narrow band of lower-salinity water persisted from Louisiana to the western Texas inner shelf during January–May 2008 (Fig. 10). The salinity at the Galveston Bay mouth decreased by about 10 psu from January to May, which can be attributed to the increasing Mississippi discharge from January to May in 2008 (Mississippi discharge data at https://waterdata.usgs.gov/usa/nwis/uv?site_no=07374000, last access: 7 November 2019). Starting from June 2008, the salinity along the western Texas shelf gradually increased as higher-salinity water from the southwestern boundary moved upcoast. The salinity at the Galveston Bay mouth increased from less than 20 psu in June to >30 psu in August (Fig. 10), about the same magnitude of salinity change from January to May. It suggests that the influence of the seasonally varying shelf circulation on salinity at the Texas coast is comparable to that of the seasonal variation in the MAR discharge.

4.2 Influence of the MAR discharge on shelf transport and salinity

Longshore transport plays a key role in redistributing freshwater from the estuarine bays along the shelf. The results

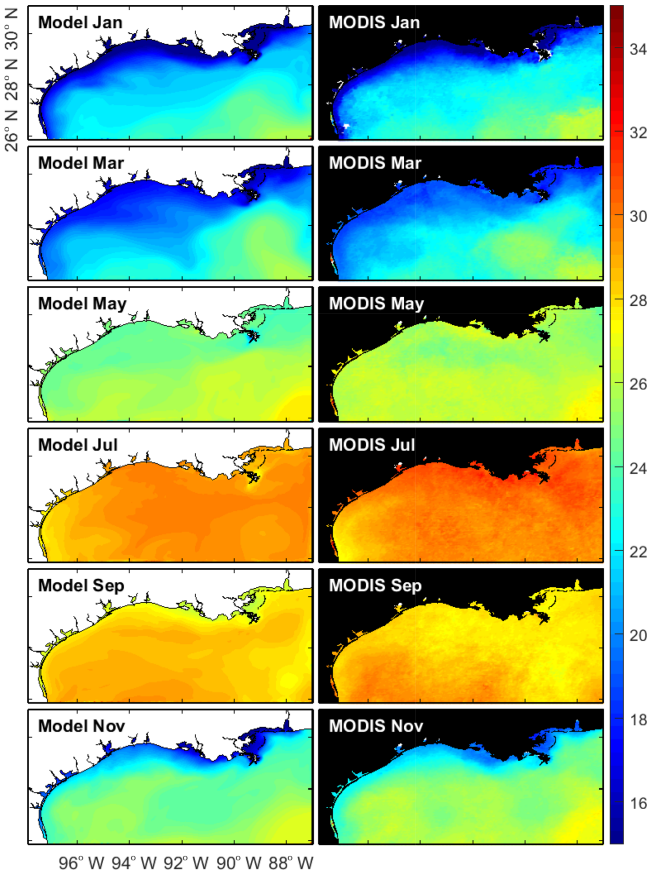

Figure 7. Temperature comparison (monthly average) between the model (left panels) and MODIS satellite data (right panels) for selected months in 2008.

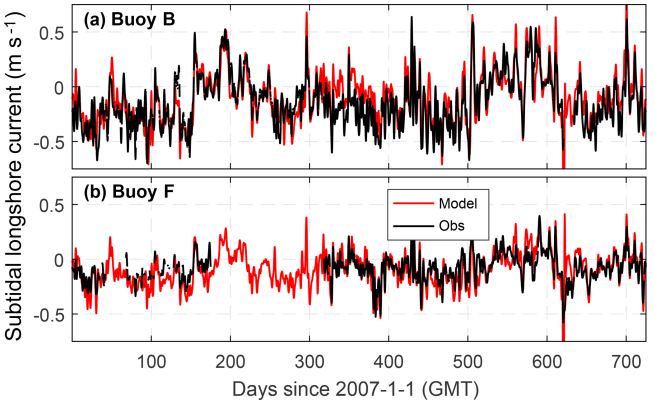

Figure 8. Comparison of the subtidal east–west surface shelf current between the model (red line) and observations (black line) at two TABS buoys (see Fig. 2 for their locations).

from three numerical experiments show that, under the January wind, the downcoast longshore transport among four selected cross-shelf sections varies little. The longshore transport is enhanced by the MAR discharge (long-term mean) by 10 %–14 % ($\sim 80\,000\,m^3\,s^{-1}$), about 4 times the long-term mean river discharge from MAR ($\sim 22\,000\,m^3\,s^{-1}$) (Fig. 11). The transport, however, is greatly reduced under the July wind and it decreases downcoast, with the magnitude being 1 order smaller on the Texas shelf compared to that under the January wind. The difference in longshore transport is related to the shelf circulations, which exhibit distinctly different patterns under different wind conditions (Fig. S3). Under the January wind, the surface shelf current flows downcoast, while under the July wind, it is weak and mainly in a direction normal to the coastline, resulting in a much smaller longshore transport.

The influence of the MAR discharge on shelf salinity also depends on the wind condition and the resulting shelf current. Surface salinity maps averaged over days 250–300 show distinctly different spatial patterns of the lower-salinity water under different wind conditions (Fig. 12). The patterns are similar to the results from the 2007–2008 realistic run (Fig. 10). Under the winter wind, lower-salinity water is trapped nearshore by the shelf current, forming a narrow band along the coast. Under the summer wind, on the other hand, water on the Texas shelf is replenished by saltier water originating from the southwest, leading to a tongue-shaped saltier-water intrusion toward the lower-salinity water over the Louisiana shelf. Consequently, salinity is higher on the Texas shelf and lower on the Louisiana shelf when compared to that under the winter wind.

4.3 Influence of the MAR discharge on Texas coast: salinity, stratification, and mixing

Numerical experiments reveal different time and spatial scales with which the surface salinity in Texas coastal water responds to the MAR discharge (Fig. 13). At the Galveston Bay mouth, the salinity begins to decrease from about day 25 in response to the MAR discharge and continues to decrease until around day 100 when it reaches a quasi-steady state. The MAR discharge (long-term mean) reduces the salinity by about 10 psu under the January wind but only by 5–6 psu under the July wind. Further south at the Port Aransas mouth, the response time doubles to about 50 d, with the MAR discharge reducing the salinity by about 6 psu under the January wind. Salinity changes little in response to discharges from Galveston Bay and the MAR discharge under the July wind. As the influence from Galveston Bay is very limited at the Aransas Bay mouth even under a downcoast wind, it is reasonable to assume the influence will be even smaller under an upcoast wind.

Vertical profiles of salinity along a section from the Trinity Bay, along the Houston Ship Channel and the adjoining shelf, show that the MAR discharge increases salinity stratification on the shelf (Fig. 14). The lower-salinity water along the coastline increases the cross-shelf baroclinic pressure gradient, leading to a stronger stratification. There is a distinctive difference between Jan-GAM and Jul-GAM. A stronger stratification on the inner shelf appears under the July wind,

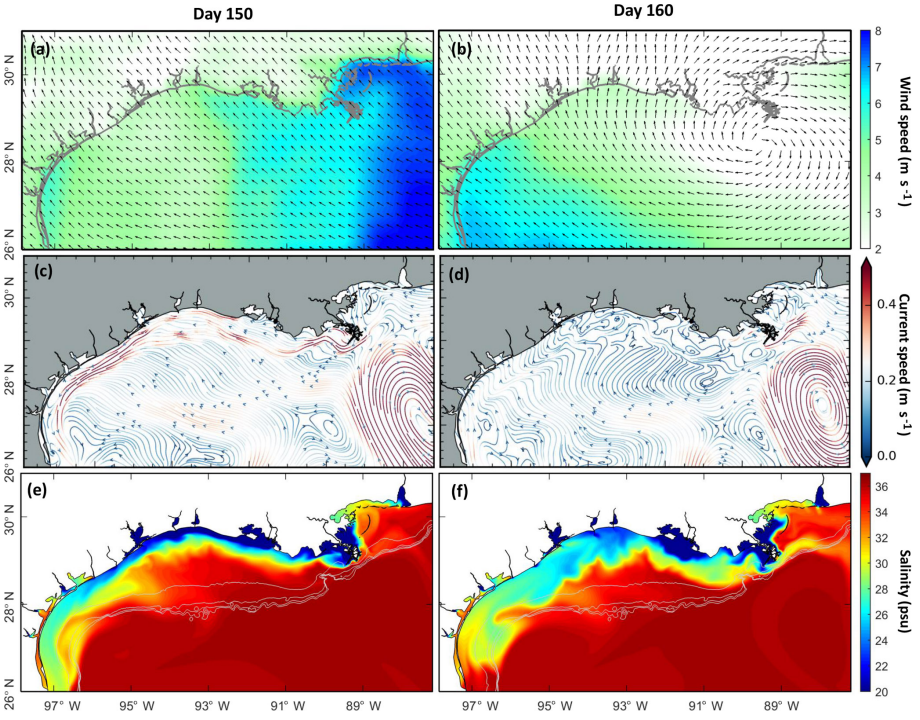

Figure 9. Comparison of the observed wind field and the modeled surface residual current and surface salinity on day 150 (31 May 2007) and day 160 (10 June 2017). The filled colors indicate the daily mean wind speed **(a, b)**, the speed of the residual current **(c, d)**, and salinity **(e, f)**.

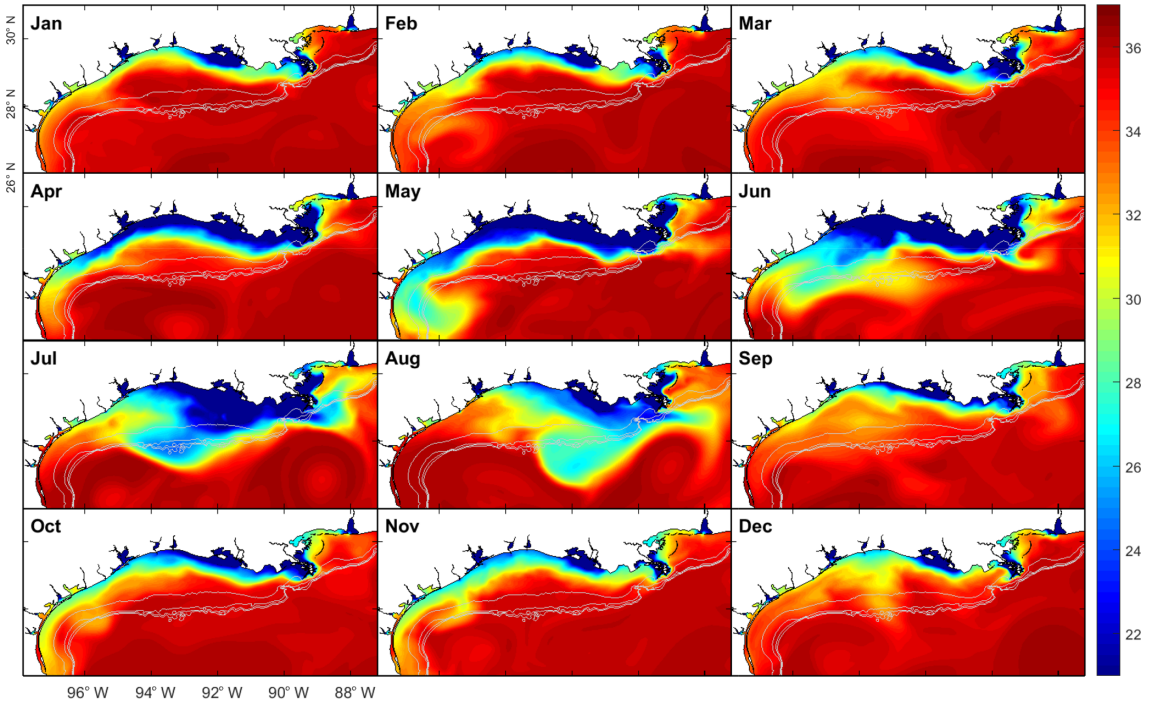

Figure 10. The modeled monthly mean surface salinity in 2008, with the grey contour lines denoting depth contours of 50, 100, 150, and 200 m.

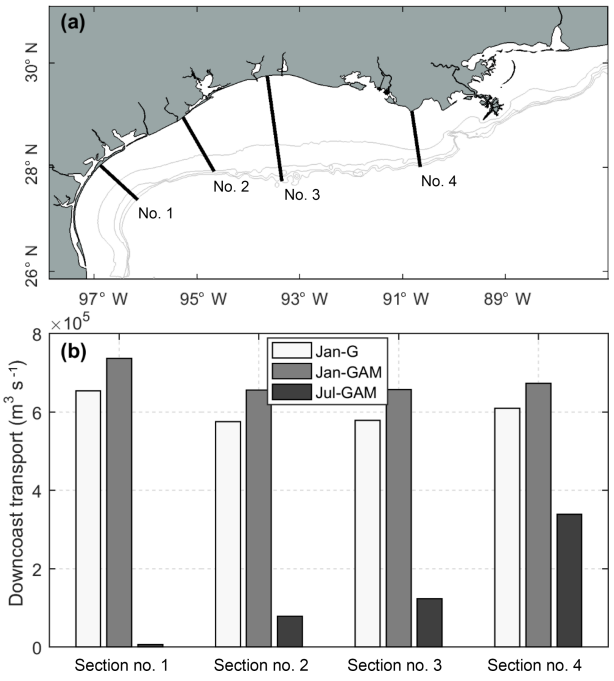

Figure 11. Downcoast longshore transport at four selected cross-shelf sections for three numerical experiments with constant long-term mean river discharges: river discharges into Galveston Bay only with January 2018 wind (Jan-G) and the MAR discharge as well as discharges into Galveston Bay with January 2018 wind (Jan-GAM) or July 2018 wind (Jul-GAM).

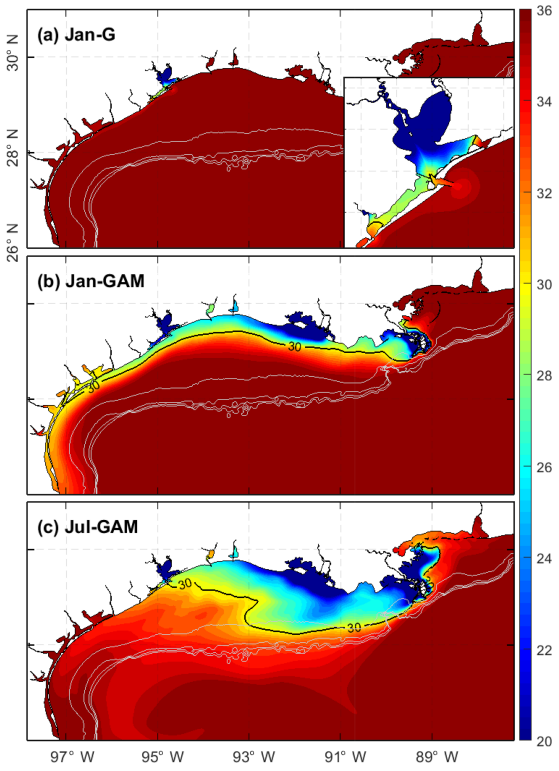

Figure 12. Surface salinity distributions averaged over days 250–300 from three numerical experiments. Grey contour lines denote depth contours for 50, 100, 150, and 200 m.

with the bottom-surface salinity difference as large as 4 psu. Vertical mixing on the inner Texas shelf is weakened due to the MAR discharge, particularly under the July wind. The vertical diffusivities are 1 or 2 orders of magnitude smaller than those under the January wind. Under the July wind, the stratification along the ship channel becomes stronger, probably because of higher salinity near the bay mouth and/or a weaker wind in July with a mean speed of 4.79 m s^{-1} relative to a mean speed of 6.88 m s^{-1} in January (Fig. S1). Higher salinity near the mouth induces a stronger horizontal salinity gradient, leading to stronger circulation and stratification.

4.4 Influence of the MAR discharge on estuarine–coastal exchange

Salinity change due to remote river input and a shift in the wind field affects the estuarine dynamics, such as estuarine circulation, salt flux, and estuarine–coastal exchange. We examined the change in exchange flow and salinity at the Galveston Bay mouth due to remote river influence and a different shelf current. Following Lerzak et al. (2006), we calculated the tidally averaged and cross-sectionally varying components (u_e and S_e) from the along-channel velocity u and salinity S. From the vertical profiles of u_e and S_e at the deepest part between the two jetties at the bay mouth, it is evident that in the lower layer u_e is strongest (maximum of 6 cm s^{-1})

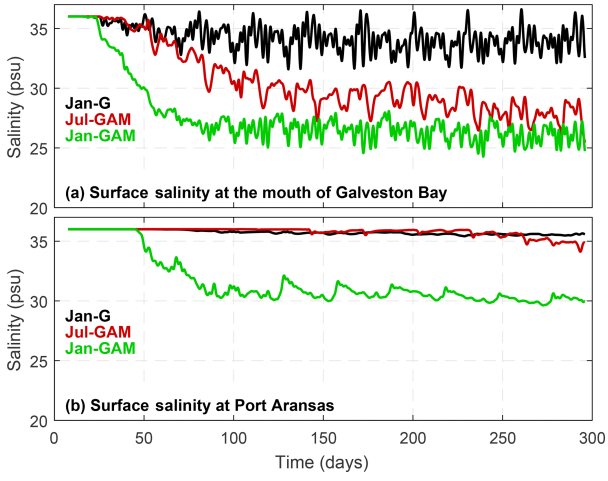

Figure 13. Subtidal surface salinity at the mouth of **(a)** Galveston Bay and **(b)** Aransas Bay for three numerical experiments.

and S_e is largest (maximum of 0.95 psu) for the case Jan-G, indicating the strongest exchange flow (i.e., estuarine circulation) compared to the other two cases with the MAR discharge (Fig. 15). In contrast, the case Jan-GAM shows the weakest bottom u_e (maximum of 4 cm s^{-1}) and the smallest bottom S_e (maximum of 0.60 psu). The MAR discharge

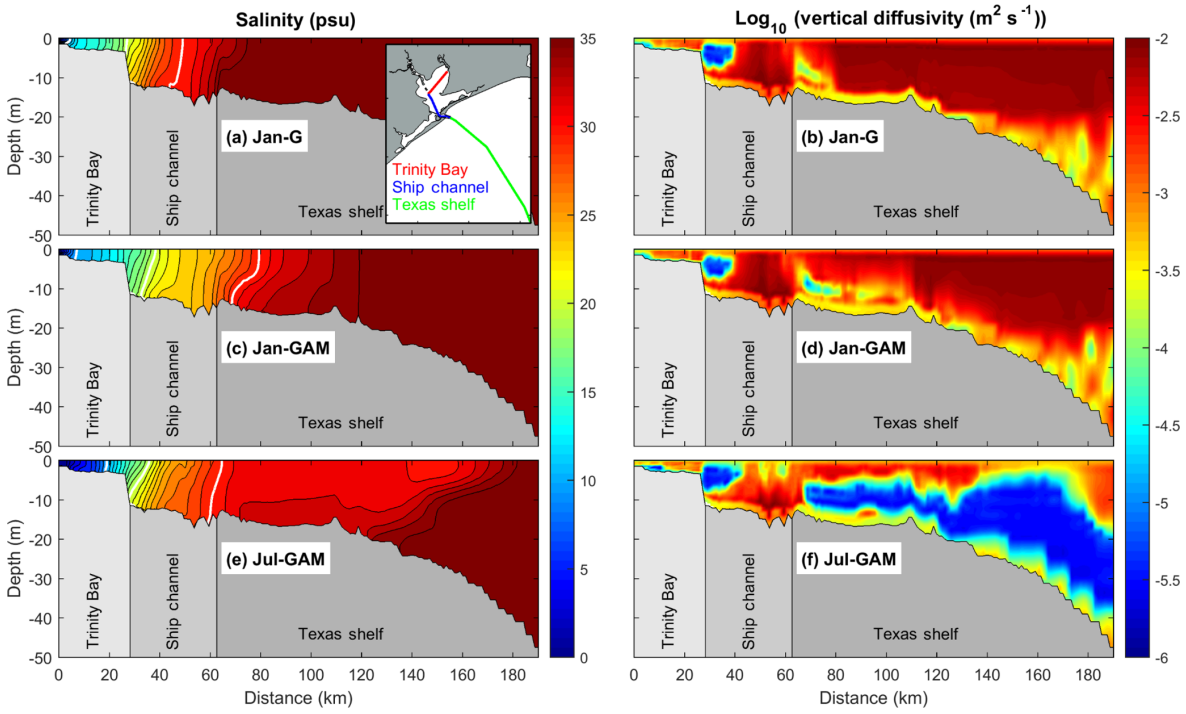

Figure 14. Salinity **(a, c, e)** and vertical diffusivity **(b, d, f)** averaged over days 250–300 from three numerical experiments for the section through Trinity Bay, the Galveston Bay ship channel, and the Texas shelf: see the inset in **(a)** for the section location. In **(a)**, the bold white lines denote salinity contours of 10, 20, and 30 psu.

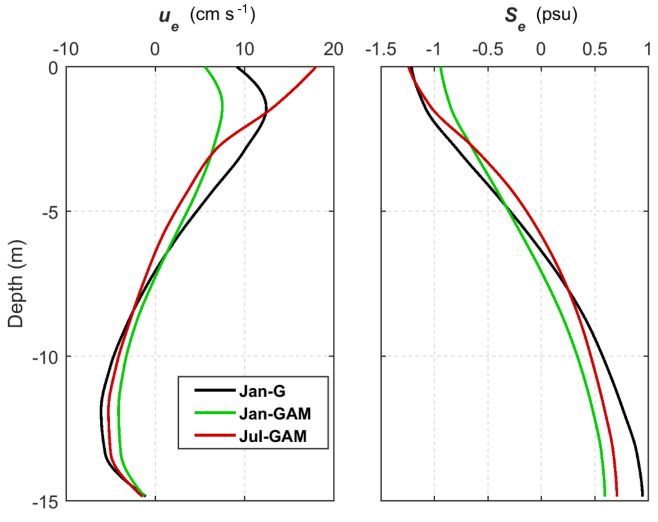

Figure 15. Vertical profiles of exchange flow (u_e) and salinity (S_e) at the deepest part of the Galveston Bay mouth averaged over days 250–300 for three numerical experiments.

under the January wind condition decreases the salinity at the bay mouth the most and results in the weakest horizontal salinity gradient and exchange flow.

The influence of the MAR discharge on the dynamics of Galveston Bay was further examined with total exchange flow (TEF) using the isohaline framework method proposed by MacCready (2011), which was found to be a precise way to quantify landward salt transport (Chen et al., 2012). In this method, the tidally averaged volume flux of water with salinity greater than s is defined as

$$Q(s) = \left\langle \int_{A_s} u \mathrm{d}A \right\rangle, \tag{3}$$

where A_s is the tidally varying portion of the cross section with salinity greater than s. In our case, we calculated $Q(s)$ for the salinity bins from 0 to 35 psu with an interval of 0.5 psu. The volume flux in a specific salinity class is defined as

$$-\frac{\partial Q}{\partial s} = -\lim_{\delta s \to 0} \frac{Q(s+\delta s/2) - Q(s-\delta s/2)}{\delta s}, \tag{4}$$

where the minus sign indicates that a positive value of $-\partial Q/\partial s$ corresponds to inflow for a given salinity class. The total exchange flow (Q_{in}), the flux of water into the estuary due to all tidal and subtidal processes, is then calculated as

$$Q_{\mathrm{in}} \equiv \int \frac{-\partial Q}{\partial s} |_{\mathrm{in}} \mathrm{d}s \ . \tag{5}$$

The resulting salt flux into the estuary (F_{in}) is given by

$$F_{\mathrm{in}} = \int s(-\frac{\partial Q}{\partial s})\Big|_{\mathrm{in}} \mathrm{d}s, \tag{6}$$

Table 2. Total exchange flow (Q_{in}) and the resulting salt flux (F_{in}) at the Galveston Bay mouth, as well as the mean residence time of the bay (T_{res}) based on the isohaline method in MacCready (2011).

Case ID[a]	Q_{in} ($m^3\ s^{-1}$)	F_{in} (kg salt s^{-1})	T_{res} (days)	S^{b}_{mean} (psu)
Jan-G	1.93×10^3	6.75×10^4	13.0	20
Jan-GAM	1.46×10^3	3.47×10^4	16.0	13
Jul-GAM	1.80×10^3	5.30×10^4	13.1	16

[a] See Fig. 11 for an explanation of idealized runs. [b] Mean salinity (volume-weighted average over days 250–300) inside the bay.

and the ratio of salt mass inside the estuary to the salt influx gives the mean residence time (T_{res}):

$$T_{res} = \frac{\int s dV}{F_{in}}, \quad (7)$$

where V is the estuarine volume.

Table 2 lists the values of Q_{in}, F_{in}, and T_{res} for three numerical experiments. For the exchange flow, Q_{in} is largest for the case Jan-G and smallest for the case Jan-GAM. The MAR discharge under the January wind condition causes the largest decrease in salinity at the Galveston Bay mouth (Fig. 13a), effectively slowing down the water exchange between the bay and coastal ocean. The reduction in Q_{in} caused by the remote discharge ($470\ m^3\ s^{-1} = 24\ \%$ reduction) is 1.8 times the long-term mean river input into Galveston Bay ($259\ m^3\ s^{-1}$). Moreover, F_{in} for the case Jan-GAM is about half of that in the case Jan-G. As a result, T_{res} of the bay is largest in the case Jan-GAM, although the difference in T_{res} is not as large as that in F_{in} because the bay has the smallest salt mass in the case Jan-GAM (Table 2). This analysis also suggests that the exchange between the bay and coastal ocean is likely stronger during summer than during winter under the same river discharge condition.

5 Summary

An unstructured-grid hydrodynamic model with a hybrid vertical grid was developed and validated for water level, current velocity, salinity, and temperature for Galveston Bay as well as over the shelf in the northern GoM. The good model performance, particularly in terms of salinity (vertically and horizontally), is at least in part attributable to the inclusion of multiple river plumes along the coastline as well as the interaction between estuaries and the shelf. This model provides a good platform that can be used for other purposes in future studies. Its flexibility in the horizontal and vertical grids allows for refinement in any region of interest without a penalty in the time step (due to the semi-implicit scheme). For example, it would be relatively easy to adapt the model by refining the grid inside any target bay, e.g., Corpus Christi Bay.

The 2007–2008 model run reveals the seasonally varying influence of the MAR discharge on the Texas shelf. Three numerical experiments were carried out to examine the extent to which the major rivers in the region influence local coastal bay systems in Texas. The MAR discharge has a great influence on the salinity regime along the Texas coast and its influence depends on the wind-controlled shelf circulation. Winter wind drives a stronger downcoast longshore transport with its magnitude at least 1 order larger than that under summer wind. The MAR discharge (long-term mean) enhances the downcoast transport by 10 %–14 % under winter wind, and it lowers the salinity by up to 10 psu at the mouth of Galveston Bay and 6 psu at the mouth of Port Aransas. Vertical mixing is also sensitive to wind forcing. Summer wind tends to displace low-salinity water further offshore, while the winter wind constrains the low-salinity water to a narrow band against the shoreline. As a result, the stratification is stronger and vertical mixing is weaker over the shelf during summer. The lower-salinity condition on the Texas shelf decreases the longitudinal salinity gradient at the bay mouth, leading to a weakened estuarine circulation and weaker salt exchange.

This study demonstrates the necessity of including the remote influence of the MAR discharge for modeling Texas coastal systems, particularly for processes associated with relatively long timescales (e.g., months). Receiving relatively small freshwater discharge and being limited by narrow outlets and small tidal ranges, the estuarine bay systems along the Texas coast, e.g., Galveston Bay, Aransas Bay, and Corpse Christi Bay, are characterized by relatively slow water exchange and long flushing times. In this study, we show that the exchange flow plays an important role for water renewal and that the exchange flow varies greatly depending on the wind field and the resulting shelf current. Modulation by the MAR discharge, when coupled with downcoast wind conditions, could have a great influence on the dynamics of estuaries along the Texas coast.

Data availability. All the observational data used for model validation are available online. Salinity data are extracted from TDWB (https://waterdatafortexas.org/coastal). Continuous monitoring data on temperature and water level are extracted from NOAA Tide and Current (https://tidesandcurrents.noaa.gov/). Surface buoy current data are extracted from TABS (http://pong.tamu.edu/tabswebsite/). Daily satellite data (4 km resolution) are extracted from https://podaac.jpl.nasa.gov/. Shelf-wide summer survey data for 2008 are accessible at the National Oceanographic Data Center (NODC) with the accession number 0069471 (https://www.data.gov/). The model output is available upon request. All URLs in this section were last accessed on 7 November 2019.

Supplement. The supplement related to this article is available online at: https://doi.org/10.5194/os-15-951-2019-supplement.

Author contributions. JD and KP led the effort for model development, data analysis, and preparation of the paper. JS, YJZ, FY, and ZW provided guidelines for the model configuration in terms of forcings and boundary conditions. XY assisted in the visualization of modeled and observed data. NNR provided the shelf-wide survey data for the model validation. All authors were involved in writing the paper.

Competing interests. The authors declare that they have no conflict of interest.

Acknowledgements. The numerical simulation was performed on the high-performance computer cluster at the College of William and Mary.

Financial support. This study was partially supported by the Texas Coastal Management Program, the Texas General Land Office, and NOAA through CMP contract no. 19-040-000-B074.

Review statement. This paper was edited by Eric J. M. Delhez and reviewed by Ivica Janeković and one anonymous referee.

References

Androulidakis, Y. S., Kourafalou, V. H., and Schiller, R. V.: Process studies on the evolution of the Mississippi River plume: Impact of topography, wind and discharge conditions, Cont. Shelf Res., 107, 33–49, https://doi.org/10.1016/j.csr.2015.07.014, 2015.

Barkan, R., McWilliams, J. C., Shchepetkin, A. F., Molemaker, M. J., Renault, L., Bracco, A., and Choi, J.: Submesoscale dynamics in the northern Gulf of Mexico. Part I: Regional and seasonal characterization, and the role of river outflow, J. Phys. Oceanogr., 47, 2325–2346, https://doi.org/10.1175/JPO-D-17-0035.1, 2017.

Bauer, R. T.: Reproductive ecology of a protandric simultaneous hermaphrodite, the Shrimp Lysmata Wurdemanni (Decapoda: Caridea: Hippolytidae), J. Crustac. Biol., 22, 742–749, https://doi.org/10.1163/20021975-99990288, 2002.

Bianchi, T. S., DiMarco, S. F., Cowan, J. H., Hetland, R. D., Chapman, P., Day, J. W., and Allison, M. A.: The science of hypoxia in the northern Gulf of Mexico: A review, Sci. Total Environ., 408, 1471–1484, https://doi.org/10.1016/j.scitotenv.2009.11.047, 2010.

Bracco, A., Choi, J., Joshi, K., Luo, H., and McWilliams, J. C.: Submesoscale currents in the northern Gulf of Mexico: Deep phenomena and dispersion over the continental slope, Ocean Model., 101, 43–58, https://doi.org/10.1016/j.ocemod.2016.03.002, 2016.

Carrere, L., Lyard, F., Cancet, M., and Guillot, A.: FES 2014, a new tidal model on the global ocean with enhanced accuracy in shallow seas and in the Arctic region, in: Abstracts of the EGU General Assembly 2015, Vienna, Austria, 12–17 April 2015, available at: http://adsabs.harvard.edu/abs/2015EGUGA..17.5481C (last access: 7 November 2019), 2015.

Chen, C., Beardsley, R. C., and Cowles, G.: An unstructured grid, finite-volume coastal ocean model (FVCOM) system, Oceanography, 19, 78–89, https://doi.org/10.5670/oceanog.2006.92, 2006.

Chen, S.-N., Geyer, W. R., Ralston, D. K., and Lerczak, J. A.: Estuarine exchange flow quantified with isohaline coordinates: Contrasting long and short estuaries, J. Phys. Oceanogr., 42, 748–763, https://doi.org/10.1175/JPO-D-11-086.1, 2012.

Cho, K., Reid, R. O., and Nowlin Jr., W. D.: Objectively mapped stream function fields on the Texas-Louisiana shelf based on 32 months of moored current meter data, J. Geophys. Res., 103, 10377–10390, https://doi.org/10.1029/98JC00099, 1998.

Chu, P. P., Ivanov, L. M., and Melnichenko, O. V.: Fall-winter current reversals on the Texas-Louisiana continental shelf, J. Phys. Oceanogr., 35, 902–910, https://doi.org/10.1175/JPO2703.1, 2005.

Cochrane, J. D. and Kelly, F. J.: Low-frequency circulation on the Texas-Louisiana continental shelf, J. Geophys. Res., 91, 10645–10659, https://doi.org/10.1029/JC091iC09p10645, 1986.

DiMarco, S. F., Howard, M. K., and Reid, R. O.: Seasonal variation of wind-driven diurnal current cycling on the Texas-Louisiana continental shelf, Geophys. Res. Lett., 27, 1017–1020, https://doi.org/10.1029/1999GL010491, 2000.

Du, J., Park, K., Shen, J., Dzwonkowski, B., Yu, X., and Yoon, B. I.: Role of baroclinic processes on flushing characteristics in a highly stratified estuarine system, Mobile Bay, Alabama, J. Geophys. Res.-Oceans, 123, 4518–4537, https://doi.org/10.1029/2018JC013855, 2018a.

Du, J., Shen, J., Zhang, Y. J., Ye, F., Liu, Z., Wang, Z., Wang, Y. P., Yu, X., Sisson, M., and Wang, H. V.: Tidal response to sea-level rise in different types of estuaries: The importance of length, bathymetry, and geometry, Geophys. Res. Lett., 45, 227–235, https://doi.org/10.1002/2017GL075963, 2018b.

Du, J. and Park, K.: Estuarine salinity recovery from an extreme precipitation event: Hurricane Harvey in Galveston Bay, Sci. Total Environ., 670, 1049–1059, https://doi.org/10.1016/j.scitotenv.2019.03.265, 2019a.

Dukhovskoy, D. S., Morey, S. L., Martin, P. J., O'Brien, J. J., and Cooper, C.: Application of a vanishing, quasi-sigma, vertical coordinate for simulation of high-speed, deep currents over the Sigsbee Escarpment in the Gulf of Mexico, Ocean Model., 28, 250–265, https://doi.org/10.1016/j.ocemod.2009.02.009, 2009.

Dzwonkowski, B., Park, K., and Collini, R.: The coupled estuarine-shelf response of a river-dominated system during the transition from low to high discharge, J. Geophys. Res.-Oceans, 120, 6145–6163, https://doi.org/10.1002/2015JC010714, 2015

Fennel, K., Hetland, R., Feng, Y., and DiMarco, S.: A coupled physical-biological model of the Northern Gulf of Mexico shelf: model description, validation and analysis of phytoplankton variability, Biogeosciences, 8, 1881–1899, https://doi.org/10.5194/bg-8-1881-2011, 2011.

Gierach, M. M., Vazquez-Cuervo, J., Lee, T., and Tsontos, V. M.: Aquarius and SMOS detect effects of an extreme Mississippi River flooding event in the Gulf of Mexico, Geophys. Res. Lett., 40, 5188–5193, https://doi.org/10.1002/grl.50995, 2013.

Hetland, R. D. and DiMarco, S. F.: How does the character of oxygen demand control the structure of hypoxia on the Texas-Louisiana continental shelf?, J. Marine Syst., 70, 49–62, https://doi.org/10.1016/j.jmarsys.2007.03.002, 2008.

Huang, W. J., Cai, W.-J., Castelao, R. M., Wang, Y., and Lohrenz, S. E.: Effects of a wind-driven cross-shelf large river plume on biological production and CO_2 uptake on the Gulf of Mexico during spring, Limnol. Oceanogr., 58, 1727–1735, https://doi.org/10.4319/lo.2013.58.5.1727, 2013.

Justić, D., Rabalais, N. N., and Turner, R. E.: Effects of climate change on hypoxia in coastal waters: A doubled CO_2 scenario for the northern Gulf of Mexico, Limnol. Oceanogr., 41, 992–1003, https://doi.org/10.4319/lo.1996.41.5.0992, 1996.

Kantha, L. H. and Clayson, C. A.: An improved mixed layer model for geophysical applications, J. Geophys. Res., 99, 25235–25266, https://doi.org/10.1029/94JC02257, 1994.

Kim, C.-K. and Park, K.: A modeling study of water and salt exchange for a micro-tidal, stratified northern Gulf of Mexico estuary, J. Marine Syst., 96–97, 103–115, https://doi.org/10.1016/j.jmarsys.2012.02.008, 2012.

Kuitenbrouwer, D., Reniers, A., MacMahan, J., and Roth, M. K.: Coastal protection by a small scale river plume against oil spills in the Northern Gulf of Mexico, Cont. Shelf Res., 163, 1–11, https://doi.org/10.1016/j.csr.2018.05.002, 2018.

Laurent, A., Fennel, K., Hu, J., and Hetland, R.: Simulating the effects of phosphorus limitation in the Mississippi and Atchafalaya River plumes, Biogeosciences, 9, 4707–4723, https://doi.org/10.5194/bg-9-4707-2012, 2012.

Lehrter, J. C., Ko, D. S., Murrell, M. C., Hagy, J. D., Schaeffer, B. A., Greene, R. M., Gould, R. W., and Penta, B.: Nutrient distributions, transports, and budgets on the inner margin of a river-dominated continental shelf, J. Geophys. Res.-Oceans, 118, 4822–4838, https://doi.org/10.1002/jgrc.20362, 2013.

Lerczak, J., Geyer, W. R., and Chant, R. J.: Mechanisms driving the time-dependent salt flux in a partially stratified estuary, J. Phys. Oceanogr., 36, 2296–2311, https://doi.org/10.1175/JPO2959.1, 2006.

Li, Y., Nowlin Jr., W. D., and Reid, R. O.: Mean hydrographic fields and their interannual variability over the Texas-Louisiana continental shelf in spring, summer, and fall, J. Geophys. Res., 102, 1027–1049, https://doi.org/10.1029/96JC03210, 1997.

Lucena, Z. and Lee, M. T.: Characterization of Streamflow, Suspended Sediment, and Nutrients Entering Galveston Bay from the Trinity River, Texas, May 2014–December 2015, U.S. Geological Survey Scientific Investigations Report 2016–5177, Reston, Virginia, USA, 38, https://doi.org/10.3133/sir20165177, 2017.

MacCready, P.: Calculating estuarine exchange flow using isohaline coordinates, J. Phys. Oceanogr., 41, 1116–1124, https://doi.org/10.1175/2011JPO4517.1, 2011.

Martin, P. J.: Description of the Navy Coastal Ocean Model Version 1.0, NRL Report NRL/FR/7322–00–9962, Naval Research Laboratory, Stennis Space Center, MS, USA, 2000.

Nowlin Jr., W. D., Jochens, A. E., Dimarco, S. F., Reid, R. O., and Howard, M. K.: Low-frequency circulation over the Texas-Louisiana continental shelf, in: Circulation in the Gulf of Mexico: Observations and Models, edited by: Sturges, W. and Lugo-Fernandez, A., Geophysical Monograph Series 161, AGU, Washington, DC, 219–240, https://doi.org/10.1029/161GM17, 2005.

Oey, L.-Y.: Eddy- and wind-forced shelf circulation, J. Geophys. Res., 100, 8621–8637, https://doi.org/10.1029/95JC00785, 1995.

Oey, L.-Y. and Lee, H.-C.: Deep eddy energy and topographic Rossby waves in the Gulf of Mexico, J. Phys. Oceanogr., 32, 3499–3527, https://doi.org/10.1175/1520-0485(2002)032<3499:DEEATR>2.0.CO;2, 2002.

Oey, L.-Y., Ezer, T., and Lee, H.-C.: Loop current, rings and related circulation in the Gulf of Mexico: A review of numerical models and future challenges, in: Circulation in the Gulf of Mexico: Observations and Models, edited by: Sturges, W. and Lugo-Fernandez, A., Geophysical Monograph Series 161, AGU, Washington, DC, 31–56, https://doi.org/10.1029/161GM04, 2005.

Ohlmann, J. C. and Niiler, P. P.: Circulation over the continental shelf in the northern Gulf of Mexico, Prog. Oceanogr., 64, 45–81, https://doi.org/10.1016/j.pocean.2005.02.001, 2005.

Rabalais, N. N., Turner, R. E., Justić, D., Dortch, Q., Wiseman, W. J., and Sen Gupta, B. K.: Nutrient changes in the Mississippi River and system responses on the adjacent continental shelf, Estuaries, 19, 386–407, https://doi.org/10.2307/1352458, 1996.

Rabalais, N. N., Turner, R. E., and Scavia, D.: Beyond science into policy: Gulf of Mexico hypoxia and the Mississippi River, BioScience, 52, 129–142, https://doi.org/10.1641/0006-3568(2002)052[0129:BSIPGO]2.0.CO;2, 2002.

Rabalais, N. N., Turner, R. E., Sen Gupta, B. K., Boesch, D. F., Chapman, P., and Murrell, M. C.: Hypoxia in the northern Gulf of Mexico: Does the science support the plan to reduce, mitigate, and control hypoxia?, Estuaries Coasts, 30, 753–772, https://doi.org/10.1007/BF02841332, 2007.

Rayson, M. D., Gross, E. S., and Fringer, O. B.: Modeling the tidal and sub-tidal hydrodynamics in a shallow, micro-tidal estuary, Ocean Model., 89, 29–44, https://doi.org/10.1016/j.ocemod.2015.02.002, 2015.

Rego, J. L. and Li, C.: Storm surge propagation in Galveston Bay during Hurricane Ike, J. Marine Syst., 82, 265–279, https://doi.org/10.1016/j.jmarsys.2010.06.001, 2010.

Rong, Z., Hetland, R. D., Zhang, W., and Zhang, X.: Current-wave interaction in the Mississippi-Atchafalaya river plume on the Texas-Louisiana shelf, Ocean Model., 84, 67–83, https://doi.org/10.1016/j.ocemod.2014.09.008, 2014.

Sebastian, A., Proft, J., Dietrich, J. C., Du, W., Bedient, P. B., and Dawson, C. N.: Characterizing hurricane storm surge behavior in Galveston Bay using the SWAN + ADCIRC model, Coast. Eng., 88, 171–181, https://doi.org/10.1016/j.coastaleng.2014.03.002, 2014.

Shchepetkin, A. F. and McWilliams, J. C.: The regional oceanic modeling system (ROMS): A split-explicit, free-surface, topography-following-coordinate oceanic model, Ocean Model., 9, 347–404, https://doi.org/10.1016/j.ocemod.2004.08.002, 2005.

Stanev, E. V., Grashorn, S., and Zhang, Y. J.: Cascading ocean basins: Numerical simulations of the circulation and interbasin exchange in the Azov-Black-Marmara-Mediterranean Seas system, Ocean Dynam., 67, 1003–1025, https://doi.org/10.1007/s10236-017-1071-2, 2017.

Umlauf, L. and Burchard, H.: A generic length-scale equation for geophysical turbulence models, J. Mar. Res., 61, 235–265, https://doi.org/10.1357/002224003322005087, 2003.

Wang, D.-P., Oey, L.-Y., Ezer, T., and Hamilton, P.: Near-surface currents in DeSoto Canyon (1997–99): Comparison of current meters, satellite observation, and model simulation, J. Phys. Oceanogr., 33, 313–326, https://doi.org/10.1175/1520-0485(2003)033<0313:NSCIDC>2.0.CO;2, 2003.

Wang, L. and Justić, D.: A modeling study of the physical processes affecting the development of seasonal hypoxia over the inner Louisiana-Texas shelf: Circulation and stratification, Cont. Shelf Res., 29, 1464–1476, https://doi.org/10.1016/j.csr.2009.03.014, 2009.

Willmott, C. J.: On the validation of models, Phys. Geogr., 2, 184–194, https://doi.org/10.1080/02723646.1981.10642213, 1981.

Ye, F., Zhang, Y. J., Wang, H. V., Friedrichs, M. A. M., Irby, I. D., Alteljevich, E., Valle-Levinson, A., Wang, Z., Huang, H., Shen, J., and Du, J.: A 3D unstructured-grid model for Chesapeake Bay: Importance of bathymetry, Ocean Model., 127, 16–39, https://doi.org/10.1016/j.ocemod.2018.05.002, 2018.

Zavala-Hidalgo, J., Morey, S. L., and O'Brien, J. J.: Seasonal circulation on the western shelf of the Gulf of Mexico using a high-resolution numerical model, J. Geophys. Res., 108, 3389, https://doi.org/10.1029/2003JC001879, 2003.

Zavala-Hidalgo, J., Gallegos-García, A., Martínez-López, B., Morey, S. L., and O'Brien, J. J.: Seasonal upwelling on the western and southern shelves of the Gulf of Mexico, Ocean Dynam., 56, 333–338, https://doi.org/10.1007/s10236-006-0072-3, 2006.

Zhang, X., Hetland, R. D., Marta-Almeida, M., and DiMarco, S. F.: A numerical investigation of the Mississippi and Atchafalaya freshwater transport, filling and flushing times on the Texas-Louisiana shelf, J. Geophys. Res., 117, C11009, https://doi.org/10.1029/2012JC008108, 2012.

Zhang, Y. and Baptista, A. M.: SELFE: A semi-implicit Eulerian-Lagrangian finite-element model for cross-scale ocean circulation, Ocean Model., 21, 71–96, https://doi.org/10.1016/j.ocemod.2007.11.005, 2008.

Zhang, Y. J., Ateljevich, E., Yu, H. C., Wu, C. H., and Yu, J. C. S.: A new vertical coordinate system for a 3D unstructured-grid model, Ocean Model., 85, 16–31, https://doi.org/10.1016/j.ocemod.2014.10.003, 2015.

Zhang, Y. J., Ye, F., Stanev, E. V, and Grashorn, S.: Seamless cross-scale modeling with SCHISM, Ocean Model., 102, 64–81, https://doi.org/10.1016/j.ocemod.2016.05.002, 2016.

Zeng, X., Zhao, M., and Dickinson, R. E.: Intercomparison of bulk aerodynamic algorithms for the computation of sea surface fluxes using TOGA COARE and TAO data, J. Climate, 11, 2628–2644, https://doi.org/10.1175/1520-0442(1998)011<2628:IOBAAF>2.0.CO;2, 1998.

Science of the Total Environment 670 (2019) 1049–1059

Contents lists available at ScienceDirect

Science of the Total Environment

journal homepage: www.elsevier.com/locate/scitotenv

Estuarine salinity recovery from an extreme precipitation event: Hurricane Harvey in Galveston Bay

Jiabi Du *, Kyeong Park

Department of Marine Sciences, Texas A&M University at Galveston, Galveston, TX 77554, United States of America

HIGHLIGHTS

- The model reproduces well the dramatic response of Galveston Bay to Harvey.
- Salinity recovery time was two months on average with great spatial variability.
- Salinity recovery time responses non-linearly with the amount of stormwater input.
- Tidal pumping was the primary mechanism for salt influx through the bay entrance.
- Tidal pumping induced salt influx was facilitated by the shelf current.

GRAPHICAL ABSTRACT

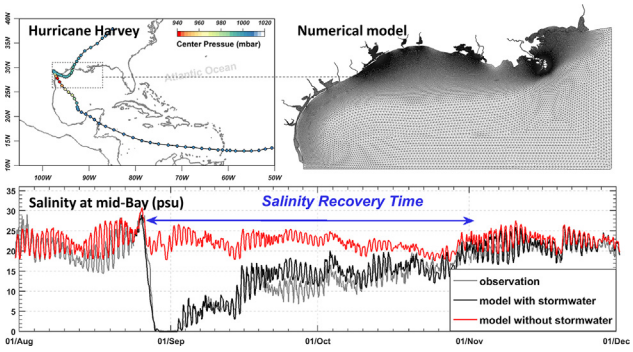

ARTICLE INFO

Article history:
Received 12 February 2019
Received in revised form 16 March 2019
Accepted 17 March 2019
Available online 19 March 2019

Editor: Damia Barcelo

Keywords:
Stormwater
Salt flux
Tidal pumping
Hydrodynamic model
Gulf of Mexico
SCHISM

ABSTRACT

With a warming climate and a more humid atmosphere, extreme precipitation events are projected to occur more frequently in future. Understanding how coastal systems respond to and recover from such acute events is of fundamental significance for environmental assessment and management. A hydrodynamic model was used to examine the estuarine responses in Galveston Bay to Hurricane Harvey, an extreme precipitation event with a return period of larger than 1000 years. The enormous freshwater input during Harvey caused long-lasting elevated water level, extraordinarily strong along-channel velocity, sharp decreases in salinity, and huge river plumes, all of which were well reproduced by the model. The salinity recovery time (T_R) was estimated as a measure of the system resiliency to stormwater input. Over the entire bay, the T_R had a mean of two months, but with great variability ranging from less than 10 days near the bay entrance to over three months in the inner part of Trinity Bay and the middle of East Bay. The spatially varying T_R was explained by different contributions of exchange flow and tidal pumping to salt flux. At the bay entrance, tidal pumping facilitated by the shelf current was the dominant mechanism for salt influx, while exchange flow and tidal pumping had a comparable contribution to salt influx to Trinity Bay. The spatial pattern of the T_R appears consistent with the changes in the phytoplankton community in the bay. A series of numerical experiments with different amounts of stormwater reveals a non-linear relationship between the bay-wide mean T_R and the amount of stormwater, with the rate of increase in T_R decreasing when stormwater input increases. The present approach using a hydrodynamic model will be able to provide a quick assessment of the environmental pressure from extreme events.

* Corresponding author.
E-mail address: jdu@tamug.edu (J. Du).

https://doi.org/10.1016/j.scitotenv.2019.03.265

1. Introduction

Extreme precipitation is projected to occur more frequently under the warming climate (Knight and Davis, 2009; Donat et al., 2016; Pfahl et al., 2017). Extreme precipitations, along with other types of extreme events (e.g., drought and heat wave), are posing increasing threats and pressure to ecosystems (Knapp et al., 2008), particularly in coastal areas (Weyhenmeyer et al., 2004; Cardoso et al., 2008). Large quantity of freshwater and sediment, resulting from extreme precipitation events, have great potential to renew estuarine water (Hagy et al., 2006), decrease salinity drastically (Du et al., 2019a), enhance turbidity (Zhang et al., 2013), bury benthic fauna (Posey et al., 1996), and shift plankton community (Scheffer et al., 2001; Peierls et al., 2003; Liu et al., 2019). The influence can be beneficial or detrimental, and the recovery from the acute perturbation may last for days, months, or even years, depending on the resiliency of the coastal system (Paerl et al., 2006). Many estuarine species such as plankton, fish, and seagrass have a certain range of salinity tolerance and can be stressed under too low or too high salinities. For instance, prolonged exposure to low-salinity condition can lead to enhanced mortality of eastern oyster (Munroe et al., 2013; Casas et al., 2018). Understanding the salinity recovery process is therefore of fundamental importance. Hurricane Harvey (2017), one of the most devastating hurricanes that hit the U.S. in recent history, brought enormous precipitation over the Texas-Louisiana coast, serving as a great example to examine the estuarine response to an extreme precipitation event, particularly in terms of salinity recovery.

Hurricane Harvey (hereinafter referred to as Harvey) intensified quickly in the northern Gulf of Mexico before making landfall on August 26, 2017 along the mid-Texas coast as a Category 4 hurricane (Fig. 1). Harvey brought record-breaking precipitation, with the return period of the peak 3-day precipitation exceeding 1000 years (van Oldenborgh et al., 2018), and caused more than 80 fatalities and over $150 billion economic losses, mostly due to the extraordinary flooding (Emanuel, 2017; Balaguru et al., 2018). Over the 5-day period from August 26 to 30, Harvey dumped 92.7×10^9 m^3 of water across Texas and Louisiana (Fritz and Samenow, 2017), making it the wettest tropical cyclone in the U.S. history. The extraordinary amount of water load even caused up to 21 mm subsidence of Earth's crust (Milliner et al., 2018). A freshwater load of 11.1×10^9 m^3 was estimated to discharge into Galveston Bay (about 3 times the bay volume), making the entire bay virtually fresh for several days (Du et al., 2019a). Due to the limited coverage of monitoring stations inside the bay, however, the speed and controlling mechanism(s) of salinity recovery are still not clearly understood. Furthermore, large sea-surface slope due to input of huge freshwater and mixing due to strong wind greatly disturbed the circulation inside and outside of the bay, making the salt exchange between the estuary and coastal ocean very different from that under normal conditions.

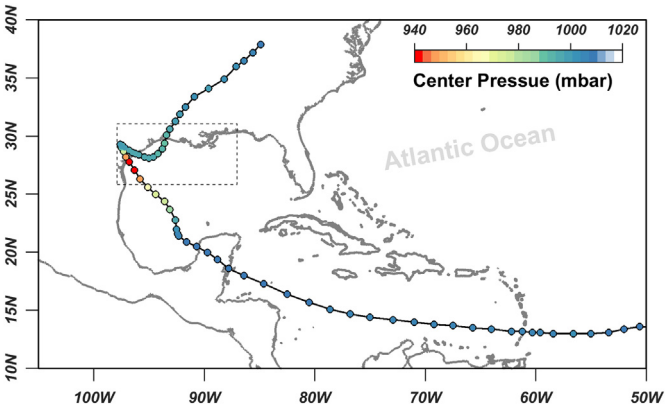

Fig. 1. Track of Hurricane Harvey from the National Hurricane Center (https://www.nhc.noaa.gov/data/hurdat/hurdat2-1851-2017-050118.txt, accessed on March 10, 2019), the center pressure (dot color), and the numerical model domain (rectangle). (For interpretation of the references to color in this figure legend, the reader is referred to the web version of this article.)

Numerical models have been used to simulate storm conditions. Munroe et al. (2013) applied a model to study the effect on salinity in Delaware Bay of Hurricane Irene and Tropical Storm Lee (2011), which combined to dump 50% of the average annual cumulative precipitation into the watershed, and suggested a linkage between the prolonged low-salinity exposure and oyster mortality rate. Gong et al. (2007) applied a model to investigate the effect of Hurricane Isabel (2003) on the changes of stratification, salt flux, and the recovery time for the York River estuary. Numerical simulations of extreme precipitation events that make the entire estuary completely fresh are, however, rarely reported. In this study, we applied a hydrodynamic model to examine the salinity recovery in Galveston Bay after Harvey by calculating a timescale, "salinity recovery time" (T_R). We found large spatial variability of T_R in Galveston Bay and identified the underlying mechanisms responsible for the spatial heterogeneity. The timescale introduced and the methods used in this study shall be applicable to any estuary, serving as an efficient diagnostic tool for environmental assessment and management.

2. Methods

We employed the Semi-implicit Cross-scale Hydroscience Integrated System Model (SCHISM: Zhang et al., 2015, 2016), an open-source community-supported modeling system based on unstructured grids, derived from the early SELFE model (Zhang and Baptista, 2008). The model is based on the turbulence-averaged Navier-Stokes equations, including continuity, momentum, salt-balance, and heat-balance equations, under the hydrostatic approximation. It uses a semi-implicit Galerkin finite-element method for momentum advection and a finite-volume method for the mass advection. It uses the generic length-scale model of Umlauf and Burchard (2003) with the stability function of Kantha and Clayson (1994) for turbulence closure. The model has the capability of employing a very flexible vertical grid system, robustly and faithfully resolving the complex topography in estuarine and oceanic systems without any smoothing (Du et al., 2018a; Ye et al., 2018). A more detailed description of the SCHISM, including the governing equations, horizontal and vertical grids, numerical solution methods, and boundary conditions, can be found in Zhang et al. (2015, 2016).

The model domain (Fig. 2a) covers the entire Texas, Louisiana, Mississippi, and Alabama coasts, including the shelf as well as major estuaries (e.g., Galveston Bay), which allows to simulate the interactions between Galveston Bay and the shelf ocean that are critically important for salt and water exchange (Du et al., 2019b). The grid system contains 142,972 horizontal elements, with the resolution ranging from 40 m in the narrow ship channel of Galveston Bay to 10 km in the open ocean. The fine grid for the ship channel (Fig. 2b, c) is aligned with the channel orientation in order to accurately simulate the salt intrusion process (Ye et al., 2018). Vertically, a hybrid *s-z* grid is used, with 10 sigma layers for depths <20 m and another 30 *z*-layers for depths from 20 to 4000 m. The bathymetry used in the model is based on the coastal relief model (3 arc-second resolution: https://www.ngdc.noaa.gov). The local bathymetry in Galveston Bay is augmented by 10-m resolution DEM (digital elevation model) bathymetric data (https://catalog.data.gov/dataset/galveston-texas-coastal-digital-elevation-model) to resolve the narrow ship channel (150 m wide, 10–15 m deep) that extends from the bay entrance all the way to Port of Houston. When forced by realistic boundary conditions, including the open boundary conditions from FES2014 global tide (Carrere et al., 2015) and global HYCOM model output (https://www.hycom.org/data/glbu0pt08), atmospheric forcing from the European Centre for Medium-Range Weather Forecasts (ECMWF: https://www.ecmwf.int), and river discharges from 15 USGS gaging stations, the model gives a very good reproduction of the observed hydrodynamic conditions in 2007–2008 inside the Galveston Bay and over the

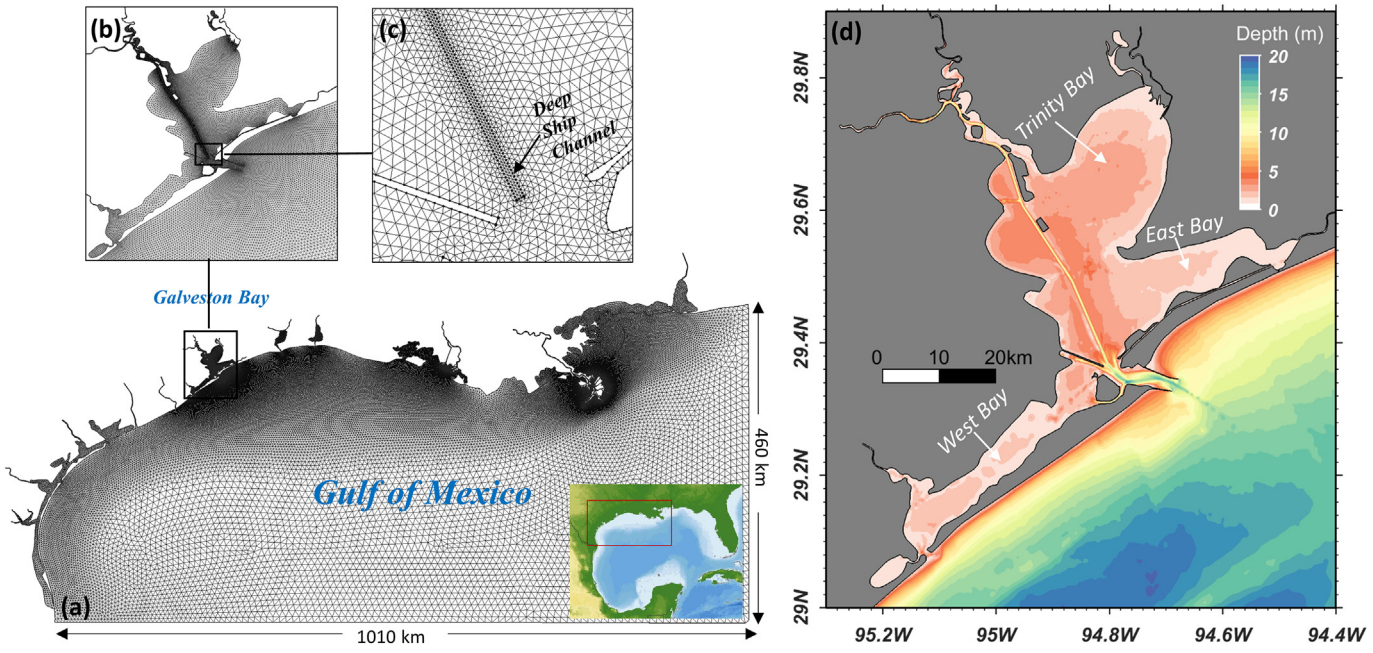

Fig. 2. The model domain with the horizontal grid (a), zoom-ins for the Galveston Bay (b) and its narrow, deep ship channel (c), and the bathymetry of Galveston Bay (d).

Texas- Louisiana shelf in terms of water level, salinity, temperature, stratification, and shelf current. A more detailed description of the model configuration, including the grid system, bathymetry, boundary conditions, and the 2007–2008 model validation results can be found in Du et al. (2019b).

We applied this model for the simulation of Harvey. For hurricane simulations, it is essential to ensure the credibility of the wind field as well as the freshwater load used for forcing conditions. The wind field was extracted from the ECMWF, which agrees well with the data for the hurricane track and location of hurricane eye from the National Hurricane Center (Fig. 3). It also agrees well with another independent data for hourly wind speed and direction from the NOAA station at the bay entrance (Fig. A1). For the freshwater input, it is important to note that Galveston Bay received not only freshwater from major rivers but

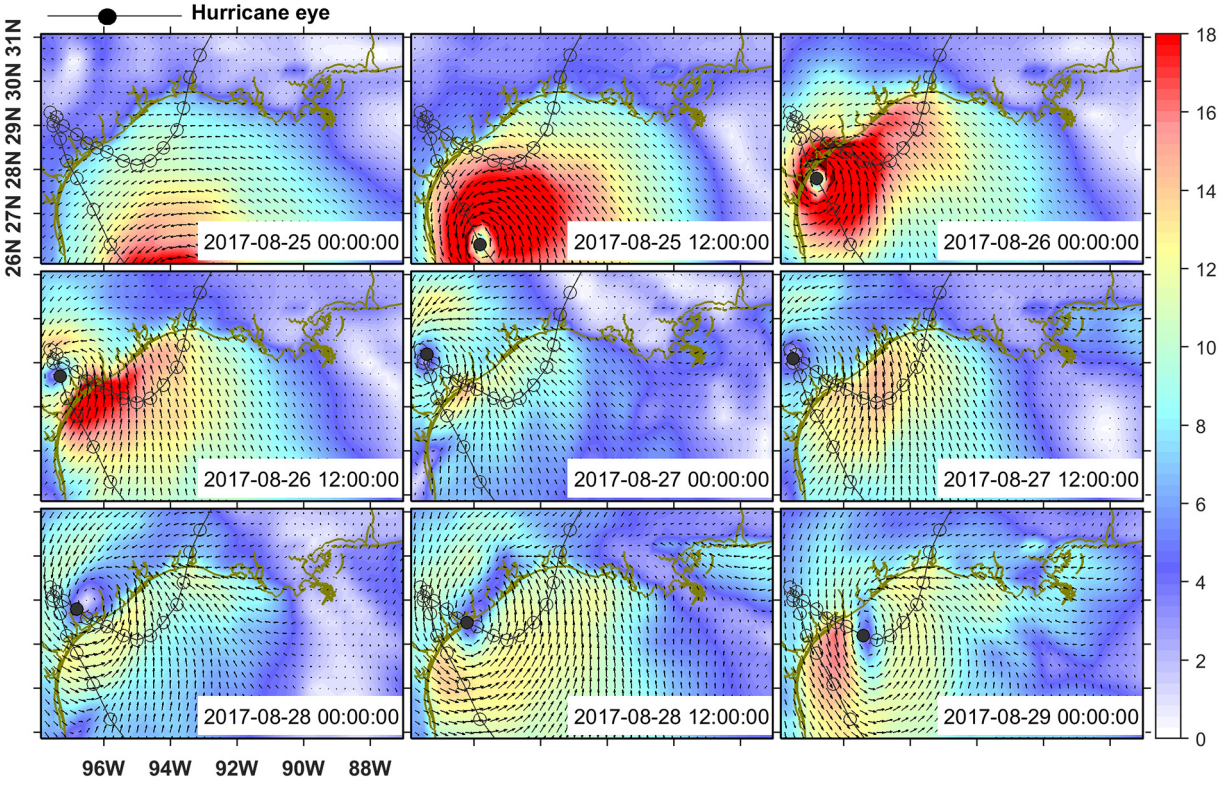

Fig. 3. Wind field from the European Centre for Medium-Range Weather Forecasts (ECMWF) and the hurricane track from the National Hurricane Center. The filled color denotes the wind speed ($m\ s^{-1}$) at 10 m above ground and the open circles denote the hurricane track with the black solid circle indicating the hurricane eye for the given time. Note the high consistency in the location of hurricane eye between two independent datasets. (For interpretation of the references to color in this figure legend, the reader is referred to the web version of this article.)

also an enormous amount of freshwater through surface runoff and groundwater along the bay's coastline. Du et al. (2019a) estimated that 11.1×10^9 m^3 of freshwater entered the bay during Harvey, and 34% of it was through surface runoff and groundwater along the coastline. To account for this input, 65 point sources evenly distributed along the bay's coastline were considered (Fig. 4d). The daily discharge along the coastline was estimated by distributing the total coastline load (3.73×10^9 m^3) in proportion to the daily precipitation (Fig. 4c) and allocating the coastline load evenly to the 65 point source locations.

This method of accounting for the freshwater input through surface runoff and groundwater is not perfect. There was likely a delay between the time of precipitation and the time surface runoff and groundwater reached the bay, which would introduce errors when estimating the daily discharge in proportion to the daily precipitation. Allocating the total coastline load evenly to the 65 point source locations is also subject to uncertainties since the spatial allocation shall depend on the spatial distribution of precipitation and land use/land cover of the watershed. A better way would be to apply a watershed model to estimate the freshwater input through surface runoff and groundwater. However, most of the freshwater input along the coastline occurred on August 24–31, 2017 (Fig. 4c) while the main focus of this study is the salinity recover after Harvey, which was associated with a much longer timescale on the order of months (Fig. 5b). The bay received an enormous amount of freshwater, about 3 times the bay volume, which made the entire bay virtually fresh (Du et al., 2019a). Hence, a more accurate estimate of the freshwater input along the coastline may affect the progression of the bay water becoming fresh but is not likely to alter the post-storm process of salinity recovery. Furthermore, the model reproduces well not only the recovery of salinity in September and October but also the sudden drop in salinity to zero during Harvey (Fig. 5), providing confidence in the method of allocating the freshwater input along the coastline.

To examine the estuarine recovery from the impact of the Harvey's stormwater ΔQ (the freshwater load due to Harvey, defined as the difference between the discharge during Harvey and the pre-storm condition: see Fig. 4a–c), a numerical experiment without ΔQ was conducted. From the difference between two model runs with and without ΔQ, the salinity recovery time (T_R) for Harvey was estimated as the time for salinity values from the two model runs to converge (Fig. 5b). This definition is more robust compared to conventional methods that determine the recovery time as the time for salinity to recover to its pre-storm condition (e.g., Walker, 2001; Frazer et al., 2006). As the forcing conditions in an estuary, the adjacent shelf, and the atmosphere would not be the same before and after a storm, using the pre-storm condition as a reference will not be able to take into account the natural variability in salinity (Gong et al., 2007). We then conducted six additional numerical experiments with 10%, 20%, 30%, 40%, 50%, and 200% of ΔQ and estimated the corresponding T_R to further investigate the system's response to different amounts of stormwater input. The extraordinary Harvey's stormwater (ΔQ) is rare, with the return period exceeding 1000 years (van Oldenborgh et al., 2018), but precipitation events with smaller intensities (e.g., 10%–50% of ΔQ) are likely to occur more frequently. The results from numerical experiments were used to examine the relationship between T_R and stormwater input.

3. Results

3.1. Model-observation comparison: influence of stormwater

The model with the Harvey's stormwater ΔQ reproduces well the notable estuarine responses to Harvey. The subtidal water level is well simulated by the model (Fig. 6a). Typical storm surges mainly caused by wind generally last for one or two days (e.g., Valle-Levinson et al., 2002; Li et al., 2006; Shen et al., 2006; Rego and Li, 2010; Sebastian et al., 2014). During Harvey, however, the water level elevated by >1 m lasted over 6 days, which would not have been possible without ΔQ. Enormous freshwater input caused the water level 0.4–0.5 m higher in the middle and upper bay relative to the bay entrance (see Fig. 5a in Du et al., 2019a). The resulting surface slope generated strong along-channel velocity with the seaward speed exceeding 3 m s^{-1} at the buoy station in the lower reach of the San Jacinto River estuary, which was also reproduced well by the model with ΔQ (Fig. 6b). The model reproduces the tidal (astronomical) variation in velocity before and after Harvey, but it fails to reproduce the tidal variation that persisted on August 26–28. It should be noted that this discrepancy in velocity at the beginning of Harvey would not affect the model's credibility in simulating the salinity recovery after Harvey, the main topic of this study. Salinity decreased sharply throughout the bay and the entire bay became virtually fresh during Harvey, and it took months for salinity to return to pre-storm conditions, which the model also reproduces very well (Fig. 5).

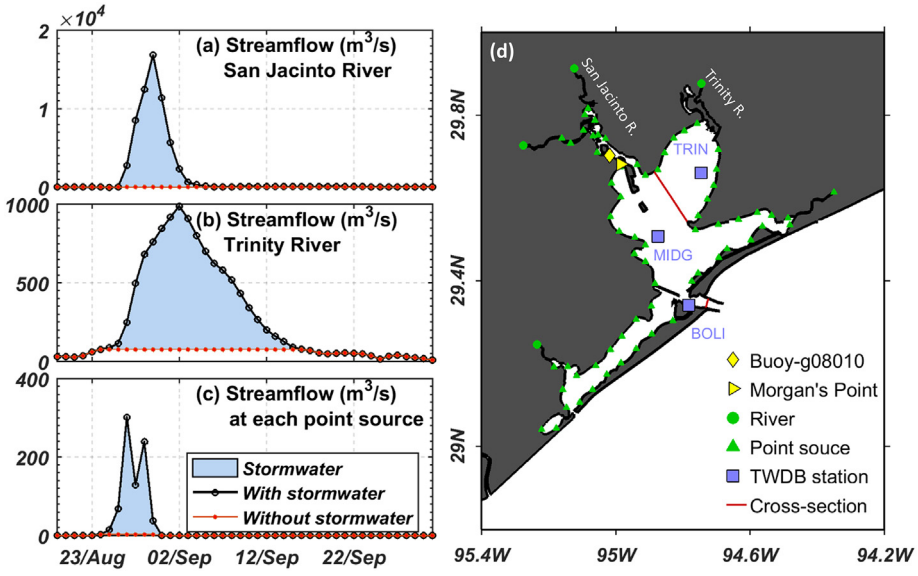

Fig. 4. River discharge from two major rivers, San Jacinto River (a) and Trinity River (b), and the estimated coastline freshwater load (c) at each of 65 point sources (d). The blue shade in (a)–(c) denotes the Harvey's stormwater ΔQ (the freshwater load due to Harvey, defined as the difference between the discharge during Harvey and the pre-storm condition). Also shown in (d) are the locations of major river input, monitoring stations for salinity, water level, and velocity, and two cross-sections (one across the bay entrance and the other across the mouth of Trinity Bay). (For interpretation of the references to color in this figure legend, the reader is referred to the web version of this article.)

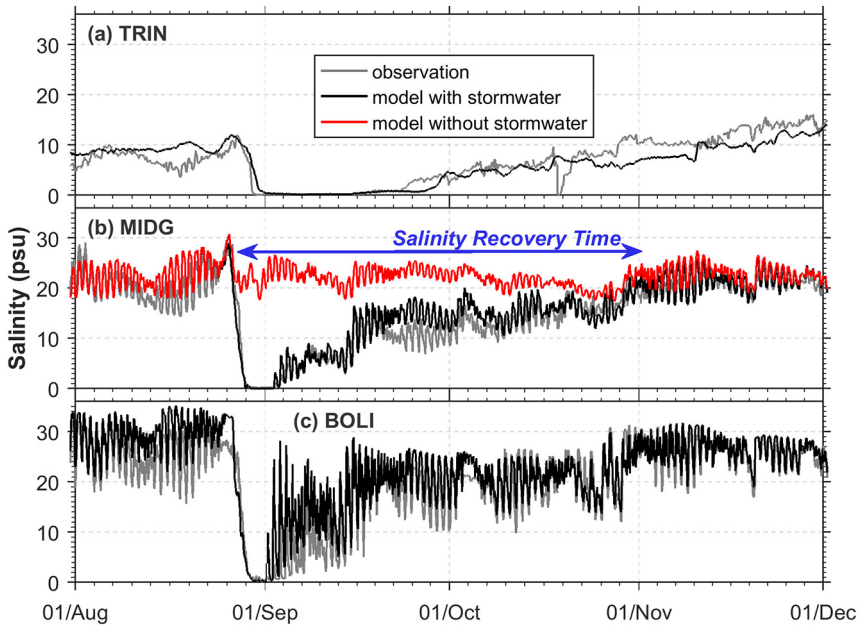

Fig. 5. The model-observation comparison for salinity at three TWDB (Texas Water Development Board) monitoring stations (see Fig. 4d for their locations). In (b), the red line shows the model result without the Harvey's stormwater, and the double arrow indicates the salinity recovery time (T_R). (For interpretation of the references to color in this figure legend, the reader is referred to the web version of this article.)

Five metrics, the model skill (*Skill*: Willmott, 1981) and Nash–Sutcliffe model efficiency index (NSE: Nash and Sutcliffe, 1970) as well as the coefficient of determination (R^2), root mean square error (*RMSE*), and mean absolute error (*MAE*), were examined for quantitative assessment of the model performance:

$$Skill = 1 - \frac{\sum_{i=1}^{N} |M_i - O_i|^2}{\sum_{i=1}^{N} \left(|M_i - \overline{O}| + |O_i - \overline{O}| \right)^2} \quad (1)$$

$$NSE = 1 - \frac{\sum_{i=1}^{N} (M_i - O_i)^2}{\sum_{i=1}^{N} \left(O_i - \overline{O} \right)^2} \quad (2)$$

where O_i and M_i are the observed and modeled variables, respectively, with the overbar indicating the temporal average over the number of observations (N). *Skill*, ranging from 0 to 1, provides an index of model-data agreement, with a *skill* of 1 indicating perfect agreement and a *skill* of 0 indicating complete disagreement. *NSE* is a normalized

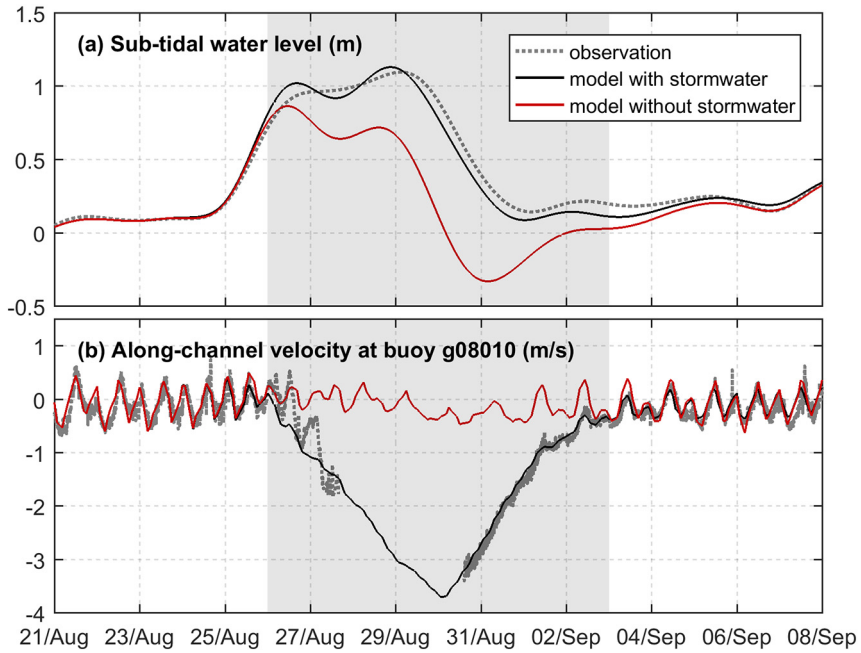

Fig. 6. The model-observation comparison for subtidal water level (m) at Morgan's Point (a) and along channel velocity (m s^{-1}) at buoy g080101 (b) (see Fig. 4d for their locations). The grey shades indicate the period of intense stormwater input from August 26 to September 3, 2017 based on the freshwater load from San Jacinto River in Fig. 4a.

statistic that indicates how well the plot of the data vs. model fits the 1:1 line. *NSE* can have values ≤1, with values between 0.50 and 0.65 considered as threshold values to indicate a model of sufficient quality (Moriasi et al., 2007; Ritter and Muñoz-Carpena, 2013). R^2 indicates the portion of the variance in the observed data explained by the model. R^2 ranges from 0 to 1, and typically values >0.5 are considered acceptable (Moriasi et al., 2007). The magnitude of *RMSE* and *MAE* indicates the average deviation between model and data.

These five metrics calculated for subtidal water level, along-channel velocity, and salinity suggest a satisfactory model performance for the 10-day period during Harvey as well as over the entire simulation period (Table 1). For salinity, in particular, *Skills* > 0.85, *NSEs* > 0.73, R^2 > 0.79, and *RMSEs* and *MAEs* are small relative to the observed ranges for the entire simulation period. The model performance is even better for the 10-day period during Harvey when dramatic changes in hydrodynamic conditions took place. The model also simulates well the overall shape, direction, and offshore extent of huge river plumes (Fig. 7). The good agreement between model and observation provides credibility of the model as well as the forcing conditions including wind and freshwater input.

3.2. Salinity recovery time (T_R)

The mean T_R averaged over the entire bay was about 62 days. The T_R exhibits great spatial variability and ranges from 6 to 108 days, with the smallest values (<10 days) at and near the three outlets, increasing values of up to about 60 days when moving upstream, and even larger values inside Trinity Bay where a maximum of >90 days was obtained in the bay's inner part (Fig. 8f). T_R is symmetric around the ship channel, and it increases when moving away from the channel. The tongue-shaped distribution of T_R is mainly attributable to the stronger salt intrusion along the deep ship channel (Du et al., 2018b). The strength of gravitational circulation, a typical two-layer circulation in an estuary with a landward bottom inflow driven by density gradient and a seaward surface outflow driven by surface slope, is proportional to water depth (MacCready and Geyer, 2010) and the stronger circulation along the deep channel tends to move the bottom higher salinity water faster to the upper estuary. Moreover, the differential longitudinal advection of saline water during flood tide, characterized by stronger flood current at deep channel than at shallow shoal (Huzzey and Brubaker, 1988), also contributes to the strong salt intrusion in deep ship channel (Lerczak and Geyer, 2004). Interestingly, the salinity recovery was very different between West Bay and East Bay, with much larger T_R in East Bay, even though the two bays share similar shape and bathymetry and have a similar distance relative to the main bay entrance. The much smaller T_R in West Bay can be attributed to the relatively wide outlet, San Luis Pass (1 km wide), relative to East Bay with a narrow outlet, Rollover Pass (52 m wide).

A series of numerical experiments with different amount of stormwater consistently shows that the lower part of the bay near the mouth is associated with the shortest T_R while the inner part of Trinity Bay and the middle of East Bay are associated with the longest T_R (Fig. 8). The bay-wide mean T_R exhibits a non-linear relationship with the amount of stormwater (Fig. 8h). The mean T_R increases rapidly and almost linearly with increasing stormwater from 10% to 30% of the Harvey's stormwater ΔQ, beyond which the rate of increase in the mean T_R reduces considerably. Once the bay becomes fresh with large stormwater, further increases in stormwater cannot make the bay fresher. However, larger stormwater input will always lower the salinity in the adjacent coastal sea, resulting in fresher ocean water (Fig. A2) and thus longer salinity recovery time. This relationship allows us to estimate the salinity recovery time for Galveston Bay once the stormwater amount is known.

Table 1
Metrics for model-observation comparison for the subtidal water level at Morgan's Point, along-channel velocity at buoy g08010, and salinity at three TWDB stations (see Fig. 4d for the station locations) over the entire simulation period and the 10-day period during Hurricane Harvey.

Comparison period	Variable	*Skill*	*NSE*	R^2	*RMSE*	*MAE*
Simulation period (7/1–12/31/2017)	Subtidal water level	0.98	0.91	0.92	0.07 m	0.04 m
	Along-channel velocity	0.94	0.78	0.79	0.16 m s^{-1}	0.13 m s^{-1}
	Salinity at TRIN	0.85	0.77	0.84	3.5 psu	2.4 psu
	Salinity at MIDG	0.94	0.73	0.83	3.0 psu	2.2 psu
	Salinity at BOLI	0.93	0.75	0.80	3.6 psu	2.7 psu
During Harvey (8/25–9/4/2017)	Subtidal water level	0.99	0.96	0.98	0.07 m	0.07 m
	Along-channel velocity	0.98	0.94	0.94	0.23 m s^{-1}	0.15 m s^{-1}
	Salinity at TRIN	0.96	0.85	0.93	1.8 psu	1.4 psu
	Salinity at MIDG	0.99	0.95	0.96	2.3 psu	1.4 psu
	Salinity at BOLI	0.96	0.83	0.87	4.6 psu	3.3 psu

4. Discussion

4.1. Mechanisms for salinity recovery

Salt mass inside an estuary, and thus salinity, is determined by the competition of salt influx and outflux. For steady state, the two opposing salt fluxes are balanced, resulting in constant salinities inside the estuary at subtidal timescales. The salinity recovery is controlled by the magnitude of salt influx. To understand the salt mass exchange between ocean and estuary and between the main bay and the sub-bay, the salt fluxes through the bay entrance cross-section and another cross-section that separates Trinity Bay from Galveston Bay were calculated (see Fig. 4d for their locations). By decomposing the normal velocity u and salinity S into tidally and cross-sectionally averaged (u_o and S_o), tidally averaged and cross-sectionally varying (u_e and S_e), and tidally and cross-sectionally varying (u_t and S_t) components, the contributions on salt flux (F_s) from three different mechanisms can be determined (Lerczak et al., 2006):

$$\begin{aligned} F_s &= \left\langle \int uSdA \right\rangle = \left\langle \int (u_o + u_e + u_t)(S_o + S_e + S_t)dA \right\rangle \\ &\approx \left\langle \int (u_o S_o + u_e S_e + u_t S_t)dA \right\rangle \equiv -Q_f S_o + F_e + F_t \end{aligned} \tag{3}$$

where A is the time-varying cross-sectional area; the angled bracket denotes tidal average; and Q_f is the subtidal volume discharge rate. The three terms on the right-hand side of Eq. (3) represent the subtidal salt flux due to cross-sectional average advective transport ($-Q_f S_o$), shear dispersion due to vertical and lateral shear transport (F_e), and tidal oscillatory salt transport due to temporal correlations between u and S (F_t). While salt outflux is mainly due to $-Q_f S_o$ (by freshwater discharge), salt influx is mainly due to F_e (by exchange flow) and F_t (by tidal pumping). For steady state, the outflux ($-Q_f S_o$) is balanced by the influx ($F_e + F_t$). Depending on the tidal energy and estuarine geometry, the relative importance of these two salt influx mechanisms varies.

The total salt influx ($F_e + F_t$) through the bay entrance was much larger than that across the Trinity Bay section (Fig. 9) even though the bay mouth is much narrower (2.5 km) compared to the Trinity Bay section (16 km). It is the difference in this total salt influx between the two sections that caused the spatially varying salinity recovery time (Fig. 8f). Except during the time under the direct impact of Harvey (i.e., between late August and early September), F_e was comparable between the two cross-sections, with a magnitude of 100–1000 kg salt s^{-1}. However, F_t was much larger, at least by one order of magnitude, at the bay entrance than at the Trinity Bay section (Table 2), largely owing to the larger tidal fluctuations in salinity and velocity. The salinity data show large tidal fluctuations near the bay entrance (Fig. 5c), and that the tidal fluctuations decreased upstream with virtually no tidal fluctuation in Trinity

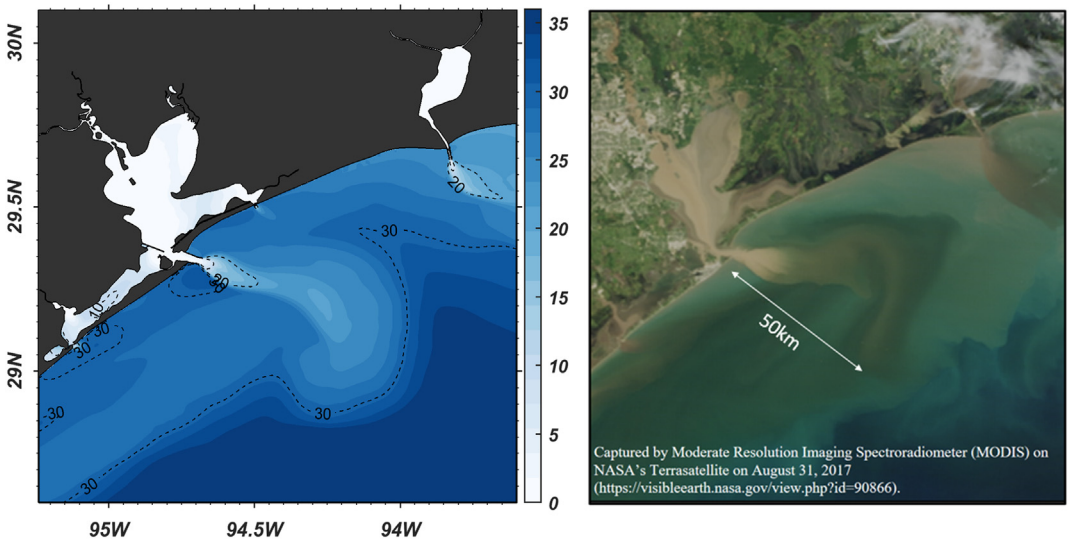

Fig. 7. Comparison of the modeled river plumes indicated by low salinity (a snapshot at 16:00 GMT on August 31, 2017) and the MODIS satellite image on August 31, 2017. Note that the overall shape, in terms of plume direction and offshore extent, is similar and that the model not only captures the plume from Galveston Bay but also that from Sabine Lake (in the upper-right corner).

Bay (Fig. 5a). Under normal conditions, i.e., from October to December, F_t was about 5–6 times larger than F_e at the bay entrance, indicating the dominant control of salt exchange from tidal pumping (Table 2). On the contrary, F_t and F_e were comparable at the Trinity Bay section, indicating a weak tidal exchange.

Both F_t and F_e showed great temporal variation at both cross-sections. At the bay entrance, both F_t and F_e increased drastically at the time of huge freshwater load (Fig. 9a and Table 2), which can be attributable to the increase in salinity gradient. The salinity inside the bay decreased quickly to zero during Harvey while the salinity on the shelf outside of the bay did not. Observational data show that the salinity on the shelf outside of Galveston Bay dropped from 32 to 16–20 psu during Harvey (Fig. 7 in Du et al., 2019a), whereas the salinity just inside the bay entrance dropped from 30 psu to 0 (Fig. 5c), resulting in a dramatic increase in salinity gradient. As the primary driving force for the exchange flow (MacCready and Geyer, 2010), increased salinity gradient enhances the exchange flow and thus F_e. Increased salinity gradient also causes a large fluctuation in salinity at the bay mouth between flood and ebb tides, enhancing the tidal pumping and thus F_t. The narrow outlet also helps tidal pumping. The tidal current through the narrow outlet is strong with a maximum speed of ~1 m s^{-1} despite the micro-tidal range (mean of 0.3 m), which leads to strong tidal pumping and thus F_t.

At the Trinity Bay section, on the other hand, there was no landward salt flux between late August and early September as the huge freshwater

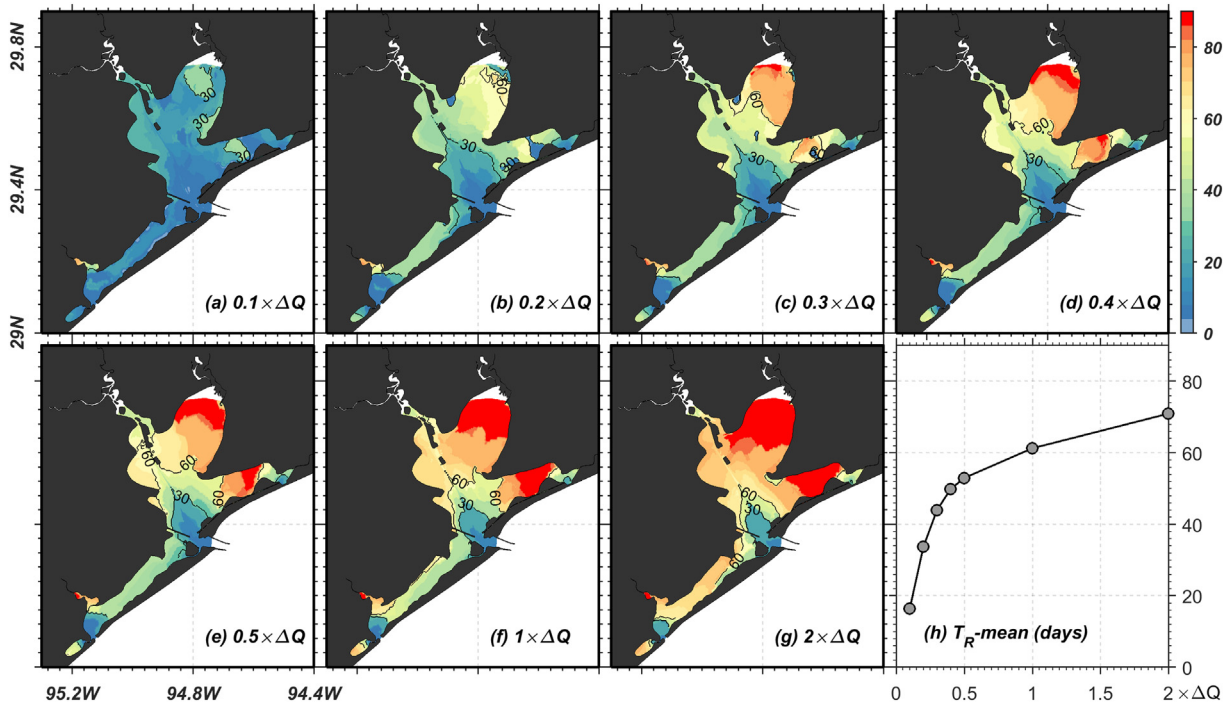

Fig. 8. Distribution of salinity recovery time (T_R) in days for different amounts of stormwater, i.e., 10%, 20%, 30%, 40%, 50%, 100% and 200% of the Harvey's stormwater ΔQ (a–g), and the variations in the bay-wide mean T_R as a function of stormwater (h). The blank areas in the upper bay indicate the region with salinity <5 psu even without the stormwater input for which T_R is not calculated.

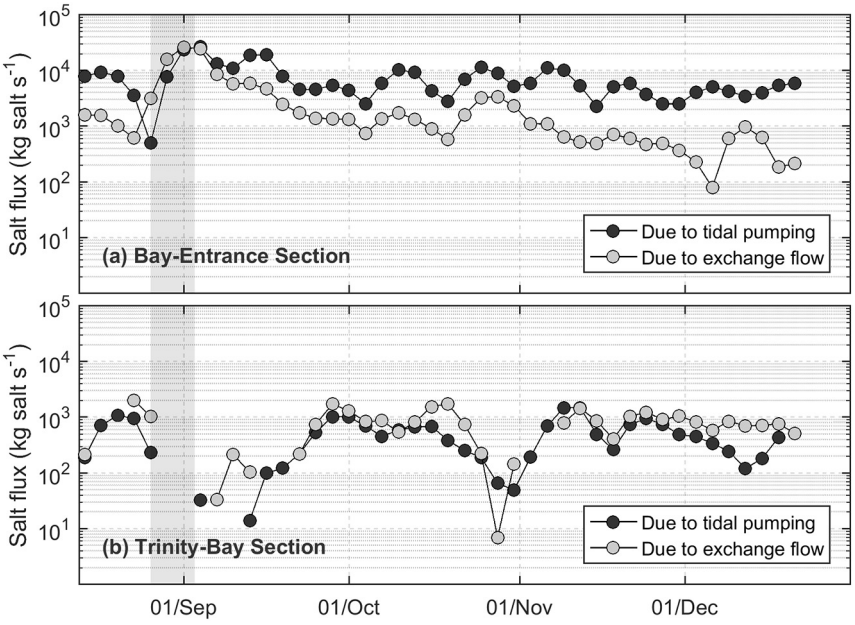

Fig. 9. Salt flux due to tidal pumping and exchange flow through the sections across the bay entrance (a) and the Trinity Bay (b), showing the samples at an interval of 3 days: see Fig. 4d for the locations of sections. The grey shades indicate the period of intense stormwater input from August 26 to September 3, 2017. Only the landward salt flux by tidal pumping or exchange flow is shown in (b), with the missing values indicating the seaward salt flux. Note the log scale for the y-axis, and that the orders of magnitude are very different between the two sections and between the two mechanisms of tidal pumping and exchange flow.

load pushed the bay water seaward (Fig. 9b). In addition, the salinity in the main bay (Fig. 5b) dropped to zero earlier than that in Trinity Bay (Fig. 5a), resulting in the reversed salinity gradient over a few days (Fig. 10). These two mechanisms combined to result in seaward flux of salt between late August and early September, i.e., during the time under the direct impact of the Harvey's stormwater. As the strong salt intrusion along the ship channel led to the normal salinity gradient (i.e., higher salinity in the main bay than in Trinity Bay), landward salt influx resumed after mid-September.

The shelf current also plays an important role for the strong tidal pumping at the bay entrance. Shelf transport is known to affect greatly the water exchange between ocean and estuary (Du and Shen, 2017; Zhang et al., 2019). Salinity snapshots on September 13–14, about two weeks after the stormwater release, show clearly how the shelf current facilitated the salt exchange (Fig. 11). Over a tidal cycle, the bay "breathed out" low salinity water during ebb. As the along-shelf current moved the bulb of low salinity water off the bay entrance, the bay "breathed in" new high salinity water during the following flood. This process helped maintain relatively high salinity gradient and enhanced the salt flux due to tidal pumping and exchange flow at the bay entrance. On the other hand, with no equivalent renewal process at the Trinity Bay section, water mass just moved back and forth over a tidal cycle, resulting in relatively small salinity gradient and salt flux between the main bay and the sub-bay, and leading to a long stalling of low salinity water (Fig. 5a) and thus long salinity recovery time (Fig. 8f). While the shelf current enhancing tidal pumping at the bay entrance, its influence depends on direction as well as strength. For instance, an upcoast shelf current is likely more effective than a downcoast shelf current in enhancing tidal pumping for Galveston Bay as a downcoast shelf current may reduce the salinity on Texas shelf by bringing low-freshwater from the Mississippi-Atchafalaya River system (Du et al., 2019b).

4.2. Implications of slow salinity recovery on estuarine ecosystem

Input of stormwater affects not only the hydrodynamic processes but also the processes related to water quality and estuarine ecosystem. The influence of stormwater can be short- or long-lasting, depending greatly on the recovery speed of physical conditions (e.g., salinity, temperature, and estuarine circulation), the exchange processes (e.g., nutrient exchange between estuary and ocean), as well as the resiliency of marine species to the exposure of freshwater (Conner et al., 1989; Greening et al., 2006; Paerl et al., 2006; Wetz and Paerl, 2008; Munroe et al., 2013; Tweedley et al., 2016). Many species in estuaries are sensitive to salinity level. For example, plankton community (both phyto- and zooplankton), fish, and marsh are typically distributed along the salinity gradient and grow better under a specific optimal salinity range. Long exposure to low salinity may lead to devastating mortality, particularly for benthic species that have limited mobility, e.g., oysters (Munroe et al., 2013).

The spatial variation of the salinity recovery time (Fig. 8f) appears to be consistent with the changes in the phytoplankton community in Galveston Bay during and after Harvey. The phytoplankton community in the lower bay was dominated by estuarine and marine species before Harvey, transitioned to primarily freshwater species immediately

Table 2
Salt flux contribution from tidal pumping and exchange flow at the bay entrance section and the Trinity Bay section. Average values for October–December reflect the normal conditions, while average values for August–September reflect conditions with stormwater.

Section	Contribution from	Salt flux (kg salt s^{-1}) averaged over		
		August–September	October–December	August–December
Bay entrance	Tidal pumping (F_t)	10,794	5693	7547
	Exchange flow (F_e)	6707	1002	3072
Trinity Bay	Tidal pumping (F_t)	306	515	438
	Exchange flow (F_e)	−232	770	405

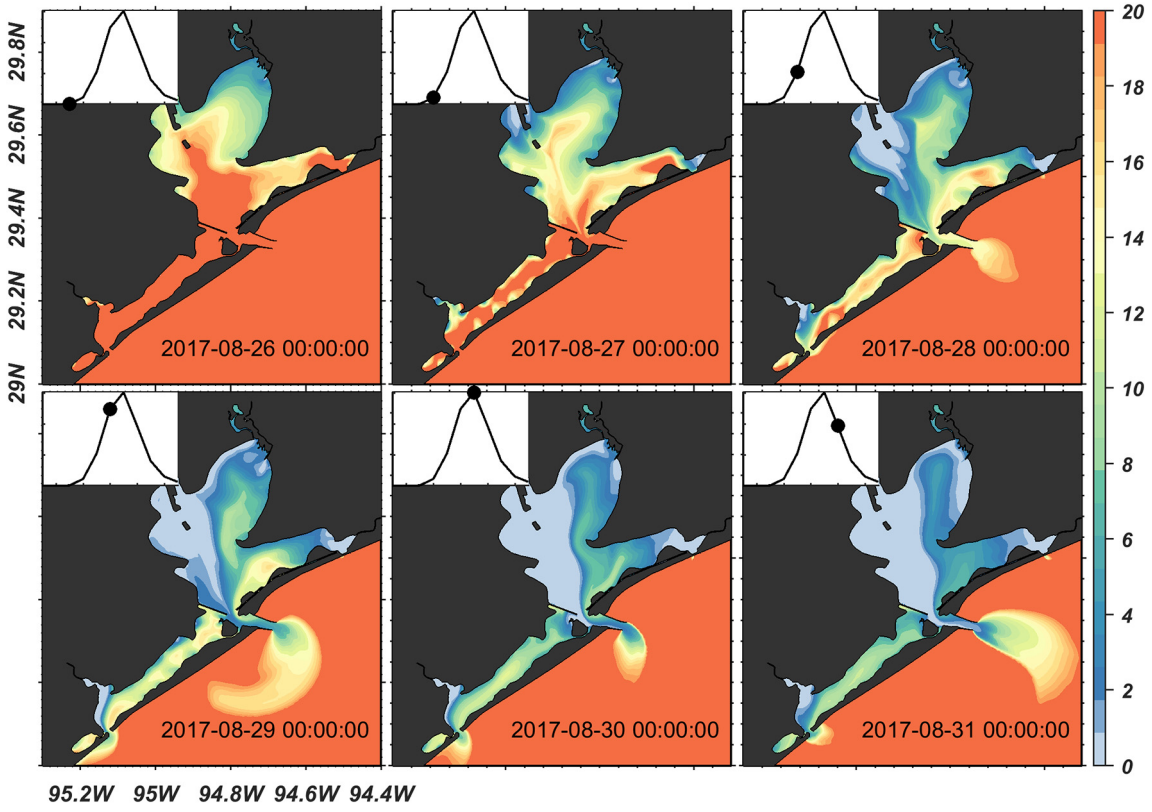

Fig. 10. Snapshots of salinity map before and during the release of the Harvey's stormwater, with the insets showing the corresponding time of the streamflow from San Jacinto River. Note the salinity difference between the main bay and Trinity Bay. Salinity in Trinity Bay was smaller compared to the main bay before the stormwater release. The salinity trend, however, was reversed during the stormwater release because of a faster decreasing of salinity in the main bay due to very large stormwater release from San Jacinto River, resulting in the reversed salinity gradient between the main bay and Trinity Bay.

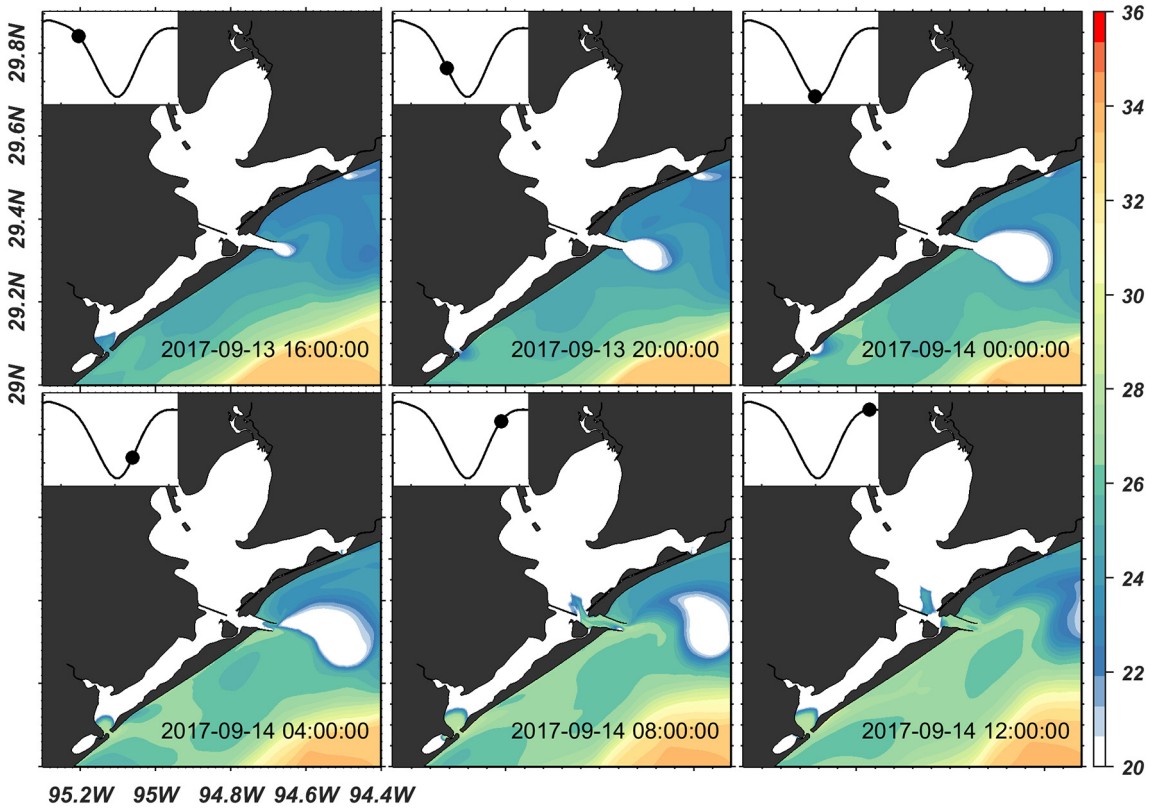

Fig. 11. Snapshots of salinity map with the insets showing the corresponding tidal phase. Note how the detachment of low salinity water on the shelf facilitates salt influx due to tidal pumping during the next flooding current.

following the flooding event, and back to marine phytoplankton similar to pre-Harvey conditions after one month following the storm (McAmis et al., 2018; Steichen et al., 2018; Liu et al., 2019). The recovery in the phytoplankton community was slower in the upper bay (J.L. Steichen, personal communication).

5. Conclusion

Extreme precipitation events are rare but likely to occur more frequently under the warming climate. This study takes the record-breaking precipitation event during Hurricane Harvey as an example to examine how the estuarine salinity recovers after a storm and discuss the underlying mechanisms for the spatially varying salinity recovery time. The salinity recovery time had a mean of two months over the entire Galveston Bay, but with great spatial variability. The spatial variability was explained by different contributions to salt influx from exchange flow and tidal pumping. Tidal pumping facilitated by the shelf current was the dominant mechanism for salt influx at the bay entrance, while the contributions from tidal pumping and exchange flow were comparable for salt influx to Trinity Bay. Numerical experiments reveal that the bay-wide mean salinity recovery time has a non-linear relationship with the stormwater input, with the rate of increase in the recovery time decreasing when stormwater input increases.

The spatial distribution of salinity recovery time and the underlying mechanisms are likely applicable for shallow estuaries with narrow outlets, which are common along the northern Gulf of Mexico, e.g., Apalachicola Bay, Mobile Bay, Matagorda Bay, Aransas Bay, and Corpus Christi Bay. The role of the shelf current for salinity recovery as identified by the present study shall also be applicable to other estuaries. The recovery time of salinity seems to be a useful timescale for the impact assessment of extreme precipitation events on estuarine systems. The present approach using a hydrodynamic model will be able to provide a relatively quick assessment of the environmental pressure of extreme events on target estuaries, highlighting the importance of validated hydrodynamic models that can reproduce both the normal and extreme conditions. The approach is not limited to extreme precipitation, but can also be applied to other extreme events such as severe drought and flood.

Supplementary data to this article can be found online at https://doi.org/10.1016/j.scitotenv.2019.03.265.

Acknowledgements

We like to acknowledge the TWDB (Texas Water Development Board), TABS (Texas Automated Buoy System), and USGS (U.S. Geological Survey) for the sources of the continuous monitoring data. We also like to acknowledge the Texas Coastal Management Program, the Texas General Land Office and NOAA for partial funding of this study through CMP Contract #19-040-000-B074. The numerical simulations were performed on the High-Performance Computing systems at College of William and Mary.

References

Balaguru, K., Foltz, G.R., Leung, L.R., 2018. Increasing magnitude of hurricane rapid intensification in the central and eastern tropical Atlantic. Geophys. Res. Lett. 45 (9), 4238–4247. https://doi.org/10.1029/2018GL077597.

Cardoso, P.G., Raffaelli, D., Lillebø, A.I., Verdelhos, T., Pardal, M.A., 2008. The impact of extreme flooding events and anthropogenic stressors on the macrobenthic communities' dynamics. Estuar. Coast. Shelf Sci. 76 (3), 553–565. https://doi.org/10.1016/j.ecss.2007.07.026.

Carrere, L., Lyard, F., Cancet, M., Guillot, A., 2015. FES 2014, a new tidal model on the global ocean with enhanced accuracy in shallow seas and in the Arctic region, In: Abstracts of the EGU General Assembly 2015. Vienna, Austria, April 12–17, 2015. http://adsabs.harvard.edu/abs/2015EGUGA..17.5481C.

Casas, S.M., Lavaud, R., La Peyre, M.K., Comeau, L.A., Filgueira, R., La Peyre, J.F., 2018. Quantifying salinity and season effects on eastern oyster clearance and oxygen consumption rates. Mar. Biol. 165, 90. https://doi.org/10.1007/s00227-018-3351-x.

Conner, W.H., Day Jr., J.W., Baumann, R.H., Randall, J.M., 1989. Influence of hurricanes on coastal ecosystems along the northern Gulf of Mexico. Wetl. Ecol. Manag. 1 (1), 45–56. https://doi.org/10.1007/BF00177889.

Donat, M.G., Lowry, A.L., Alexander, L.V., O'Gorman, P.A., Maher, N., 2016. More extreme precipitation in the world's dry and wet regions. Nat. Clim. Chang. 6 (5), 508–513. https://doi.org/10.1038/nclimate2941.

Du, J., Shen, J., 2017. Transport of riverine material from multiple rivers in the Chesapeake Bay: important control of estuarine circulation on the material distribution. J. Geophys. Res. Biogeo. 122 (11), 2998–3113. https://doi.org/10.1002/2016JG003707.

Du, J., Shen, J., Zhang, Y.J., Ye, F., Liu, Z., Wang, Z., Wang, Y.P., Yu, X., Sisson, M., Wang, H.V., 2018a. Tidal response to sea-level rise in different types of estuaries: the importance of length, bathymetry, and geometry. Geophys. Res. Lett. 45 (1), 227–235. https://doi.org/10.1002/2017GL075963.

Du, J., Park, K., Shen, J., Dzwonkowski, B., Yu, X., Yoon, B.I., 2018b. Role of baroclinic processes on flushing characteristics in a highly stratified estuarine system, Mobile Bay, Alabama. J. Geophys. Res. Oceans 123 (7), 4518–4537. https://doi.org/10.1029/2018JC013855.

Du, J., Park, K., Dellapenna, T.M., Clay, J.M., 2019a. Dramatic hydrodynamic and sedimentary responses in Galveston Bay and adjacent inner shelf to Hurricane Harvey. Sci. Total Environ. 653, 554–564. https://doi.org/10.1016/J.SCITOTENV.2018.10.403.

Du, J., Park, K., Shen, J., Zhang, Y.J., Yu, X., Ye, F., Wang, Z., Rabalais, N.N., 2019b. A hydrodynamic model for Galveston Bay and the shelf in the northwestern Gulf of Mexico. Ocean Sci. Discuss. https://doi.org/10.5194/os-2019-9 in review.

Emanuel, K., 2017. Assessing the present and future probability of Hurricane Harvey's rainfall. P. Natl. A. Sci. USA. 114 (48), 12681–12684. https://doi.org/10.1073/pnas.1716222114.

Frazer, T.K., Notestein, S.K., Jacoby, C.A., Littles, C.J., Keller, S.R., Swett, R.A., 2006. Effects of storm-induced salinity changes on submersed aquatic vegetation in Kings Bay. Florida. Estuar. Coast. 29 (6A), 943–953. https://doi.org/10.1007/bf02798655.

Fritz, A., Samenow, J., 2017. Harvey Unloaded 33 Trillion Gallons of Water in the U.S. https://www.washingtonpost.com/news/capital-weather-gang/wp/2017/08/30/harvey-has-unloaded-24-5-trillion-gallons-of-water-on-texas-and-louisiana/?utm_term=.92eae8c1e7da, Accessed date: 10 March 2019.

Gong, W., Shen, J., Reay, W.G., 2007. The hydrodynamic response of the York River estuary to Tropical Cyclone Isabel, 2003. Estuar. Coast. Shelf S. 73 (3–4), 695–710. https://doi.org/10.1016/j.ecss.2007.03.012.

Greening, H., Doering, P., Corbett, C., 2006. Hurricane impacts on coastal ecosystems. Estuar. Coast. 29 (6), 877–879. https://doi.org/10.1007/BF02798646.

Hagy, J.D., Lehrter, J.C., Murrell, M.C., 2006. Effects of hurricane Ivan on water quality in Pensacola Bay. Florida. Estuar. Coast. 29 (6A), 919–925. https://doi.org/10.1007/BF02798651.

Huzzey, L.M., Brubaker, J.M., 1988. The formation of longitudinal fronts in a coastal plain estuary. J. Geophys. Res. 93 (C2), 1329–1334. https://doi.org/10.1029/JC093iC02p01329.

Kantha, L.H., Clayson, C.A., 1994. An improved mixed layer model for geophysical applications. J. Geophys. Res. 99 (C12), 25235–25266. https://doi.org/10.1029/94JC02257.

Knapp, A.K., Beier, C., Briske, D.D., Classen, A.T., Luo, Y., Reichstein, M., Smith, M.D., Smith, S.D., Bell, J.E., Fay, P.A., Heisler, J.L., Leavitt, S.W., Sherry, R., Smith, B., Weng, E., 2008. Consequences of more extreme precipitation regimes for terrestrial ecosystems. BioScience 58 (9), 811–821. https://doi.org/10.1641/B580908.

Knight, D.B., Davis, R.E., 2009. Contribution of tropical cyclones to extreme rainfall events in the southeastern United States. J. Geophys. Res. Atmos. 114, D23102. https://doi.org/10.1029/2009JD012511.

Lerczak, J.A., Geyer, W.R., 2004. Modeling the lateral circulation in straight, stratified estuaries. J. Phys. Oceanogr. 34 (6), 1410–1428. https://doi.org/10.1175/1520-0485(2004)034<1410:MTLCIS>2.0.CO;2.

Lerczak, J.A., Geyer, W.R., Chant, R.J., 2006. Mechanisms driving the time-dependent salt flux in a partially stratified estuary. J. Phys. Oceanogr. 36 (12), 2296–2311. https://doi.org/10.1175/JPO2959.1.

Li, M., Zhong, L., Boicourt, W.C., Zhang, S., Zhang, D.-L., 2006. Hurricane-induced storm surges, currents and destratification in a semi-enclosed bay. Geophys. Res. Lett. 33 (2), L02604. https://doi.org/10.1029/2005GL024992.

Liu, B., D'Sa, E.J., Joshi, I.D., 2019. Floodwater impact on Galveston Bay phytoplankton taxonomy, pigment composition and photo-physiological state following Hurricane Harvey from field and ocean color (Sentinel-3A OLCI) observations. Biogeosci. Discuss. https://doi.org/10.5194/bg-2018-504 in review.

MacCready, P., Geyer, W.R., 2010. Advances in estuarine physics. Annu. Rev. Mar. Sci. 2, 35–58. https://doi.org/10.1146/annurev-marine-120308-081015.

McAmis, A. K., Steichen, J. L., Quigg, A., 2018. The effects of Hurricane Harvey on the phytoplankton community in Galveston Bay. In: Abstracts of the 2018 GERS Meeting: Ecosystem Resilience and Restoration in a Changing World, Galveston, Texas, November 8–10, 2018.

Milliner, C., Materna, K., Bürgmann, R., Fu, Y., Moore, A.W., Bekaert, D., Adhikari, S., Argus, D.F., 2018. Tracking the weight of Hurricane Harvey's stormwater using GPS data. Sci. Adv. 4 (9), eaau2477. https://doi.org/10.1126/sciadv.aau2477.

Moriasi, D.N., Arnold, J.G., Van Liew, M.W., Bingner, R.L., Harmel, R.D., Veith, T.L., 2007. Model evaluation guidelines for systematic quantification of accuracy in watershed simulations. T. ASABE 50, 885–900. https://doi.org/10.1016/j.jhydrol.2012.12.004.

Munroe, D., Tabatabai, A., Burt, I., Bushek, D., Powell, E.N., Wilkin, J., 2013. Oyster mortality in Delaware Bay: impacts and recovery from Hurricane Irene and Tropical Storm Lee. Estuar. Coast. Shelf Sci. 135, 209–219. https://doi.org/10.1016/j.ecss.2013.10.011.

Nash, J.E., Sutcliffe, J.V., 1970. River flow forecasting through conceptual models, part I - a discussion of principles. J. Hydrol. 10 (3), 282–290. https://doi.org/10.1016/0022-1694(70)90255-6.

Paerl, H.W., Valdes, L.M., Joyner, A.R., Peierls, B.L., Piehler, M.F., Riggs, S.R., Christian, R.R., Eby, L.A., Crowder, L.B., Ramus, J.S., Clesceri, E.J., Buzzelli, C.P., Luettich Jr., R.A., 2006. Ecological response to hurricane events in the Pamlico Sound system, North Carolina,

and implications for assessment and management in a regime of increased frequency. Estuar. Coast. 29 (6), 1033–1045. https://doi.org/10.1007/BF02798666.
Peierls, B.L., Christian, R.R., Paerl, H.W., 2003. Water quality and phytoplankton as indicators of hurricane impacts on a large estuarine ecosystem. Estuaries 26 (5), 1329–1343. https://doi.org/10.1007/BF02803635.
Pfahl, S., O'Gorman, P.A., Fischer, E.M., 2017. Understanding the regional pattern of projected future changes in extreme precipitation. Nat. Clim. Chang. 7 (6), 423–427. https://doi.org/10.1038/nclimate3287.
Posey, M., Lindberg, W., Alphin, T., Vose, F., 1996. Influence of storm disturbance on an offshore benthic community. B. Mar. Sci. 59 (3), 523–529.
Rego, J.L., Li, C., 2010. Storm surge propagation in Galveston Bay during Hurricane Ike. J. Mar. Sys. 82 (4), 265–279. https://doi.org/10.1016/j.jmarsys.2010.06.001.
Ritter, A., Muñoz-Carpena, R., 2013. Performance evaluation of hydrological models: statistical significance for reducing subjectivity in goodness-of-fit assessments. J. Hydrol. 480, 33–45. https://doi.org/10.1016/j.jhydrol.2012.12.004.
Scheffer, M., Carpenter, S., Foley, J.A., Folke, C., Walker, B., 2001. Catastrophic shifts in ecosystems. Nature 413, 591–596.
Sebastian, A., Proft, J., Dietrich, J.C., Du, W., Bedient, P.B., Dawson, C.N., 2014. Characterizing hurricane storm surge behavior in Galveston Bay using the SWAN+ADCIRC model. Coast. Eng. 88, 171–181. https://doi.org/10.1016/j.coastaleng.2014.03.002.
Shen, J., Wang, H., Sisson, M., Gong, W., 2006. Storm tide simulation in the Chesapeake Bay using an unstructured grid model. Estuar. Coast. Shelf Sci. 68 (1–2), 1–16. https://doi.org/10.1016/j.ecss.2005.12.018.
Steichen, J. L., Windham, R., Hala, D., Kaiser, K., Labonté, J. M., Petersen, L. H., Bacosa, H., Bretherton, L., Kamalanathan, M., Setta, S., Quigg, A., 2018. Rapid physicochemical and biological assessment of Galveston Bay in the wake of Hurricane Harvey. In: Abstracts of the 2018 Ocean Sciences Meeting, AGU, Portland, Oregon, February 11–16, 2018.
Tweedley, J.R., Hallettt, C.S., Warwick, R.M., Clarke, K.R., Potter, I.C., 2016. The hypoxia that developed in a microtidal estuary following an extreme storm produced dramatic changes in the benthos. Mar. Freshw. Res. 67 (3), 327–341. https://doi.org/10.1071/MF14216.
Umlauf, L., Burchard, H., 2003. A generic length-scale equation for geophysical turbulence models. J. Mar. Res. 61 (2), 235–265. https://doi.org/10.1357/002224003322005087.
Valle-Levinson, A., Wong, K.-C., Bosley, K.T., 2002. Response of the lower Chesapeake Bay to forcing from Hurricane Floyd. Cont. Shelf Res. 22 (11−13), 1715–1729. https://doi.org/10.1016/S0278-4343(02)00034-1.
van Oldenborgh, G. J., van der Wiel, K., Sebastian, A., Singh, R., Arrighi, J., Otto, F., Haustein, K., Li, S., Vecchi, G., Cullen, H., 2018. Corrigendum: Attribution of extreme rainfall from Hurricane Harvey, August 2017. Environ. Res. Lett. 13, 019501. doi:https://doi.org/10.1088/1748-9326/aaa343.
Walker, N.D., 2001. Tropical storm and hurricane wind effects on water level, salinity, and sediment transport in the river-influenced Atchafalaya-Vermilion Bay System, Louisiana, USA. Estuaries 24 (4), 498–508. https://doi.org/10.2307/1353252.
Wetz, M.S., Paerl, H.W., 2008. Estuarine phytoplankton responses to hurricanes and tropical storms with different characteristics (trajectory, rainfall, winds). Estuar. Coast. 31 (2), 419–429. https://doi.org/10.1007/s12237-008-9034-y.
Weyhenmeyer, G.A., Willén, E., Sonesten, L., 2004. Effects of an extreme precipitation event on water chemistry and phytoplankton in the Swedish Lake Mälaren. Boreal Environ. Res. 9 (5), 409–420.
Willmott, C.J., 1981. On the validation of models. Phys. Geogr. 2 (2), 184–194. https://doi.org/10.1080/02723646.1981.10642213.
Ye, F., Zhang, Y.J., Wang, H.V., Friedrichs, M.A.M., Irby, I.D., Alteljevich, E., Valle-Levinson, A., Wang, Z., Huang, H., Shen, J., Du, J., 2018. A 3D unstructured-grid model for Chesapeake Bay: importance of bathymetry. Ocean Model 127, 16–39. https://doi.org/10.1016/j.ocemod.2018.05.002.
Zhang, Y., Baptista, A.M., 2008. SELFE: A semi-implicit Eulerian-Lagrangian finite-element model for cross-scale ocean circulation. Ocean Model 21 (3–4), 71–96. https://doi.org/10.1016/j.ocemod.2007.11.005.
Zhang, Q., Brady, D.C., Ball, W.P., 2013. Long-term seasonal trends of nitrogen, phosphorus, and suspended sediment load from the non-tidal Susquehanna River Basin to Chesapeake Bay. Sci. Total Environ. 452-453, 208–221. https://doi.org/10.1016/j.scitotenv.2013.02.012.
Zhang, Y.J., Ateljevich, E., Yu, H.C., Wu, C.H., Yu, J.C.S., 2015. A new vertical coordinate system for a 3D unstructured-grid model. Ocean Model 85, 16–31. https://doi.org/10.1016/j.ocemod.2014.10.003.
Zhang, Y.J., Ye, F., Stanev, E.V., Grashorn, S., 2016. Seamless cross-scale modeling with SCHISM. Ocean Model 102, 64–81. https://doi.org/10.1016/j.ocemod.2016.05.002.
Zhang, H., Cheng, W., Chen, Y., Shi, Z., Gong, W., Liu, S., 2019. Importance of large-scale coastal circulation on bay-shelf exchange and residence time in a subtropical embayment, the northern South China Sea. Ocean Coast. Manage. 168, 72–89. https://doi.org/10.1016/j.ocecoaman.2018.10.033.

Science of the Total Environment 653 (2019) 554–564

Contents lists available at ScienceDirect

Science of the Total Environment

journal homepage: www.elsevier.com/locate/scitotenv

Dramatic hydrodynamic and sedimentary responses in Galveston Bay and adjacent inner shelf to Hurricane Harvey

Jiabi Du [a,*], Kyeong Park [a], Timothy M. Dellapenna [a], Jacinta M. Clay [b]

[a] Department of Marine Sciences, Texas A&M University at Galveston, Galveston, TX 77554, United States
[b] Earth, Environmental and Planetary Sciences, Brown University, Providence, RI 02912, United States

HIGHLIGHTS

- Dramatic changes in hydrodynamic and sedimentary processes were observed in Galveston Bay during and following Harvey.
- Salinity recovery time for the bay from the unprecedented precipitation was around 2 months.
- We propose a freshwater fraction method for estimating freshwater load during extreme precipitation events.
- Freshwater load into the bay due to Harvey was estimated to be 11.1×10^9 m^3, about 3 times the entire bay's volume.
- 9.86×10^7 metric tons of sediment were delivered by Harvey, equivalent to 18 years of average sediment load.

GRAPHICAL ABSTRACT

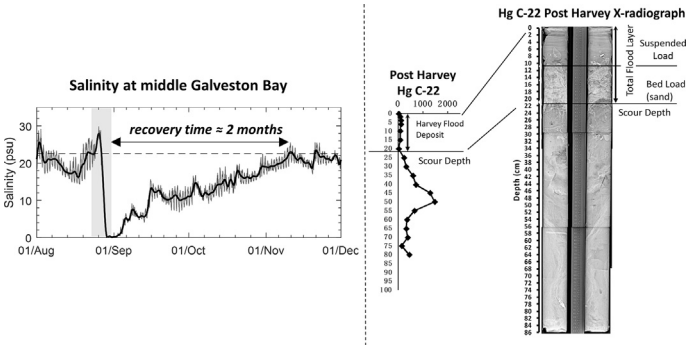

ARTICLE INFO

Article history:
Received 7 September 2018
Received in revised form 28 October 2018
Accepted 29 October 2018
Available online 31 October 2018

Editor: Damia Barcelo

Keywords:
Hurricane Harvey
Galveston Bay
Extreme precipitation
Recovery time
Freshwater load
Sediment load

ABSTRACT

Hurricane Harvey, one of the worst hurricanes that hit the United States in recent history, poured record-breaking rainfall across the Houston metropolitan area. Based on a comprehensive set of data from various sources, we examined the dramatic responses in hydrodynamic and sedimentary processes of Galveston Bay to this extreme event. Using a freshwater fraction method that circumvents the uncertainties in surface runoff and groundwater discharge, the freshwater load into the bay during Harvey and the following month was estimated to be 11.1×10^9 m^3, about 3 times the bay volume, which had completely refreshed the entire bay. Harvey also delivered 9.86×10^7 metric tons of sediment into the bay, equivalent to 18 years of average annual sediment load. At a site inside the San Jacinto Estuary, acute bed erosion of 48 cm followed by deposition of 22 cm of new sediment was observed from the sediment cores. Slow salinity recovery (~2 month) and a thick flood deposit (~10.5 cm average over the entire bay) had likely impacted the ecosystem in the bay and the adjacent inner shelf. Estuaries with similar bathymetric and geometric characteristics, i.e., shallow bathymetry with narrow outlets, are expected to experience similar dramatic estuarine responses while extreme precipitation events are expected to occur more frequently under the warming climate.

1. Introduction

Hurricanes, typhoons, and other cyclonic storms often produce sudden, massive disturbances in estuaries and other coastal ecosystems around the world. Disturbances in physical conditions induced by

* Corresponding author at: 1001 Texas Clipper Rd, Galveston, TX 77554, United States.
E-mail address: jdu@tamug.edu (J. Du).

https://doi.org/10.1016/j.scitotenv.2018.10.403
0048-9697/

high-speed wind, large freshwater input, and storm surge tend to be short-lived, typically on the timescale of days (Eyre and Twigg, 1997; Greening et al., 2006; Li et al., 2006; Park et al., 2007; Cho et al., 2012). Changes in ecosystems due to excessive nutrient and sediment input as well as turn-over of the estuarine water, on the other hand, can last for months or even years (Paerl et al., 2001; Burkholder et al., 2004; Miller et al., 2006). Alterations in marshes, submerged aquatic vegetation, phytoplankton, zooplankton, food web, and estuarine landscape following major storms have been observed in many coastal systems (Michener et al., 1997; Cardoso et al., 2008; Park et al., 2014). Recovery from the disturbance depends on storm intensities, flushing capacities, and the resiliency of the ecosystem. Estuaries that have been frequently affected by hurricanes are shown to have a relatively rapid recovery in water quality and biota, and may even benefit from the scouring by storms (Burkholder et al., 2004). Pulses of nutrient input can lead to the increase of productivity in both short- and long-term timescales (Paerl et al., 2001, 2006; Miller et al., 2006; Wetz and Paerl, 2008). Furthermore, storms have long been recognized as key agents of geomorphic change to coastal wetlands and their effects on vegetation and soils may be permanent on an ecological timescale (Cahoon, 2006). Large influxes of sediment have contributed to the maintenance of existing wetlands or even creation of new ones (Conner et al., 1989; Zhang and Blomquist, 2018).

Extreme precipitation from tropical cyclones has increased over the past few decades (Knight and Davis, 2009; Donat et al., 2016; Pfahl et al., 2017). It is generally expected that storm and hurricane activities will be affected by climate change in the future, primarily because of a warmer and moister environment (Trenberth et al., 2005, 2018). Anthropogenic climate change is commonly projected to lead to a greater incidence of high-intensity hurricanes (Rotunno et al., 2009; Knutson et al., 2010, 2015). Increased upper ocean heat content and water vapor due to global warming will result in a higher possibility of extreme rainfall (Knight and Davis, 2009; Risser and Wehner, 2017; Trenberth et al., 2018). Responses of the ocean and coastal systems to extreme precipitation events have attracted increasing attention worldwide (e.g., Chambers et al., 2007; De Carlo et al., 2007; Du et al., 2017). Hurricane Harvey provides a notable example of the estuarine response to an extreme precipitation event.

Hurricane Harvey (hereinafter referred to as Harvey) intensified quickly in the northern Gulf of Mexico before making landfall on August 26, 2017 along the mid-Texas coast as a Category 4 hurricane. Harvey brought record-breaking precipitation, with the return period of the peak 3-day precipitation exceeding 1000 years (van Oldenborgh et al., 2018), and caused more than 80 fatalities and over $150 billion economic losses, mostly due to the extraordinary flooding (Emanuel, 2017; Balaguru et al., 2018). Over the 5-day period from August 26 to 30, Harvey dumped 92.7 billion m^3 of water across Texas and Louisiana (Fritz and Samenow, 2017), with a maximum precipitation of more than 1200 mm, as reported from some weather stations. Devastating rainfall occurred in the Houston metropolitan area when Harvey stalled near the southeast Texas coast, with a portion of the storm system remaining over the warm waters of the Gulf of Mexico for more than 4 days (Fig. 1a) (Risser and Wehner, 2017; Sarkar et al., 2018; Wang et al., 2018). It is commonly believed that the hydrodynamics and ecosystem of the bay and adjacent inner shelf were dramatically affected by the acute event. However, till now, there has been no accurate estimation of how much freshwater and sediment were discharged into Galveston

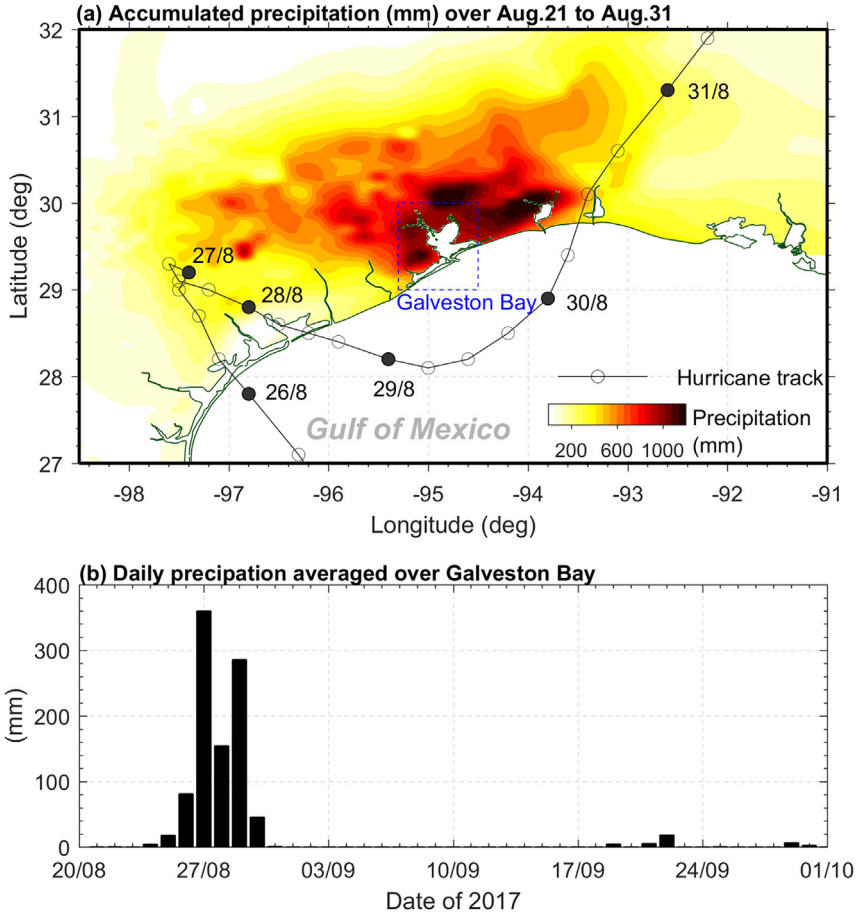

Fig. 1. (a) Accumulated precipitation during Hurricane Harvey between August 21 and 31, 2017 and (b) daily precipitation averaged over Galveston Bay (30 weather stations). In (a), the 6-hourly track (all times in UTC) of Hurricane Harvey, based on data from National Hurricane Center (https://www.nhc.noaa.gov), is shown with circles. Precipitation data in (b) are based on daily records extracted from Global Historical Climatology Network (https://www.ncdc.noaa.gov).

Bay during Harvey. These estimates are of great interest to biogeochemical and ecological research as well as environmental assessment as they are intimately related to the way the system is flushed and to the timescales with which the system recovers. Recovering from a hurricane is essential for ecosystems as well as for human society. The sustained low-salinity condition because of excessive freshwater input may cause a big shift in phytoplankton, zooplankton, coral reef, and fishery communities (Mallin et al., 1999; Paerl et al., 2001; Roman et al., 2005).

During Harvey, monitoring stations maintained by several agencies worked normally despite the strong wind and intense flooding, providing a valuable and comprehensive dataset for major hydrodynamic variables. We also collected multiple sediment cores before and after Harvey throughout Galveston Bay. Based on the available data set, we examine the temporal and spatial variation of estuarine dynamics during Harvey, estimate the timescales with which the estuarine system recovered from this extreme event, calculate the freshwater load discharging into Galveston Bay during Harvey, and estimate the thickness of the storm deposit and the amount of sediment delivered to Galveston Bay as a result of Harvey. Estimating freshwater load during an extreme precipitation event is not easy as large volumes of freshwater typically discharges into a coastal system through surface runoff and groundwater discharge, which is usually not accounted for by gauge stations. Here, we present an approach based on a mass balance concept that the export volume of freshwater leaving the bay is to be replenished by the freshwater load.

2. Materials

2.1. Study area

Galveston Bay, located along the northeastern Texas Coast of the Gulf of Mexico, is a typical shallow bar-built estuary, with a narrow (2.4 km wide) tidal inlet, called Bolivar Roads, which separates Galveston Island and Bolivar Peninsula. It has a surface area of 1.55×10^9 m^2 and a mean depth of 2.46 m (based on 10-m DEM data extracted from https://www.ngdc.noaa.gov). It has a deep ship channel (~15 m deep) extending about 80 km from the mouth all the way to the Houston Port, which is the second largest seaport in the U.S. in terms of total shipping tonnage (http://porthouston.com/about-us/statistics/). The bay receives annual mean river discharge of 350 m^3 s^{-1} (or yearly load of 1.1×10^{10} m^3, about 3 times the total bay volume) from three major rivers, including Trinity River (mean discharge 271 m^3 s^{-1} in 1988–2017), San Jacinto River (mean discharge 65 m^3 s^{-1} in 2006–2017), and Buffalo Bayou (mean discharge 14 m^3 s^{-1} in 2000–2017). The river discharge rates are based on the data from the USGS gauge stations and the hydrological model in Schoenbaechler et al. (2012). The streamflow is mainly determined by precipitation, with a mean annual rainfall of 1264 mm (Lucena and Lee, 2017). Water exchange with the coastal ocean is limited, with a mean turn over time of 30–60 days depending on the river discharge as well as wind condition (Solis and Powell, 1999; Rayson et al., 2016). Galveston Bay has long been considered as a hot spot for environmental and biogeochemical studies owing to the dense population and its extensive petrochemical complex, the second largest in the world (Santschi et al., 2001; Warnken et al., 2001; Tang et al., 2002; Al Mukiami et al., 2018a). The bay, on the other hand, is also a known nursing habitat for multiple valuable fisheries, including white and brown shrimp (Stunz et al., 2010), and provides 14% of the U.S. wild catch of oysters (Haby et al., 2009).

2.2. Data collection and analysis

A comprehensive data set for the conditions in Galveston Bay and adjacent inner shelf as well as the forcing conditions were assembled from various sources (Table 1; Fig. 2). Data for water level and wind were collected from three NOAA tidal gauge stations (Galveston Bay Entrance, Eagle Point and Morgan's Point: https://tidesandcurrents.noaa.gov), current velocity from four Texas Automated Buoy System (TABS) stations (g08010, g06010, B, and F: http://pong.tamu.edu/tabswebsite), salinity from four TABS stations (Buoy-Morgans, Buoy-Eagle, Buoy-B, and Buoy-F) and four Texas Water Development Board (TWDB) stations (BOLI, MIDG, TRIN, and FISH: https://waterdatafortexas.org/coastal). For forcing conditions, daily precipitation data were collected from Global Historical Climatology Network (GHCN: https://www.ncdc.noaa.gov), streamflow

Table 1
Location, measurement depth and interval, and data source for monitoring stations.

Station ID	Longitude	Latitude	Parameter	Depth	Sampling interval	Source
TRIN	−94.7460	29.6610	Salinity	1.49 m	1 h	TWDB[a]
FISH	−94.8540	29.6700	Salinity	2.27 m	1 h	TWDB
MIDG	−94.8750	29.508	Salinity	3.10 m	1 h	TWDB
BOLI	−94.7830	29.3420	Salinity	2.88 m	1 h	TWDB
g08010	−95.0183	29.7030	Current	Surface	6 min	TABS[b]
g06010	−94.7408	29.3422	Current	Surface	6 min	TABS
B	−94.8991	28.9823	Current, salinity	Surface	30 min	TABS
F	−94.2416	28.8425	Current, salinity	Surface	30 min	TABS
Buoy-Morgans[d]	−94.9850	29.6817	Salinity	Surface	6 min	TABS
Buoy-Eagle[e]	−94.9183	29.4800	Salinity	Surface	6 min	TABS
Morgans Point	−94.9850	29.6817	Water level		6 min	NOAA[c]
Eagle Point	−94.9183	29.4800	Water level		6 min	NOAA
Bay Entrance	−94.7250	29.3567	Water level, wind		6 min	NOAA

[a] TWDB: Texas Water Development Board (https://waterdatafortexas.org/coastal).
[b] TABS: Texas Automated Buoy System (http://pong.tamu.edu/tabswebsite).
[c] NOAA: National Oceanic and Atmospheric Administration (https://tidesandcurrents.noaa.gov).
[d] Salinity data at Buoy-Morgans are from the TABS buoy station 8770613, which is at the same location as the NOAA station at Morgans Point.
[e] Salinity data at Buoy-Eagle are from the TABS buoy station 8771013, which is at the same location as the NOAA station at Eagle Point.

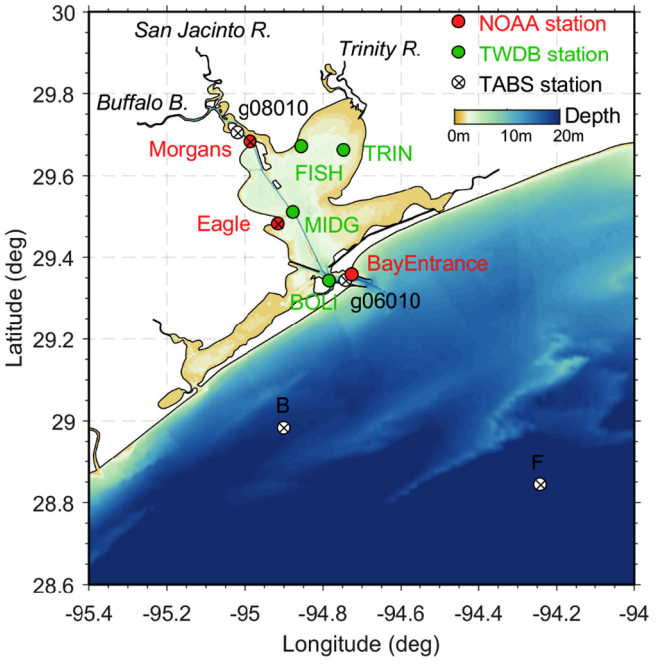

Fig. 2. Map of Galveston and its adjacent shelf showing bottom bathymetry (color; unit: m) and NOAA gauge stations (red solid circles), TABS buoy stations (circles with ×), and TWDB stations (green solid circles). (For interpretation of the references to color in this figure legend, the reader is referred to the web version of this article.)

data were extracted from three USGS stations (08066500, 08067252, and 08074000: https://waterdata.usgs.gov/usa/nwis/), and data for reservoir storage at Lake Houston, Addicks Reservoir and Barker Reservoir were from another three USGS stations (08072000, 08073000, and 08072500). At the Wallisville station (USGS 08067252), water level data at both upstream and downstream of the Wallisville Barrier were collected in order to examine the effect of flood-control activities during and after Harvey. The data have a temporal resolution ranging from 6 min to an hour. Noise and unreasonable data (e.g., negative salinity or values larger than 40 psu) were cleaned by manually setting the upper/lower bounds and removing abnormal spikes. Hourly averaging was applied for all datasets. Despite the strong wind conditions during Harvey, almost all the monitoring stations including buoys, tidal gauges, and weather stations functioned properly to provide useable data, with some but not significant data gaps.

Between 2011 and 2013 a series of vibra cores were collected from the Galveston Bay system, including the San Jacinto Estuary as well as the Clear Lake subestuary, to assess sedimentation rates and also mercury (Hg) input (Al Mukiami et al., 2018a,b). The data from these cores provided a basis for comparisons of the impact of Hurricane Harvey. From October 2017 to May 2018, 64 pushcores were collected from the Galveston and Trinity Bays as well as the San Jacinto Estuary and the Clear Lake subestuary, using 7.62-cm diameter, 0.6-m long polycarbonate core barrels. Upon return to the lab, the polycarbonate pushcores were x-rayed using a large animal veterinarian X-ray machine with a digital panel. The thicknesses of the Harvey flood layer were visually determined from the X-radiographs based on textural variations in the strata. The flood layer thicknesses for individual cores were mapped and contoured using ArcGIS, and a sediment volume was determined for the flood layer based on the contoured data. Using the storm layer deposit volume, a mass of the storm layer was determined using the density of quartz (2.65 g cm^{-3}) for sediment density and the water content of 70% for the sediment (an average value from the surface samples of the sediment cores).

2.3. Freshwater load estimation: a freshwater fraction method

By using continuous monitoring data of salinity and velocity at the bay entrance, we estimated the net freshwater export during and after Harvey by applying a freshwater fraction method, for which we need the escape velocity and salinity at the bay mouth. This method was based on the concept of freshwater fraction (Dyer, 1973), which has been widely used in calculations of estuarine turnover or residence time (Huang and Spaulding, 2002; Sheldon and Alber, 2006; Du and Shen, 2016; Du et al., 2018). Applying a freshwater fraction method requires an estimation of the cross-sectional average normal escape velocity, while only the surface velocity data were available at buoy g06010 at the bay mouth. We used the 2-year numerical model results (Du and Park, A cross-scale numerical model for the Northwestern Gulf of Mexico, in prep.) to find a relationship that estimates the cross-sectional average normal velocity (y) as a function of the surface velocity at buoy g06010 (x): $y = F(x) = 0.0686x^2 + 0.6132x + 0.0215$ ($r^2 = 0.98$). The relationship is non-linear but rather robust, i.e., relatively small range of variation in y for a given x (Fig. 3). Then, we estimated the freshwater export rate Q_f:

$$Q_f = F(v_{buoy\_obs})A\frac{(s_{sea}-s)}{s_{sea}} \quad (1)$$

where v_{buoy_obs} is the observed surface velocity at buoy g06010, A is the cross-sectional area, s is the observed salinity at BOLI, and s_{sea} is the coastal sea salinity (for which we used 27 psu based on the pre-storm condition). In Eq. 1, we assumed that the salinity data at BOLI were representative of the mean salinity at the bay mouth. With the close proximity between BOLI and the bay mouth, this assumption was not likely to generate significant errors.

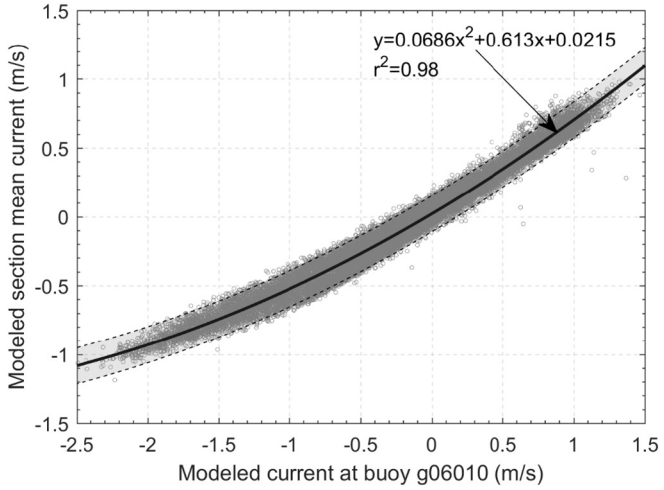

Fig. 3. Relationship between current at the buoy g06010 station and cross-section average normal current, based on hourly numerical model results in 2007–2008, showing a quadratic polynomial regression (bold solid line) and its 95th confidence interval (dashed lines).

3. Results and discussion

3.1. Precipitation and streamflow: influence from flood control structures

The majority of the Galveston Bay watershed received more than 1000 mm of precipitation during Harvey, with the peaks in precipitation occurring on August 27 and 29 (Fig. 1b). Most of the precipitation within the Galveston Bay watershed happened between August 26 to 30 and this period is referred to as the precipitation period in this study. Precipitation in the following month was very low, with a maximum daily precipitation of 18 mm on September 22. As a result, the streamflow into Galveston Bay during Harvey and in the following month is considered mostly from Harvey precipitation.

Hydraulic response, as shown in the streamflow at three USGS stations, is characterized by rapid increases in river discharge from August 26 (Fig. 4a). While the time period of increasing discharge was similar for all three stations, the duration of recession varied significantly. At the Trinity-Romayor station (80 km upriver from the Trinity River mouth), the streamflow started to increase from August 26, peaked on August 30 and decreased quickly afterward, reaching the pre-storm condition (the condition before the precipitation period) around September 5. In total, it took about 7 days for the streamflow to drop to the pre-storm condition, which was far shorter than those at the other two stations. At the Buffalo Bayou station, for example, it took more than one month for the streamflow to decrease to its pre-storm condition. This was not in line with the expectation of the different hydraulic response between forested and urban watersheds; generally, a faster recession is expected for an urban watershed (e.g., Buffalo Bayou) than for a forested watershed (e.g., Trinity River) because of more impermeable ground and higher runoff in urban areas (Shuster et al., 2005).

The unusual hydraulic response was related to the human-built flood control structures. The Addicks and Barker Reservoirs, located west of Houston and built in the 1940s, are key infrastructures designed to relieve the potential flooding risk from western and downtown Houston. Water level in the reservoirs increased dramatically after the large Harvey precipitation, with an increasing rate as high as 0.15 m per hour. Addicks Reservoir started to release water at 7 am on August 28 (UTC), while Barker Reservoir started releasing a day later. Released water from both reservoirs went into Buffalo Bayou. The releasing rate of Addicks Reservoir at the beginning was about 133 m^3 s^{-1}, and it lasted for about 43 days before the water levels inside the reservoirs recovered to their pre-storm levels (Fig. 4b). The long-lasting release resulted in the slow but long recession of the streamflow at the Buffalo

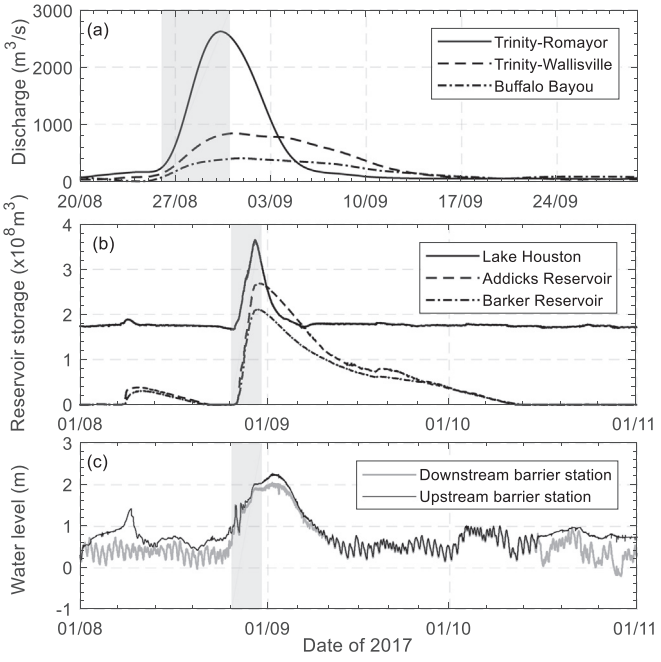

Fig. 4. (a) River discharge at three USGS stations, (b) water storage at three reservoirs, and (c) water level at the upstream and downstream stations of the Wallisville Barrier. For the Wallisville station in (a), the tidal signal is removed. In (b), discharge from Lake Houston leads to the streamflow in San Jacinto River, while Addicks and Barker Reservoirs in Buffalo Bayou. Grey shading indicates the period of August 26–30, during which heavy precipitation occurred.

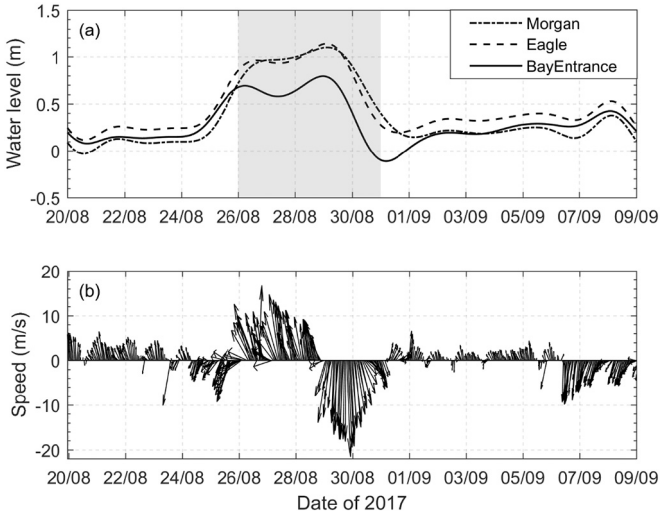

Fig. 5. (a) Observed sub-tidal water level at three NOAA tidal gauge stations and (b) wind at the Bay Entrance NOAA gauge station. Grey shading in (a) indicates the period of August 26–30, during which heavy Harvey precipitation occurred.

Bayou station. Lake Houston, which discharges into San Jacinto River, also released reservoir water during and after Harvey, but the release had much higher rates and lasted only for about 7 days.

Interestingly, the recession of streamflow was also slow and long-lasting at the Trinity-Wallisville station (6 km upriver from the Trinity River mouth). However, comparison of water levels between the upstream and downstream stations of the Wallisville Barrier suggested there was no flood controlling activities during Harvey. With controlling activities, the water level upstream of the barrier would be higher with a much weaker tidal signal compared to the station downstream of the barrier, as shown before the precipitation period and after mid-October (Fig. 4c). We speculate that the vast forest watershed upstream of the Wallisville Barrier had stored a large volume of water derived from the rainfall in the soil and groundwater aquifer and its slow discharge resulted in the observed long-lasting recession in the streamflow at the Wallisville station.

3.2. Subtidal water level

The sub-tidal water level (low-pass filtered signal with a cut-off period of 48 h) at the three NOAA tidal gauge stations (see Fig. 2 for their locations) started to increase on August 25, with the first peak occurring on August 26, and the elevated water level maintained or slightly increased until August 29 (Fig. 5a). After August 29, it decreased and took about 2 days to return to the pre-storm condition. Two stations inside the bay (Eagle Point and Morgan's Point) showed larger increases in water level, with a maximum sub-tidal water level of 1.2 m observed on August 29. The sub-tidal water level at Bay Entrance was 0.4–0.5 m lower than those at in-bay stations during the precipitation period. What is surprising is that the elevated water level had maintained itself for over 4 days, quite different from the case during typical tropical storms. Typical tropical storms produce a storm surge with a rapid rise and fall of water level that generally lasts for one or two days (e.g., Valle-Levinson et al., 2002; Li et al., 2006; Shen et al., 2006; Cho et al., 2012; Brown et al., 2014; Sebastian et al., 2014; Ye et al., 2018).

The atypically long-lasting peak surge in Galveston Bay can be attributable to the stalling of Harvey and the prolonged heavy precipitation near the Texas Coast (Fig. 1).

The elevated water level can be caused by two processes, wind-induced surge and freshwater piling, with their relative contribution varying in time. On August 25 right before precipitation started to increase, the westward wind increased rapidly (Fig. 5b), with the resulting onshore Ekman transport starting to raise the water level inside the bay (Fig. 5a). On August 26, the northwestward wind increased rapidly, pushing water directly into the bay (see relatively strong landward current at offshore buoys in Fig. 6c,d) and further raising the water level inside the bay. The water level decreased a little from August 26 to 27 and then increased again until August 29 (Fig. 5a). This second increase in water level was maintained by high precipitation and the resulting freshwater input from major rivers and surface runoff. The narrow outlet of Bolivar Roads limited water exchange between the bay and coastal ocean, which amplified the impact of freshwater piling on the water level inside the bay. The relatively strong southward wind on August 29–30 (Fig. 5b) may have led to a higher water level at Bay Entrance than at Morgan's/Eagle Point, but the fact that the surface slope remained the same (Fig. 5a) indicates the dominance of freshwater piling even during the later precipitation period. With continuous freshwater input from the reservoirs (Fig. 4), the entire bay's water level had been somewhat elevated for at least another week, although the surface slope no longer existed after September 1 (Fig. 5a).

3.3. Landward current

Data at the four TABS buoy stations (see Fig. 2 for their locations) were examined for the water exchange between the bay and the coastal ocean. During the onshore Ekman transport-favoring westward wind condition on August 25, landward surface velocity was observed at the upper bay and bay mouth (Fig. 6a,b). The flow then turned to the seaward direction as the precipitation started to increase rapidly and the seaward flow intensified throughout the precipitation period. The large freshwater input from major rivers and surface runoff during the precipitation period resulted in a surface slope inside the bay (the water level at the bay entrance lower by 0.4–0.5 m relative to those in the middle and upper bay in Fig. 5a), which pushed water out of the bay. As the narrow outlet limited water exchange between the bay and coastal ocean, the impact of freshwater piling on water level was amplified and resulted in very strong seaward flow throughout the bay, with peaks greater than 3 m s^{-1} at the upper bay and 2 m s^{-1} at

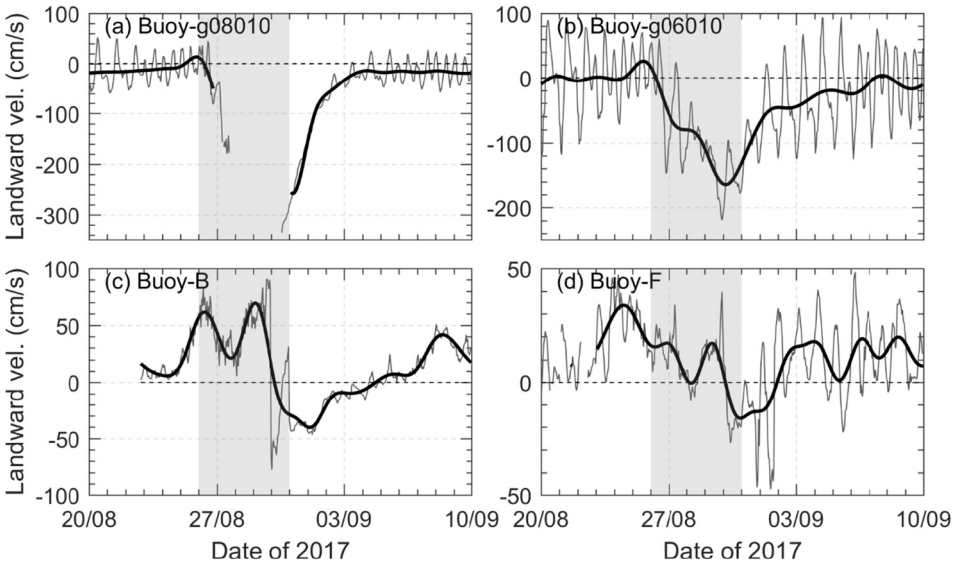

Fig. 6. Landward velocity measured at four TABS buoy stations, with the bold line indicating the sub-tidal component. Grey shading indicates the period of August 26–30, during which heavy precipitation occurred.

the mouth (Fig. 6a,b). The northward wind on August 26–28 (Fig. 5b) was not strong enough to counter the seaward barotropic current inside the bay. At offshore buoys, partly owing to strong northwestward wind, there was an evident landward surface current during most of the precipitation period until August 29 (Fig. 6c,d). The surface current flowed seaward over the following several days, in accordance with southeastward wind. After the precipitation period, it took 5–10 days for the surface current to recover to the pre-storm condition, with a shorter recovery time at the upper bay and at the offshore buoys and a longer recovery time at the bay mouth, probably due to large freshwater storage inside the bay and the narrow outlet.

3.4. Salinity and recovery time

Understanding the salinity change, particularly in terms of the time it takes to recover to pre-storm condition, is an essential component for the assessment of the hurricane impact on the ecosystem. Data from the four TWDB stations (see Fig. 2 for their locations) shows dramatic decreases in salinity throughout the bay during the precipitation period (Fig. 7). At all six stations inside the bay, salinity decreased to virtually zero, with salinity dropping to less than 2 psu for 4 days even near the bay mouth. With the high-speed wind and the resulting strong vertical mixing during the precipitation period, we consider it reasonable

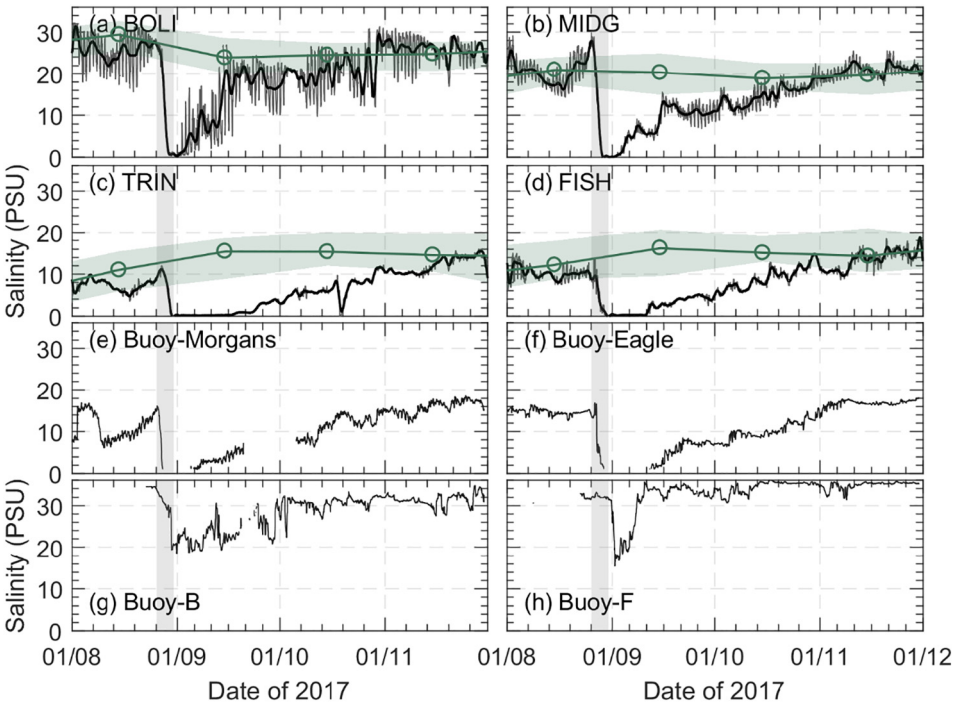

Fig. 7. Observed salinity at (a–d) four TWDB monitoring stations and (e–h) four TABS buoy stations, with grey shading indicating the period of August 26–30. In (a–d), the bold black lines indicate the sub-tidal component and the green lines with open circles are the monthly long-term median with the green shadings indicating the 25th and 75th percentiles. (For interpretation of the references to color in this figure legend, the reader is referred to the web version of this article.)

to assume that the mid-depth salinity at these stations was representative of the entire water column and that the entire bay became virtually fresh toward the end of the precipitation period. The observation of freshwater species of zooplankton near the bay mouth during the surveys soon after Harvey provides anecdotal evidence for the bay becoming fresh during this period of time (H. Liu, personal communication). At station TRIN, salinity remained zero for more than 20 days, which is in part due to its location near the Trinity River mouth and the slow tidal exchange in this region. It is interesting to note that there were distinctive increases in salinity, particularly at MIDG and TRIN, right before the precipitation period, probably due to the intrusion of coastal saline water during the period of low freshwater discharge.

Recovery time for salinity was quite different for different locations, ranging from a half month at the bay entrance to 2 months at the mid-bay and Trinity Bay stations. Salinity recovery time was associated with the strength of tidal exchange. There was little tidal signal in salinity at TRIN and FISH, particularly while under the influence of Harvey. Whereas, the tidal signal was strong at BOLI (near the mouth) and moderate at MIDG (mid-bay). This suggests a stronger tidal exchange near the mouth than in the Trinity Bay. It is worthy of note that the recovery times for other particulate or non-conservative riverine materials (e.g., nutrient, organic matter, contaminant) are typically different from the salinity recovery due to their settling and transformation processes. For instance, particulate matters tend to have a longer residence time in a partially estuary due to the trapping by estuarine circulation (Du and Shen, 2017).

Surface salinity at the buoy stations also shows a dramatic decrease outside of the bay (Fig. 7g,h). Salinity decreased from 32 psu to as low as 16 psu within a single day at buoy F (about 80 km offshore). The lowest salinity recorded at buoy F was even lower than that at buoy B (about 20 km offshore), indicating a large low-salinity river plume extending much further offshore than in the longshore direction. This also suggests that the low-salinity plume came out of the bay with a momentum of such a magnitude that the Coriolis effect could not readily deflect it to the southwest toward buoy B.

3.5. Freshwater load into Galveston Bay

From the salinity at the four TWDB stations (Fig. 7), it is clear that the entirety of Galveston Bay had been totally flushed out during Harvey, suggesting the freshwater load exceeded the water volume of the bay. By applying a freshwater fraction method, we show here that the total freshwater input was multiple times the volume of the bay. The estimated freshwater export rate peaked on August 29–30, with a maximum flow of over 20,000 $m^3\ s^{-1}$ (Fig. 8). The cumulative freshwater export through the bay mouth between August 26 and September 30 was estimated to be $8.88 \times 10^9\ m^3$, 94% of which occurred over the period between August 26 and September 7. Note that this estimation did not include the amount of freshwater exported from the other two outlets, San Luis Pass in the West Galveston Bay and Rollover Pass in the East Galveston Bay, since no salinity data was available for these two outlets. The exchange through Bolivar Roads, the main bay entrance, was estimated to account for 80% of the flow, with San Luis Pass accounting for the other 20% and minimal contribution from Rollover Pass (Galveston Bay National Estuary Program, 1994). Therefore, we estimated that the total freshwater load into Galveston Bay during Harvey and the following one month was $11.1 \times 10^9\ m^3$, which is equivalent to approximately 3 times of the Galveston Bay's entire volume ($3.81 \times 10^9\ m^3$).

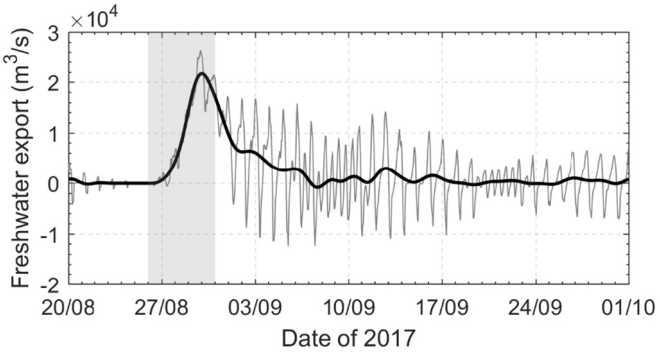

Fig. 8. Freshwater export rate estimated at the bay entrance using the freshwater fraction method, with the bold line indicating the subtidal component. Grey shading indicates the period of August 26–30, during which heavy Harvey precipitation occurred.

A budget for the freshwater load is summarized in Table 2. The freshwater input from Trinity River and Buffalo Bayou were directly based on the USGS measured streamflow. The input from San Jacinto River was based on the data at the USGS gauge station (08072000) and the hydrological model in Schoenbaechler et al. (2012). Precipitation on the bay surface was calculated as the product of total precipitation around Galveston Bay (0.95 m) and the bay area ($1.55 \times 10^9\ m^2$). It is interesting to note that the San Jacinto River contributed 73% of the total freshwater discharge from the three major rivers during this period. In comparison, the long-term data indicate that San Jacinto River ($65\ m^3\ s^{-1}$) contributes 19% of the total ($350\ m^3\ s^{-1}$). The "others" in Table 2 that include surface runoff and groundwater input was estimated from the residual of the water budget. The budget suggests that 34% of the freshwater input might have come in as surface runoff and groundwater discharge along the shoreline, the 2nd largest source next to San Jacinto River.

3.6. Sedimentary responses

Along with large input of freshwater, Harvey also delivered a massive sediment load to the bay. A MODIS satellite image captured on August 31, 2017 shows an extraordinary sediment plume extending up to 55 km offshore from the bay mouth and that the entire bay was highly turbid (https://visibleearth.nasa.gov/view.php?id=90866). Analyses of the core data reveal an extensive flood deposit extending across the entire bay, including the sub-bay systems of Clear Lake, Trinity Bay, East Galveston Bay and the San Jacinto Estuary. Based on an isopach map of storm flood layer thickness (Fig. 9), the total volume of the flood layer was found to be $1.24 \times 10^8\ m^3$, with an average flood layer thickness of 10.5 cm for the entire map area. The thickest deposits were found within the San Jacinto Estuary (not including the dredged channel) with thicknesses exceeding 50 cm in some places. Thicker deposits were also found adjacent to the mouth of Clear Lake with a maximum thickness of 22 cm, above the Texas City Dike with a maximum thickness of 37 cm, and within Trinity Bay with a thickness of 20 cm. Less sediment was deposited in East Galveston Bay where the flood layer was thinnest, with an average thickness of 9 cm. East Galveston Bay and its drainage basin did not receive as much rain and less of the exiting flood was advected into East Galveston Bay. The Texas City Dike extends 8 km out from Texas City into Galveston Bay (Fig. 9), blocking the transport of sediment from Galveston Bay to West Galveston Bay. The Texas City Dike trapped a significant portion of the Galveston Bay Hurricane Harvey deposit, preventing it from being transported to West Galveston Bay.

During non-flood conditions, the salt wedge of Galveston Bay typically resides within the middle of the San Jacinto Estuary, well above

Table 2
Budget of freshwater load during Hurricane Harvey and the following month (August 26–September 30, 2017).

Budget of freshwater load ($\times 10^9\ m^3$)	
Total freshwater load	11.1
Trinity River	1.00
Buffalo Bayou	0.60
San Jacinto River	4.30
Precipitation to the bay surface	1.47
Others[a] (surface runoff + groundwater)	3.73

[a] Residual from the budget.

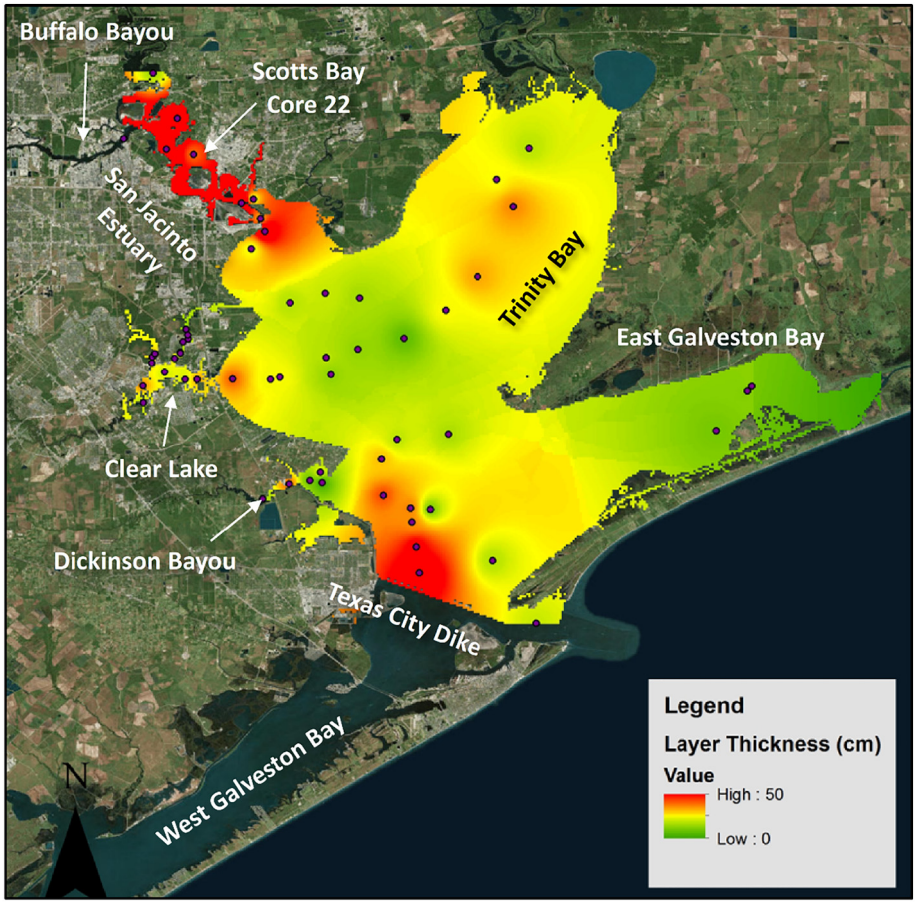

Fig. 9. An isopach map of the Hurricane Harvey flood layer. Note the thickest flood layer within the San Jacinto Estuary and above the Texas City Dike. It is also thicker at the mouth of Clear Lake and within Trinity Bay, but is thinner in East Galveston Bay.

Morgan's Point (Fig. 2), which is where the San Jacinto Estuary empties into the upper Galveston Bay. During Harvey, the salt wedge was pushed all the way through the bay into the Gulf of Mexico. The position of the salt wedge within an estuary is a primary control on the distribution of sediment. The salt wedge traps coarser bedload above the salt wedge (Wolanski et al., 1996; Carlin et al., 2015) and generally only suspended sediment is deposited seaward of the salt wedge, other than coarse sediment delivered by shoreline erosion (Dellapenna et al., 2003). Analyses of the Core 22 in Scott Bay (see Fig. 9 for its location) reveal that, prior to Harvey, the entire lower San Jacinto Estuary was mud dominated (Al Mukiami et al., 2018a,b). Within the San Jacinto Estuary and specifically at the Core 22 site, extensive Hg contamination has been observed (Al Mukiami et al., 2018a) and the Hg profiles within the cores provide excellent stratigraphic controls for correlation between cores (Fig. 10). There is a prominent Hg spike at 77 cm in the pre-Harvey core and at 51 cm in the post-Harvey core. The pre-Harvey core collected in 2013 and additional cores collected in 2016 at the Core 22 site all reveal comparable Hg profiles. While the pre-Harvey core contained no significant or discernable sand layers within the upper 1 m of the core (Al Mukiami et al., 2018b), aligning the Hg spikes in both cores shows that ~48 cm of mud was eroded and 22 cm of new sediment was deposited on top of the scoured surface during Harvey. Analyses of the X-radiograph reveal that, of the 22 cm of flood deposit, the lower 12 cm consists of shell gravel and sand and the upper 10 cm consists of mud. The coarse-basal portion of the flood layer represents bedload transport, which would have occurred when the salt wedge was pushed seaward of this site and the mud was likely deposited from the suspended load after the salt wedge re-intruded up the bay. These observations suggest that there were intense and prolonged currents, consistent with those shown in Fig. 6a, to have eroded 48 cm of bay bottom. The presence of 12 cm of bedload suggests that there was significant transport of bedload sediment from both San Jacinto River as well as Buffalo Bayou. San Jacinto River and Lake Houston flooded only for approximately one week, however, Buffalo Bayou contains the Barker and Addicks Reserviors and the controlled releases resulted in a 44-day flood (Fig. 4b). The post-Harvey core was collected on October 13, 2017, the day that Buffalo Bayou discharge returned to background levels and one month after the highest period of discharge, suggesting that much of the flood deposit was likely derived from Buffalo Bayou.

It should be noted that Buffalo Bayou flows through one of the largest petrochemical industrial complexes in the world and is known to contain heavily contaminated sediments (Al Mukiami et al., 2018a). The U.S. Army Corps of Engineers (C. Maglio, personal communication) reported up to 5 m of flood material deposited during Harvey within the Houston Ship channel inside the San Jacinto Estuary. Although our focus in this study was primarily outside of the dredged channel, we did collect box cores within the channel in December 2017. Despite the maximum depth of 60 cm of the box core, most of the box cores could not penetrate the entire Hurricane Harvey flood deposit, indicating that the flood layer was thicker than 60 cm in these locations.

The estimated volume of the entire flood layer of 1.24×10^8 m^3 is equivalent to a mass of 9.86×10^7 metric tons with the density of quartz (2.65 g cm^{-3}) for the sediment density and an average water content for the flood deposit (70%). Trinity River provides an average annual sediment load of 4.23×10^6 metric tons (Dellapenna et al., 2006) and accounts for 77% of a long-term mean total freshwater discharge (271 of 350 m^3 s^{-1}) into Galveston Bay. With the assumption of the remaining 23% of the freshwater discharge coming in with the same sediment concentration, we can estimate 5.49×10^6 metric tons for the average

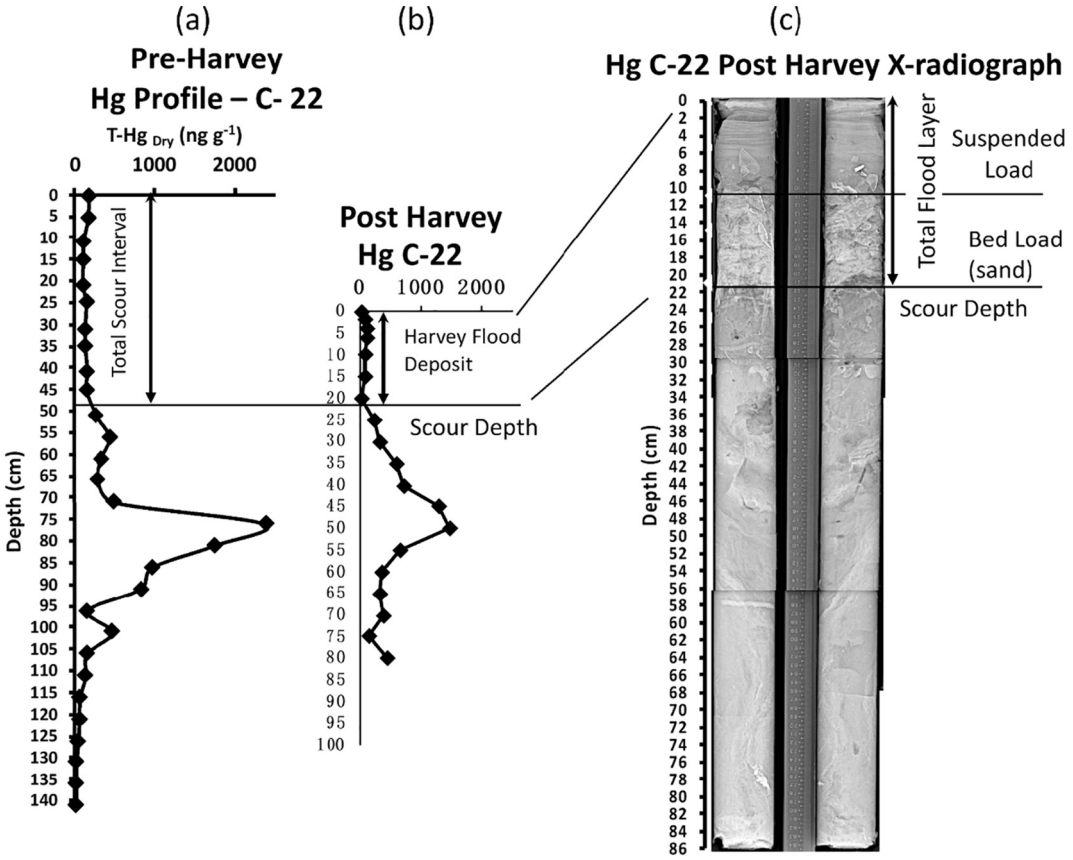

Fig. 10. (a) Pre-Harvey Hg sediment profile from Al Mukiami et al. (2018a), (b) post-Harvey Hg sediment profile, and (c) X-radiograph of post-Harvey vibracore at Core 22 site in Scott Bay.

annual sediment load into Galveston Bay. Comparison of this average annual sediment load to the sediment load during Harvey indicates that the amount of sediment delivered to the bay during Harvey is equivalent to 18 years of average annual sediment load to the bay.

3.7. Implications on water quality and ecosystem

A direct impact from the tremendous freshwater input was the low salinity condition that lasted as long as 2 months inside the bay. Estuarine systems are usually resilient to short-term variations of salinity but a long-lasting low salinity condition could have large impacts. A half-month to 2-month low salinity water, however, is not rare in Galveston Bay, particularly in the upper bay and Trinity Bay. During the summer of 2007, for example, salinity at TRIN remained almost zero for more than 100 days (https://waterdatafortexas.org/coastal/stations/TRIN). The long-lasting exposure to low-salinity water may be more impactful to the offshore ecosystem. Low salinity water of 15 psu was observed at the buoy F, which is close to the Flower Garden Banks, a known and valuable coral reef habitat in the northern Gulf of Mexico. A low salinity that lasted for longer than 5 days could cause fatal mortality on the coral reef and even eliminate some coral species intolerant to lower salinity as reported in Kaneohe Bay, Hawaii after major storm floods (Jokiel et al., 1993). The salinity at buoy F, however, was measured at the surface whereas coral reefs exist from 17 m deep and continue to 49 m deep in the Flower Garden Banks. Further studies are needed for the impact of Harvey on the subsurface salinity and thus on the offshore coral reefs.

The extremely large sediment load into the bay is likely to have a significant impact on the benthos. It is well established that elevated sedimentation rates impact both the abundance and diversity of benthic communities (Chou et al., 2004; Naser, 2011). Thrush et al. (2004) summarized, based on the previous field and laboratory studies, that a critical threshold of episodic deposition of 2 cm in an estuary will quickly create anaerobic conditions within the seabed, resulting in the death of the resident faunal community. The benthic and pelagic coupling within an estuary is central to the nutrient cycling and overall productivity of the system, and an interruption of this coupling resulting from elevated sedimentation rates can have dramatic impacts on the entire ecosystem (Eyre and Ferguson, 2006). While the average amount of sedimentation across Galveston Bay from Harvey was 10.5 cm, there was over 36 cm in some areas in the open bay and 20–50 cm of sedimentation in much of the San Jacinto Estuary. This suggests the potential for a devastating interruption of the benthic-pelagic coupling of the bay and a significant interruption to the nutrient cycling.

Although not addressed in this study, the most serious impact perhaps might have come from the industrial discharge into Galveston Bay as carried by surface runoff. The ambient areas next to Galveston Bay are highly industrialized, especially by the petrochemical industry. It has been estimated that 30–50% of the U.S. petrochemical production and oil refineries are situated around Galveston Bay (Santschi et al., 2001). During Harvey, about 149 million gallons of raw sewage and industrial discharges poured into neighboring communities and waterways. About 100 companies, including Valero Energy, ExxonMobil, and Arkema, reported chemical spills, some of which undoubtedly reached the bay (Horney et al., 2018). The industrial discharges will certainly degrade the health of the ecosystem and their impacts can be long-lasting (Mallin et al., 1999).

4. Conclusion

With a comprehensive dataset, this study examined the dramatic estuarine responses in hydrodynamic and sedimentary processes to Hurricane Harvey, one of the most devastating hurricanes, mainly due to extreme large precipitation. The extreme precipitation is the major

driving force accounting for the rare occurrences of several acute responses, including elevated water level lasting for more than 4 days, strengthened along-channel velocity exceeding 3 m s^{-1}, intense sediment scouring and subsequent deposition of large amount of sediment, and huge sediment plumes extending far offshore. Such estuarine responses are likely to occur in similar coastal systems, especially those characterized with shallow bathymetry and narrow outlets, which are common around the northern Gulf of Mexico (e.g., Sabine Lake, Mobile Bay, and Corpse Christi Bay). As the frequency of extreme precipitation events is projected to increase under a warming climate, it is essential to understand how coastal systems response and recover from these events.

Because of the uncertainty in estimating groundwater discharge and surface runoff along the shoreline, it is usually difficult to obtain an accurate freshwater load estimation during extreme precipitation events. We propose a freshwater fraction method by using high-frequency observational data for salinity and velocity at the estuary mouth. This approach can be modified to be applied for other riverine materials if high-frequency data are available. Its applicability, however, may be hampered by the non-conservative behavior (source-sink processes inside the estuary) of certain materials. With the transformation timescales of non-conservative materials (e.g., nutrients) typically longer than days, the materials can be regarded as conservative during the storm condition.

With this approach, we present in this study the first estimates of the freshwater and sediment loads into Galveston Bay during Harvey. The estimated freshwater load during Harvey and the following month was 11.1×10^9 m^3, about 3 times the water volume of Galveston Bay. This excessive freshwater is believed to have completely flushed out the original estuarine water, resulting in virtually fresh bay for more than a few days. Estuarine recovery time, in terms of salinity, was about 2 months averaged over the bay. Slow recovery at the upper estuary was primarily due to the weak tidal exchange and relatively large width. Harvey also delivered a 1.24×10^8 m^3 flood deposit into the bay, containing an estimated 9.86×10^7 metric tons, equivalent to 18 years of average annual sediment load to the bay.

Acknowledgments

We thank the anonymous reviewers for their helpful comments. We like to acknowledge the TWDB (Texas Water Development Board), TABS (Texas Automated Buoy System), and USGS (U.S. Geological Survey) for the sources of the continuous monitoring data. We thank Mason Bell and Lindsay Credites for sample collection and processing and Victoria Bartlett for GIS support and map preparation. All the monitoring data used in this study are publically accessible online. Numerical model results of the cross-sectional mean velocity at the bay mouth are made accessible at https://zenodo.org/deposit/1475307.

References

Al Mukiami, M.E., Kaiser, K., Williams, J.R., Dellapenna, T.M., Louchourn, P., Santschi, P.H., 2018a. Centennial record of anthropogenic impacts in Galveston Bay: evidence from trace metals (Hg, Pb, Ni, Zn) and lignin oxidation products. Environ. Pollut. 237, 887–899. https://doi.org/10.1016/j.envpol.2018.01.027.

Al Mukiami, M., Dellapenna, T.M., Williams, J.R., 2018b. Enhanced land subsidence in Galveston Bay, Texas: interactions between sediment accumulation rates and relative sea level rise. Estuar. Coast. Shelf Sci. 207, 183–193. https://doi.org/10.1016/j.ecss.2018.03.023.

Balaguru, K., Foltz, G.R., Leung, L.R., 2018. Increasing magnitude of hurricane rapid intensification in the central and eastern tropical Atlantic. Geophys. Res. Lett. 45, 4238–4247. https://doi.org/10.1029/2018GL077597.

Brown, M.M., Mulligan, R.P., Miller, R.L., 2014. Modeling the transport of freshwater and dissolved organic carbon in the Neuse River Estuary, NC, USA following Hurricane Irene (2011). Estuar. Coast. Shelf Sci. 139, 148–158. https://doi.org/10.1016/j.ecss.2014.01.005.

Burkholder, J., Eggleston, D., Glasgow, H., Brownie, C., Reed, R., Janowitz, G., Posey, M., Melia, G., Kinder, C., Corbett, R., Toms, D., Alphin, T., Deamer, N., Springer, J., 2004. Comparative impacts of two major hurricane seasons on the Neuse River and western Pamlico Sound ecosystems. Proc. Natl. Acad. Sci. U.S.A. 101 (25), 9291–9296. https://doi.org/10.1073/pnas.0306842101.

Cahoon, D.R., 2006. A review of major storm impacts on coastal wetland elevations. Estuar. Coasts 29 (6A), 889–898. https://doi.org/10.1007/BF02798648.

Cardoso, P.G., Raffaelli, D., Lillebø, A.I., Verdelhos, T., Pardal, M.A., 2008. The impact of extreme flooding events and anthropogenic stressors on the macrobenthic communities' dynamics. Estuar. Coast. Shelf Sci. 76 (3), 553–565. https://doi.org/10.1016/j.ecss.2007.07.026.

Carlin, J.A., Dellapenna, T.M., Strom, K., Noll IV, C.J., 2015. The influence of a salt wedge intrusion on fluvial suspended sediment and the implications for sediment transport to the adjacent coastal ocean: a study of the lower Brazos River, TX, USA. Mar. Geol. 359, 134–147. https://doi.org/10.1016/j.margeo.2014.11.001.

Chambers, J.Q., Fisher, J.I., Zeng, H., Chapman, E.L., Baker, D.B., Hurtt, G.C., 2007. Hurricane Katrina's carbon footprint on U.S. Gulf Coast forests. Science 318 (5853), 1107. https://doi.org/10.1126/science.1148913.

Cho, K.-H., Wang, H.V., Shen, J., Valle-Levinson, A., Teng, Y.-C., 2012. A modeling study on the response of Chesapeake Bay to hurricane events of Floyd and Isabel. Ocean Model 49–50, 22–46. https://doi.org/10.1016/j.ocemod.2012.02.005.

Chou, L.M., Yu, J.Y., Loh, T.L., 2004. Impacts of sedimentation on soft-bottom benthic communities in the southern islands of Singapore. Hydrobiologia 515 (1–3), 91–106. https://doi.org/10.1023/B:HYDR.0000027321.23230.2f.

Conner, W.H., Day Jr., J.W., Baumann, R.H., Randall, J.M., 1989. Influence of hurricanes on coastal ecosystems along the northern Gulf of Mexico. Wetl. Ecol. Manag. 1 (1), 45–56. https://doi.org/10.1007/BF00177889.

De Carlo, E.H., Hoover, D.J., Young, C.W., Hoover, R.S., Mackenzie, F.T., 2007. Impact of storm runoff from tropical watersheds on coastal water quality and productivity. Appl. Geochem. 22 (8), 1777–1797. https://doi.org/10.1016/j.apgeochem.2007.03.034.

Dellapenna, T.M., Kuehl, S.A., Schaffner, L.C., 2003. Ephemeral deposition, seabed mixing and fine-scale strata formation in the York River estuary, Chesapeake Bay. Estuar. Coast. Shelf Sci. 58, 621–643. https://doi.org/10.1016/S0272-7714(03)00174-4.

Dellapenna, T.M., Allison, M.A., Gill, G.A., Lehman, R.D., Warnken, K.W., 2006. The impact of shrimp trawling and associated sediment resuspension in mud dominated, shallow estuaries. Estuar. Coast. Shelf Sci. 69, 519–530. https://doi.org/10.1016/j.ecss.2006.04.024.

Donat, M.G., Lowry, A.L., Alexander, L.V., O'Gorman, P.A., Maher, N., 2016. More extreme precipitation in the world's dry and wet regions. Nat. Clim. Chang. 6, 508–513. https://doi.org/10.1038/NCLIMATE2941.

Du, J., Shen, J., 2016. Water residence time in Chesapeake Bay for 1980–2012. J. Mar. Syst. 164, 101–111. https://doi.org/10.1016/j.jmarsys.2016.08.011.

Du, J., Shen, J., 2017. Transport of riverine material from multiple rivers in the Chesapeake Bay: important control of estuarine circulation on the material distribution. J. Geophys. Res. Biogeosci. 122, 2998–3013. https://doi.org/10.1002/2016JG003707.

Du, J., Shen, J., Bilkovic, D.M., Hershner, C.H., Sisson, M., 2017. A numerical modeling approach to predict the effect of a storm surge barrier on hydrodynamics and long-term transport processes in a partially mixed estuary. Estuar. Coasts 40 (2), 387–403. https://doi.org/10.1007/s12237-016-0175-0.

Du, J., Park, K., Shen, J., Dzwonkowski, B., Yu, X., Yoon, B.I., 2018. Role of baroclinic processes on flushing characteristics in a highly stratified estuarine system, Mobile Bay, Alabama. J. Geophys. Res. Oceans 123. https://doi.org/10.1029/2018JC013855.

Dyer, K.R., 1973. Estuaries: A Physical Introduction. 1st edition. John Wiley and Sons, London, England.

Emanuel, K., 2017. Assessing the present and future probability of Hurricane Harvey's rainfall. Proc. Natl. Acad. Sci. U.S.A. 114 (48), 12681–12684. https://doi.org/10.1073/pnas.1716222114.

Eyre, B.D., Ferguson, A.J.P., 2006. Impact of a flood event on benthic and pelagic coupling in a sub-tropical east Australian estuary (Brunswick). Estuar. Coast. Shelf Sci. 66 (1–2), 111–122. https://doi.org/10.1016/j.ecss.2005.08.008.

Eyre, B., Twigg, C., 1997. Nutrient behaviour during post-flood recovery of the Richmond River estuary, northern NSW, Australia. Estuar. Coast. Shelf Sci. 44 (3), 311–326. https://doi.org/10.1006/ecss.1996.0124.

Fritz, A., Samenow, J., 2017. Harvey Unloaded 33 Trillion Gallons of Water in the U.S. The Washington Post, September 2, 2017. https://www.washingtonpost.com/news/capital-weather-gang/wp/2017/08/30/harvey-has-unloaded-24-5-trillion-gallons-of-water-on-texas-and-louisiana/?utm_term=.0c5e249acbb7.

Galveston Bay National Estuary Program, 1994. The State of the Bay: A Characterization of the Galveston Bay Ecosystem. Galveston Bay National Estuary Program Publication GBNEP-44 (232 pp.).

Greening, H., Doering, P., Corbett, C., 2006. Hurricane impacts on coastal ecosystems. Estuar. Coasts 29 (6A), 877–879. https://doi.org/10.1007/BF02798646.

Haby, M.G., Miget, R.J., Falconer, L.L., 2009. Hurricane Damage Sustained by the Oyster Industry and the Oyster Reefs Across the Galveston Bay System With Recovery Recommendations. TAMU-SG-09-201. The Texas A&M University System, College Station, TX (51 pp.).

Horney, J.A., Casillas, G.A., Baker, E., Stone, K.W., Kirsch, K.R., Camargo, K., Wade, T.L., McDonald, T.J., 2018. Comparing residential contamination in a Houston environmental justice neighborhood before and after Hurricane Harvey. PLoS One 13 (2), e0192660. https://doi.org/10.1371/journal.pone.0192660.

Huang, W., Spaulding, M., 2002. Modelling residence-time response to freshwater input in Apalachicola Bay, Florida, USA. Hydrol. Process. (15), 3051–3064 https://doi.org/10.1002/hyp.1088.

Jokiel, P.L., Hunter, C.L., Taguchi, S., Watarai, L., 1993. Ecological impact of a fresh-water "reef kill" in Kaneohe Bay, Oahu, Hawaii. Coral Reefs 12, 177–184. https://doi.org/10.1007/BF0033447.

Knight, D.B., Davis, R.E., 2009. Contribution of tropical cyclones to extreme rainfall events in the southeastern United States. J. Geophys. Res.-Atmos. 114, D23102. https://doi.org/10.1029/2009JD012511.

Knutson, T.R., McBride, J.L., Chan, J., Emanuel, K., Holland, G., Landsea, C., Held, I., Kossin, J.P., Srivastava, A.K., Sugi, M., 2010. Tropical cyclones and climate change. Nat. Geosci. 3 (3), 157–163. https://doi.org/10.1038/ngeo779.

Knutson, T.R., Sirutis, J.J., Zhao, M., Tuleya, R.E., Bender, M., Vecchi, G.A., Villarini, G., Chavas, D., 2015. Global projections of intense tropical cyclone activity for the late twenty-first century from dynamical downscaling of CMIP5/RCP4.5 scenarios. J. Clim. 28 (18), 7203–7224. https://doi.org/10.1175/JCLI-D-15-0129.1.

Li, M., Zhong, L., Boicourt, W.C., Zhang, S., Zhang, D.L., 2006. Hurricane-induced storm surges, currents and destratification in a semi-enclosed bay. Geophys. Res. Lett. 33 (2), L02604. https://doi.org/10.1029/2005GL024992.

Lucena, Z., Lee, M.T., 2017. Characterization of Streamflow, Suspended Sediment, and Nutrients Entering Galveston Bay From the Trinity River, Texas, May 2014–December 2015. U.S. Geological Survey Scientific Investigations Report 2016–5177. (38 pp.). https://doi.org/10.3133/sir20165177.

Mallin, M.A., Posey, M.H., Shank, G.C., McIver, M.R., Ensign, S.H., Alphin, T.D., 1999. Hurricane effects on water quality and benthos in the Cape Fear watershed: natural and anthropogenic impacts. Ecol. Appl. 9 (1), 350–362.

Michener, W.K., Blood, E.R., Bildstein, K.L., Brinson, M.M., Gardner, L.R., 1997. Climate change, hurricanes and tropical storms, and rising sea level in coastal wetlands. Ecol. Appl. 7 (3), 770–801.

Miller, W.D., Harding Jr., L.W., Adolf, J.E., 2006. Hurricane Isabel generated an unusual fall bloom in Chesapeake Bay. Geophys. Res. Lett. 33, L06612. https://doi.org/10.1029/2005GL025658.

Naser, H.A., 2011. Effects of reclamation on macrobenthic assemblages in the coastline of the Arabian Gulf: a microcosm experimental approach. Mar. Pollut. Bull. 62 (3), 520–524. https://doi.org/10.1016/j.marpolbul.2010.11.032.

van Oldenborgh, G.J., van der Wiel, K., Sebastian, A., Singh, R., Arrighi, J., Otto, F., Haustein, K., Li, S., Vecchi, G., Cullen, H., 2018. Corrigendum: Attribution of extreme rainfall from Hurricane, August 2017 (Environ. Res. Lett. 12 124009). Environ. Res. Lett. 13, 019501. https://doi.org/10.1088/1748-9326/aaa343.

Paerl, H.W., Bales, J.D., Ausley, L.W., Buzzelli, C.P., Crowder, L.B., Eby, L.A., Fear, J.M., Go, M., Peierls, B.L., Richardson, T.L., Ramus, J.S., 2001. Ecosystem impacts of three sequential hurricanes (Dennis, Floyd, and Irene) on the United States' largest lagoonal estuary, Pamlico Sound, NC. Proc. Natl. Acad. Sci. U.S.A. 98 (10), 5655–5660. https://doi.org/10.1073/pnas.101097398.

Paerl, H.W., Valdes, L.M., Joyner, A.R., Peierls, B.L., Piehler, M.F., Riggs, S.R., Christian, R.R., Eby, L.A., Crowder, L.B., Ramus, J.S., Clesceri, E.J., Buzzelli, C.P., Luettich, R.A., 2006. Ecological response to hurricane events in the Pamlico Sound system, North Carolina, and implications for assessment and management in a regime of increased frequency. Estuar. Coasts 29 (6), 1033–1045. https://doi.org/10.1007/BF02798666.

Park, K., Valentine, J.F., Sklenar, S., Weis, K.R., Dardeau, M.R., 2007. The effects of Hurricane Ivan in the inner part of Mobile Bay, Alabama. J. Coast. Res. 23 (5), 1332–1336. https://doi.org/10.2112/06-0686.1.

Park, K., Powers, S.P., Bosarge, G.S., Jung, H.-S., 2014. Plugging the leak: barrier island restoration following Hurricane Katrina enhances habitat quality for oysters in Mobile Bay, Alabama. Mar. Environ. Res. 94, 48–55. https://doi.org/10.1016/j.marenvres.2013.12.003.

Pfahl, S., O'Gorman, P.A., Fischer, E.M., 2017. Understanding the regional pattern of projected future changes in extreme precipitation. Nat. Clim. Chang. 7, 423–427. https://doi.org/10.1038/NCLIMATE3287.

Rayson, M.D., Gross, E.S., Hetland, R.D., Fringer, O.B., 2016. Time scales in Galveston Bay: an unsteady estuary. J. Geophys. Res. Oceans 121, 2268–2285. https://doi.org/10.1002/2015JC011181.

Risser, M.D., Wehner, M.F., 2017. Attributable human-induced changes in the likelihood and magnitude of the observed extreme precipitation during Hurricane Harvey. Geophys. Res. Lett. 44 (24), 12,457–12,464. https://doi.org/10.1002/2017GL075888.

Roman, M.R., Boicourt, W.C., Kimmel, D.G., Miller, W.D., Adolf, J.E., Bichy, J., Harding Jr., L.W., Houde, E.D., Jung, S., Zhang, X., 2005. Chesapeake Bay plankton and fish abundance enhanced by Hurricane Isabel. Eos 86 (28), 261–268. https://doi.org/10.1029/2005EO280001.

Rotunno, R., Chen, Y., Wang, W., Davis, C., Dudhia, J., Holland, G.J., 2009. Large-eddy simulation of an idealized tropical cyclone. Bull. Am. Meteorol. Soc. 90 (12), 1783–1788. https://doi.org/10.1175/2009BAMS2884.1.

Santschi, P.H., Presley, B.J., Wade, T.L., Garcia-Romero, B., Baskaran, M., 2001. Historical contamination of PAHs, PCBs, DDTs, and heavy metals in Mississippi River Delta, Galveston Bay and Tampa Bay sediment cores. Mar. Environ. Res. 52 (1), 51–79. https://doi.org/10.1016/S0141-1136(00)00260-9.

Sarkar, S., Singh, R.P., Chauhan, A., 2018. Anomalous changes in meteorological parameters along the track of 2017 Hurricane Harvey. Remote. Sens. Lett. 9 (5), 487–496. https://doi.org/10.1080/2150704X.2018.1441562.

Schoenbaechler, C., Guthrie, C.G., Lu, Q., 2012. Coastal Hydrology for the Trinity-San Jacinto Estuary. Hydrology Report. Texas Water Development Board, Austin, TX.

Sebastian, A., Proft, J., Dietrich, J.C., Du, W., Bedient, P.B., Dawson, C.N., 2014. Characterizing hurricane storm surge behavior in Galveston Bay using the SWAN+ADCIRC model. Coast. Eng. 88, 171–181. https://doi.org/10.1016/j.coastaleng.2014.03.002.

Sheldon, J.E., Alber, M., 2006. The calculation of estuarine turnover times using freshwater fraction and tidal prism models: a critical evaluation. Estuar. Coasts 29, 133–146. https://doi.org/10.1007/BF02784705.

Shen, J., Wang, H., Sisson, M., Gong, W., 2006. Storm tide simulation in the Chesapeake Bay using an unstructured grid model. Estuar. Coast. Shelf Sci. 68, 1–16. https://doi.org/10.1016/j.ecss.2005.12.018.

Shuster, W.D., Bonta, J., Thurston, H., Warnemuende, E., Smith, D.R., 2005. Impacts of impervious surface on watershed hydrology: a review. Urban Water J. 2 (4), 263–275. https://doi.org/10.1080/15730620500386529.

Solis, R.S., Powell, G.L., 1999. Hydrogaphy, mixing characteristics, and residence times of Gulf of Mexico estuaries. In: Bianchi, T.S., Pennock, J.R., Twilley, R.R. (Eds.), Biogeochemistry of Gulf of Mexico Estuaries. John Wiley, NY, pp. 29–61.

Stunz, G.W., Minello, T.J., Rozas, L.P., 2010. Relative value of oyster reef as habitat for estuarine nekton in Galveston Bay, Texas. Mar. Ecol. Prog. Ser. 406, 147–159. https://doi.org/10.3354/meps08556.

Tang, D., Warnken, K.W., Santschi, P.H., 2002. Distribution and partitioning of trace metals (Cd, Cu, Ni, Pb, Zn) in Galveston Bay waters. Mar. Chem. 78, 29–45. https://doi.org/10.1016/S0304-4203(02)00007-5.

Thrush, S.F., Hewitt, J.E., Cummings, V.J., Ellis, J.I., Hatton, C., Lohrer, A., Norkko, A., 2004. Muddy waters: elevating sediment input to coastal and estuarine habitats. Front. Ecol. Environ. 2 (6), 299–306.

Trenberth, K.E., Fasullo, J., Smith, L., 2005. Trends and variability in column-integrated atmospheric water vapor. Clim. Dyn. 24 (7–8), 741–758. https://doi.org/10.1007/s00382-005-0017-4.

Trenberth, K.E., Cheng, L., Jacobs, P., Zhang, Y., Fasullo, J., 2018. Hurricane Harvey links to ocean heat content and climate change adaptation. Earth's Future 6, 730–744. https://doi.org/10.1029/2018EF000825.

Valle-Levinson, A., Wong, K.-C., Bosley, K.T., 2002. Response of the lower Chesapeake Bay to forcing from Hurricane Floyd. Cont. Shelf Res. 22, 1715–1729. https://doi.org/10.1016/S0278-4343(02)00034-1.

Wang, S.-Y.S., Zhao, L., Yoon, J.-H., Klotzbach, P., Gillies, R.R., 2018. Quantitative attribution of climate effects on Hurricane Harvey's extreme rainfall in Texas. Environ. Res. Lett. 13, 054014. https://doi.org/10.1088/1748-9326/aabb85.

Warnken, K.W., Gill, G.A., Griffin, L.L., Santschi, P.H., 2001. Sediment-water exchange of Mn, Fe, Ni and Zn in Galveston Bay, Texas. Mar. Chem. 73, 215–231. https://doi.org/10.1016/S0304-4203(00)00108-0.

Wetz, M.S., Paerl, H.W., 2008. Estuarine phytoplankton responses to hurricanes and tropical storms with different characteristics (trajectory, rainfall, winds). Estuar. Coasts 31 (2), 419–429. https://doi.org/10.1007/s12237-008-9034-y.

Wolanski, E., Huan, N.N., Dao, L.T., Nhan, N.H., Thuy, N.N., 1996. Fine-sediment dynamics in the Mekong River estuary, Vietnam. Estuar. Coast. Shelf Sci. 43 (5), 565–582. https://doi.org/10.1006/ecss.1996.0088.

Ye, F., Zhang, Y.J., Wang, H.V., Friedrichs, M.A.M., Irby, I.D., Alteljevich, E., Valle-Levinson, A., Wang, Z., Huang, H., Shen, J., Du, J., 2018. A 3D unstructured-grid model for Chesapeake Bay: importance of bathymetry. Ocean Model 127, 16–39. https://doi.org/10.1016/j.ocemod.2018.05.00.

Zhang, Q., Blomquist, J.D., 2018. Watershed export of fine sediment, organic carbon, and chlorophyll-a to Chesapeake Bay: spatial and temporal patterns in 1984–2016. Sci. Total Environ. 619, 1066–1078. https://doi.org/10.1016/j.scitotenv.2017.10.279.

Science of the Total Environment 697 (2019) 134219

Contents lists available at ScienceDirect

Science of the Total Environment

journal homepage: www.elsevier.com/locate/scitotenv

Corrigendum

Corrigendum to "Dramatic hydrodynamic and sedimentary responses in Galveston Bay and adjacent inner shelf to hurricane Harvey" [Sci. Total Environ. 653 (2019), 554–564]

Jiabi Du [a,*], Kyeong Park [a], Timothy M. Dellapenna [a], Jacinta M. Clay [b]

[a] Department of Marine Sciences, Texas A&M University at Galveston, Galveston, TX 77554, United States
[b] Earth, Environmental and Planetary Sciences, Brown University, Providence, RI 02912, United States

The authors regret to make the following corrections for the estimation of freshwater export rate (Q_f) and total freshwater load into Galveston Bay due to Hurricane Harvey. In estimating the cross-sectional average normal velocity at the bay entrance (Section 2.3 in the published article), we mistakenly used the velocity measured at buoy g06010 (near the mouth of the bay) as the surface velocity while the velocity was actually measured at 6 m deep (i.e., mid-depth), which resulted in underestimation of F and thus Q_f. With the mid-depth observed velocity, following exactly the same methodology as in published article, we obtained a new relationship between current at buoy g06010 and cross-sectional average normal current (updated Fig. 3). The freshwater export rate during Hurricane Harvey and the following month was recalculated using this new relationship (updated Fig. 8). The maximum freshwater export rate now is 28,000 m^3/s (was 26,000 m^3/s in the published article); the total freshwater load is 14.0×10^9 m^3 (was 11.1×10^9 m^3 in the published article); the input along the coastline ("others") is increased to 6.63×10^9 m^3 from 3.73×10^9 m^3 (updated Table 2). These estimates provide very important information with respect to the influence of Hurricane Harvey and would be valuable for other researchers. Therefore, we believe it is necessary to make this corrigendum.

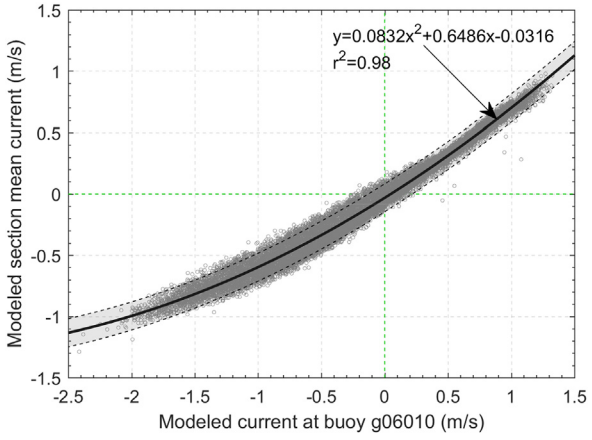

Updated Fig. 3. Relationship between current at the buoy g06010 station and cross-section average normal current, based on hourly numerical model results in 2007–2008, showing a quadratic polynomial regression (bold solid line) and its 95th confidence interval (dashed lines).

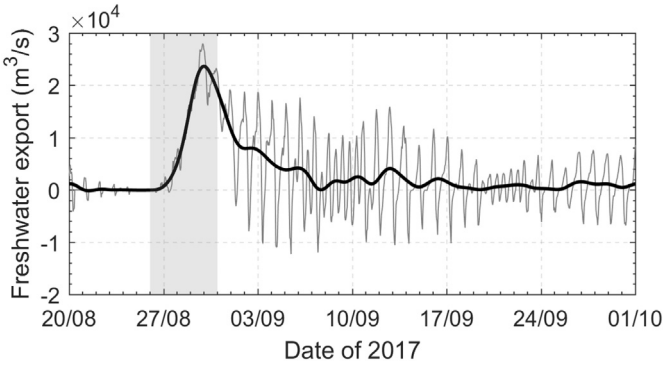

Updated Fig. 8. Freshwater export rate estimated at the bay entrance using the freshwater fraction method, with the bold line indicating the

DOI of original article: https://doi.org/10.1016/j.scitotenv.2018.10.403.
* Corresponding author.
E-mail address: jdu@tamug.edu (J. Du).

https://doi.org/10.1016/j.scitotenv.2019.134219

subtidal component. Grey shading indicates the period of August 26–30, during which heavy Harvey precipitation occurred.

Updated Table 2: Budget of freshwater load during Hurricane Harvey and the following month (August 26–September 30, 2017).

Budget of freshwater load ($\times 10^9$ m^3)	
Total freshwater load	14.0
Trinity River	1.00
Buffalo Bayou	0.60
San Jacinto River	4.30
Precipitation to the bay surface	1.47
Others[a] (surface runoff + groundwater)	6.63

a Residual from the budget.

Science of the Total Environment 704 (2020) 135364

Contents lists available at ScienceDirect

Science of the Total Environment

journal homepage: www.elsevier.com/locate/scitotenv

Massive pollutants released to Galveston Bay during Hurricane Harvey: Understanding their retention and pathway using Lagrangian numerical simulations

Jiabi Du [a,*], Kyeong Park [b], Xin Yu [c], Yinglong J. Zhang [c], Fei Ye [c]

[a] Department of Applied Ocean Physics & Engineering, Woods Hole Oceanographic Institution, MA 02543, USA
[b] Department of Marine Sciences, Texas A&M University at Galveston, TX 77554, USA
[c] Virginia Institute of Marine Science, College of William and Mary, Gloucester, VA 23062, USA

HIGHLIGHTS

- A large quantity of pollutants was released into Galveston Bay during Harvey.
- LET is introduced to quantify spatially varying susceptibility to released pollutant.
- Huge differences in pollutant susceptibility between during and after storm release.
- Pollutant discharge after the storm discharge can be more damaging than expected.
- Fate of released pollutant is subject to both estuarine and shelf circulations.

GRAPHICAL ABSTRACT

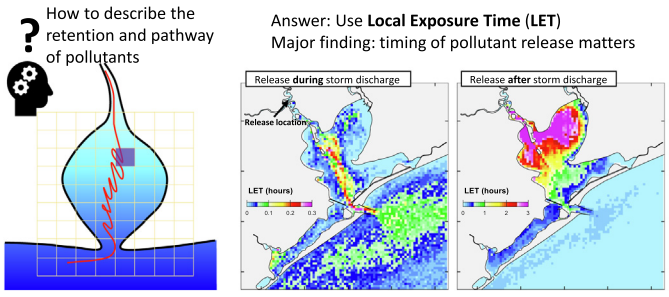

ARTICLE INFO

Article history:
Received 1 October 2019
Received in revised form 1 November 2019
Accepted 1 November 2019
Available online 21 November 2019

Editor: Dr. Damia Barcelo

Keywords:
Storm discharge
Retention
Local exposure time
Particle tracking
SCHISM

ABSTRACT

Increasing frequency of extreme precipitation events under the future warming climate makes the storm-related pollutant release more and more threatening to coastal ecosystems. Hurricane Harvey, a 1000-year extreme precipitation event, caused massive pollutant release from the Houston metropolitan area to the adjacent Galveston Bay. 0.57×10^6 tons of raw sewage and 22,000 barrels of oil, refined fuels and chemicals were reportly released during Harvey, which would likely deteriorate the water quality and damage the coastal ecosystem. Using a Lagrangian particle-tracking method coupled with a validated 3D hydrodynamic model, we examined the retention, pathway, and fate of the released pollutants. A new timescale, local exposure time (LET), is introduced to quantitatively evaluate the spatially varying susceptibility inside the bay and over the shelf, with a larger LET indicating the region is more susceptible to the released pollutants. We found LET inside the bay is at least one order of magnitude larger for post-storm release than storm release due to a quick recovery in the system's flushing. More than 90% of pollutants released during the storm exited the bay within two days, while those released after the storm could stay inside the bay for up to three months. This implies that post-storm release is potentially more damaging to water quality and ecosystem health. Our results suggest that not only the amount of total pollutant load but also the release timing should be considered when assessing a storm's environmental and ecological influence, because there could be large amounts of pollutants steadily and slowly discharged after storm through groundwater, sewage systems, and reservoirs.

* Corresponding author.
E-mail address: jdu@whoi.edu (J. Du).

https://doi.org/10.1016/j.scitotenv.2019.135364
0048-9697/

1. Introduction

Pollutant release frequently happens during storm events, especially those accompanied by strong precipitation. The increasing frequency of extreme precipitation events under a warming climate and a more humid atmosphere (Knight and Davis, 2009; Donat et al., 2016; Pfahl et al., 2017) makes the storm-related pollutant release even more threatening to coastal ecosystems in the future. Massive wastewater, nutrient, bacteria, heavy metal, or petrochemical products can be washed away by surface runoff or spilled due to flooding and discharged into receiving waters. Their influence on coastal environments can be catastrophic, particularly for coastal embayment where water exchange with the coastal ocean is slow and pollutants can stay for a long time. Damages to the water quality, marine environment, marine mammals, and fishery due to released pollutants have been extensively observed (Weyhenmeyer et al., 2004; Cardoso et al., 2008; Wetz and Yoskowitz, 2013). Recovery time from such extreme events for the receiving waters in terms of hydrodynamics or ecosystem health can take months or even years, depending on the amount of freshwater load, pollutant concentration, flushing capacity, and resiliency of the ecosystem (Paerl et al., 2001).

Environmental assessment for pollutant release usually focuses more on the total pollutant load while rarely taking into account the timing of release. Often, more pollutants are released during storm discharge, but the flushing is also stronger during the storm. Their influence on the coastal water quality is therefore not necessarily linearly proportional to the total loading (Taylor et al., 2011). As suggested by Dettmann (2001), more fraction of pollutants will be exported out of coastal systems when the flushing capacity is higher. Taking the massive pollutants released from the Houston metropolitan area in Texas to the adjacent Galveston Bay during Hurricane Harvey as an example, we show here that the release timing is critically important and the susceptibility of coastal waters to pollutant can be more serious than expected when pollutants are released after the storm discharge.

Hurricane Harvey, the wettest tropical cyclone on record in the U.S., made landfall on August 26, 2017 along the mid-Texas coast as a Category 4 hurricane and brought unprecedented rainfall to the Texas-Louisiana coast, with a return period of the peak 3-day precipitation exceeding 1000 years (van Oldenborgh et al., 2018). Intense rain with the daily precipitation averaged over the bay area larger than 50 mm lasted for 5 days (i.e., August 26–30). Maximum accumulative precipitation reached 1539 mm (60.58 in.) (Mathews, 2019), causing more than 80 deaths and over 150 billion dollars of economic loss. It was estimated that Harvey delivered 14×10^9 m^3 of freshwater (~3.7 times of the bay's volume) and deposited 9.9×10^7 metric tons of sediment (equivalent to 18 years of average annual sediment load) to Galveston Bay (Du et al., 2019a,b). The bay became virtually fresh for a few days, and salinity recovery inside the bay took about 2 months on average (Du and Park, 2019).

To make things worse, many petrochemical facilities were flooded, resulting in chemical pollutant leak or release (Fig. 1a). The flooding and the subsequent pollutant release are of great concern, since Houston is known as the second-largest petrochemical industry hubs in the world (Santschi et al., 2001) and the fourth largest city in the U.S. in terms of population size. Harvey was estimated to cause release of 0.57×10^6 tons of raw sewage (Phillips, 2018) and more than 22,000 barrels of oil, refined fuels and chemicals (Flitter and Valdmanis, 2017) to Galveston Bay. Harvey's aftermath lasted for a long time, e.g., drastic mortality and slow recovery of oysters (Christine Jensen, personal communication) and excessive skin problems for dolphins (Stuckey, 2017).

To date, some questions regarding the impacts of released pollutants during Harvey are still not answered. For example, how were the released pollutants dispersed inside and outside the bay? How long did they stay inside the bay and where did the pollutants aggregate? What are their pathway differences between the normal condition and during storm discharge? Understanding these questions is essential for environmental assessment, water quality management, and ecosystem restoration.

In this study, we used a Lagrangian particle-tracking method coupled with a validated 3D hydrodynamic model to examine the retention and pathway of pollutants released during Hurricane Harvey. Due to the random nature of particle movement and the large number of released particles, it is unpractical to analyze the pathway for each particle. To this end, we introduce a new transport timescale, called local exposure time, to describe the spatially varying susceptibility and to synthesize the mean characteristics of particle dispersion. Considering the increasing intensity and frequency of precipitation events, this study for Hurricane Harvey will be instructive for future research.

The paper is structured as follows: Section 2 briefly introduces the 3D numerical model, the coupled Lagrangian particle-tracking method, and two transport timescales used to quantify the particle retention and describe their pathway. Section 3 presents the results of Lagrangian simulations, with special focus on the difference between post-storm release and storm release. Section 4 discusses the importance of timing on the particles' retention and pathway, as well as the role of shelf and ocean circulations for the dispersion of particles after they exited the coastal system.

2. Methods

2.1. Hydrodynamic model

We employed the Semi-implicit Cross-scale Hydroscience Integrated System Model (SCHISM: Zhang et al., 2015, 2016), an open-source community-supported modeling system based on unstructured grids, derived from the early SELFE model (Zhang and Baptista, 2008). SCHISM uses a highly efficient semi-implicit finite-element/finite-volume method with a Eulerian-Lagrangian algorithm to solve the turbulence-averaged Navier-Stokes equations, under the hydrostatic approximation. It uses the generic length-scale model of Umlauf and Burchard (2003) with the stability function of Kantha and Clayson (1994) for turbulence closure. One of the major advantages of the model is that it has the capability of employing a very flexible vertical grid system, robustly and faithfully resolving the complex topography in estuarine and oceanic systems without any smoothing (Zhang et al., 2016; Stanev et al., 2017; Du et al., 2018a; Ye et al., 2018).

The model domain (Fig. 1c) covers the entire Texas, Louisiana, Mississippi, and Alabama coasts, including the shelf as well as major estuaries (e.g., Galveston Bay). The model grid has a resolution ranging from 40 m in the narrow ship channel of Galveston Bay to 2.5 km on average over the shelf and 10 km in the open ocean. Vertically, a hybrid *s-z* grid is used, with 10 sigma layers for depths less than 20 m and another 30 *z*-layers for depths from 20 to 4000 m with shaved cells near the bottom. The bathymetry used in the model is based on the coastal relief model (3 arc-second resolution: https://www.ngdc.noaa.gov/mgg/coastal/crm.html, last access: September 25, 2019). The local bathymetry in Galveston Bay is augmented with 10-m resolution DEM (digital elevation model) bathymetric data (https://catalog.data.gov/dataset/galveston-texas-coastal-digital-elevation-model, last access: September 25, 2019) to resolve the narrow ship channel (150 m wide, 10–15 m deep) that extends from the bay entrance all the way to Port of Houston. When forced by realistic boundary conditions, including the open boundary conditions from

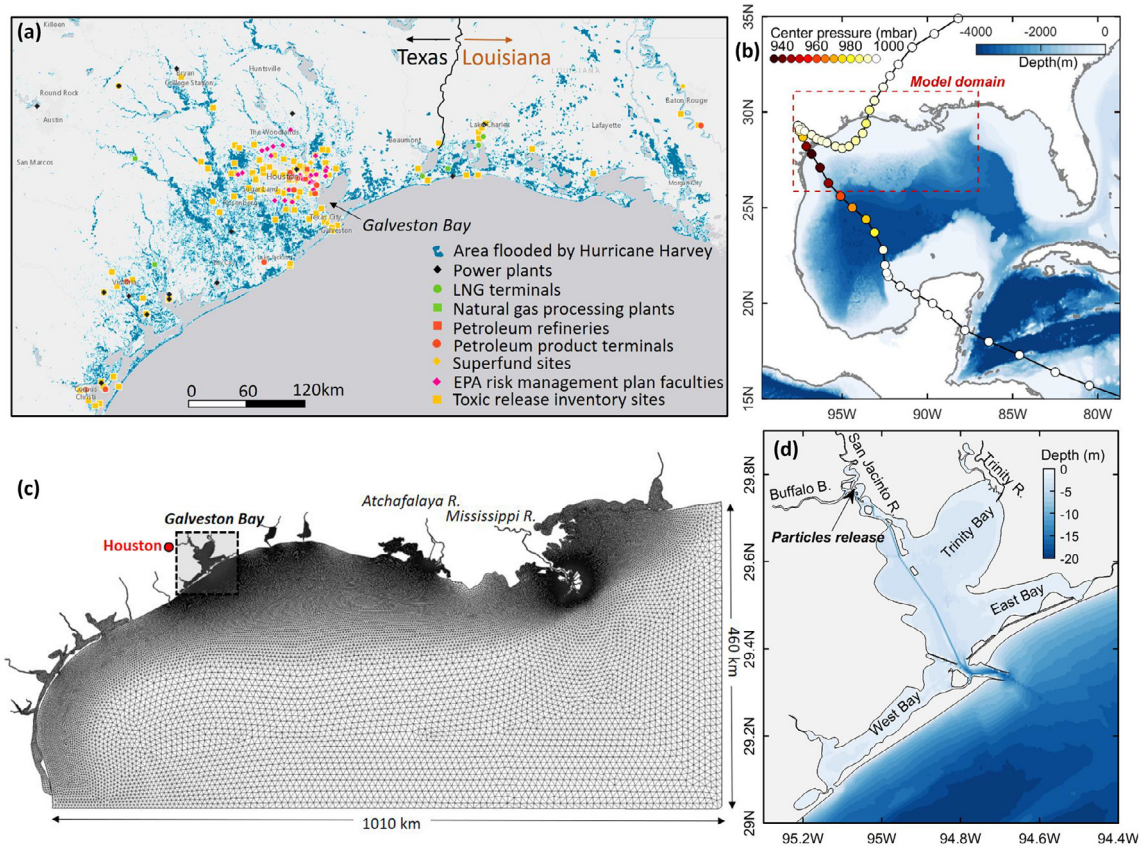

Fig. 1. (a) A map showing the energy and industrial facilities exposed to the flooding induced by Hurricane Harvey's heavy rainfall (modified from the figure in https://ucsusa.maps.arcgis.com/apps/MapJournal/index.html?appid=1e958eff5c3e45a983e52ad523c2ffdd, last access: September 25, 2019). (b) Track of Hurricane Harvey, with colored circles denoting the center pressure and blue background colors for the bathymetry in the Gulf of Mexico. Track of the hurricane is based on the data from the National Hurricane Center (https://www.nhc.noaa.gov/data/hurdat/hurdat2-1851-2017-050118.txt, last access: September 25, 2019). (c) Horizontal grid of the numerical model. (d) Bathymetry of Galveston Bay, with the black arrow indicating the location where particles are released in numerical simulations. (For interpretation of the references to color in this figure legend, the reader is referred to the web version of this article.)

FES2014 global tide (Carrere et al., 2015) and global HYCOM model output (https://www.hycom.org/data/glbu0pt08, last access: September 25, 2019), atmospheric forcing from the European Centre for Medium-Range Weather Forecasts (ECMWF: https://www.ecmwf.int, last access: September 25, 2019), and freshwater discharges for 15 rivers, the model gives a good reproduction of the observed hydrodynamic conditions in 2007–2008 inside the Galveston Bay and over the Texas-Louisiana shelf in terms of water level, salinity, temperature, stratification, and shelf currents (Du et al., 2019c).

The model has been applied to simulate the hydrodynamic conditions during Hurricane Harvey, and it reproduced well the dramatic estuarine responses, including the long-lasting elevated water level, extraordinarily strong along-channel velocity, sharp decreases and long recovery of salinity, and huge river plumes on the shelf (Du and Park, 2019). The validated hydrodynamic model provides reliable hydrodynamic fields, with which the following Lagrangian simulations are coupled.

2.2. Lagrangian particle tracking

A Lagrangian particle tracking method coupled with the 3D hydrodynamic model outputs was used to simulate the dispersion of pollutants. At the junction between San Jacinto River and Buffalo Bayou (Fig. 1d), 1378 particles (neutrally buoyant) were released every day at 00:00 from August 1st to October 1st, 2017. The release location was selected because the most serious pollutant release was from the petrochemical facilities along the Buffalo Bayou and San Jacinto River (Fig. 1a). A random walk was implemented in the particle tracking module to include the influence of the diffusion processes. The movements of particles are governed by advective and diffusive transport processes.

$$X^{n+1} = X^n + \left(U + \frac{\partial K_x}{\partial x}\right)\Delta t + R\sqrt{6K_x\Delta t} \quad (1)$$

$$Y^{n+1} = Y^n + \left(V + \frac{\partial K_y}{\partial y}\right)\Delta t + R\sqrt{6K_y\Delta t} \quad (2)$$

$$Z^{n+1} = Z^n + \left(W + \frac{\partial K_z}{\partial z}\right)\Delta t + R\sqrt{6K_z\Delta t} \quad (3)$$

where (X, Y, Z) is the location of the particle; U, V, and W are the water velocity components in the Cartesian coordinates of x, y, and z, respectively; n and $n+1$ indicate the current and next time steps, respectively; Δt is the time interval; R is a uniform random number between -1 and 1; and K_x, K_y, and K_z are turbulent diffusion coefficients in the x, y, and z directions, respectively.

2.3. Transport timescales

Two transport timescales were calculated to quantify the retention of the particles. One is the transit time, which measures the duration of a particle staying inside a defined domain and is calculated as the time difference between entering and exiting the

domain (Shen and Haas, 2004). The mean transit time (ϕ) averaged over the N particles is calculated as

$$\phi = \frac{1}{N}\sum_{i=1}^{N}(t_{2i} - t_{1i}) \quad (4)$$

where t_2 is the time when the particle exits the domain (i.e., Galveston Bay in this study) for the first time, and t_1 is the time when the particle enters the domain. The transit time here does not consider the returning of particles.

The local exposure time (LET) is the other timescale used. It is a new concept derived from the traditional exposure time that measures the overall lifetime a particle spends inside a given domain. The exposure time includes the duration after the particle returns into the domain (Delhez, 2006). LET is the mean exposure time of a set of particles within a defined region. Different from traditional exposure time that gives one scalar value, LET allows us to examine the spatial variability as we can separate the domain into many small regions. LET can be calculated as,

$$LET = \frac{1}{N}\sum_{i=1}^{N}\int \sigma_i dt \quad (5)$$

where σ_i = 1 when the particle i is inside the defined region and σ_i = 0 when the particle i is outside the defined region. The integration window with respect to t is from the particle release time to the end of model run. For this study, the hydrodynamic output from the numerical model covers the period of July 1 to December 31, 2017 (Du and Park, 2019). Another practical way to calculate the LET from numerical results is to register the time when a particle exits or enters the defined region, integrate the duration of all the visits, and average for all particles (Fig. 2). In this study, we divided the entire domain (including the bay and adjacent shelf) into 1 km × 1 km square regions and calculated the LET for each region.

Both particle's pathway and retention affect the degree to which released pollutants would influence local water quality and ecosystem health. Since it is impractical to examine the pathway of all released particles, LET provides a succinct and quantitative description of all particles. LET is the combined result of the flushing/exchange efficiency and the possibility of particles reaching the given region. It is, therefore, suitable to use LET as a measure of the susceptibleness of any given region to the released pollutant. A longer LET indicates the region is more susceptible to the pollutant. For a given region, a longer LET can be caused by several reasons including: (a) more particles passing through; (b) more visits by each particle (e.g., back-forth moving due to tide); (c) longer retention time for each visit (e.g., due to slow current).

3. Results

3.1. Particles released during storm

Particles released at the beginning of Harvey discharge (i.e., August 27, 2017) were quickly flushed out of the bay, with a median transit time of 1.5 days and 90% of the particles exiting the bay within 2 days (Fig. 3a-h). Particles moved seaward along the longitudinal axis of the bay without tidal (back-and-forth) movement (Fig. 4c). After exiting the bay, due to strong seaward momentum, particles moved offshore, reaching as far as 50 km off the bay entrance, consistent with remotely sensed sediment plume (Du and Park, 2019). The fast seaward movement was primarily caused by the strong ebbing along-channel current during Harvey. The velocity measured at the bay entrance and the upper bay showed the current (tidal + subtidal) was in seaward direction during the entire storm discharge period, with the maximum ebbing velocity exceeding 3 m s^{-1} in the upper bay (Du et al., 2019a).

As a result, the transit time was rather small during the storm discharge period, with a minimum value of 1 day. The transit time shows a linearly decreasing trend from August 1 to August 30 (Fig. 4a), because particles released before Harvey were subject to quick flushing during the storm discharge. Therefore, the transit time for particles released before Harvey is merely the time difference between the particle release time and the beginning of storm discharge. It suggests that an episodic flooding event can efficiently refresh the entire bay, thus playing an important role in the overall water renewal.

3.2. Particles released after storm

The movement, pathway, and transit time of particles released after the storm discharge were distinctly different from those released at the beginning of Harvey. Particles moved seaward slowly, with a median transit time of 60–90 days (Fig. 3i-p). Particles moved back and forth under the influence of tidal currents and were dispersed over the entire bay (Fig. 4e). It took a long time for particles to exit low-flushing regions such as Trinity Bay and East Bay. After exiting the bay, particles tended to move downcoast and mostly concentrated on the inner shelf (Figs. 2k-o and 3d). Surprisingly, the transit time quickly reverted to that under normal condition (~80 days) right after the storm discharge was termi-

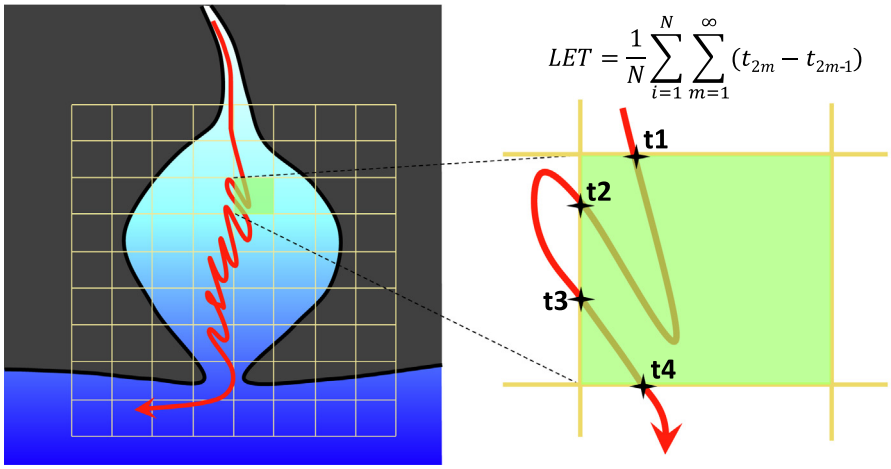

Fig. 2. Sketch diagram showing how to calculate LET in an estuary.

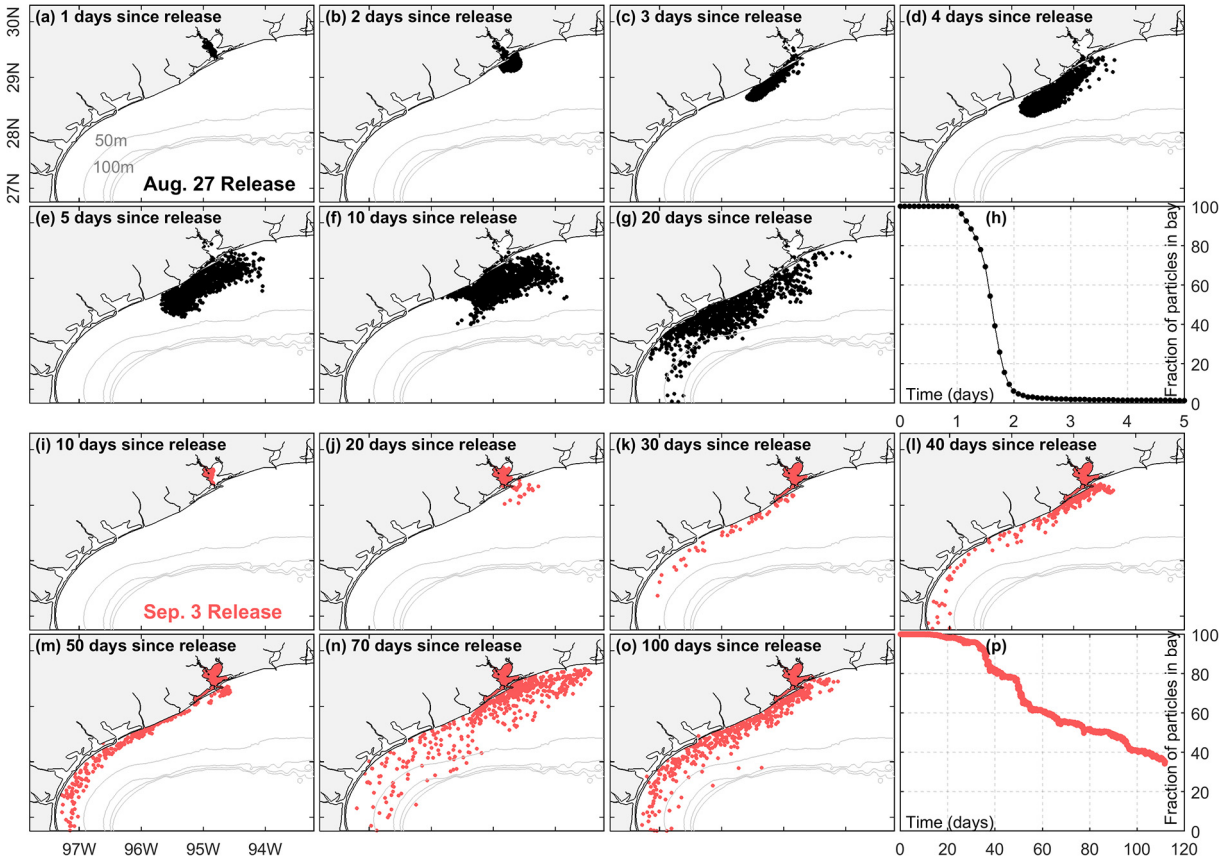

Fig. 3. For particles released on August 27, 2017 at the beginning of storm discharge: (a-g) particle distributions and (h) time series of remaining fraction inside the bay. (i-p) For particles released on September 3, 2017 (at the end of the storm discharge). Note the differences in the time frame between (a-g) for 1–20 days and (i-o) for 10–100 days.

nated. It suggests a quick recovery in flushing or water exchange after the storm, despite the fact that it took about two months for the salinity inside the bay to recover to the pre-storm condition (Du and Park, 2019).

3.3. LET to quantify the susceptibleness

For the particles released during storm (i.e., August 26–30), LET was small (Fig. 5a). With a maximum value of about 0.3 h, LET was less than 0.1 h for most regions, suggesting a fast movement and short retention of particles. LET was larger along the ship channel and decreased as moving away from the channel, indicating that most particles moved seaward along the ship channel. It is necessary to point out that stronger along-channel velocity made more particles move along the ship channel, resulting in more exposure time of particles and thus larger LETs near the ship channel.

For the particles released during September 3–7 (i.e., after the storm), LETs were at least one-order larger than those of storm release (Fig. 5b). LET reached a maximum value of about 6 h in the upper bay and had large values in Trinity Bay. It suggests that particles tended to move into Trinity Bay and stayed there for a long time, which was related to the small tidal range and slow water renewal in Trinity Bay. Salinity measurement and numerical modeling have confirmed the negligible tidal signal and slow recovery in salinity inside the Trinity Bay (Du et al., 2019a; Du and Park, 2019). LET became smaller toward downstream, primarily due to a strong tidal exchange between the lower bay and the shelf. Particles exiting the bay would have less chance to return due to shelf transport, very different from that in the middle-upper bay, where particles moved back and forth with tidal cycles.

4. Discussion

4.1. Importance of pollutant release timing

The model results draw our attention to an important but previously not well-recognized aspect concerning the pollutant susceptibility, that is, the release timing matters. Environmental assessments typically focused on the total pollutant loading (Brezonik and Stadelmann, 2002; Nazahiyah et al., 2007; Tiefenthaler et al., 2008) and paid little attention to the release timing. We demonstrate here that pollutants released after the storm will be more influential on the water quality and ecosystem health, as they will stay much longer inside the bay, than those released during storm (Fig. 5) although the amount of pollutants released after the storm is usually much smaller than that during storm. It should be noted that the loading after Harvey was still significant due to a large population and dense petrochemical industries around Galveston Bay. Furthermore, several reservoirs were controlled to release polluted water slowly. For example, Barker Reservoir, located west of Houston, released freshwater for over 40 days after the storm (Du et al., 2019a). We can imagine that pollutants in the reservoir waters were also released slowly and steadily, which, combined with those from the city and groundwater along the coastline, might deteriorate the bay's water quality well after the storm discharge.

The underlying mechanism responsible for the timing sensitivity lies in the overall ocean-estuary exchange or the flushing capacity. Slow flushing of the bay is the primary factor amplifying the timing issue. The storm discharge and the resulting seaward outflow continued for only 5–7 days and then the back-and-forth tidal current resumed. Pollutants released after the storm discharge is

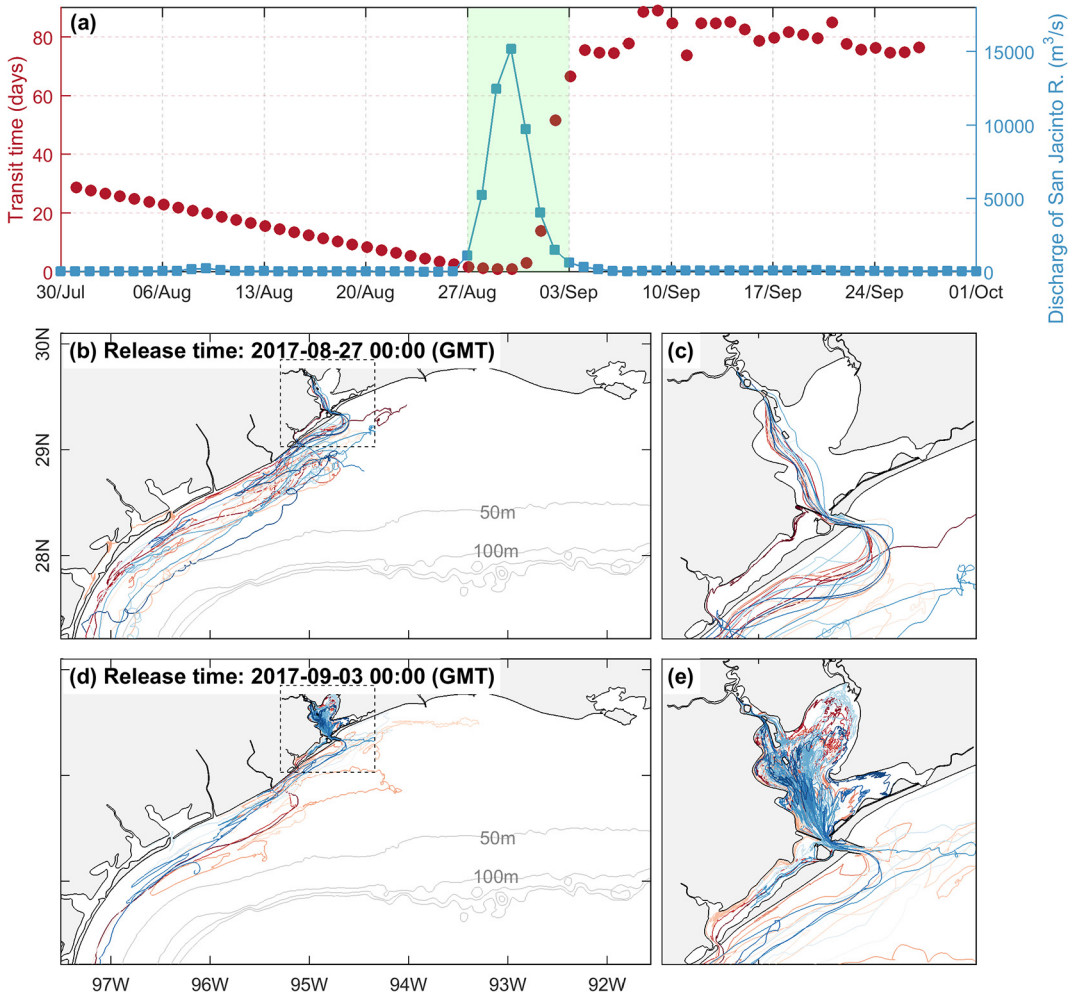

Fig. 4. (a) Time series of the median transit time and daily streamflow from San Jacinto River, with green shade highlighting the storm discharge period. (b) Tracks of 20 particles released at the beginning of storm discharge (August 27, 2017), with zoom-in shown in (c). The 20 particles are randomly selected as it is not feasible to show the pathways of all particles. (d-e) The same as (b-c) but for particles released at the end of storm discharge (September 3, 2017). (For interpretation of the references to color in this figure legend, the reader is referred to the web version of this article.)

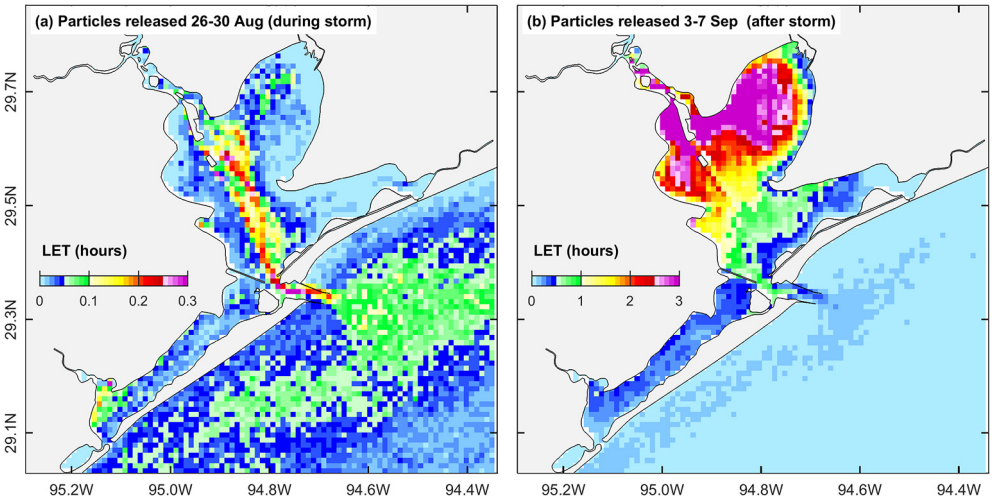

Fig. 5. Local exposure time (LET) for particles released during (a) August 26–30, 2017 and (b) September 3–7, 2017. For each square region (1 km × 1 km), the LET value is an average over all particles released during the respective 5-day period (6890 particles in total). Note the different color scales between (a) and (b). (For interpretation of the references to colour in this figure legend, the reader is referred to the web version of this article.)

subject to long retention inside the bay. If the flushing time of a system under normal condition is small, the timing sensitivity can be of less importance. For many estuarine systems in the Gulf of Mexico, however, flushing times are relatively long due to small tidal range and narrow outlets (Rayson et al., 2016; Du et al., 2018b). Relatively long flushing times are also expected for small coastal embayments with small tidal range and little freshwater discharge.

It is worthy to note estuarine systems with relatively wide mouth(s), strong tide, and large volume are unlikely to have such dramatic influence. For example, in Chesapeake Bay or San Francisco Bay, two of the largest estuaries in the U.S., the flushing time varies in a less dramatic manner, primarily due to the large volumes, and it is unlikely that the entire bay will be flushed out during a storm event (Walters et al., 1985; Du and Shen, 2016). As a result, the impact of the pollutants released before or after the storm discharge will be similar, and the amount of pollutants (loading) will become more important, although the release timing can affect some local regions, particularly near the release locations.

The fate and pathway of released pollutants in coastal bays are quite different from that in river systems where released pollutants are generally controlled by diffusion and one-way advection (Whitehead et al., 1986; Chapra and Whitehead, 2009). Complex geometric and bathymetric features in coastal bays, together with the barotropic and baroclinic interaction with shelf oceans, make the pathway and susceptibility of pollutants difficult to predict and quantify if without numerical tools and useful indexes. Using the timescale LET would significantly simplify the environmental assessment. One application of the LET is to examine the different fate and pathways of pollutants released at different locations. Numerical experiments show that LET varies greatly depending on the release location (Fig. 6). For instance, pollutants released at the Trinity River mouth tended to have more influence on East Bay (Fig. 6a), while pollutants released at Clear Lake (i.e., western shore) tended to have more impact on West Bay (Fig. 6b). It is necessary to note that LET is normalized by the number of particles released and thus indicates the average exposure for unit amount of pollutants. When assessing the susceptibility of a defined region, information about the amount of pollutants should be obtained first.

4.2. Importance of shelf and ocean circulation for pollutant dispersion

After exiting the bay, dispersion of the pollutants was directly regulated by the shelf circulation, ocean currents, and the

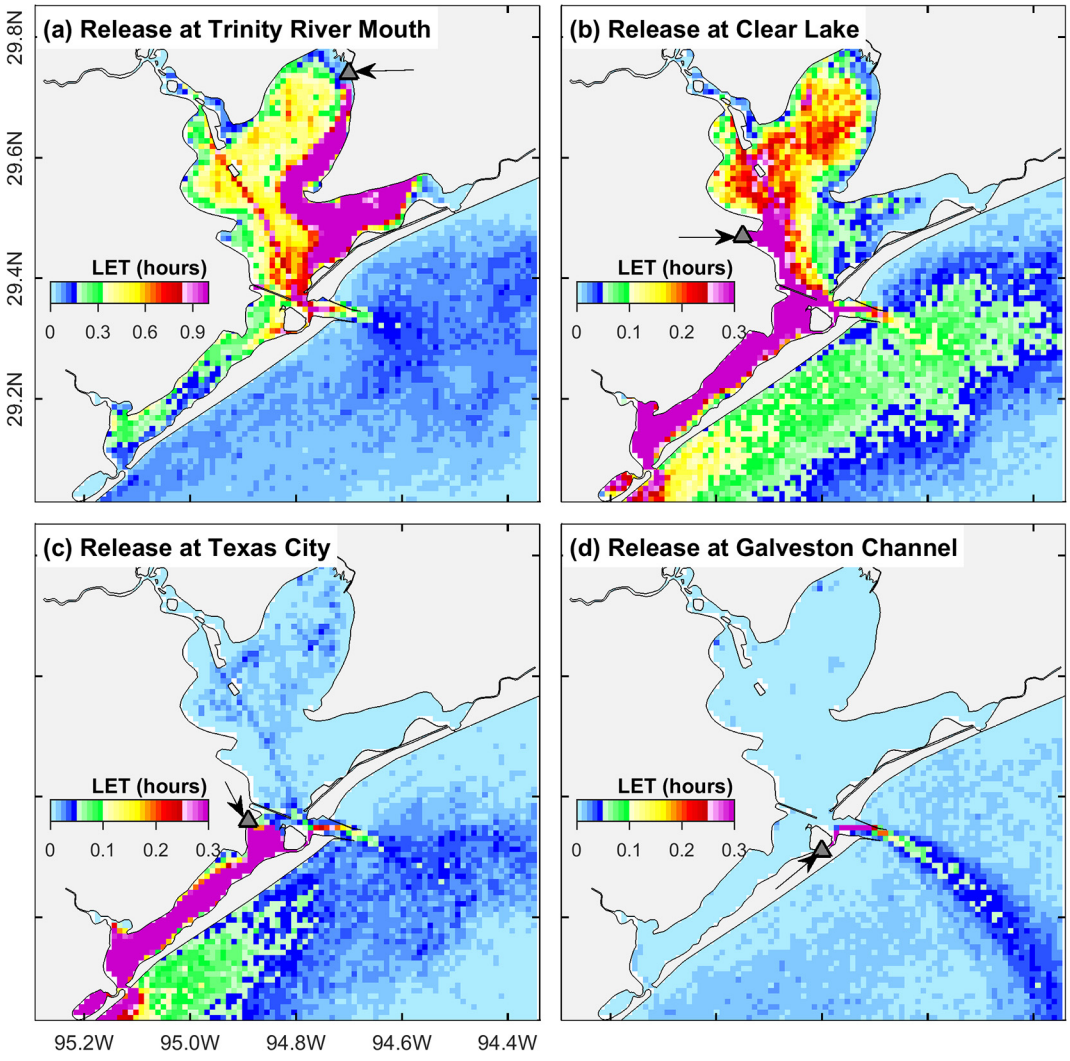

Fig. 6. LETs for particles released during August 26–30, 2017 at different locations (indicated with black triangles), including (a) Trinity River mouth, (b) Clear Lake, (c) Texas City, and (d) Galveston Channel. Note the different color scale between (a) and (b-d). (For interpretation of the references to colour in this figure legend, the reader is referred to the web version of this article.)

interaction between the shallow shelf and deep ocean. Meso-scale eddies in the ocean can be influential in altering the water exchange between ocean and shelf.

Physical oceanography in the Gulf of Mexico is characterized with intrusions of Loop Currents (Oey et al., 2005), mesoscale eddies derived from Loop Currents (Barkan et al., 2017), and one of the largest river systems in the world, Mississippi River (Rabalais et al., 2002). Despite the expectation that a strong hurricane like Harvey might affect the shelf and ocean circulation, analysis of the satellite-data based sea surface height (SSH) and geostrophic currents shows little change was induced by Harvey (Fig. 7). The SSH saw a marked increase in the coastal waters near Galveston Bay from August 24 to 31, 2017 (Fig. 7d), which was believed to be caused by the addition of large freshwater during Harvey. This analysis suggests, despite the great influence of Harvey on local coastal systems, its influence on the overall ocean circulation was negligible. However, it might be different for other hurricanes. From drifter data and numerical modeling, Curcic et al. (2016) showed Hurricane Issac in 2012 caused significant stokes drift and ocean waves. Oey et al. (2006) showed that a significant warming of Loop Current was induced by Hurricane Wilma in 2005.

After exiting the local estuarine system, pollutant dispersion in the coastal ocean will follow the usually disturbed coastal circulation and their fate may differ from that under normal conditions. It is necessary to point out that the shelf circulation on the Texas-Louisiana shelf has clear seasonality, with downcoast shelf current most of the time except during summer (Cochrane and Kelly, 1986; Cho et al., 1998). Particles released under normal conditions (taking 2007–2008 as an example) were mostly transported downcoast except during July and August (Fig. 8). One interesting pattern in the particle distribution is that the eddies along the shelf break play a role in augmenting the water exchange between the shelf and deep ocean. The mesoscale eddies (length scale ~ 100 km) may persist months in the Gulf of Mexico. For instance, the warm-core rings detach from the Loop Current episodically at an interval of 4–17 months, move slowly westward, and have lifetimes from months to a year (Sturges and Leben, 2000).

In summary, pollutant dispersion is subject to the influence of local bathymetric and geometric features and to the regulation of shelf-ocean circulations. One thing we did not include in this study is the settling or buoyancy property of pollutants. Certain types of pollutants tend to float at the sea surface due to smaller density and hydrophobic nature, while others tend to settle because of heavier density or attachment to suspended sediment. To include these kinetic processes of pollutants, one has to prove the numerical model is reasonably accurate in simulating not only the hydrodynamics but also sedimentary processes. Such efforts should be conducted in future research to facilitate the assessment of certain pollutants. As for the concern of this study, the analysis of passive particles is sufficient to support the major conclusions. Even though the retention time might be moderately or dramatically changed if settling or floating is considered, the pathway and distinct difference due to release timing will very likely maintain the same pattern.

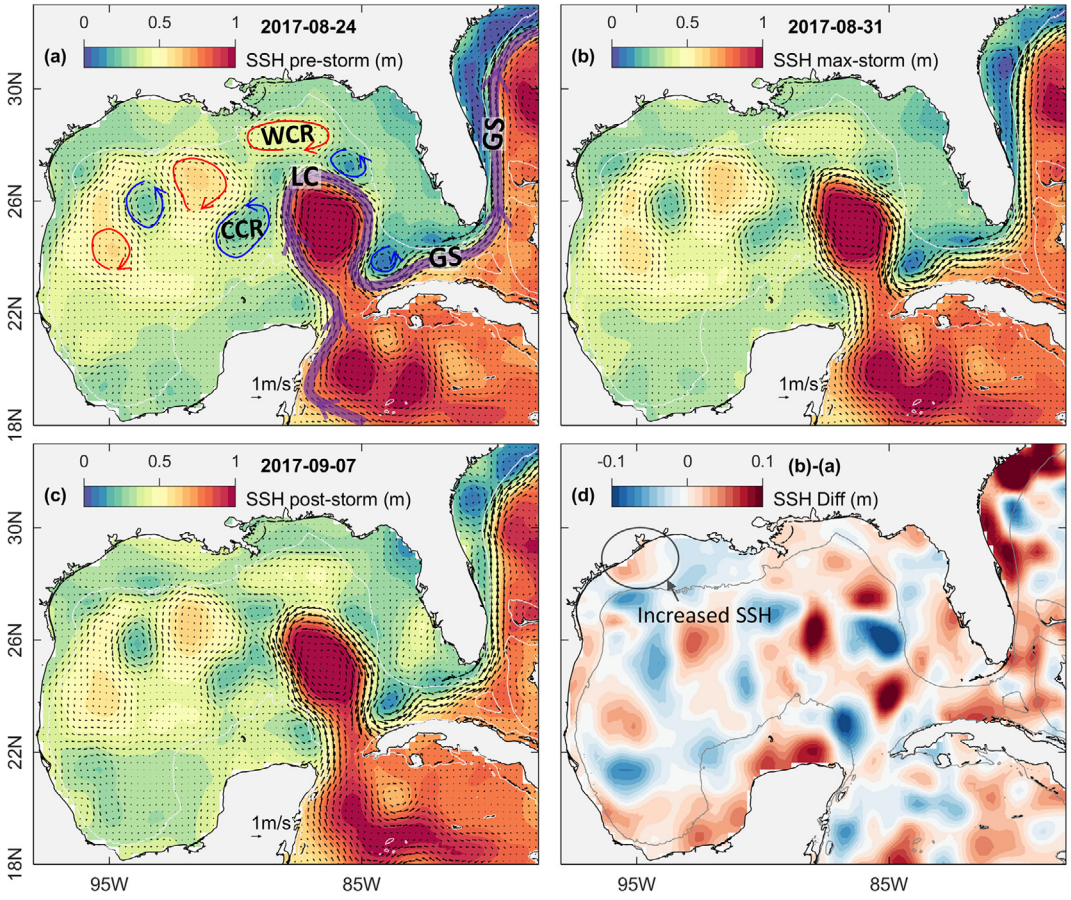

Fig. 7. Sea surface height (SSH) and geostrophic current based on satellite data (data source: ECMWF) on (a) August 24, (b) August 31, and (c) September 7, 2017. (d) The difference in SSH between August 31 (toward the end of storm discharge period) and August 24 (before the landfall of Harvey). Also marked in (a) are Gulf Stream (GS), Loop Current (LC), Warm Core Rings (WCR), and Cold Core Rings (CCR).

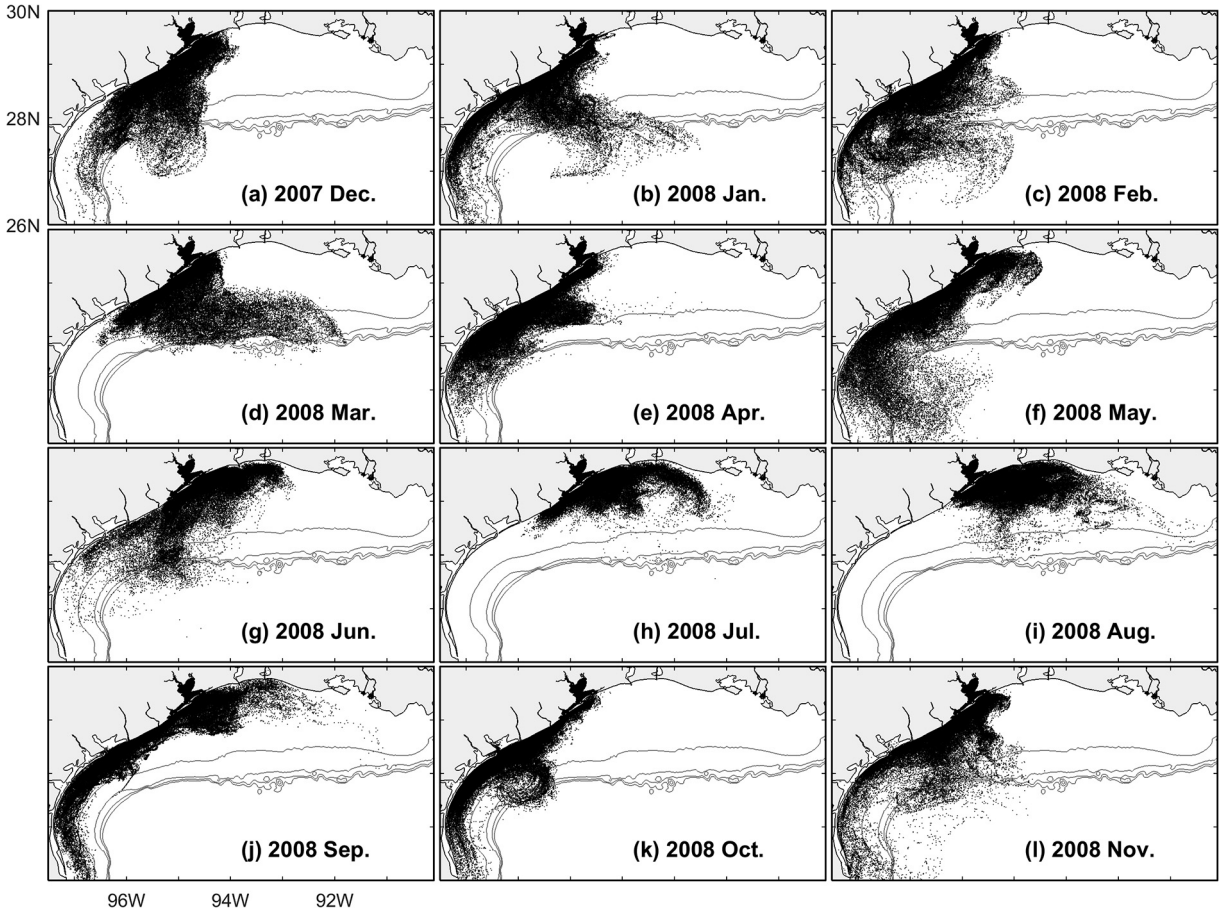

Fig. 8. Particle distributions for 345,360 particles released continuously during the previous 30 days, with 1439 particles released at each of surface and bottom four times a day (0, 6, 12, and 18 h).

5. Conclusions

Given the increasing frequency of extreme precipitation events as projected in several recent studies (e.g., Knight and Davis, 2009; Donat et al., 2016; Pfahl et al., 2017), intense pollutant releases are expected to occur more frequently in the future. This study uses a Lagrangian particle-tracking method to examine how massive pollutants released during Hurricane Harvey were dispersed inside the Galveston Bay and over the adjacent shelf. We found distinctively different retention and pathway between particles released during and after the storm discharge. Using LET, it is found that the susceptibility to the released pollutants was at least one-order greater for post-storm release than storm release. It suggests the timing of pollutant release can be more critical than the total amount of pollutants, particularly for slow flushing, small-volume estuarine systems. Our study suggests that the environmental agencies pay attention not only to the total pollutant load but also to the timing of pollutant release.

Declaration of Competing Interest

The authors declare that they have no known competing financial interests or personal relationships that could have appeared to influence the work reported in this paper.

Acknowledgments

We like to acknowledge the Texas Coastal Management Program, the Texas General Land Office and NOAA for partial funding of this project through CMP Contract #19-040-000-B074. This work was performed using computing facilities at the College of William and Mary, which were provided by contributions from the National Science Foundation, the Commonwealth of Virginia Equipment Trust Fund and the Office of Naval Research.

References

Barkan, R., McWilliams, J.C., Molemaker, M.J., Choi, J., Srinivasan, K., Shchepetkin, A. F., Bracco, A., 2017. Submesoscale dynamics in the northern Gulf of Mexico. Part II: Temperature-salinity relations and cross-shelf transport processes. J. Phys. Oceanogr. 47, 2347–2360. https://doi.org/10.1175/JPO-D-17-0040.1.

Brezonik, P.L., Stadelmann, T.H., 2002. Analysis and predictive models of stormwater runoff volumes, loads, and pollutant concentrations from watersheds in the Twin Cities metropolitan area, Minnesota, USA. Water Res. 36 (7), 1743–1757. https://doi.org/10.1016/S0043-1354(01)00375-X.

Cardoso, P.G., Raffaelli, D., Lillebø, A.I., Verdelhos, T., Pardal, M.A., 2008. The impact of extreme flooding events and anthropogenic stressors on the macrobenthic communities' dynamics. Estuarine Coastal Shelf Sci. 76 (3), 553–565. https://doi.org/10.1016/j.ecss.2007.07.026.

Carrere L., Lyard F., Cancet M., Guillot A., 2015. FES 2014, a new tidal model on the global ocean with enhanced accuracy in shallow seas and in the Arctic region, In: Abstracts of the EGU General Assembly 2015, Vienna, Austria, 12–17 April 2015. http://adsabs.harvard.edu/abs/2015EGUGA..17.5481C, last access: September 25, 2019.

Chapra, S., Whitehead, P.G., 2009. Modelling impacts of pollution in river systems: a new dispersion model and a case study of mine discharges in the Abrud, Aries and Mures River System in Transylvania, Romania. Hydrolog. Res. 40 (2–3), 306–322.

Cho, K., Reid, R.O., Nowlin, W.D., 1998. Objectively mapped stream function fields on the Texas-Louisiana shelf based on 32 months of moored current meter data. J. Geophys. Res. 103 (C5), 10377–10390. https://doi.org/10.1029/98JC00099.

Cochrane, J.D., Kelly, F.J., 1986. Low-frequency circulation on the Texas-Louisiana continental shelf. J. Geophys. Res. 91 (C9), 10645–10659. https://doi.org/10.1029/JC091iC09p10645.

Curcic, M., Chen, S.S., Özgökmen, T.M., 2016. Hurricane-induced ocean waves and stokes drift and their impacts on surface transport and dispersion in the Gulf of Mexico. Geophys. Res. Lett. 43 (6), 2773–2781. https://doi.org/10.1002/2015GL067619.

Delhez, E.J.M., 2006. Transient residence and exposure times. Ocean Sci. 2 (1), 1–9. https://doi.org/10.5194/os-2-1-2006.

Dettmann, E.H., 2001. Effect of water residence time on annual export and denitrification of nitrogen in estuaries: a model analysis. Estuaries 24, 481–490. https://doi.org/10.2307/1353250.

Donat, M.G., Lowry, A.L., Alexander, L.V., O'Gorman, P.A., Maher, N., 2016. More extreme precipitation in the world's dry and wet regions. Nat. Clim. Change 6 (5), 508–513. https://doi.org/10.1038/nclimate2941.

Du, J., Shen, J., 2016. Water residence time in Chesapeake Bay for 1980–2012. J. Mar. Sys. 164, 101–111. https://doi.org/10.1016/j.jmarsys.2016.08.011.

Du, J., Shen, J., Zhang, Y.J., Ye, F., Liu, Z., Wang, Z., Wang, Y.P., Yu, X., Sisson, M., Wang, H.V., 2018a. Tidal response to sea-level rise in different types of estuaries: the importance of length, bathymetry, and geometry. Geophys. Res. Lett. 45 (1), 227–235. https://doi.org/10.1002/2017GL075963.

Du, J., Park, K., Shen, J., Dzwonkowski, B., Yu, X., Yoon, B.I., 2018b. Role of baroclinic processes on flushing characteristics in a highly stratified estuarine system, Mobile Bay, Alabama. J. Geophys. Res. Oceans 123, 4518–4537. https://doi.org/10.1029/2018JC013855.

Du, J., Park, K., 2019. Estuarine salinity recovery from an extreme precipitation event: Hurricane Harvey in Galveston Bay. Sci. Total Environ. 670, 1049–1059. https://doi.org/10.1016/j.scitotenv.2019.03.265.

Du, J., Park, K., Dellapenna, T.M., Clay, J.M., 2019a. Dramatic hydrodynamic and sedimentary responses in Galveston Bay and adjacent inner shelf to Hurricane Harvey. Sci. Total Environ. 653, 554–564. https://doi.org/10.1016/j.scitotenv.2018.10.403.

Du J., Park K., Dellapenna T.M., Clay J.M., 2019. Corrigendum to "Dramatic hydrodynamic and sedimentary responses in Galveston Bay and adjacent inner shelf to Hurricane Harvey" [Sci. Total Environ. 653 (2019b), 554–564]. Sci. Total Environ. 697, 134219. https://doi.org/10.1016/j.scitotenv.2019.134219.

Du, J., Park, K., Shen, J., Zhang, Y.J., Yu, X., Ye, F., Wang, Z., Rabalais, N.N., 2019c. A hydrodynamic model for Galveston Bay and the shelf in the northern Gulf of Mexico. Ocean Sci. 15, 951–966. https://doi.org/10.5194/os-15-951-2019.

Flitter E., Valdmanis R., 2017. Oil and chemical spills from Hurricane Harvey big, but dwarfed by Katrina. https://www.reuters.com/article/us-storm-harvey-spills/oil-and-chemical-spills-from-hurricane-harvey-big-but-dwarfed-by-katrina-idUSKCN1BQ1E8, last access: September 26, 2019.

Kantha, L.H., Clayson, C.A., 1994. An improved mixed layer model for geophysical applications. J. Geophys. Res. 99 (C12), 25235–25266. https://doi.org/10.1029/94JC02257.

Knight, D.B., Davis, R.E., 2009. Contribution of tropical cyclones to extreme rainfall events in the southeastern United States. J. Geophys. Res. Atmos. 114 (23), D23102. https://doi.org/10.1029/2009JD012511.

Mathews B., 2019. By the numbers: Imelda was fifth wettest tropical storm to hit Lower 48. https://www.khou.com/article/weather/tropical-storm-imelda-by-the-numbers/285-edf4616d-5fcb-47fd-b7e2-fa071cc19747, last access: September 26, 2019.

Nazahiyah, R., Yusop, Z., Abustan, I., 2007. Stormwater quality and pollution loading from an urban residential catchment in Johor, Malaysia. Water Sci. Technol. 56 (7), 1–9. https://doi.org/10.2166/wst.2007.692.

Oey L.Y., Ezer T., Lee H.C., 2005. Loop Current, rings and related circulation in the Gulf of Mexico: A review of numerical models and future challenges. In: Circulation in the Gulf of Mexico: Observations and Models (Sturges, W., ed.), Geophysical Monograph Series 161, AGU, pp. 31–56. https://doi.org/10.1029/161GM04.

Oey, L.Y., Ezer, T., Wang, D.P., Fan, S.J., Yin, X.Q., 2006. Loop Current warming by hurricane Wilma. Geophys. Res. Lett. 33 (8), L08613. https://doi.org/10.1029/2006GL025873.

Paerl, H.W., Bales, J.D., Ausley, L.W., Buzzelli, C.P., Crowder, L.B., Eby, L.A., Fear, J.M., Go, M., Peierls, B.L., Richardson, T.L., Ramus, J.S., 2001. Ecosystem impacts of three sequential hurricanes (Dennis, Floyd, and Irene) on the United States' largest lagoonal estuary, Pamlico Sound, NC. Proc. Natl. Acad. Sci. U.S.A. 98 (10), 5655–5660. https://doi.org/10.1073/pnas.101097398.

Pfahl, S., O'Gorman, P.A., Fischer, E.M., 2017. Understanding the regional pattern of projected future changes in extreme precipitation. Nat. Clim. Change 7 (6), 423–427. https://doi.org/10.1038/nclimate3287.

Phillips A., 2018. Preparing for the next storm: Learning from the man-made environmental disasters that followed Hurricane Harvey. https://www.environmentalintegrity.org/wp-content/uploads/2018/08/Hurricane-Harvey-Report-Final.pdf, last access: September 26, 2019.

Rabalais N.N., Turner R.E., Wiseman Jr., W.J., 2002. Gulf of Mexico hypoxia, a.k.a. "The dead zone." Annu. Rev. Ecol. Syst. 33, 235–263. https://doi.org/10.1146/annurev.ecolsys.33.010802.150513.

Rayson, M.D., Gross, E.S., Hetland, R.D., Fringer, O.B., 2016. Time scales in Galveston Bay: an unsteady estuary. J. Geophys. Res. Oceans 121, 2268–2285. https://doi.org/10.1002/2015JC011181.

Santschi, P.H., Presley, B.J., Wade, T.L., Garcia-Romero, B., Baskaran, M., 2001. Historical contamination of PAHs, PCBs, DDTs, and heavy metals in Mississippi River Delta, Galveston Bay and Tampa Bay sediment cores. Mar. Environ. Res. 52 (1), 51–79. https://doi.org/10.1016/S0141-1136(00)00260-9.

Shen, J., Haas, L., 2004. Calculating age and residence time in the tidal York River using three-dimensional model experiments. Estuarine Coastal Shelf Sci. 61 (3), 449–461. https://doi.org/10.1016/j.ecss.2004.06.010.

Stanev, E.V., Grashorn, S., Zhang, Y.J., 2017. Cascading ocean basins: numerical simulations of the circulation and interbasin exchange in the Azov-Black-Marmara-Mediterranean Seas system. Ocean Dyn. 67 (8), 1003–1025. https://doi.org/10.1007/s10236-017-1071-2.

Stuckey A., 2017. Galveston Bay dolphins struggle to recover from Hurricane Harvey. https://www.houstonchronicle.com/news/houston-texas/houston/article/Galveston-Bay-dolphins-struggle-to-recover-from-12384929.php, last access: Sep 26, 2019.

Sturges, W., Leben, R., 2000. Frequency of ring separations from the Loop Current in the Gulf of Mexico: a revised estimate. J. Phys. Oceanogr. 30 (7), 1814–1819. https://doi.org/10.1175/1520-0485(2000) 030<1814:FORSFT>2.0.CO;2.

Taylor, D.I., Oviatt, C.A., Borkman, D.G., 2011. Non-linear responses of a coastal aquatic ecosystem to large decreases in nutrient and organic loadings. Estuaries Coasts 34 (4), 745–757. https://doi.org/10.1007/s12237-010-9312-3.

Tiefenthaler, L.L., Stein, E.D., Schiff, K.C., 2008. Watershed and land use-based sources of trace metals in urban storm water. Environ. Toxicol. Chem. 27 (2), 277–287. https://doi.org/10.1897/07-126R.1.

Umlauf, L., Burchard, H., 2003. A generic length-scale equation for geophysical turbulence models. J. Mar. Res. 61 (2), 235–265. https://doi.org/10.1357/002224003322005087.

van Oldenborgh G.J., van der Wiel K., Sebastian A., Singh R., Arrighi J., Otto F., Haustein K., Li S., Vecchi G., Cullen H., 2018. Corrigendum: Attribution of extreme rainfall from Hurricane Harvey, August 2017 (2017 Environ. Res. Lett. 12 124009). Environ. Res. Lett. 13(1), 019501. https://doi.org/10.1088/1748-9326/aaa343.

Walters, R.A., Cheng, R.T., Conomos, T.J., 1985. Time scales of circulation and mixing processes of San Francisco Bay waters. Hydrobiologia 129, 13–26. https://doi.org/10.1007/BF00048685.

Wetz, M.S., Yoskowitz, D.W., 2013. An 'extreme' future for estuaries? Effects of extreme climatic events on estuarine water quality and ecology. Mar. Pollut. Bull. 69 (1–2), 7–18. https://doi.org/10.1016/j.marpolbul.2013.01.020.

Weyhenmeyer, G.A., Willén, E., Sonesten, L., 2004. Effects of an extreme precipitation event on water chemistry and phytoplankton in the Swedish Lake Mälaren. Boreal Environ. Res. 9 (5), 409–420.

Whitehead, P.G., Williams, R.J., Hornberger, G.M., 1986. On the identification of pollutant or tracer sources using dispersion theory. J. Hydrol. 84 (3–4), 273–286.

Ye, F., Zhang, Y.J., Wang, H.V., Friedrichs, M.A.M., Irby, I.D., Alteljevich, E., Valle-Levinson, A., Wang, Z., Huang, H., Shen, J., Du, J., 2018. A 3D unstructured-grid model for Chesapeake Bay: importance of bathymetry. Ocean Model. 127, 16–39. https://doi.org/10.1016/j.ocemod.2018.05.002.

Zhang, Y.J., Ateljevich, E., Yu, H.C., Wu, C.H., Yu, J.C.S., 2015. A new vertical coordinate system for a 3D unstructured-grid model. Ocean Model. 85, 16–31. https://doi.org/10.1016/j.ocemod.2014.10.003.

Zhang, Y.J., Ye, F., Stanev, E.V., Grashorn, S., 2016. Seamless cross-scale modeling with SCHISM. Ocean Model. 102, 64–81. https://doi.org/10.1016/j.ocemod.2016.05.002.

Zhang, Y., Baptista, A.M., 2008. SELFE: A semi-implicit Eulerian-Lagrangian finite-element model for cross-scale ocean circulation. Ocean Model. 21 (3–4), 71–96. https://doi.org/10.1016/j.ocemod.2007.11.005.

Appendix C

Galveston Bay Sediment transport model

Kyeong Park[ab] and Jaibi Du[c]

[a]Department of Marine and Coastal Environmental Science, Texas A&M University at Galveston

[b]Department of Oceanography, Texas A&M University

[c]Department of Applied Ocean Physics and Engineering, Woods Hole Oceanographic Institute

Indroduction

This chapter is a reporting of the development of a sediment transport model for Galveston Bay based on the existing three-dimensional hydrodynamic model reported in Du et al. (2019). This report describes the hydrodynamic-sediment transport model and presents preliminary results of the sediment transport model simulation run for the year of 2007.

Hydrodynamic Model

We employed the Semi-implicit Cross-scale Hydroscience Integrated System Model (SCHISM: Zhang et al., 2015, 2016), an open-source community-supported modeling system, derived from the early SELFE model (Zhang and Baptista, 2008). SCHISM uses highly efficient semi-implicit finite-element/finite-volume method with a Eulerian-Lagrangian algorithm to solve the turbulence-averaged Navier-Stokes equations under the hydrostatic approximation. It uses the generic length-scale model of Umlauf and Burchard (2003) with the stability function of Kantha and Clayson (1994) for turbulence closure. One of the major advantages of the SCHISM is that it has the capability of employing a very flexible vertical grid system, robustly and faithfully resolving the complex topography in estuarine and oceanic systems without any smoothing (Stanev et al., 2017; Ye et al., 2018). A more detailed description of the SCHISM, including the governing equations, horizontal and vertical grids, numerical solution methods, and boundary conditions, can be found in Zhang et al. (2015, 2016).

The model domain covers the Texas, Louisiana, Mississippi, and Alabama coasts, including the shelf as well as major estuaries (e.g., Mobile Bay, Mississippi River, Atchafalaya River, Sabine Lake, Galveston Bay, Matagorda Bay, and Corpus Christi Bay) (Fig. 1). The domain also includes part of the deep ocean to set the open boundary far away from the shelf so as to avoid imposing boundary conditions at topographically complex locations. The horizontal grid contains 142,972 surface elements (triangular and quadrangular), with the resolution ranging from 10 km in the open ocean to 2.5 km on average on the shelf (shallower than 200 m) to 40 m at the Houston Ship Channel, a narrow but deep channel along the longitudinal axis of Galveston Bay. The fine grid for the ship channel is carefully aligned with the channel orientation in order to accurately

simulate the salt intrusion process. Vertically, a hybrid *s-z* grid is used, with 10 sigma layers for depths less than 20 m and another 30 *z* layers for depths from 20 to 4000 m (20, 25, 30, 35, 40, 50, 60, 70, 80, 90, 100, 125, 150, 200, 250, 300, 350, 400, 500, 600, 700, 800, 900, 1000, 1250, 1500, 2000, 2500, 3000, 4000 m); shaved cells are automatically added near the bottom in order to faithfully represent the bathymetry and thus the bottom-controlled processes. This hybrid *s-z* vertical grid enables the model to better capture the stratification in the upper surface layer while keeping the computational cost reasonable for simulations of the deep waters.

The bathymetry used in the model is based on the coastal relief model (3 arc-second resolution: https://www.ngdc.noaa.gov). The local bathymetry in Galveston Bay is augmented by 10-m resolution DEM bathymetric data to resolve the narrow ship channel (150 m wide, 10-15 m deep) that extends from the bay entrance all the way to Port of Houston. Bathymetry of the ship channels in other rivers, such as Mississippi, Atchafalaya, and Sabine rivers, is manually set following the NOAA navigational charts. The depth in the model domain ranges from 3400 m in the deep ocean to less than 1 m in Galveston Bay.

The model was validated for the two-year conditions in 2007-2008 and was forced by the observed river discharge, reanalysis atmospheric forcing, and open boundary conditions from global HYCOM output. Daily freshwater inputs from the USGS gauging stations were specified at 15 river boundaries (Fig. 1). For the Mississippi River, the largest in the study area, river discharge at Baton Rouge, LA (USGS 07374000) was used. For the Atchafalaya River, the second largest, the discharge data at the upper river station (USGS 07381490 at Simmesport, LA) was used, but the data before 2009 at this station are not available. However, we found a significant linear relationship between this station and the one near the river mouth (USGS 07381600 at Morgan City, LA) with a 2-day time lag (r^2 of 0.92), based on the data from 2009 to 2017. The freshwater discharge estimated at Simmesport using this relationship for 2007-2008 was used to specify the Atchafalaya River freshwater input into the Atchafalaya Bay. For the Trinity River, the major river input for Galveston Bay, river discharge at the lower reach station at Wallisville (USGS 08067252) was used, where the mean river discharge (averaged over April 2014 and April 2018) is about 56% of that at an upper reach station at Romayor (USGS 08066500). This is because the water from Romayor likely flows into wetlands and water bodies surrounding the main channel of the Trinity River before reaching Wallisville (Lucena and Lee, 2017). The river discharge data at the Wallisville station are not available before April 2014. Similar to the case for Atchafalaya River, there is a significant linear relationship between these two stations (r^2 of 0.89 with a 4-day time lag based on the data from 2014 to 2018). The freshwater discharge for 2007-2008 estimated using this relationship was used to specify the Trinity River freshwater input into Galveston Bay. River flows from other rivers were prescribed using the data at the closest USGS stations. Water temperatures at the river boundaries were also based on the data at these USGS stations.

Reanalyzed 0.25° resolution, 6-hourly atmospheric forcing, including air temperature, solar radiation, wind, humidity, and pressure at mean sea level, were extracted from the

European Centre for Medium-Range Weather Forecasts (ECMWF: https://www.ecmwf.int). SCHISM uses the bulk aerodynamic module of Zeng et al. (1998) to estimate heat flux at the air-sea interface. Both harmonic tide and subtidal water level were used to define the ocean boundary condition, with the harmonic tide (M2, S2, K2, N2, O1, Q1, K1, and P1) from the global tidal model FES2014 (Carrere et al., 2015) and the subtidal water level from the low-pass filtered (cut-off period of 15 days) daily global HYCOM output. The model was relaxed during inflow to the HYCOM output at the ocean boundary in terms of salinity, temperature, and velocity.

The hydrodynamic model reproduces well the observed water level, current velocity, salinity and temperature in Galveston Bay and adjacent shelf for both tidla and subtidal variations. Detailed model validation results canb e found in Du et al. (2019). The model also reproduces well the dramatic estuarine response during Hurricane Harvey, including the long-lasting elevated water level, extraordinarily strong along-channel velocity, sharp decreases and long recovery of salinity, and huge river plumes on the shelf (Du and Park, 2019). A sediment-transport coupled to this hydrodynamic model was used in this study for Galveston Bay.

Sediment-Transport Model

The three-diemnsional sediment model inside SCHISM adapted from Community Sediment Transport Model (Warner et al., 2008) was used in this study. We considered suspended load transport of cohesive sediments and only one particle size class representative of mud. The sediment model calculates the bottom shear stress, determines the erosion and deposition of seabed sediment, and simulates the movement of sediment particles. The mass-balance equation for suspended sediment concentration is identical to the salt-balance equation, except three addition terms for water column settling, and erosion and deposition at the water-bed interface. In the sediment-transport model used, the particle settling velocity is estimated using the formula in Soulsby (1997). For the bottom cell, the depositional flux is estimated by the product of the settling velocity and the sediment concentration at the bottom cell. The erosional flux is parameterized following Ariathurai and Arulanandan (1978) as function of bed erodibility, sediment porosity of the top bed layer, volumetric fraction of sediment, and critical shear stress for erosion. The detailed description of the algorithms for settling and depositional and erosional flux can be found in Pinto et al. (2012).

The sediment-transport model was initialized with a constant sediment concentration (0.05 g l^{-1}) over the entire domain. We conducted model runs that considered sediment loading from main rivers, that is, sediment released at the head of three rivers including Trinity River, San Jacinto River (Lake Houston), and Buffalo Bayou. With no information available for riverine sediment input, a constant sediment concentration (0.5 g l^{-1}) was imposed at the three river boundaries. Because of this rather arbitrary boundary condition for sediment concentration of incoming river water, the model results presented below should be viewed as relative concentrations.

The model was run for one year (2007) when the Trinity river inflow varied from <100 to over 1,500 $m^3 s^{-1}$, and the model results during a low-flow (day 50-70 with river inflow of ~100 $m^3 s^{-1}$) and a high-flow (day 190-210 with river inflow of ~1,500 $m^3 s^{-1}$) periods were examined (Fig. 2). Below are some preliminary results regarding the bottom shear stress and simulated sediment concentration distribution. Figure 3 shows the bottom shear stress averaged over the low-flow period. The bottom shear stress exceeds 0.1 N m^{-2}, a typical threshold to mobilize the bottom sediment and intiate erosion/resuspension only near the main bay entrance and San Luis Pass. Over the high-flow period, the average bottom shear stress exceeds 0.1 N m^{-2} where the Trinity River enters the bay as well as the main bay entrance and San Luis Pass (Fig. 4). Figure 5 shows the 95th percentile of the bottom shear stress during the first 210 days in 2007. It indicates that relatively large bottom shear stress can be attained in a relatively short time period, i.e., 5% of the time. The areas where bottom shear stress is high (red areas) are likely to see the bottom sediment resuspension and thus high suspended sediment cocnentrations. Figures 6 and 7 show the simulated surface and bottom sediment concentrations, respectively, during the low-flow period. Consistent with Fig. 5, both the surface and bottoms ediment concentrations are higher at the bay entrance and the San Luis Pass, and also in the area where the Trinity River enters the bay. The size of the plume outside of the bay is smaller at the bottom compared tot hata t the surface becausae of water column settling of sediments. Figures 8 and 9 show the simulated surface and bottom sediment concentrations, respectively, during the high-flow period. The sedimen plumes are alrger during the high-flow period compared to those during the low-flow periods owing to the larger sediment load during the high-flow period. The downcoast extension of the plume outside of the bay indicates the enhanvced shelf current during the high-flow period.

The sediment-transport model has been successfully configured for the Galveston Bay system. It is important to understand the model results provided in this report are preliminary. The mdoel needs to be further refined, for example, in terms of different particle size classes, sediment loads from main rivers, and investigation of the model sensitivity to different parameterization of settling, erosion and deposition.

References

Carrere, L., Lyard, F., Cancet, M., and Guillot, A. (2015). FES 2014, a new tidal model on the global ocean with enhanced accuracy in shallow seas and in the Arctic region. In: *Abstracts of the EGU General Assembly 2015*, Vienna, Austria, April 12-17, 2015, http://adsabs.harvard.edu/abs/2015EGUGA..17.5481C.

Du, J., Park, K., Shen, J., Zhang, Y.J., Yu, X., Ye, F., Wang, Z., and Rabalais, N.N. (2019). A hydrodynamic model for Galveston Bay and the shelf in the northern Gulf of Mexico. *Ocean Science*, 15, 951-966, doi:10.5194/os-15-951-2019.

Du, J., and Park, K. (2019). Estuarine salinity recovery from an extreme precipitation event: Hurricane Harvey in Galveston Bay. *Science of the Total Environment*, 670, 1049-1059, doi:10.1016/j.scitotenv.2019.03.265.

Kantha, L.H., and Clayson, C.A. (1994). An improved mixed layer model for geophysical applications. *Journal of Geophysical Research*, 99(C12), 25235-25266, doi:10.1029/94JC02257.

Lucena, Z., and Lee, M.T. (2017). Characterization of Streamflow, Suspended Sediment, and Nutrients Entering Galveston Bay from the Trinity River, Texas, May 2014-December 2015. U.S. Geological Survey Scientific Investigations Report 2016-5177, 38 p., https://doi.org/10.3133/sir20165177.

Pinto, L., Fortunato, A.B., Zhang, Y., Oliveira, A., and Sancho, F.E.P. (2012). Development and validation of a three-dimensional morphodynamic modelling system. *Ocean Modelling*, 57-58, 1-14, doi:10.1016/j.ocemod.2012.08.005.

Stanev, E.V., Grashorn, S., and Zhang, Y.J. (2017). Cascading ocean basins: Numerical simulations of the circulation and interbasin exchange in the Azov-Black-Marmara-Mediterranean Seas system. *Ocean Dynamics*, 67(8), 1003-1025, doi:10.1007/s10236-017-1071-2.

Umlauf, L., and Burchard, H. (2003). A generic length-scale equation for geophysical turbulence models. *Journal of Marine Research*, 61(2), 235-265, doi:10.1357/002224003322005087.

Warner, J.C., Sherwood, C.R., Signell, R.P., Harris, C.K., and Arango, H.G. (2008). Development of a three-dimensional, regional, coupled wave, current, and sediment-transport model. *Computers and Geosciences*, 34(10), 1284-1306, doi:10.1016/j.cageo.2008.02.012.

Ye, F., Zhang, Y.J., Wang, H.V., Friedrichs, M.A.M., Irby, I.D., Alteljevich, E., Valle-Levinson, A., Wang, Z., Huang, H., Shen, J., and Du, J. (2018). A 3D unstructured-grid model for Chesapeake Bay: Importance of bathymetry. *Ocean Modelling*, 127, 16-39, doi:10.1016/j.ocemod.2018.05.002.

Zhang, Y., and Baptista, A.M. (2008). SELFE: A semi-implicit Eulerian-Lagrangian finite-element model for cross-scale ocean circulation. *Ocean Modelling*, 21(3-4), 71-96, doi:10.1016/j.ocemod.2007.11.005.

Zhang, Y.J., Ateljevich, E., Yu, H.C., Wu, C.H., and Yu, J.C.S. (2015). A new vertical coordinate system for a 3D unstructured-grid model. *Ocean Modelling*, 85, 16-31, doi:10.1016/j.ocemod.2014.10.003.

Zhang, Y.J., Ye, F., Stanev, E.V, and Grashorn, S. (2016). Seamless cross-scale modeling with SCHISM. *Ocean Modelling*, 102, 64-81, doi:10.1016/j.ocemod.2016.05.002.

Zeng, X., Zhao, M., and Dickinson, R.E. (1`998). Intercomparison of bulk aerodynamic algorithms for the computation of sea surface fluxes using TOGA COARE and TAO

data. *Journal of Climate*, 11, 2628-2644, doi:10.1175/1520-0442(1998)011<2628:IOBAAF>2.0.CO;2.

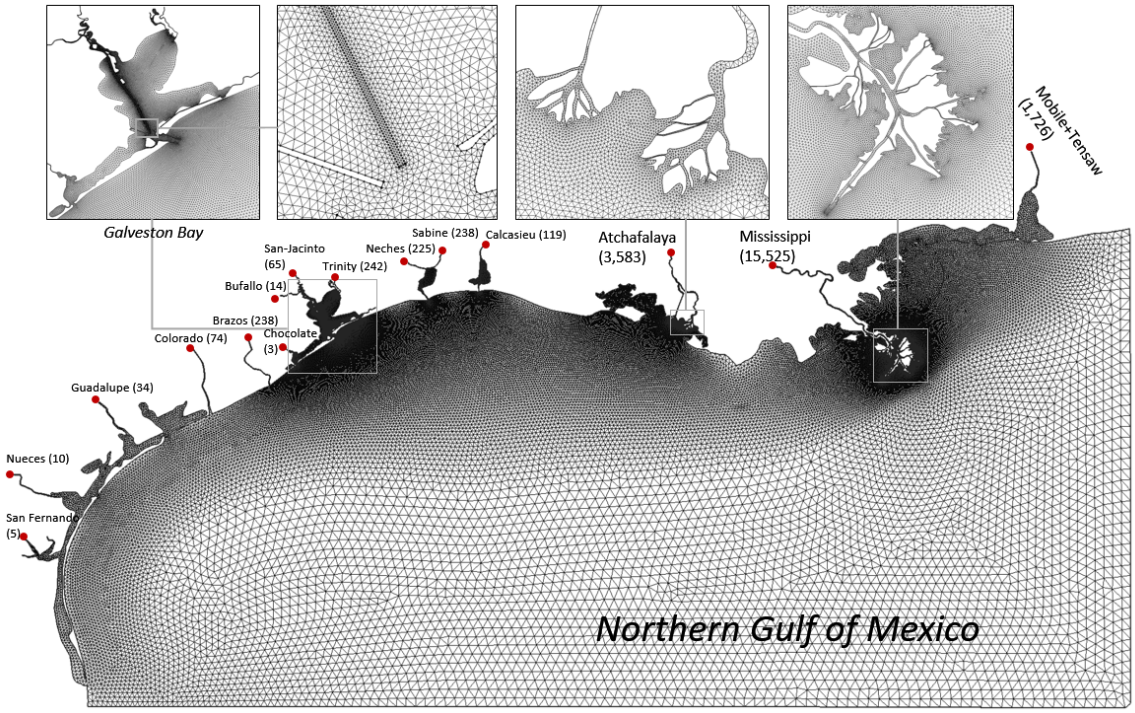

Figure 1: The model domain and the horizontal grid, with the upper panels showing zoom-ins of selected coastal systems. Locations of major river inputs are indicated with red dots, with the associated mean river discharges (m^3 s^{-1}) shown in the parentheses.

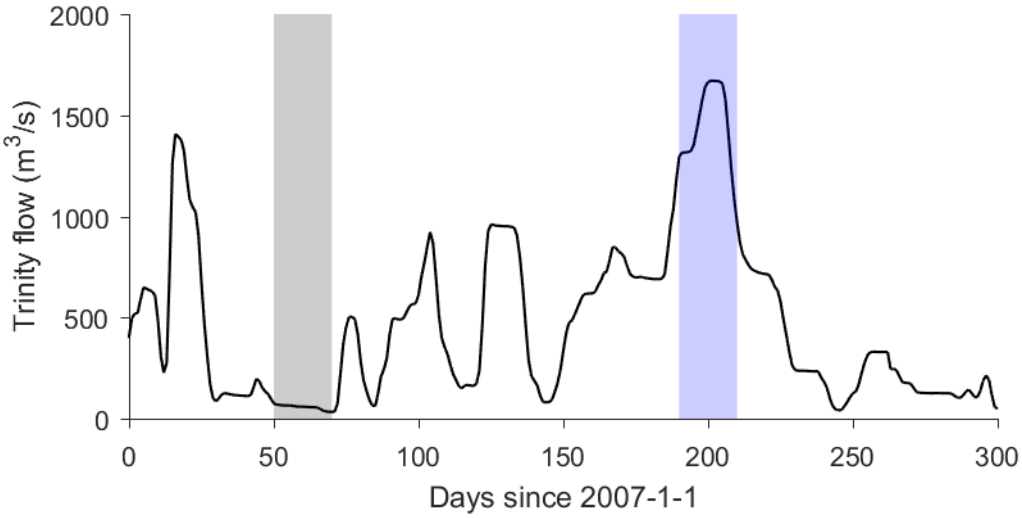

Figure 2: Freshwater discharge from Trinity River in 2007, highlighting a low-flow period (day 50-70: grey shade) and a high-flow period day 190-210: (blue shade).

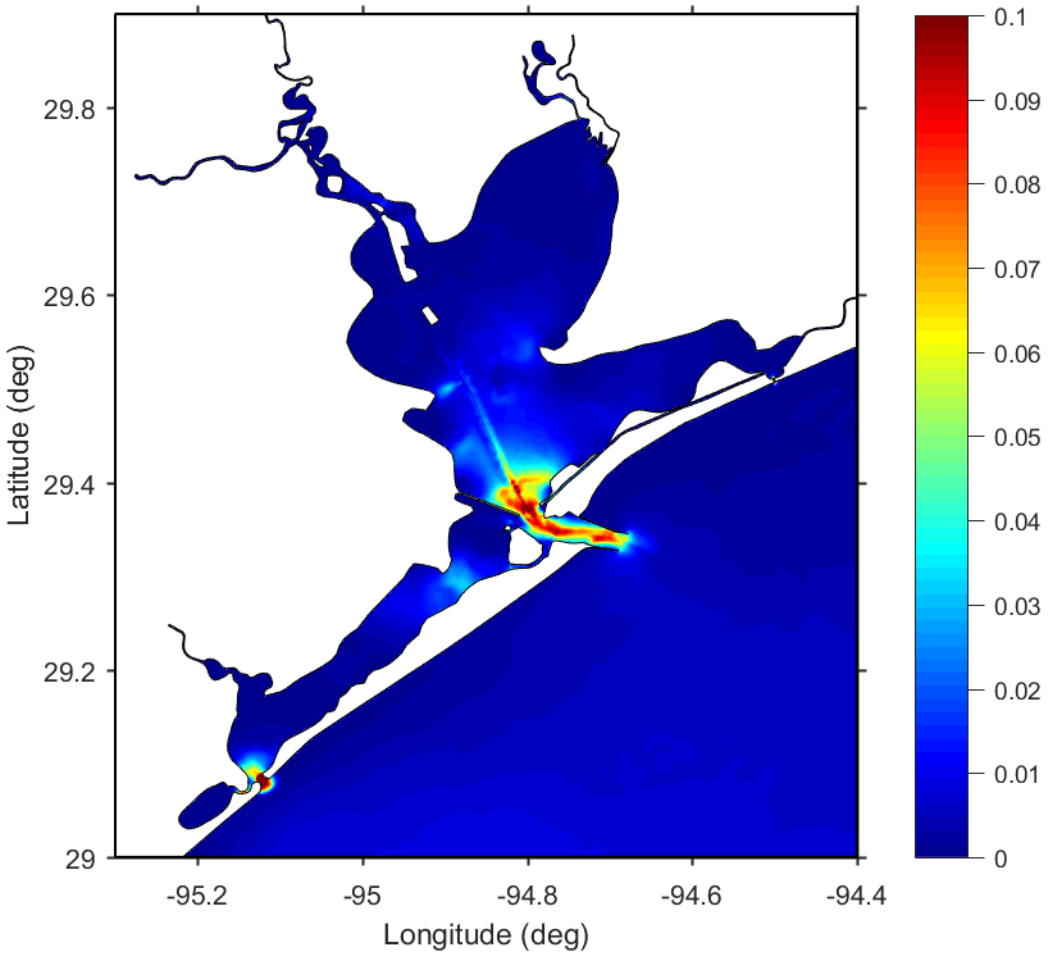

Figure 3: The mean bottom shear stress (N m^{-2}) during the low-flow period (see Fig. 2).

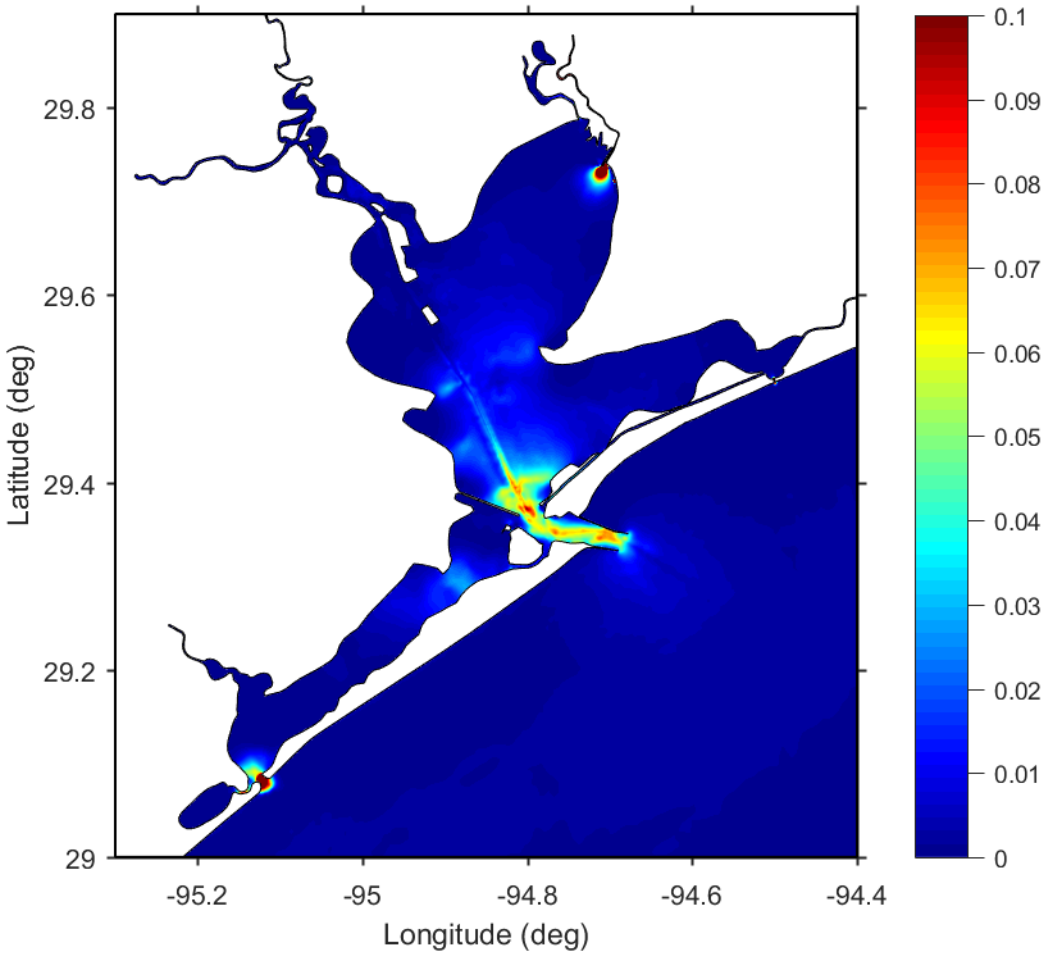

Figure 4: The mean bottom shear stress (N m^{-2}) during the high-flow period (see Fig. 2).

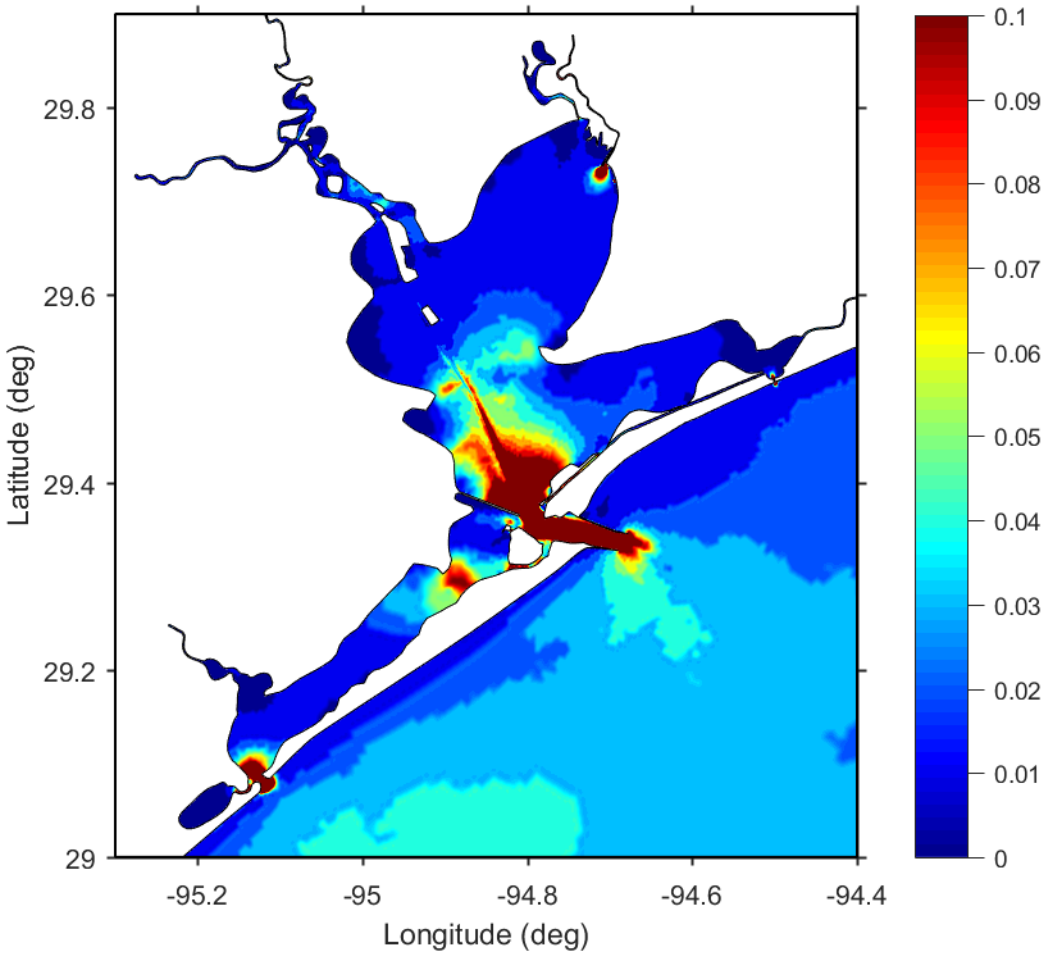

Figure 5: The 95th percentile of the bottom shear stress over the period of day 1-210 in 2007.

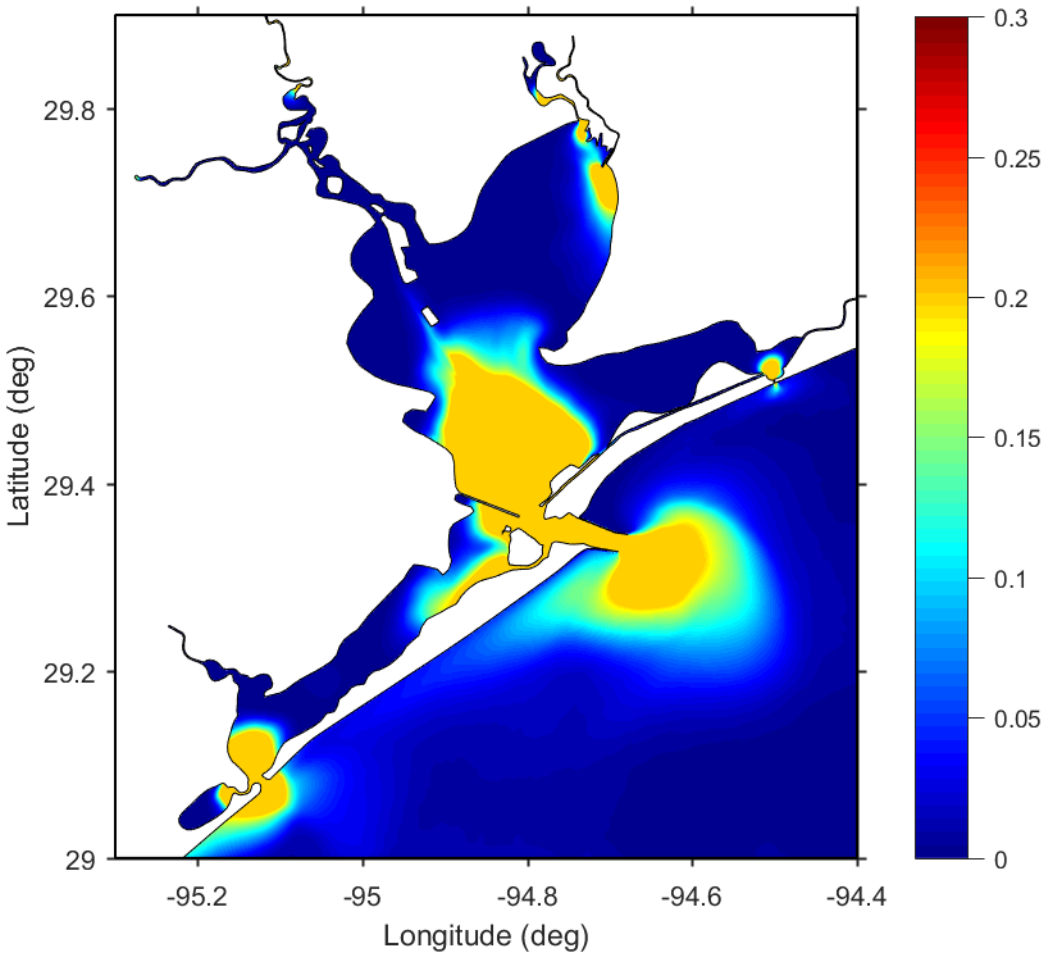

Figure 6: The simulated surface sediment concentration (g l^{-1}) during the high-flow period (see Fig. 2).

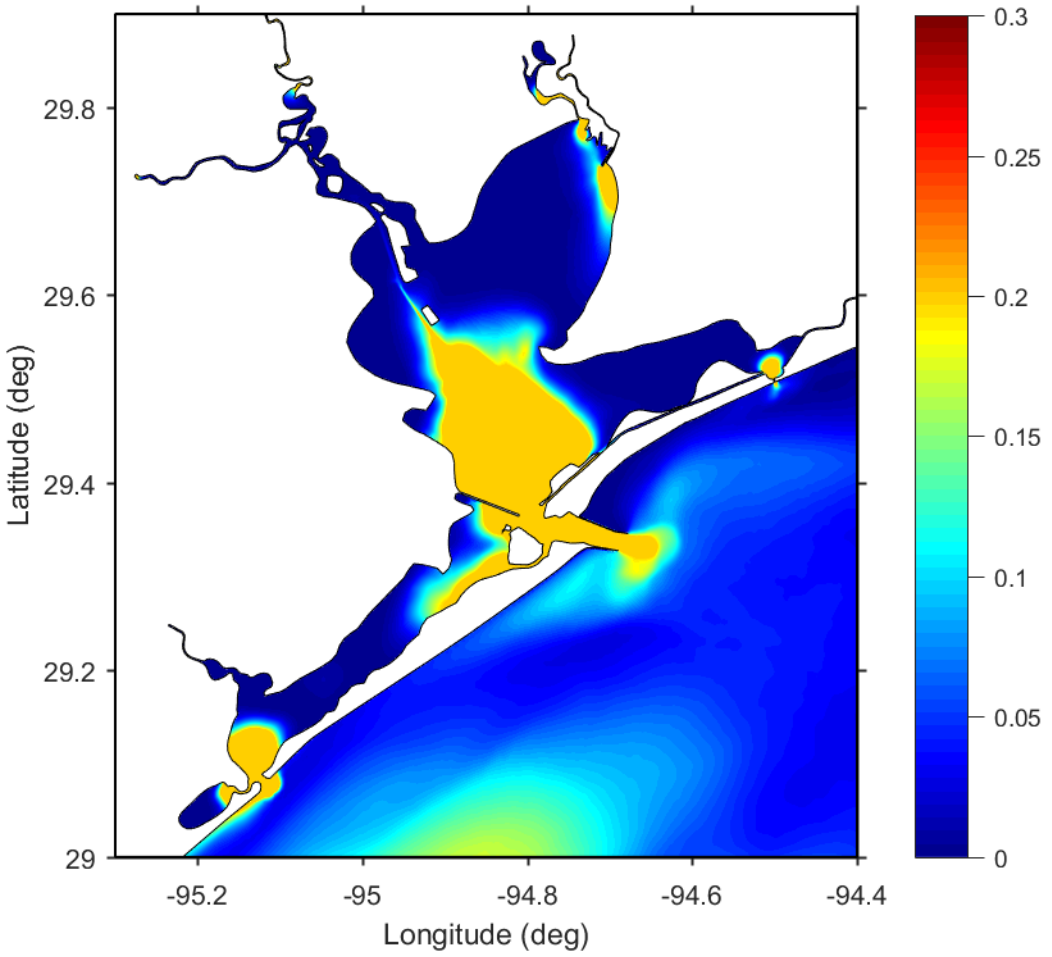

Figure 7: The simulated bottom sediment concentration (g l^{-1}) during the low-flow period (see Fig. 2).

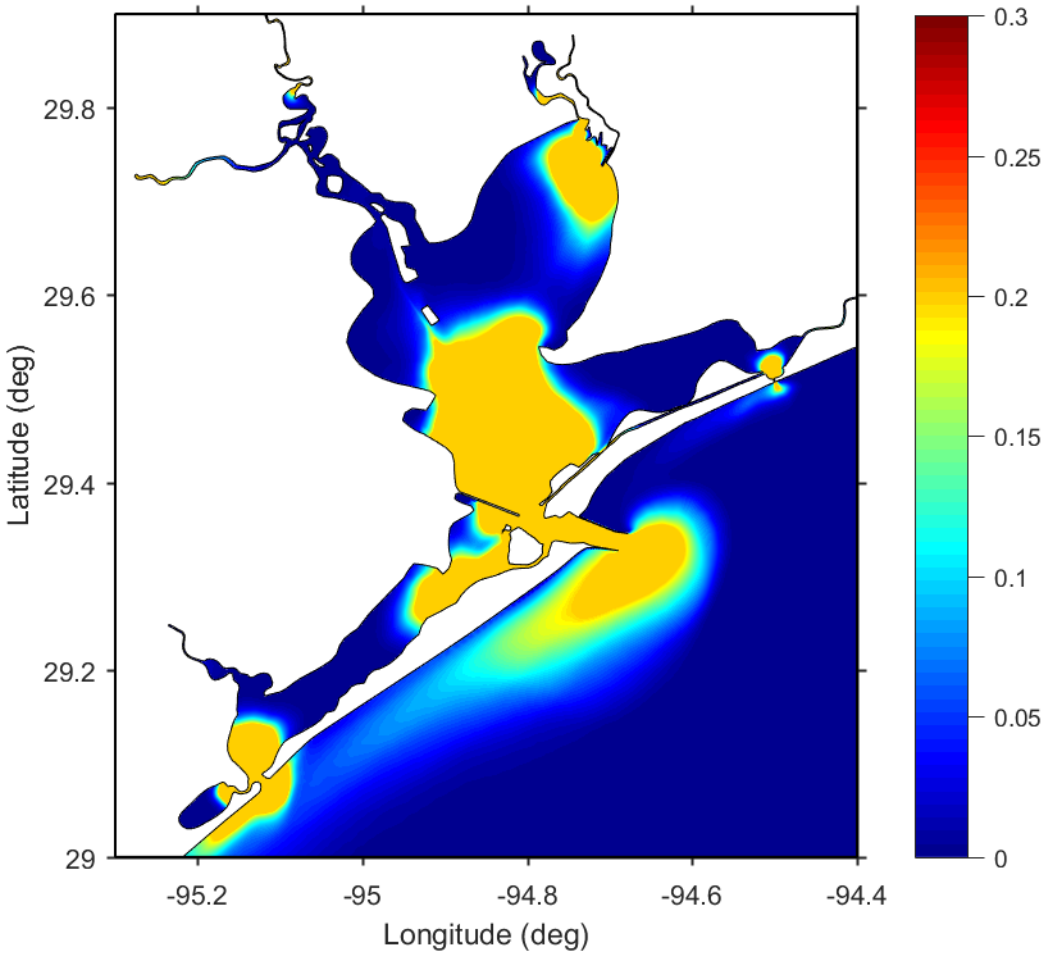

Figure 8: The simulated surface sediment concentration (g l^{-1}) during the high-flow period (see Fig. 2).

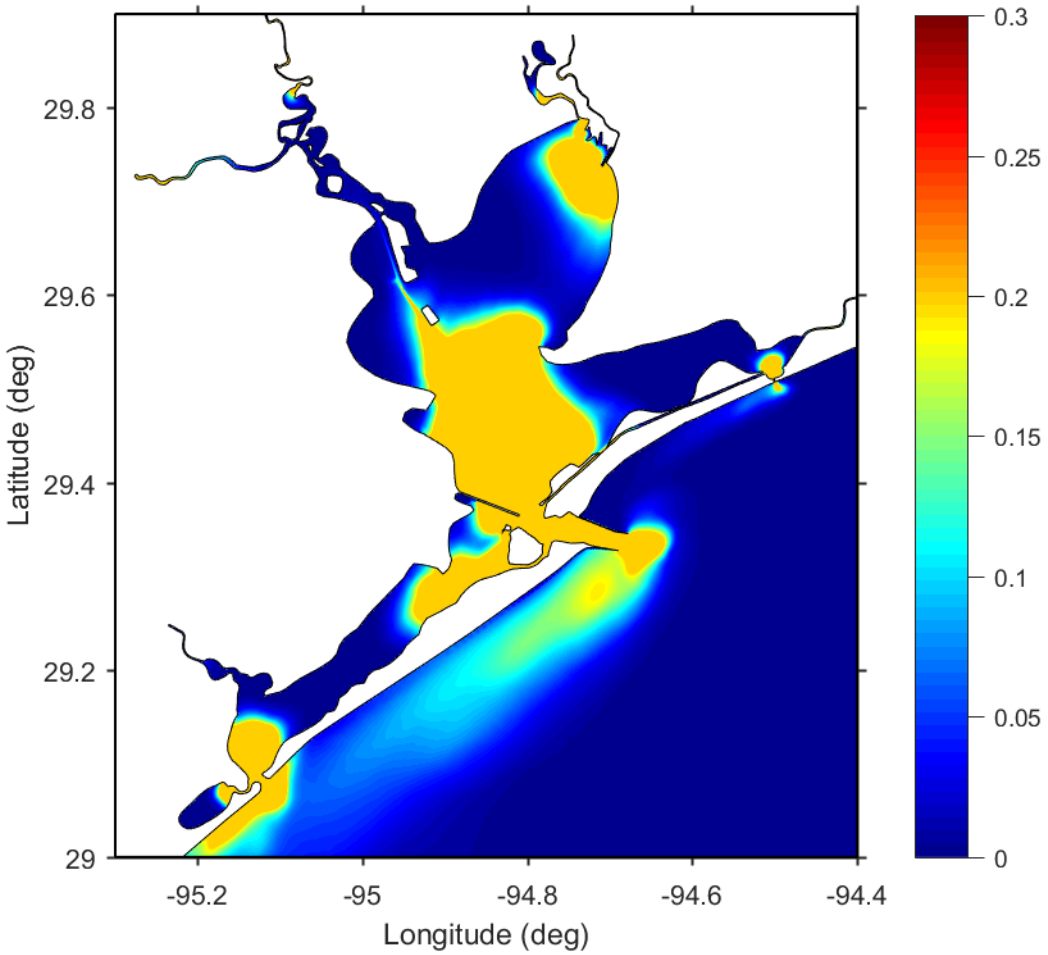

Figure 9: The simulated bottom sediment concentration (g l^{-1}) during the high-flow period (see Fig. 2).

Appendix D

Cold Front Sediment Resuspension, Age, and Residence times of suspended sediment using $^{7}Be/^{210}Pb_{xs}$ Ratio in Galveston Bay

Nicole Schmid[ab], Timothy M. Dellapenna[ab], and Kyeong Park[ab]

[a]Department of Marine and Coastal Environmental Science, Texas A&M University at Galveston

[b]Department of Oceanography, Texas A&M University

Abstract

The winds associated with the passage of meteorological fronts (cold fronts) cause waves that induce sediment remobilization/resuspension, especially in shallow estuaries such as Galveston Bay. The passage of cold fronts, collectively, over time, generate more sediment resuspension than most hurricanes and tropical storms, on an annual to decadal basis. With a warming climate, the intensity of all meteorological events is beginning to have even greater impacts on these productive ecosystems. To better understand the effects that the passage of cold fronts have on resuspending sediment, water samples were collected during frontal passages at two locations in Galveston Bay. One in the upper portion of the bay (Kemah, TX) and another closer to the mouth of the bay (Texas A&M University Boast Basin). Additionally, a Conductivity, Temperature, Depth (CTD) data logger and sensor equipped with an Optical Backscatter (OBS) turbidity measuring sensors was deployed in Trinity Bay to collect data during both frontal passages and calm water conditions. By collecting precipitation, water samples in both the upper and lower bay, and measuring the ratio of $^{7}Be/^{210}Pb$ in these samples; we can quantify the residence times of total suspended sediment (TSS) in upper and lower Galveston Bay. We found that, in general, that the age/residence time of the sediment are younger/shorter in the Upper Bay and older/longer towards the mouth of Galveston Bay. Additionally, with stronger winds and the rain that generally accompanies cold fronts, TSS concentrations are higher in upper Galveston Bay versus closer to the mouth. This is because there is more of an abundance of clay dominated mud in upper Galveston Bay and closer to the mouth the bay sediment consists of coarser mud (higher silt content, with sand); allowing for deposition to occur at a faster rate in the lower bay, where muds are coarser and have a higher fall velocity than then finer muds found within the upper bay.

1. Introduction

1.1 NGOM Estuaries

Galveston Bay is a shallow bay and, provides nursing habitat for multiple valuable fisheries, including white and brown shrimp (Stunz et al., 2010) and provides approximately 14% of the US wild catch of oysters (Haby et al., 2009). A key process in shallow estuaries is the frequency of sediment resuspension. An increased amount of sediment resuspension and deposition in an estuary may cause smothering of benthic aquatic organisms and the clogging of water intakes (Winterwept & VanKersteren, 2004). Additionally, sediment resuspension causes the redistribution of biogeochemical constituents, as well as contaminants and organic matter (Dellapenna et al., 2006, Dellapenna et al., 2020). Sediment remobilization/resuspension plays a role in many estuarine processes; especially the cycling of nutrients and pollutants in and out of an estuary (Baskaran & Santschi, 1993). Point source and nonpoint source discharges of pollutants (i.e. trace metals and hydrocarbons) can have significant environmental impacts in an estuary (e.g. Dellapenna et al., 2006; 2020). These constituents can be stored in the sediment during periods of sediment deposition and are resuspended during wind-induced wave resuspension, in addition to any other resuspension events (Dellapenna et al., 2006). Particle reactive contaminants generally move slowly through an estuarine system, transported through the abundant cycles of deposition and resuspension during hydrological stages (tides, etc.) (Saari et al., 2010).

Wind plays an important role in determining water level in many shallow-water, microtidal coastal plain estuaries, including Galveston Bay (Cox et al., 2002). Surface gravity waves are the primary mechanisms driving sediment resuspension in shallow, microtidal estuaries (Booth et al., 2000). South-east prevailing winds tend to generate wave fetch that results in increased water-column mixing and erosion (Ward Jr, 1980). Wind-induced currents and wave resuspension are important sources of energy for sediment transport within an ecosystem and can be dominant in shallow, microtidal estuaries, affecting a large portion, if not all of the water column (Booth et al., 2000). High concentrations of total suspended sediment are most often associated with meteorologically driven events, especially winter cold fronts in Northern Gulf of Mexico estuaries (Perez et al., 2000).

Based on findings in Walker and Hammack (2000), sediment resuspension and transport are maximized during the passage of winter storms over Louisiana estuaries. Throughout a study performed in Fourleague Bay, Louisiana, northerly winds were found to have the greatest wind velocities; and wind direction played an important role in the transport of water and sediment (Perez et al., 2000). The

residence time of suspended sediment in the water column is defined here as the average length of time during which the sediment resides within the bay as suspended sediment. The residence times of suspended sediment in the water column has been found to range from a few days in low-energy estuaries to several weeks in high-energy estuaries (Olsen et al., 1986).

1.2 Cold Fronts

In Galveston Bay, there are on average, 20-30 cold fronts a year that pass, whereas hurricanes and tropical storms impact the bay on average once every 1.5 years, collectively (Walker and Hammack, 2000, Roberts et al., 1987, Byrne, 1975). Overall, cold fronts occur generally between October through April and have a fairly consistent nature in characteristics (Walker and Hammack, 2000, Roberts et al., 1987). The consistent nature of cold fronts begins as a passage defined by a shift from a southerly to northly wind direction that propagates in a clockwise direction (Perez et al., 2000). The nature of cold fronts is thought to be more effective on the coastal environment than tropical storms due to higher occurrence frequency and larger area of coverage along with shifts (Moeller et al., 1993). This is due to the creation of waves caused by the wind shifts that transports fluid mud from one area to another (Kemp, 1986). The larger spatial extend of cold fronts causes them to affect an entire bay. Cold fronts have a greater impact than both hurricanes and tropical storms that tend to affect a smaller spatial area and occur at a lesser frequency (Moeller et al., 1993, Pepper et al., 1999; Roberts et al., 1987). There is a natural variability of wind including the orientation, propagation direction and speed, and strength of winds produced during cold front events that dictates the effect of suspended sediment movement within an estuary (Moeller et al., 1993).

1.3 Sediment Resuspension

Turbidity is a measure of the degree to which water loses its transparency (Hardenbergh, 1938) and is due to both the presence of suspended particles, including sediment, as well as phytoplankton, particulate organic matter and other particulates (MacIntyre & Cullen, 1996; Biggs, 1970). Total suspended sediment (TSS) is the quantification of the mass of sediment that is suspended in the water column. TSS is characterized as being particles that settle too slowly to fall out of suspension during slack water (Sanford and Halka, 1993). Suspended sediment is derived from the erosion, or resuspension and

deposition of sediment at the water-sediment interface (Ha & Park., 2012). TSS concentrations can also vary widely depending upon riverine input, wind forcing's, drainage basin size, depth, area of the bay, sediment composition, and tidal range (Perez et al., 2000). Additionally, Perez et al. 2000 found that total suspended sediment peaks were highly correlated to post-frontal winds.

1.4 Characteristics associated with Cold Fronts

Cold fronts are accompanied by a high variability of wind speed and wind direction that largely affect TSS concentrations and fluxes (Perez et al., 2000). Wind direction and speed have been shown to be the primary factors controlling TSS, sediment transport and circulation (Walker and Hammack, 2000). During these winter storms, wind speed causes the strongest sediment resuspension (Walker and Hammack, 2000). Sanford and Halka (1993), stated that sediment is 2-4 times more erodible shortly after being deposited versus sediments that were deposited for over a year. Booth et al. (2000) state that resuspension events are highest during fall, winter, and early spring due to frequent and intensive cold front events. In relation to cold fronts, winds above 10 m/s can cause resuspension greater than 80% of bottom sediments based on a study performed in Louisiana (Booth et al., 2000). Contaminant transport frequently occurs during storm events, especially if there is heavy precipitation (Du et al., 2020). Water bodies can be heavily impacted by pollution/contaminants from industrial activity, etc. (i.e. heavy metals) (Saari et al., 2010).

Cold fronts are important mechanisms for resuspending/remobilizing sediment in shallow estuaries, such as Galveston Bay (Carlin et al., 2016). Dellapenna et al. (2006) estimated that the sediment resuspension that results from cold fronts have an annual equivalence of 200-270% of the suspended sediment load from Galveston Bay's fluvial source. Sediment resuspension associated with strong cold fronts can reintroduce trace elements and pollutants back into the water column. Thus, increasing the time that these particles are in the water column and adsorbed to sediments (Olsen et al., 1986).

1.5 Isotopes

Short-lived radionuclides can be useful for studying seasonal particle dynamics under different flow regimes (Saari et al., 2010). Short half-lives, for example, 53 days for ^{7}Be and 24 days for for ^{234}Th,

23 years for ^{210}Pb, provide an advantage when considering recent events that cause sediment redistribution (Taylor et al., 2013).

^{7}Be is a cosmogenic radionuclide produced in both the stratosphere and troposphere as a result of cosmic ray spallation of nitrogen and oxygen (Brost et al., 1991). Following atmospheric fallout, ^{7}Be rapidly adsorbs to fine sediment particles (Taylor et al., 2013). ^{7}Be also serves as an indicator of recent sedimentation and transport of surface material on a catchment scale (Taylor et al., 2013). Many studies have demonstrated that deposition of ^{7}Be closely reflects rainfall volume, making it a useful tracer for studying events that relate to rainfall, such as cold fronts (Olsen et al., 1986; Baskaran & Santschi, 1993; Baskaran, Coleman, & Santschi; 1993, Taylor et al., 2013; Evrard et al. ,2015; Taylor et al., 2019). During cold front events when sediment resuspension is high, ^{7}Be within the bed sediment can be recycled back into the water column and interact with newly delivered ^{7}Be (Olsen et al., 1986).

^{210}Pb is a member of the ^{238}U decay chain. When ^{238}U decays in soils, it become ^{226}Ra and then decays into ^{222}Rn. Since radon is a noble gas, it emits from the land into the atmosphere where it decays to ^{210}Pb (atmospheric) (Baskaran, Coleman & Santschi, 1993). ^{210}Pb is released from the atmosphere and delivered from the surface via wet and dry fallout. ^{210}Pb is called $^{210}Pb_{xs}$ once it has adsorbed to particles by the decay of its' parent isotope.

Fallout patterns of ^{7}Be and ^{210}Pb are tightly correlated leading to these nuclides being useful for dependent tracers (Baskaran, Coleman, & Santschi, 1993). The similarities of ^{7}Be and ^{210}Pb as tracers include similar atmospheric deposition and strong adsorption to similar particles; meaning they do not preferentially adsorb to specific particle sizes or compositions. Therefore, using the activity ratio of these two particles is less variable than either isotope individually (Matisoff et al., 2005). Once radionuclides adsorb to sediment particles, they are strongly and nearly irreversibly bound to these particles, making it possible to study the movement and obtain the age of suspended sediment (Taylor et al., 2012). ^{210}Pb and ^{7}Be activities in the water column (dissolved and particulate) have been found to vary with precipitation and river discharge (Baskaran & Swarzenski, 2007; Sommerfield et al., 1999). The measurement of ^{7}Be and ^{210}Pb nuclide activity in sediment quantifies the time that the particles were tagged by the tracers deposited atmospherically (Matisoff et al., 2005). Sediment that has been recently labeled by radionuclides in the water were shown to display a similar ^{7}Be /^{210}Pb activity ratio to the rainfall event (Evrard et al., 2015). The ratio of ^{7}Be /^{210}Pb can also be used to quantify the proportion of resuspended bottom material in the water column (Olsen et al., 1989). Baskaran and Santschi, found that

concentrations of ^{7}Be are quickly diluted into coastal waters and sediment in 1-2 days following rainfall events.

In Galveston Bay, ^{7}Be activity in rainfall has previously been measured to contain 2 Bq[1]/L (Baskaran et al., 1993). Higher percentages of ^{210}Pb have been found to be related to $^{210}Pb_{xs}$[2] that becomes resuspended from bottom sediment (Baskaran & Santschi, 1993). Previous studies have found that over 95% of samples taken in Galveston Bay have $^{7}Be/^{210}Pb$ activity ratios of less than 250 dpm[3]/L (Baskaran, et al., 1993). In Galveston Bay, average concentrations of ^{7}Be and ^{210}Pb were 87,124 and 155 dpm/L and 6.75,6.85, and 11.4 dpm/L, respectively for three years. The inconsistency of seasonal trends in bulk depositional fluxes of ^{7}Be and ^{210}Pb lead to the main influence being based on the amount of precipitation during a specific year (Baskaran, Coleman, & Santschi, 1993).

1.6 Objective of Study

Collecting suspended sediment within the water column to test for TSS during cold fronts, along with instrumental data collection may permit quantification of sediment resuspension during the passage of a frontal system. The two radio-isotopes described above will be applied using the method developed by Matisoff et al., (2005) to find the age of suspended sediment in upper and lower Galveston Bay. The methodology will be explained in further detail in the Methods section below. The data collection for utilization of the method will be performed by collecting water samples in both the upper and lower bay, along with precipitation during the events. The activity of two radioisotopes will then be measured in the samples collected. The age of the sediment should be younger in the Upper Bay and older towards the mouth of Galveston Bay. Additionally, with stronger winds and the rain that generally accompanies cold fronts, TSS concentrations will be significantly higher in upper Galveston Bay versus closer to the mouth. This is because there is more of an abundance of mud in upper Galveston Bay, whereas the lower bay (closer to the mouth) contains a larger abundance of sand/shells as well as silt; allowing for deposition to occur at a faster rate than finer muds due to their respective fall velocities (Figure 1). Understanding physical processes, such as sediment resuspension, allows for proper management strategies to be

[1] Bq: becquerel is the SI derived unit of radioactivity.
[2] $^{210}Pb_{xs}$ is is the atmospherically derived ^{210}Pb from its decay parent isotope ^{226}Ra (Saari *et al.*, 2010).
[3] Dpm: disintegrations per minute

developed to ensure a stable and productive ecosystem for the species that live in the estuary (Walker and Hammack., 2000).

2. Background

Galveston Bay is a shallow, microtidal estuary and is the second largest in Texas, with a surface area of 1600 km^2. The average depth of the bay is 2.1 m and contains a ship channel with dimensions of 150 m in width and 10-15 m deep, oriented along the main axis of the bay (50 km long) (Du & Park, 2019). The exchange of tidal water flows through Bolivar Roads, which is the tidal inlet between Bolivar Peninsula and Galveston Island. An additional tidal inlet exists 47 km to the west and services Christmas Bay and the western half of West Galveston Bay. Average water residence time within Galveston Bay is approximately 40 days (Solis and Powell, 1999). Trinity Bay comprises the northeastern portion of Galveston Bay (Fig. 1), has depths generally ranging between 3-4 meters (Dellapenna et al., 2006) and the Trinity River flows into the head northeastern end of the bay. The Trinity River accounts for approximately 90% of the freshwater input and is the largest sediment source into Galveston Bay (SAGE, 2002, USGS, 2005). Another significant sediment load within the bay is the ongoing maintenance of the Houston Ship Channel. In waters deeper than 1.5m, Trinity Bay bottom sediment is mud dominated (approx. 40% of total bay area) (Dellapenna et al., 2006). Mud is the dominant sediment composition of the majority of the Galveston Bay system (Figure 1).

Adjacent to upper Galveston Bay is Houston, the fourth largest city in the USA. This metropolitan area directly drains into the San Jacinto River and Houston ship channel. Houston is the third largest seaport in the USA in terms of shipping tonnage and has been cited as one of the most polluted water bodies in the USA (EPA, 1980). Further south of Houston is the Houston-Texas City-Galveston area that is highly industrialized, specifically by petroleum, petrochemical, and chemical industries and has been estimated to contain 30-50% of total US chemical production and oil refineries (Santschi et al., 2001). Additionally, Galveston Bay receives over half of the total permitted wastewater discharges for the state of Texas and around 5 km^3 per year of wastewater input (EPA, 1980). Although in recent years, there has been improvement of cleanliness of waterways where nutrients, trace metals, and trace organics do not indicate a greatly polluted system (Santschi et al., 2001).

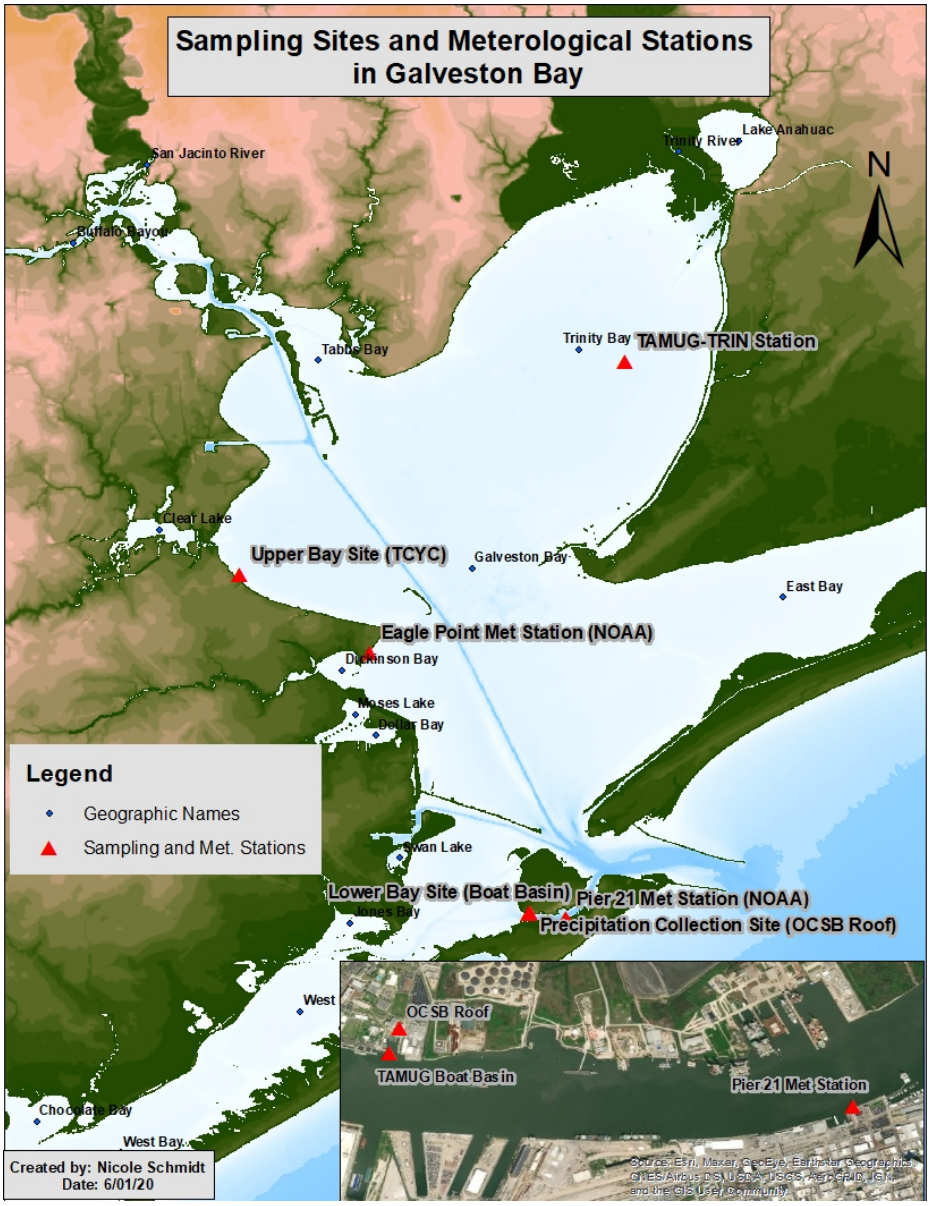

Figure 1: Suspended sediment, CTD deployment, and precipitation data collection sites from September 2019 to February 2020.

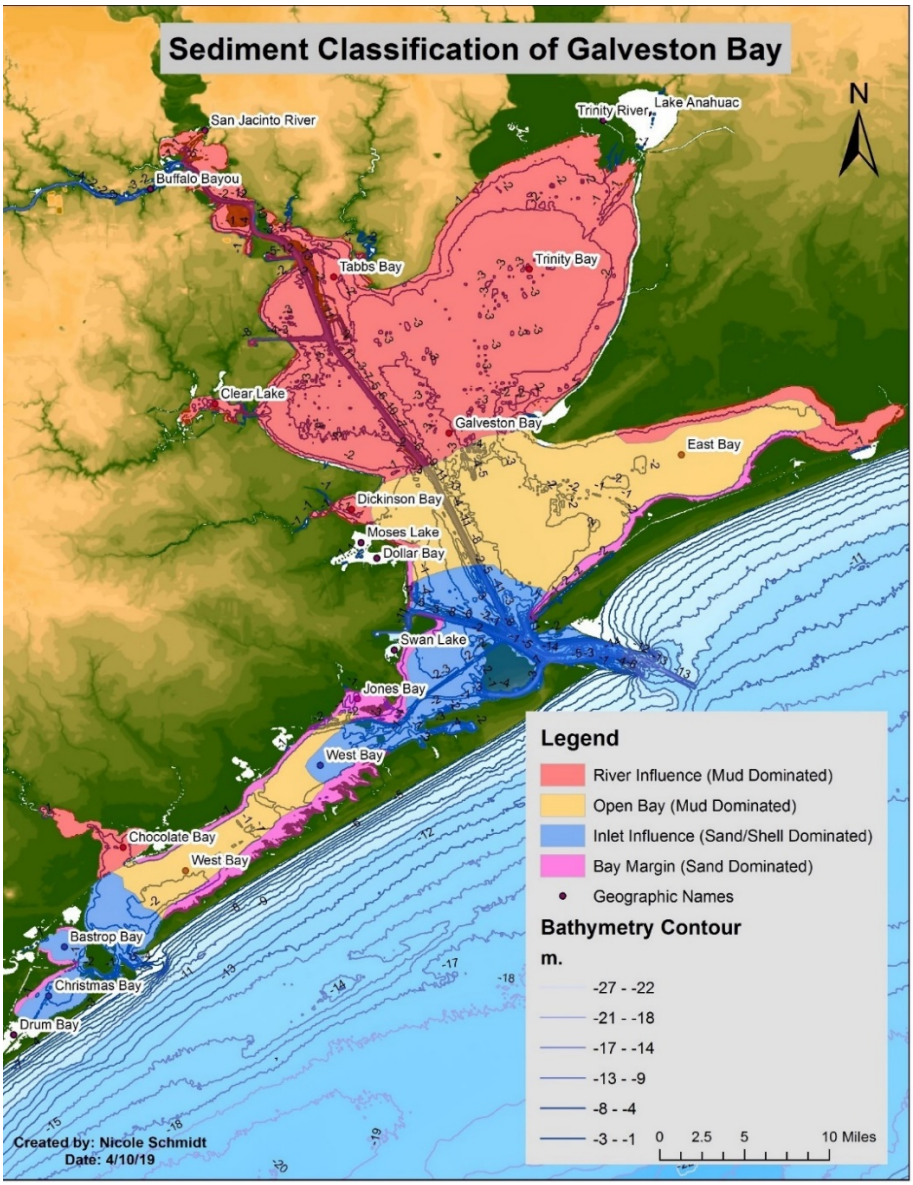

Figure 2: Sediment classification of polygons represented as polygons transcribed from Submerged Lands of Galveston-Houston area physical map. Source: Coastal Geology Lab TAMUG referenced from University of Texas Bureau of Economic Geology: Submerged Lands of Texas, Galveston- Houston Area Plate V. Distribution of Wetlands and Benthic Macroinvertebrates (1985)

Objectives

4.1 Research Questions:

1) What is the residence time of suspended sediment in the Upper Bay and Lower Galveston Bay using the Matisoff Method?
2) Is TSS higher in the Upper Bay versus the Lower Bay?
3) Is TSS higher during ebb or flood tide?
4) Is activity concentration higher in upper Galveston bay versus the lower bay?
5) Stronger winds, higher TSS?
6) Based on one data collection at the boat basin during a Tropical Storm (September 27, 2019), was the TSS higher during this than the TSS measured during cold fronts?

The purpose of this study is to understand the relationship between cold fronts and sediment resuspension. As mentioned above, Dellapenna et al., (2006) found that the passage of cold fronts, on an annual basisl volumetrically resuspends an order of magnitude more sediment than shrimp trawling and is equivalent to 200-270% of annual fluvial sediment input. Most meteorologically driven sediment resuspension occurs during the passage of northern cold fronts which mainly occur during winter months (Henry 1979, Hardy and Henderson, 2003).

By collecting precipitation, water samples in both the upper and lower bay, and measuring the ratio of $^{7}Be/^{210}Pb$ in these samples; we can quantify the residence times of suspended sediment in upper and lower Galveston bay. We hypothesize that the age of the sediment should be younger in the Upper Bay and older towards the mouth of Galveston Bay. Additionally, with stronger winds and the rain that generally accompanies cold fronts, total suspended sediment (TSS) concentrations will be significantly higher in upper Galveston Bay versus closer to the mouth. This is because there is more of an abundance of clay dominated mud in upper Galveston Bay and closer to the mouth contains coarser mud (higher silt content, with sand); allowing for deposition of coarser mud to occur at a faster rate than finer muds.

3. Methods/Data Collection

4.1 *Suspended Sediment Collection*

Figure 3: Texas Corinthians Yacht Club sampling site.

The Texas Corinthians Yacht Club (TCYC) pier located near Kemah, TX, was selected for our sampling location for suspended sediment from the bay. The pier extends 470 m into the bay, with the water depth of 2 m at end of the pier, permitting open water sampling. Water sampling was achieved by attaching a bilge pump to a 4 m long, 3.81 cm diameter aluminum pole, with the bilge pump being mounted 10 cm above the bottom of the pole to prevent penetration into the sediment while still collecting suspended sediment from the bottom. Five samples were collected from October 2019 to February 2020 at Texas Corinthians Yacht Club (TCYC) pier in Kemah, TX and four from September 2019 to February 2020 at the Texas A&M Galveston Boat Basin. Three to Four 20-liter polypropylene carboys were filled at each collection site per collection event.

Following collection, a portion of the samples were homogenized and about 1-2 liters of water were set aside to filter to determine TSS (g L^{-1}). TSS was measured using a Millipore filtration system connected to a vacuum pump filtered through a .45-micron filter. The filter weight and initial volume was recorded along with the post filter weight and volume. These were used to calculate TSS in g L^{-1}. The rest of the water was siphoned and sediment was separated by centrifugation. Once sediment was separated, it was air-dried and ground to a powder in a mortar and pestle, then placed in a test tube for radioisotope analyses. The dried sediment in the test tubes was placed in the germanium gamma well detector and counted for 24 to 36 hours.

Table 1: Wind speed and direction recorded during time of collection at the TAMUG Boat Basin and TCYC.

Boat Basin			
Date	**Time Collected**	**Wind Speed and Gusts (m/s)**	**Wind Direction**
9/27/2019	11:30 AM	N/A	N/A
1/29/2020	3:00 PM	6-7 m/s & 10 m/s gusts	WNW
2/21/2020	4:45 PM	6 m/s & 7.5 m/s gusts	NNE
TCYC			
Date	**Time Collected**	**Wind Speed & Gusts (m/s)**	**Wind Direction**
10/14/2019	11:00 AM - 1:30 PM	N/A	ESE
10/25/2019	1:00 PM - 2:00 PM	7.5 m/s & 13 m/s gusts	NNW
11/12/2019	4:30 PM	8 m/s & 11.5 m/s gusts	N
1/29/2020	1:30 PM	6 m/s	WNW
2/13/2020	2:00 PM -2:45 PM	6 m/s & 8 m/s gusts	N
2/21/2020	3:00 PM	6 m/s & 10 m/s gusts	NNE

4.2 CTD Deployment

An RBR CTD (conductivity, temperature and dept sensor) with two Seapoint optical back-scatter sensors (turbidity) was mounted to a homemade frame (pod) built for deployment in Trinity Bay from January 27, 2020 to February 27, 2020. One sensor was mounted 50 cm above the bed, and the other sensor was mounted 150 cm above the bed (Figure 2). The reasoning for the sensor placements at a specific height relates to the bottom boundary layer (BBL), which is the layer where hydrodynamics

Figure 4: The image on the left is the homemade pod built for deployment in Trinity Bay (right image).

control erosion/deposition of suspended sediment (Ha & Park, 2012). Three 45 kg of dumbbell weights were mounted at the base of the pod to keep it from moving during strong cold front events. Water was collected during deployment and upon retrieval to calibrate the sensors for TSS.

4.3 Turbidity Sensor Calibration

The calibration of the CTD Seapoint turbidity sensors was performed in the lab using sediment and water that was collected on site during deployment of the CTD in Trinity Bay. Prior to running the calibration, the sediment was sieved in order to obtain only the mud (silt and clay) fraction from the sample, which are generally suspended and thus measured during the deployment. The sediment was first filtered through a 250-microns sieve to remove larger shells, etc. and then through a 63-micron sieve to obtain the mud fraction. The leftover sample was centrifuged and evaporated to only contain the mud used for the calibration. The amount of tins and weight of sediment per sample added during the calibration were referenced from Minella et al. (2008), where they used to measure around 10 to 15 samples containing between 0.25 to 2.5 grams of sediment per tin. Similarly, 0.3 to 5.0 grams of sediment were measured into 18 different tins. Around 10 liters of the collected water was poured into a bucket where the calibration took place. The turbidity sensors were attached to a pole and placed in the bucket. A paint stirrer attachment was connected to a drill to allow for continuous homogenization of the bucket. The CTD was set to run on 6Hz profiling to constantly collect data.

Figure 5: Setup for CTD Turbidity Sensor Calibration conducted on 7/22/20.

The drill was inserted to homogenize the water and after this became homogenized, a mud sample was mixed with 1 L of the water from the bucket and mixed back in. After a few minutes, the bucket became equilibrated and around 400-600 mL of the water in the bucket was subsampled for filtering. The steps explained above were repeated 18 times in order to obtain a homogenized subsample after each tin was added. The subsamples were then filtered using the method described in the Suspended Sediment Collection section, above.

4.4 Precipitation Collection

Figure 6: Precipitation jug with attachments mounted on the roof of OCSB located at Texas A&M University at Galveston.

Precipitation was collected on the roof of the Ocean and Coastal Studies building at Texas A&M Galveston Campus (Figure 6). The rain collector was placed on top of OCSB for ease of deployment when rain events occured in Galveston. This location was chosen under the assumption that rainfall is relatively similar throughout Galveston Bay. Based on regular cold front patterns, they generally extend at over the entire area of the bay, making the deployment at OCSB in Galveston a reasonable location for use of the Matisoff method. Activity measurements of ^{210}Pb and ^{7}Be from rain water is necessary to perform the Matisoff method, to determine the "initial" age of the two radio-isotopes for each frontal passage event.

The water was collected using a 20-liter jug with a large funnel attached to the opening along with a 2-liter bucket of water next to it for more collection. Additionally, a rain gauge was attached to the container that held the jug. This was deployed before each rain event from January 2020 to February 2020. Following collection, the containers were acidified with HCl that had a pH of 1-3 and were then transferred to a 2-4-liter container. One to two days prior to acidification of the sample; iron hydroxide was added to the sample to separate the nuclides/particles from the water and was left overnight (2 mL $Fe(OH)_2/L$). Ammonium was slowly added to form aggregates and allowed to settle until it was possible to siphon as much excess water as possible. The rest of the sample was centrifuged to separate more water from the aggregates. Once the sample was combined into one falcon tube, 2 mL of 1M HCl was added to the tube and poured into a test tube. An additional 2 mL of 1M HCl was added to the falcon tube to collect the remainder of the sample. The sample was then transferred to the germanium gamma well

326 detector and counted for 24-36 hours. These isotopes were not measured as a ratio, but as individual
327 isotopes.

328 *Table 2: Rain gauge measurements and amount of precipitation recovered from TAMUG OCSB Roof.*

Date	Rain Gauge (mm)	Precipitation Recovered (L)
1/29/2020	2	0.3
2/13/2020	32	2.5
2/21/2020	2	0.25

329

330 Due to low activity ratios of ^{210}Pb in two precipitation samples (1/29/2020 & 2/21/2020), the hotblock
331 acid digestion method was used. The two water samples were weighed and placed into a hotblock
332 container (Figure 7). While the hotblock was being preheated, 0.25 mL of ^{209}Po tracer was added,
333 followed by 15 mL HNO_3 and 15 mL HCl. The sample heated in the hotblock at 165^{o}C for 30 minutes.
334 To prepare the silver planchet for the Alpha counter, 50 mL of diluted HCl and 5 mL ascorbic acid were
335 added and the set to stir for approximately 24 hours. After the 24 hours, the silver planchet is removed
336 and cleaned with acetone and deionized water and set to count in the Alpha counter for 24-48 hours. ^{210}Pb
337 was then calculated from the activity of ^{209}Po and ^{210}Po.

338

339 *Figure 7: Hotblock used for acid digestion method for low ^{210}Pb activity samples*

340 ***4.5 Suspended Sediment Residence Time Method (Matisoff et al., 2005)***

341 Listed below are the assumptions due to ^{7}Be/^{210}Pb$_{xs}$ chronometer. These assumptions allow for
342 uniformity during deposition and following adsorption onto particles. First, it is assumed that dry fallout
343 flux can be included with wet fallout where both are delivered during precipitation events. Where the

precipitation events generate suspended sediment (for this specific study, cold fronts). Secondly, both isotopes are assumed to be delivered to atmosphere in a constant proportion, disregarding season, latitude, or proximity to ocean. This second assumption separates the highly variable nature of atmospheric flux of each isotope separately. Third, following atmospheric fallout, both isotopes are assumed to rapidly adsorb to particulate matter and remain on the particles during further transport until collection. The fourth assumption states that both isotopes are not differentially adsorbed onto organics or partitioned differently. Lastly, by considering the ratio of ^{7}Be and ^{210}Pb, makes it possible to eliminate differences along flow path that is caused by particle grain size and mineralogical variations and because both isotopes have similar adsorption behavior.

With the assumptions given above, decreases in $^{7}Be/^{210}Pb_{xs}$ ratio can be caused by 2 end-member cases. Matisoff *et al*. (2005) reached the conclusion that these two radionuclides are the best indicator of suspended sediment age because of characteristics that make them act the same when deposited into the given environment. For the first case it is possible to calculate if the ratio for precipitation is known. For

$$A = (^{7}Be)_{sample}$$
$$A_o = (^{7}Be)_{source}$$
$$B = (^{210}Pb_{xs})_{sample}$$
$$B_o = (^{210}Pb_{xs})_{source}$$

the second case, 'New' sediment is defined as the sediment particles that have a $^{7}Be/^{210}Pb_{xs}$ ratio equal to precipitation. This means that sediment particle age is the time since the ^{7}Be isotope tag was delivered to sediment particles. In the second case, $^{7}Be/^{210}Pb_{xs}$ ratio in suspended sediment can decrease by the addition of ^{7}Be -deficient sediment from bottom sediment erosion or entrainment of old (^{7}Be -depleted) bottom sediment.

$$A = (^{7}Be)_{sample}$$
$$A_o = (^{7}Be)_{source}$$
$$B = (^{210}Pb_{xs})_{sample}$$
$$B_o = (^{210}Pb_{xs})_{source}$$

1) First Case:

364 a. Activities of ^{7}Be & ^{210}Pb in sediment are given by

$$A = A_o \, e^{-(\lambda_{^{7}Be} t)}$$
$$B = B_o \, e^{-(\lambda_{^{210}Pb} t)}$$

365

366 b. $^{7}Be/^{210}Pb_{xs}$ ratio in suspended sed. Sample is given by ratio A/B

$$\frac{A}{B} = \frac{A_o}{B_o} e^{-(\lambda_{^{7}Be} - \lambda_{^{210}Pb})t}$$

367

368 c. Age of sediment given by

$$t = \frac{-1}{(\lambda_{^{7}Be} - \lambda_{^{210}Pb})} \ln\left(\frac{A}{B}\right) + \frac{1}{(\lambda_{^{7}Be} - \lambda_{^{210}Pb})} \ln\left(\frac{A_o}{B_o}\right)$$

369

370 **2)** Second Case: the percentage "new" sediment in suspension is directly proportional to the
371 $^{7}Be/^{210}Pb_{xs}$ ratio

$$\%\ \text{'new' sediment} = 100 \times (A/B)/(A_o/B_o)$$

372

373 a. Percentage new sediment can also be determined from the age of sediment:

$$\%\ \text{'new' sediment} = 100 \times \exp\,[-(\lambda_{^{7}Be} - \lambda_{^{210}Pb})t]$$

374

375 b. T is the age of sediment calculated in the same way as the first case.

376

377

4. Results & Discussion

5.1 TSS Results

Table 3: Water sample collection data from TAMUG Boat Basin and Texas Corinthians Yacht Club.

Boat Basin					
Date	**Time Collected**	**Tidal Phase**	**Wind Speed & Gusts (m/s)**	**Wind Direction**	**Average TSS (g/L)**
9/27/2019	11:30 AM	ebb	10 m/s	N/A	17.5
1/29/2020	3:00 PM	flood	6-7 m/s & 10 m/s gusts	WNW	15.6
2/21/2020	4:45 PM	flood	6 m/s & 7.5 m/s gusts	NNE	11.1
TCYC					
Date	**Time Collected**	**Tidal Phase**	**Wind Speed & Gusts (ms^{-1})**	**Wind Direction**	**Average TSS (g/L)**
10/14/2019	11:00 AM - 1:30 PM	ebb	12.5 **ms^{-1}**	ESE	49.4
10/25/2019	1:00 PM - 2:00 PM	flood	7.5 **ms^{-1}** & 13 **ms^{-1}** gusts	NNW	25.5
11/12/2019	4:30 PM	flood	8 **ms^{-1}** & 11.5 **ms^{-1}** gusts	N	16.8
1/29/2020	1:30 PM	flood	6 **ms^{-1}**	WNW	20.6
2/13/2020	2:00 PM -2:45 PM	ebb	6 **ms^{-1}** & 8 **ms^{-1}** gusts	N	12.2
2/21/2020	3:00 PM	flood	6 **ms^{-1}** & 10 **ms^{-1}** gusts	NNE	11.3

The first few water collection deployments were conducted on September 27th 2019 at the TAMUG Boat Basin. Collections during October 14th and 21st, and November 11th of 2019 were at TCYC. All of this data was filtered to collect TSS (g L^{-1}) of the water. The sediment from the last three samples were separated from the water by centrifugation and placed in test tubes to be sent to Carol Wilson of the Department of Geology and Geophysics at LSU to be counted on a gamma detector.

Unfortunately, precipitation data was not collected; therefore, the Matisoff method of suspended sediment age estimation cannot be tested with these deployments. Another round of water collection sampling was conducted on January 29th and February 21st of 2020, where samples were collected at both the TAMUG Boat Basin and TCYC. Water collection was also conducted on February 13th 2020, but only at TCYC. TSS data was processed by filtering approximately 1 L of homogenized water collected at each site for each deployment and is presented in Table 3. This data was also filtered to find TSS and the remaining water was centrifuged to separate the sediment to be counted on the gamma detector.

TSS concentrations varies among the samples and is largely dependent on wind speed and gusts. Wind direction also influences the resuspension of bottom sediments during cold fronts. Six out of the 9 samples were collected during flood tide, whereas, the other three were collected during ebb tide. There was only one ebb tide sample for the lower bay site, which was also collected during a cold front. Comparing ebb tide versus flood tide in the upper bay site; ebb tide had higher TSS concentration with a north wind (2/13/2020 vs. 2/21/2020). Looking at the upper bay and the lower bay with corresponding wind speeds, TSS concentrations were observed to be higher during ebb tide. Comparing these two, TSS concentration was highest at TCYC with an ebb tide. When comparing wind speed/gusts and locations (upper bay vs. lower bay), TSS concentration was generally higher at TCYC. This was observed for the last measured cold front event (2/21/2020). This can be attributed to the mud-dominated composition of bottom sediment that characterizes upper Galveston Bay. For all samples collected, it is observed that the stronger the wind speed and gusts, the higher the TSS concentration is because the wind causes sediment to be resuspended from the bay bottom. Lastly, comparing the sample collected during a tropical storm (9/27/2019) versus the cold front with a similar wind speed (10/14/2019 & 11/12/2019). The two cold front events have an average TSS concentration of 32.9 gL^{-1}, which was higher than the TSS concentration measured from the tropical storm. The higher TSS concentration measured during cold fronts was likely due to the direction of wind and the size and duration of the tropical storm. As stated above in the introduction, cold fronts cover more area than a tropical storm, creating a larger impact on shallow water estuaries, such as Galveston Bay.

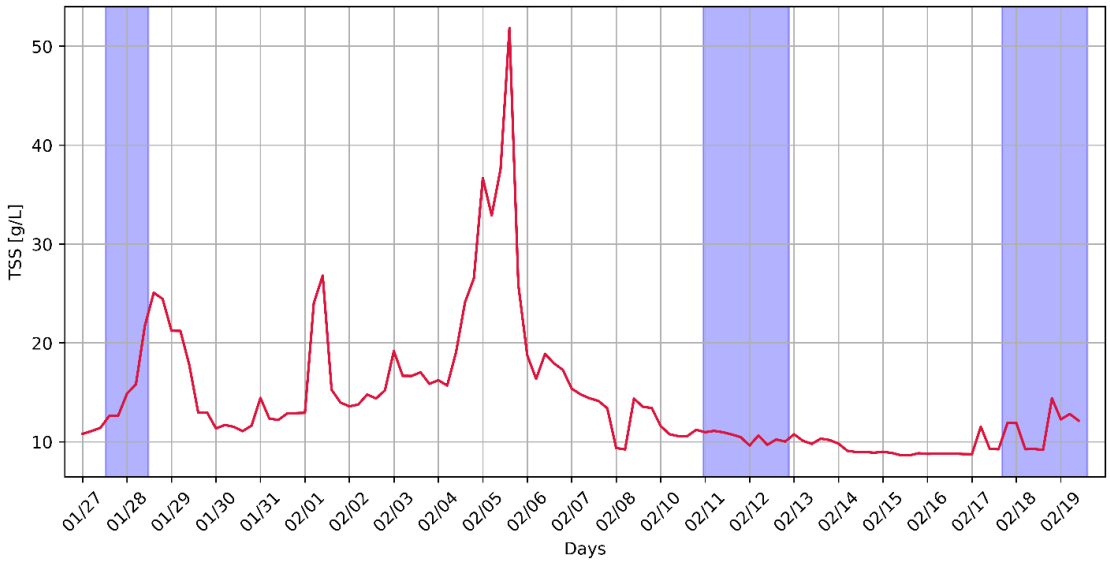

Figure 8: TSS (g/L) from TAMUG-Trin CTD Deployment (9A),

TSS concentrations were also determined from the OBS sensor attached to the CTD during the TRIN pod deploymen January 27 to February 27 in Trinity Bay. TSS concentrations were calculated using the linear equation formula (y = 0.1774x + 8.552) derived from the in-lab CTD turbidity sensor calibration (Figure 8). TSS concentrations throughout the deployment averaged between 8-10 g/L. The TSS concentration spiked following cold front events, aside from the largest peak that occurred 2/5-7/2020. The peak correlates to a winter storm, but there was no rain, therefore precipitation isotope data could not be collected. Following this peak, TSS concentrations do not increase again until 2/18/2020, which matches with the last sampled cold front event (2/18-21/2020).

5.2 Mooring Deployment

Data recorded from the CTD deployment in Trinity Bay was plotted and compared with a NOAA TCOONS station located within Galveston Bay (Eagle Point, TX). At the Eagle Point Station, the sensor height water temperature is measured at 1.3 m below MLLW. The conductivity sensor height is not

Figure 9: NOAA TCOONS Eagle Point, TX meteorological station.

available (Figure 9). This station was chosen because it was within the closest proximity (26.02 km) to the TAMUG-TRIN Pod Station (Figure 1).

Figure 11 displays the CTD data collected during the TRIN Pod deployment. The salinity is lower during every cold front passage, which is likely the result of freshwater added to the bay as a results of the associated rainfall events (Figure 11A). Following the first cold front passage salinity lowers to 10 PSU (practical salinity units) and raises to nearly 14 PSU. Despite the largest rainfall event from January 26-28 (Figure 13 & 14), the salinity does not lower until a few days later. This could be attributed to the rain measurement being in Moses Lake, where it may have taken more time for the majority of the freshwater to flow to the deployment site (Trinity Bay). The lowest salinity follows the rain event on February 13th (Table 2, Figure 13), which, like the first event, lower salinity is measured a couple days following the event. Measured salinity becomes fairly uniform for the remainder of the deployment below 10 PSU. The measured pressure from the CTD fluctuates throughout deployment. Pressure is lower than average during cold fronts. When wind speed increases, pressure decreases (Figure 11B & 11A).

Based on the comparison of the observed temperature from the CTD and NOAA (Eagle Point) found that both instruments follow the same trend where temperature from the CTD tends to be lower (Figure 11E). The decrease in water temperature follows the passage of the cold fronts (1/29-30,2/7-8, 2/13-15, and 2/20). This is similar for measured conductivity, but the CTD measurements tend to be lower than NOAA; and towards the end of deployment, they do not follow a similar trend (Figure 11F). The Eagle Point conductivity sensor measurements slightly increase during each cold front event. The CTD conductivity measurements also increase during these events, aside from the measurements recorded from 1/28-1/30, which were the opposite. The change in the CTD conductivity sensor is likely due to biofouling of the instrument sensor, beginning around 2/08/2020, as discussed in more detail below.

Figure 12A shows wind speed, gusts (m/s) and wind direction (degrees) data taken from NOAA Eagle Point, TX station from the same dates that the CTD was deployed. The figure below (12B) overlays TSS on top of the NOAA wind data. The TSS concentrations spike for the cold front passages of 1/29-30 and 2/7-8, however, the TSS concentrations are very much lower for the cold front passages of 2/13-15, and 2/20 and overall, the TSS concentrations are suppressed for the time series starting on 2/08. When the pod was pulled, it was completely biofouled. The suppressed TSS concentrations from 2/08 to the end of the time series is likely suppressed due to biofouling.

Table 4: Water sample collection data from TAMUG Boat Basin and Texas Corinthians Yacht Club

Date	**TCYC TSS concentration**	**TRIN Pod TSS concentration**	**Percent Difference**
1/29/2020	20.6 gL^{-1}	21 gL^{-1}	2%
2/13/2020	12.2 gL^{-1}	10.7 gL^{-1}	12.2%
2/21/2020	11.3 gL^{-1}	12 gL^{-1}	5.8%

Table 4 shows the TSS concentrations from TCYC and from the TRIN pod site from the same days as well as the percent difference. In each case, the TSS concentrations are generally comparable, with the greatest percent difference being 12.2% for 2/13. However, when comparing TSS concentrations at the TRIN pod site to wind speed, from around 2/08 onward (Fig. 10), the TSS concentrations are greatly suppressed compared to the TSS concentrations during previous high wind events earlier in the time series. As mentioned above, significant biofouling appears to have started on 2/08, suggesting that the only reliable comparison for TSS between TCYC and the TRIN pod location is the 1/29 measurements, where the percent difference is only 2%. This would indicate that TCYC provides a fair estimate of suspended sediment concentrations for upper Galveston Bay, including Trinity Bay.

Figure 10: Wind speed, gusts (m/s) and wind direction (deg) vs. Time obtained from NOAA Eagle Point, TX station (10A), and Wind speed, gusts (m/s) and TSS (g/L) vs. Time (10B).

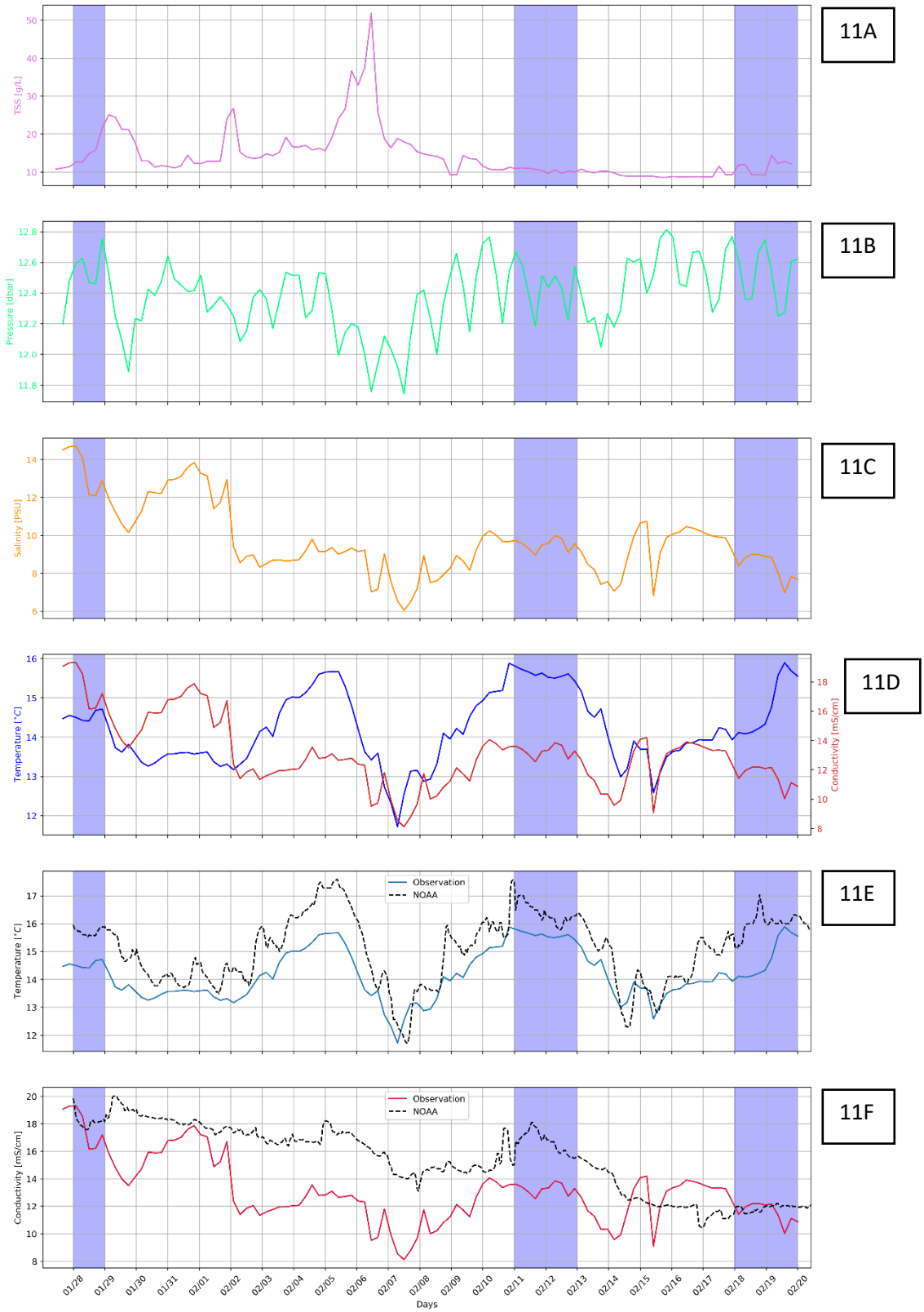

Figure 11: Data measured from the CTD deployed in Trinity Bay (Top to Bottom: TSS (12A), Pressure (12B), Salinity (12C) and Temperature and Conductivity (12D), Observed and NOAA temperature (12E), Observed and NOAA conductivity (12F) vs. Time.

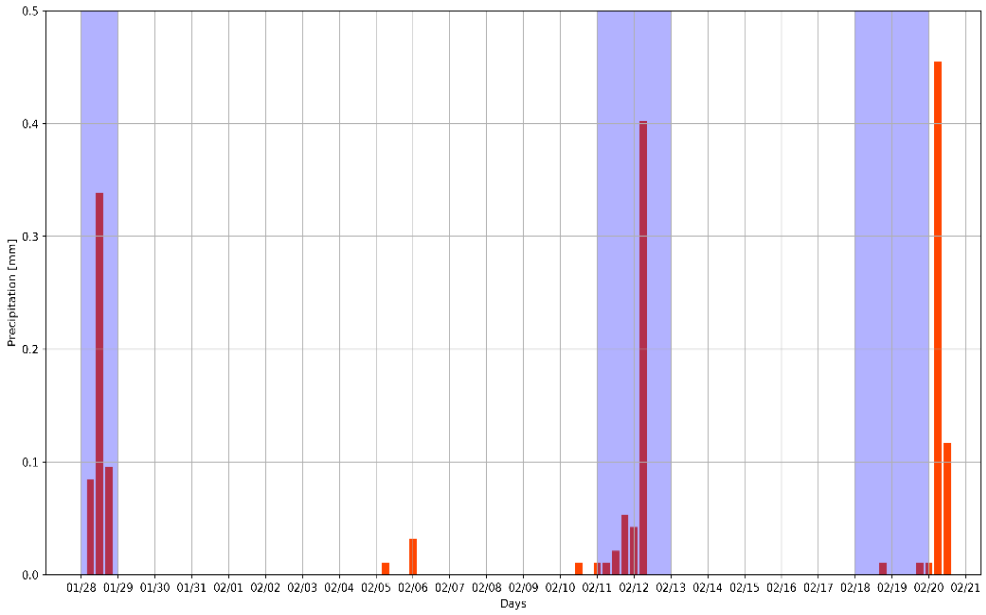

Figure 10: Total precipitation measured from USGS Moses Lake-Galveston Bay station near Texas City, TX for the months of January and February 2020.

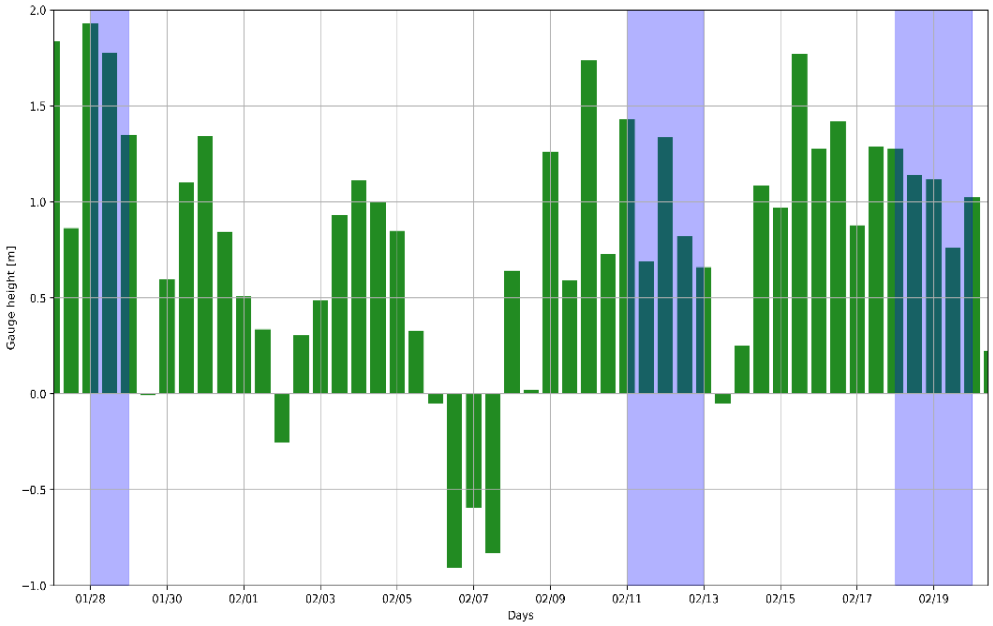

Figure 11: Stream gauge height measured from USGS Clear Creek station near Friendswood, TX for the months of January and February 2020.

5.3 Resident times of TSS

Table 5: ^{210}Pb Activity Concentrations (Bq/kg) of Sediment and Precipitation samples.

	Tide	TCYC	Tide	Boat Basin	Precipitation (OCSB Roof)
Dates		**Activity Concentration (Bq/kg)**		**Activity Concentration (Bq/kg)**	**Activity Concentration (Bq/kg)**
1/29/2020	in	33.654 ± 3.571	in	85.498 ± 9.287	1.378 ± 0.13
2/13/2020	out	66.442 ± 6.354		Not Collected	44.183 ± 5.197
2/21/2020	in	71.916 ± 7.740	in	62.119 ± 6.790	0.554 ± 0.0481

Table 6: ^{7}Be Activity Concentrations (Bq/kg) of Sediment and Precipitation samples.

	Tide	TCYC	Tide	Boat Basin	Precipitation (OCSB Roof)
Dates		**Activity Concentration (Bq/kg)**		**Activity Concentration (Bq/kg)**	**Activity Concentration (Bq/kg)**
1/29/2020	in	97.550 ± 3.397	in	185.474 ± 8.743	38.736 ± 2.312
2/13/2020	out	203.822 ± 5.914		Not Collected	481.894 ± 7.418
2/21/2020	in	116.720 ± 6.550	in	78.883 ± 5.187	63.321 ± 2.531

Activity concentrations of ^{210}Pb and ^{7}Be in Tables 5 and 6 are obtained from the Germanium gamma detector for sediment samples in both TCYC and the TAMUG Boat Basin along with precipitation samples from the OCSB roof. ^{7}Be activity concentrations in all samples are higher than ^{210}Pb. This is attributed to the larger injection of ^{7}Be into the stratosphere, which enhances the stratospheric-tropospheric exchange (Baskaran et al., 1993, Olsen et al., 1985). Another reason for the differences between ^{7}Be and ^{210}Pb fluxes in the spring is linked to the proportions of scavenging from stratiform and convective clouds (Baskaran et al., 1993). The activity concentration of precipitation tends to vary widely between each cold front event. This is due to the fluctuation of rainfall collected between cold front events (Table 2), where the largest amount of rainfall correlates to the highest activity concentration of both ^{7}Be and ^{210}Pb. Activity concentrations within the suspended sediment are higher than precipitation, aside from the samples collected on 2/13/2020.

In relation to tidal phases, it is only possible to compare flood versus ebb tide at TCYC. For both isotopes, activity concentrations are higher during the ebb tide. The ebb tide causes more rain/isotopes to

come into contact with the sampling site since cold fronts generally come from the north. In addition to this observation, it is important to note that there was also the largest volume of rainfall during the cold front (Table 2). The combination of the ebb tidal phase and large volume of rainfall can attribute to a higher activity concentration of both isotopes.

Table 4: $^{7}Be/^{210}Pb_{xs}$ ratios ± standard error calculated from activity concentrations of precipitation, suspended sediment samples with calculated suspended sediment age and percentage new sediment.

	January 29, 2020			February 13, 2020			February 21, 2020		
Source	**$^{7}Be/^{210}Pb_{xs}$**	**Age (d)**	**% New**	**$^{7}Be/^{210}Pb_{xs}$**	**Age (d)**	**% New**	**$^{7}Be/^{210}Pb_{xs}$**	**Age (d)**	**% New**
Upper Bay	4.96 ± .0056	133.77 ± 177.97	17.65 ± 9.95	4.00 ± .762	77.37 ± 6.50	36.68 ± 108.776	2.59 ± .0056	292.17 ± 268.5	2.27 ± 3.08
Lower Bay	28.11 ± .0074	166.91 ± 156.75	11.49 ± 13.12	Not Collected			1.97 ± .0005	313.03 ± 283.22	1.73 ± 2.54

Based on Matisoff et al., (2005), the $^{7}Be/^{210}Pb_{xs}$ ratio is expected to decrease as isotopes travel through a system (Upper Bay to Lower Bay). This is true for the cold front sampled on 2/21/2020, but is much different for the first cold front on 1/29/2020 where the ratio increases by a factor of 4 in the lower bay. Whereas, the age of the sediment does increase closer to the mouth of the Bay, confirming one hypothesis made. In addition to this, Matisoff et al. (2005) states that the percent/fraction of new sediment should decrease as age increases which is seen in Table 6. Unfortunately, a Lower Bay sample was not collected for 2/13/2020. The age of the Upper Bay suspended sediment for second cold front event (2/13/2020) is the lowest compared to the two other events. Additionally, the second storm also has the highest percentage of new sediment added to the water column. This is likely due to the larger volume of precipitation that covered the bay introducing the highest activity concentrations of both isotopes. The differences in these two values may correlate. The low age could be due to more new sediment and isotopes being introduced into the bottom sediment due to the large influx of rainfall. The final storm (2/21/2020) has the smallest isotopes ratio and percent new sediment, which is likely due to the limited rainfall flux during this cold front event. It also has the oldest age in both the upper bay and lower bay and validates Matisoff et al., (2005) expectation mentioned above. The older age in both samples can be linked to older ^{7}Be (measured on 1/29/2020 & 2/13/2020) still being within its half-life. This older sediment is still trapped within the bottom sediment and becomes resuspended from the bottom water and

mixes with new ^{7}Be injected from the rain event. Since there was limited rainfall, the older ^{7}Be overpowers the new. This study validates the use of Matisoff et al., (2005)'s method to determine the age of sediment in Galveston Bay.

5. Conclusion

The residence times/age of suspended sediment increases as suspended sediment moves towards the mouth of the bay. This study validates the use of Matisoff et al., (2005) method to determine the age and transport time of suspended sediment in Galveston Bay. Based on each individual storm, activity concentrations are higher in the lower bay than in the upper bay, aside from the last measured cold front (2/21/2020), which is attributed to the difference between ^{7}Be and ^{210}Pb fluxes in spring. Additionally, in every measured sample, ^{7}Be activity concentrations are higher than ^{210}Pb. In order to fully understand the activity concentrations of ^{7}Be and ^{210}Pb when used to find residence time/age of suspended sediment, additional samples need to be taken during the fall cold front season (October-December).

TSS concentrations are higher in the Upper Bay versus the Lower Bay when winds are stronger than 7 m/s. Otherwise, TSS concentrations are nearly the same when winds are below 7 m/s. This leads to the assumption that stronger winds are attributed to higher TSS concentrations due to more sediment being resuspended from the bottom. This may also, at least in part, be a result of the bay sediment in the Upper Bay having a higher clay content than the sediment within the Lower Bay. Ebb tide has higher TSS concentrations when there is a north wind in the upper bay (2/13/2020 vs. 2/21/2020), likely the result of the addition of tidal current coupled with wind waves and wind driven current imparting greater shear stress to the seabed. For both the Upper Bay and Lower Bay during corresponding wind speeds, TSS concentrations are observed to be higher during ebb tide. This is attributed to the tide bringing more fine sediment from northern parts of the bay to both sites. Comparing these two, TSS concentrations are highest at TCYC with an ebb tide. TSS concentrations are observed to be higher during cold fronts than tropical storms based on the single data measurement collected. This is attributed to the direction of wind, size and duration of storms, where cold fronts affect a larger spatial area, such as the entirety of Galveston Bay.

This study demonstrated the possibility of using ^{210}Pb and ^{7}Be to age date the suspended sediment in various locations within Galveston Bay. This allows for a more thorough understanding of the sediment transport within the bay along with the particle/pollutant residence times. Additionally, TSS data shows that cold fronts accompanied with strong wind speed and a northern wind are significant mechanisms for resuspending/remobilizing sediment in shallow estuaries.

6. Future Plans

In order to further validate the method created by Matisoff et al. (2005), more samples at both sites need to be collected. Also, adding more sites within the upper bay would create a more thorough understanding of suspended sediment in Galveston Bay. Being able to collect more samples during the main cold front occurrences (October-March) and tropical storms/hurricanes will complete the study. The ability to measure TSS concentrations and isotope ratios from the collection of these sample during cold fronts and tropical storms/hurricanes allows for a complete understanding of sediment remobilization during both types of meteorological events.

References

Baskaran, M., Coleman, C., & Santschi, P. (1993). *Atmospheric Depositional Fluxes of 7Be and 210Pb at Galveston and College Station, Texas.*

Baskaran, M., & Santschi, P. (1993). *The role of particles and colloids in the transport of radionuclides in coastal environments of Texas.*

Baskaran, M., & Swarzenski, P. (2007). Seasonal variations on the residence times and partitioning of short-lived radionuclides (234Th, 7Be and 210Pb) and depositional fluxes of 7Be and 210Pb in Tampa Bay, Florida. *Marine Chemistry, 104*(1-2), 27-42.

Booth, J., Miller, R., Mckee, B., & Leathers, R. (2000). *Radio/Infrared/Optical Sensors Branch, 4555 Overlook Ave.* SW.

Carlin, J., Lee, G., Dellapenna, T., & Laverty, P. (2016). Sediment resuspension by wind, waves, and currents during meteorological frontal passages in a micro-tidal lagoon. *Estuarine, Coastal and Shelf Science, 172*, 24-33.

Cox, D., Asce, M., Tissot, P., & Michaud, P. (n.d.). Water Level Observations and Short-Term Predictions Including Meteorological Events for Entrance of Galveston Bay, Texas.

Dellapenna, T., Allison, M., Gill, G., Lehman, R., & Warnken, K. (2006). The impact of shrimp trawling and associated sediment resuspension in mud dominated, shallow estuaries. *Estuarine, Coastal and Shelf Science, 69*(3-4), 519-530.

Dellapenna, T. M., Hoelscher, C. E., Hill, L., Al Mukaimi, M., Knap, A., 2020. How tropical cyclone flooding caused erosion and dispersal of mercury-contaminated sediment in an urban estuary: the impact of Hurricane Harvey on Buffalo Bayou and the San Jacinto Estuary, Galveston Bay, USA. *Science of the Total Environment* (in press). https://doi.org/10.1016/j.scitotenv.2020.141226

Du, J., Park, K., Yu, X., Zhang, Y.J. and Ye, F., 2020. Massive pollutants released to Galveston Bay during Hurricane Harvey: Understanding their retention and pathway using Lagrangian numerical simulations. *Science of The Total Environment*, *704*: 135364. https://doi.org/10.1016/j.scitotenv.2019.135364

Evrard, O., Laceby, J., Huon, S., Lefèvre, I., Sengtaheuanghoung, O., & Ribolzi, O. (2016). Combining multiple fallout radionuclides (137Cs, 7Be, 210Pbxs) to investigate temporal sediment source dynamics in tropical, ephemeral riverine systems. *Journal of Soils and Sediments, 16*(3), 1130-1144.

Ha, H., & Park, K. (2012). High-resolution comparison of sediment dynamics under different forcing conditions in the bottom boundary layer of a shallow, micro-tidal estuary. *Journal of Geophysical Research: Oceans, 117*(6).

Haby, M. G., Miget, R. J., & Falconer, L. L. (2009). *Hurricane Damage Sustained by the Oyster Industry and the Oyster Reefs Across the Galveston Bay System with Recovery Recommendations. College Station, TX.* TAMU-SG-09-201.: The Texas A&M University System. 51 pp.

Mabit, L., & Blake, W. (2019). *Assessing recent soil erosion rates through the use of beryllium-7 (Be-7).* Springer International Publishing.

Matisoff, G., Wilson, C., & Whiting, P. (2005). The 7Be/210PbXS ratio as an indicator of suspended sediment age or fraction new sediment in suspension. *Earth Surface Processes and Landforms, 30*(9), 1191-1201.

Minella, J. P., Merten, G. H., Reichert, J. M., & Clarke, R. T. (2008). Estimating suspended sediment concentrations from turbidity measurements and the calibration problem. *Hydrological Processes: An International Journal*, *22*(12), 1819-1830.

Moeller, C., Huht, O., Robertst, H., Gumley, L., Paul Menzeltt, W., & Abstracti Moeller, A. (1993). *Response of Louisiana Coastal Environments to a Cold Front Passage.*

Olsen, C., Larsen, I., Lowry, P., Cutshall, N., & Nichols, M. (1986). Geochemistry and deposition of 7Be in river-estuarine and coastal waters. *Journal of Geophysical Research, 91*(Cl), 896-908.

Olsen, C., Larsen, I., Lowry, P., Cutshall, N., Todd, J., Wong, G., & Casey, W. (1985). *Atmospheric Fluxes and Marsh-Soil Inventories of 7Be and 2xøpb.*

Perez, B., Day, J., Rouse, L., Shaw, R., & Wang, M. (2000). Influence of Atchafalaya River discharge and winter frontal passage on suspended sediment concentration and flux in Fourleague Bay, Louisiana. *Estuarine, Coastal and Shelf Science, 50*(2), 271-290.

Region, B., Author, U., Walker, N., & Hammack, A. (2000). *Impacts of Winter Storms on Circulation and Sediment Transport: Atchafalaya-Vermilion.*

Residence time. (2020). In *Dictionary.com*. Retrieved July 21, 2020, from https://www.dictionary.com/browse/residence-time

Saari, H., Schmidt, S., Castaing, P., Blanc, G., Sautour, B., Masson, O., & Cochran, J. (2010). The particulate 7Be/210Pbxs and 234Th/210Pbxs activity ratios as tracers for tidal-to-seasonal particle dynamics in the Gironde estuary (France): Implications for the budget of particle-associated contaminants. *Science of the Total Environment, 408*(20), 4784-4794.

Sanford, L., & Halka, J. (1993). *Assessing the paradigm of mutually exclusive erosion and deposition of mud, with examples from upper Chesapeake Bay.*

Stunz, G. W., Minello, T. J., & Rozas, L. P. (2010). Relative value of oyster reef as habitat for estuarine nekton in Galveston Bay, Texas. *Marine Ecology Progress Series*, 406, 147–159. https://doi.org/10.3354/meps08556

Taylor, A., Blake, W., Smith, H., Mabit, L., & Keith-Roach, M. (2013). Assumptions and challenges in the use of fallout beryllium-7 as a soil and sediment tracer in river basins. *Earth-Science Reviews, 126*, 85. Elsevier B.V.

545 Turner, A., & Millward, G. (2002). Suspended particles: Their role in Estuarine biogeochemical cycles. *Estuarine,*
546 *Coastal and Shelf Science, 55*(6), 857-883.

547

Appendix E

Science of the Total Environment 748 (2020) 141226

Contents lists available at ScienceDirect

Science of the Total Environment

journal homepage: www.elsevier.com/locate/scitotenv

How tropical cyclone flooding caused erosion and dispersal of mercury-contaminated sediment in an urban estuary: The impact of Hurricane Harvey on Buffalo Bayou and the San Jacinto Estuary, Galveston Bay, USA

Timothy M. Dellapenna [a,b,*], Christena Hoelscher [a,b], Lisa Hill [b], Mohammad E. Al Mukaimi [c], Anthony Knap [a,d]

[a] Department of Oceanography, Texas A&M University, 3146 TAMU, College Station, TX 77843, USA
[b] Department of Marine Sciences, Texas A&M University-Galveston Campus, 1001 Texas Clipper Road, Galveston, TX 77554, USA
[c] Department of Marine Science, Kuwait University, Marine Science Center, Al Fintas Safat 13060, Kuwait
[d] Geochemical and Environmental Research Group (GERG), Texas A&M University, 833 Graham Road, College Station, TX 77845, USA

HIGHLIGHTS

- Hurricane Harvey caused massive flooding of the San Jacinto Estuary (SJE).
- Harvey eroded/deposited 16.4 × 106/ 7.73 × 106 tons of sediment from SJE.
- Eroded sediment sourced at least 2/3.9 tons of Hg from SJE/Buffalo Bayou.
- Main source of Hg is an industrial waste-water outfall in Patrick Bayou.
- The Harvey deposit in the SJE contains ~1 ton of Hg sourced from Buffalo Bayou.

GRAPHICAL ABSTRACT

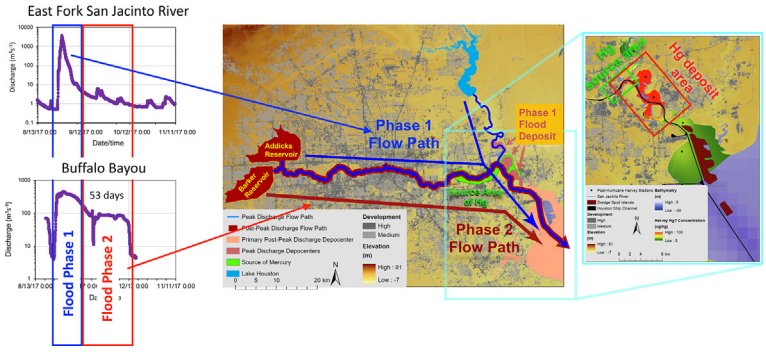

ARTICLE INFO

Article history:
Received 23 April 2020
Received in revised form 21 July 2020
Accepted 23 July 2020
Available online 31 July 2020

Editor: Damia Barcelo

Keywords:
Hurricane Harvey
Galveston Bay
San Jacinto River
Mercury
Flood deposit
Legacy contaminants

ABSTRACT

Hurricane Harvey (Harvey), a slow-moving storm, struck the Texas coast as a category 4 hurricane. Over the course of 53 days, the floodwaters of Harvey delivered 14×10^9 m^3 of freshwater to Galveston Bay. This resulted in record flooding of Houston bayous and waterways, all of which drained into the San Jacinto Estuary (SJE,) with its main tributaries being Buffalo Bayou and the San Jacinto River. The lower SJE and lower Buffalo Bayou has experienced up to 3 m of land subsidence in the past 100 years and, as a result, prior to Hurricane Harvey, up to 2 m of sediment within the upper seabed contained an archive of high concentrations of Total Hg (HgT) and other particle-bound and porewater contaminants. Within the SJE, Harvey eroded at least 48 cm of the sediment column, resulting in the transport of an estimated 16.4×10^6 tons of sediment and at least 2 tons of Hg into Galveston Bay. This eroded sediment was replaced by a Harvey storm deposit of 7.73×10^6 tons of sediment and 0.96 tons within the SJE, mostly sourced from Buffalo Bayou. Considering that the frequency of slow-moving tropical cyclones capable of delivering devastating rainfall may be increasing, then one can expect that delivery of Hg and other contaminants from the archived sediment within urbanized estuaries will increase and that what happened during Harvey is a harbinger of what is to come.

Abbreviations: BB, Buffalo Bayou; HgT, Total Mercury; SJE, San Jacinto Estuary; ng g^{-1}, nanograms per gram.

* Corresponding author at: Department of Oceanography, Texas A&M University, 3146 TAMU, College Station, TX 77843, USA.
E-mail addresses: dellapet@tamug.edu (T.M. Dellapenna), tknap@geos.tamu.edu (A. Knap).

https://doi.org/10.1016/j.scitotenv.2020.141226

1. Introduction

Many of the world's urbanized estuaries and deltas are experiencing elevated rates of subsidence (Jelgersma, 1996; Syvitski et al., 2009; Tessler et al., 2015; Al Mukaimi et al., 2018a), which can lead to the archiving of legacy contaminants in their sediments (Uncles et al., 1988; Olsen et al., 1993; Kennish, 2002; Swales et al., 2002;). If these legacy contaminants are buried by a few decimeters of sediment, they are generally believed to be buried deep enough with the seabed to no longer be susceptible to erosion (e.g. Cutshall et al., 1981; Olsen et al., 1993). However, these legacy contaminants can also be "environmental time bombs" if they do get eroded because they will then also be re-introduced to the water column where they can be broadly dispersed and detrimentally impact ecosystems and the environment. Numerous published studies have addressed the erosion of legacy contaminants within drainage basins, flood plains and river beds (e.g. Macklin et al., 1997; Turner et al., 2008; Ciszewski and Grygar, 2016) as well as within coastal landfills (O'Shea et al., 2018) and coastal mining sites (Ayuso et al., 2013). In addition, there are also numerous studies addressing the re-distribution of contaminated surficial sediments within estuaries (e.g. Cave et al., 2005; Schoellhamer et al., 2007; de Souza Machado et al., 2016; Rodriguez-Iruretagoiena et al., 2016), and the public health risk this exposure plays (Bera et al., 2019; Knap and Rusyn, 2016; Plumlee et al., 2013), however, there is a paucity of studies addressing the erosion of more deeply buried (i.e., deeper than a decimeter or more) legacy contaminants within an estuary, despite their potential existence within rapidly subsiding estuaries. This study adds to our understanding of how large storms and intense flooding within heavily industrialized and urbanized estuaries can erode nearly 0.5 cm of the bay bottom, and re-introduce and disperse tons of legacy Hg into surface sediments and the water column. Here, we assess the impact of unprecedented flooding due to Hurricane Harvey on the upper reaches of Galveston Bay, within Buffalo Bayou and the San Jacinto Estuary where there is a well-documented inventory of legacy contaminants buried down to depths greater than 50 cm (Al Mukaimi et al., 2018a).

Buffalo Bayou flows 75 km, from the Barker and Addicks reservoirs through the heart of metropolitan Houston and empties into the SJE, which then flows into Galveston Bay (Fig. 1). Houston is the fifth-largest metropolitan area in the United States, (population of 7 million) and is the fourth-largest city in the US. Houston hosts the second-largest petrochemical complex in the US and second in the world (Morse et al., 1993; Santschi et al., 2001). The Port of Houston is the second-largest seaport in the U.S. in terms of total shipping tonnage (Chambers et al., 2018). Galveston Bay and the SJE are micro-tidal, with a tidal 0.5–0.7 m tidal range (Armstrong, 1982; Solis and Powell, 1999). The bay is considered to be meteorologically dominated, given its small tides, shallow depths, and high susceptibility to wind forces (Solis and

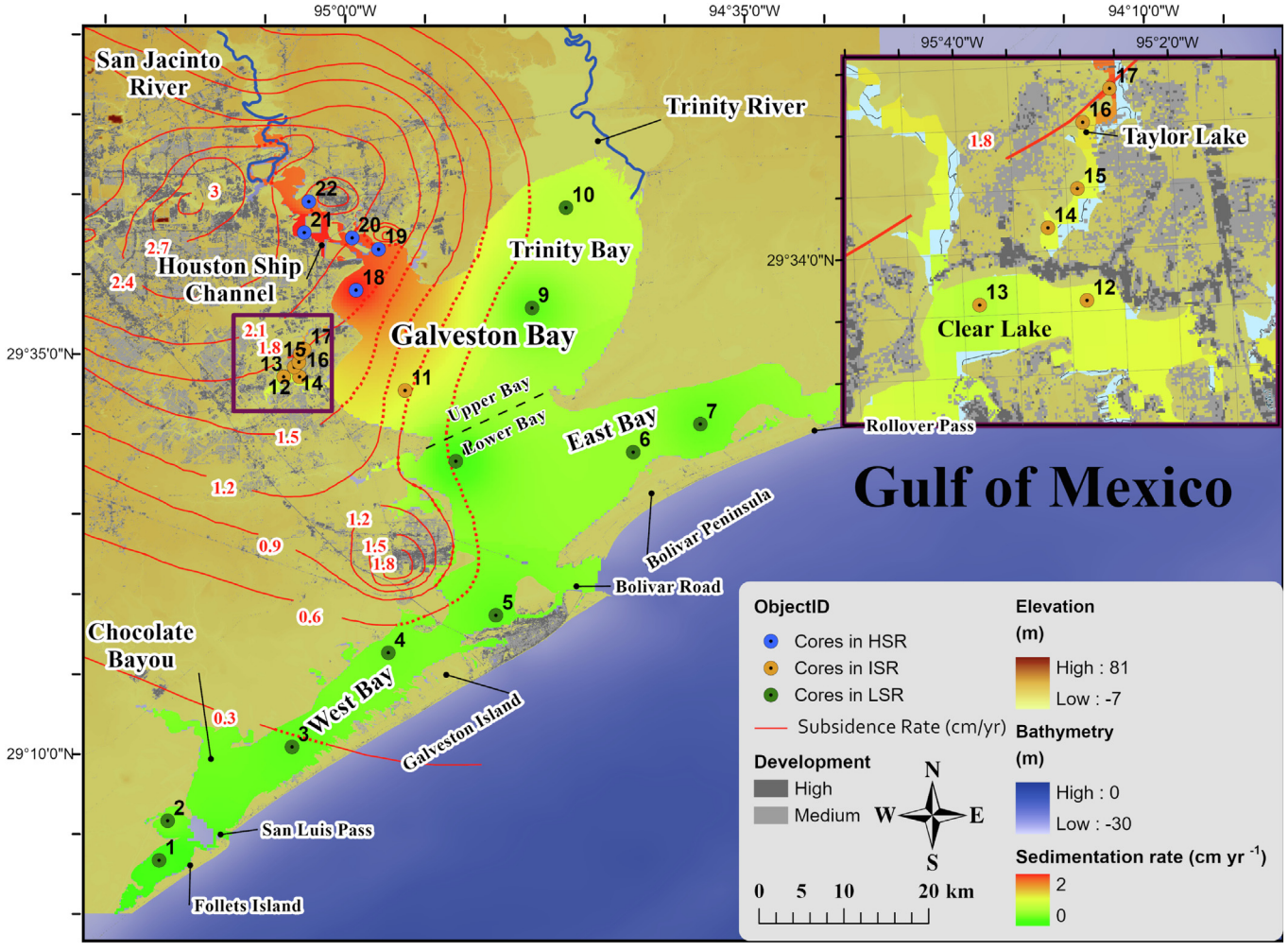

Fig. 1. Galveston Bay subsidence and sedimentation rate map contour plot (red line) of subsidence (meters) between 1906 and 2000 (HGSD, 2008). The gray shaded area represents the Trinity River incised valley (Rodriguez et al., 2005). Note, the highest subsidence was within the San Jacinto Estuary and Buffalo, with subsidence of 2.5–3.0 m (~3 cm y^{-1}) and sedimentation rates averaging 2 cm y^{-1} indicating that although there were extremely elevated sedimentation rates, sedimentation did not keep pace with subsidence (from Al Mukaimi et al., 2018a). (For interpretation of the references to color in this figure legend, the reader is referred to the web version of this article.)

Powell, 1999; Ward, 1980), with cold fronts driving much of the sediment resuspension and transport (Carlin et al., 2016).

Elevated groundwater was withdrawn to both support the expanding population of metropolitan Houston as well as the growing petrochemical complex. This has resulted in elevated land subsidence across much of both greater Houston and also upper Galveston Bay (Fig. 2), with as much as 3 m of subsidence since 1900 focus the area of lower Buffalo Bayou, the San Jacinto Estuary (SJE) and upper Galveston Bay, as the Houston Petrochemical complex (Coplin and Galloway, 1999; HGSD, 2013). Al Mukaimi et al. (2018a) addressed the question of whether sedimentation kept pace with subsidence and found that within the lower SJE, where subsidence rates averaged 3 cm yr^{-1}, sedimentation was at half of this rate, averaging 1.5 cm yr^{-1}. Al Mukaimi et al. (2018b) found that the elevated subsidence within the lower SJE resulted in the elevated preservation of legacy contaminants, including Hg, Pb, Ni, and Zn. In sediment core C-22, a peak in HgT of 2374 ng g^{-1} was found at 77 cm within the core and elevated HgT concentrations were found as deep as 110 cm (Fig. 3) with background concentrations of HgT between 20 and 50 ng g^{-1} throughout Galveston Bay.

Mercury (Hg) is one of the most detrimental global aquatic contaminants (Bank, 2012; Liu et al., 2011). In marine environments, Hg bioaccumulates as methyl mercury, contaminates seafood, and thus poses a human health hazard (Di Leonardo et al., 2006). There are likely numerous sources of Hg within the Galveston Bay drainage basin, including atmospheric outfall from coal combustion, effluent from wastewater treatment, agricultural runoff, and various industrial runoffs (Al Mukaimi et al., 2018b). However, historically, the greatest, and likely the dominant source of Hg within the drainage basin appears to be industrial wastewater runoff from Patrick Bayou (PB), a small tributary of Buffalo Bayou, with a water surface area of 0.18 km^2, located 4 km upstream from the confluence of Buffalo Bayou and the SJE. Patrick Bayou is a US Environmental Protection Agency (EPA) Superfund Site for Polyaromatic Hydrocarbons (PAHs), Polychlorinated Biphenyls (PCBs), Dioxins, Hg, and several other industrial contaminants (US EPA, 2017). Industrial wastewater discharge into PB from a Chloralkali plant located within Patrick Bayou is listed by the EPA as the likely source of the contamination (US EPA, 2017). The Texas Natural Resources Conservation Commission (TNRCC) reported that during a site inspection in 2000, sediment samples collected in PB had HgT levels as high as 41,500 ng g^{-1}. Patrick Bayou is located in an area that has experienced over 3 m of subsidence. A summary of a report from the US EPA was found online (HGAC, 2012) showing results of a sediment core collected upstream of the bridge in PB, directly in front of the outfall. A profile of HgT shows peak HgT concentration at ~130 cm depth and peak PCB's at 100 cm, indicating over 1.5 m of archived legacy contamination within Patrick Bayou.

Al Mukaimi et al. (2018a) investigating the historical input of Total Mercury (HgT) into Galveston Bay (Fig. 4A). In this study, they found that surface HgT concentrations vary widely from site to site, ranging from between 6 and 162 ng g^{-1}, with an average of 50.0 ng g^{-1}, generally following the previously reported range of 10–280 ng g^{-1} (Morse et al., 1993; Santschi et al., 2001). Al Mukaimi et al. (2018b) also

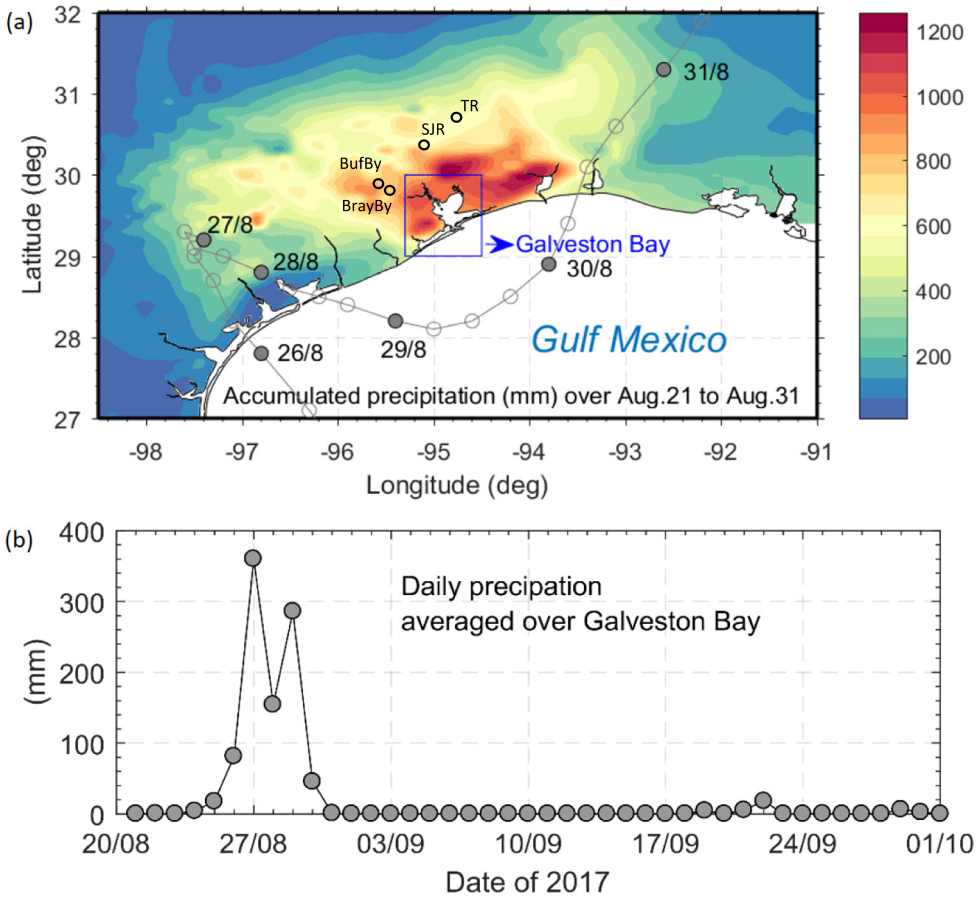

Fig. 2. Hurricane Harvey Rainfall for Metropolitan Houston and eastern Texas. (a) Accumulated precipitation during Hurricane Harvey between August 21 and 31, 2017 and (b) daily precipitation averaged over Galveston Bay (30 weather stations). In (a), the 6-hourly track (all times in UTC) of Hurricane Harvey, based on data from National Hurricane Center (https://www.nhc.noaa.gov), is shown with circles. Precipitation data in (b) are based on daily records extracted from the Global Historical Climatology Network (https://www.ncdc.noaa.gov) (after Du et al., 2019a).

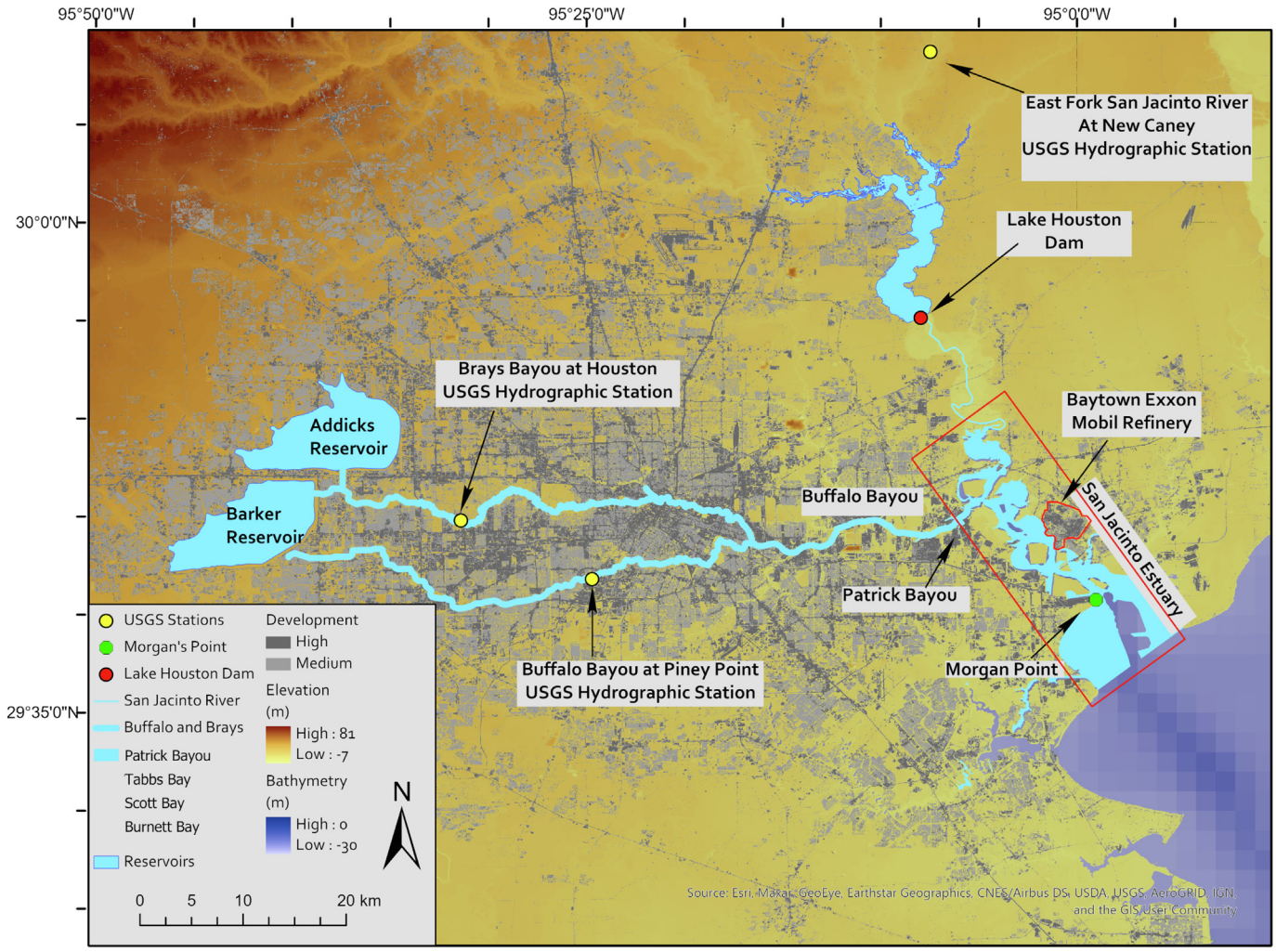

Fig. 3. Base map of the study area. Base map showing the location of the Addicks and Barker Reservoirs as well as the location of Buffalo Bayou, Patrick Bayou, and the San Jacinto Estuary.

documented background concentrations of HgT, in deeper sections of the core (Fig. 5A), likely deposited during the pre-Industrial period of the bay, ranged range from 8 to 20 ng g^{-1}. NOAA considers levels of 4–51 ng g^{-1} as background conditions (Buchman, 2008).

Hurricane Harvey (Harvey) struck the Texas coast between 25 and 27 August 2017, making landfall as a category 4 hurricane, and delivering between 76.2 and 127 cm of rain to the Houston Metropolitan area and the drainage basin of Galveston Bay (Fig. 2; NOAA, 2017). Over the course of 44 days, the floodwaters of Harvey delivered 14×10^9 m^3 of freshwater to Galveston Bay, a volume equivalent to 3.7 times the volume of the entire bay (Du et al., 2019a, 2019b). This record rainfall resulted in unprecedented flooding of Houston bayous and waterways, all of which drained into the SJE, with its main tributaries being Buffalo Bayou and the San Jacinto River. The associated river discharge delivered 149×10^6 tons of sediment to the bay, which constitutes 35 yrs. of normal fluvial sediment yield (Du et al., 2019a, 2019b).

Harvey was a slow-moving tropical cyclone. The amount of precipitation a tropical cyclone delivers is inversely proportional to the translational speed of the storm (Kossin, 2018), thus, slower-moving storms deliver more precipitation than fast-moving storms, having the potential to deliver substantially greater volumes of floodwaters. Since 1949, globally, there has been a 10% decrease in the translation speed of storms (Kossin, 2018). With an increase in anthropogenically enhanced climate change, there is also a trend towards an increase in persistent weather extremes (Mann et al., 2017), an increase in the frequency and intensity of tropical cyclones (Held and Soden, 2006; He and Soden, 2015; Vecchi and Soden, 2007; Vecchi et al., 2006, and He et al., 2017), and, with an increase in global temperature, there is also an anticipated increase in the amount of rain associated with tropical cyclones (Kossin, 2018; Walsh et al., 2016). These slow-moving storms can cause catastrophic flooding, as was the case with Harvey (2017) and more recently Hurricane Florence (2018), which struck Wilmington, NC. When this intense precipitation falls within the watersheds of urbanized/industrialized estuaries, the associated floods increase the risk of erosion and dispersal of legacy contaminated sediments (e.g. Santschi et al., 2001). If the urbanized/industrialized estuary has been subjected to elevated subsidence rates, then there is an even greater likelihood that sediments within the urban river/estuary contain an archive of elevated levels of legacy contaminants, which are potentially available for erosion and dispersal. The impact of Harvey provides the opportunity to investigate what happens when a heavily industrialized estuary, which has undergone significant land subsidence and which sediment contains an archived of legacy contaminants, is hit by a major flood event associated with a slow-moving hurricane. This paper reports on how the flooding associated with Harvey eroded and transported massive amounts of mercury contaminated sediment within Buffalo Bayou, Patrick Bayou, and the SJE. To address this question, results from vibra-cores collected and analyzed pre-Harvey are compared to results from vibra-cores and push cores collected post-Harvey within the SJE and the collection of vibra-cores in Patrick Bayou, a tributary of lower Buffalo Bayou.

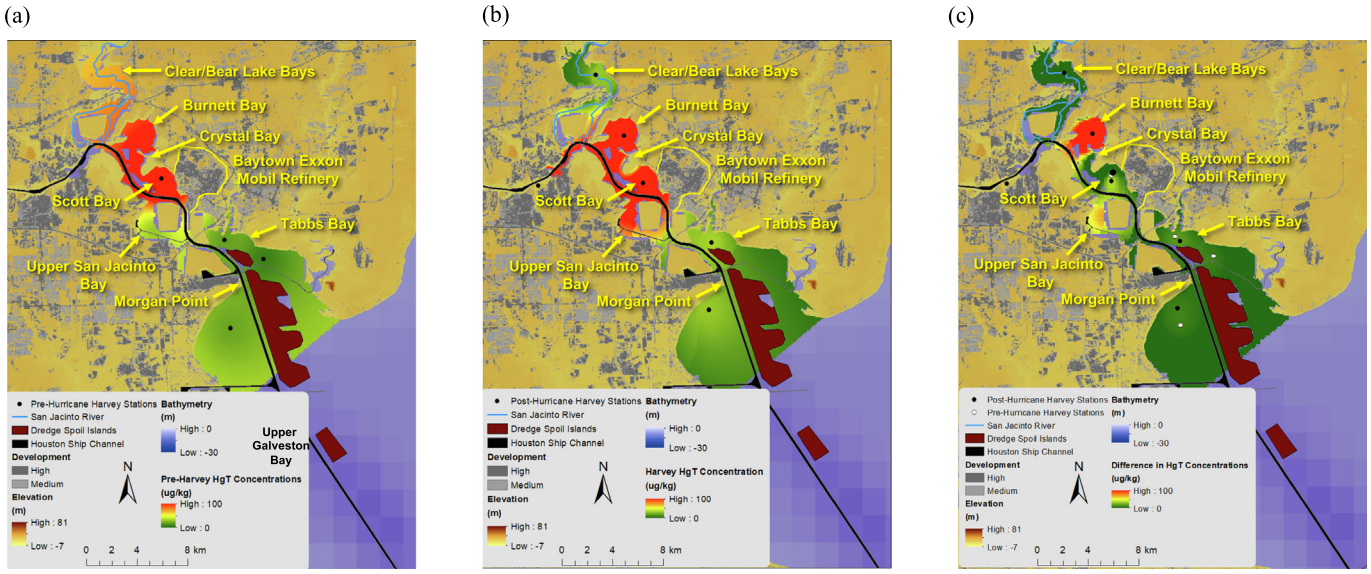

Fig. 4. Surface Sediment Total-Hg (HgT) maps for the San Jacinto Estuary (SJE). A) The pre-Harvey HgT Concentrations map for surface sediment is from Al Mukaimi et al. (2018a) and shows that the highest concentration of HgT is centered around Burnett and Scott Bay, Buffalo Bayou was not sampled pre-Harvey. B) Post Harvey HgT shows again that the highest concentrations are in Burnett and Scott Bay. Note, the map scale only goes up to 100 ng g^{-1}, but the surface sediment in Burnett and Scott Bays have HgT concentration of 670 and 195, ng g^{-1}, respectively. C) shows the HgT Difference maps and shows that the greatest enrichment of HgT was in Burnett Bay and the enrichment becomes progressively southward towards Galveston Bay. HgT is depleted in the Harvey deposit northward upstream of the confluence of Buffalo Bayou and the SJE, indicating that the source of HgT was from Buffalo Bayou and not the San Jacinto River.

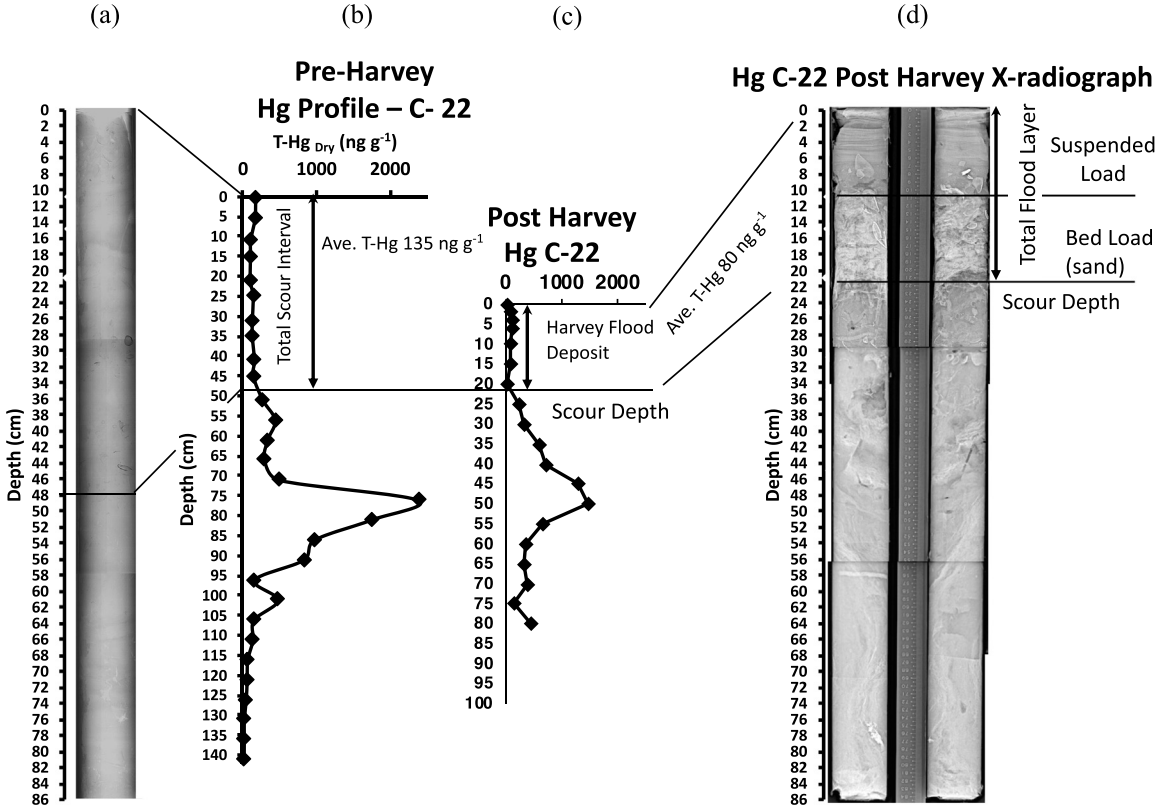

Fig. 5. Comparison of pre- and post-Hurricane Harvey core C-22 from Scott Bay. (a) Pre-Harvey Total Hg (HgT) sediment profile and (b) post-Harvey HgT sediment profile, both from Al Mukaimi et al. (2018a). (c) Hg profile and (d) x-radiograph from post-Harvey C-22. The peak HgT was used to correlate between cores. When comparing the pre-Harvey (a) and post-Harvey (c) HgT profile and x-radiographs (b) and (c), it is revealed that 48 cm of sediment was eroded. The post-Harvey x-radiograph (d) reveals an erosional surface, above which sits a shell and sand layer, which represents the flood bedload deposit. Above this, a mud dominated layer representing the suspended load deposit. Note an increase in average HgT in the Harvey deposit of 197 ng g^{-1} when compared to the pre-Harvey HgT of 80 ng g^{-1}.

2. Material and methods

2.1. Data collection and core processing

Core 22 and Patrick Bayou Core 1 were collected as vibra-cores using a 7.6 cm diameter aluminum barrels. The vibra-cores were collected using an Oztec vibra-coring head attached to a 7.6 cm diameter aluminum barrel, with core recovery ranging from 1 to 4 m. The cores were brought back to the lab, split axially, using power shears to cut the core barrel and wire used to cut the core. One half of the core was subsampled, with half of the core preserved under refrigeration for archival purposes. Core 22 was collected in August of 2012, and analyses of Core 22 are reported in Al Mukaimi et al. (2018a, 2018b). Patrick Bayou Core 1 was collected on May 8, 2019.

Push cores were collected using a repurposed Benthos® checkvalve pushcoring head, which was attached to an aluminum conduit with stainless steel hose-clamps and electrical tape. The conduit was in 1.5 m long sections that screwed together, with a maximum length of 5 m. The removable core barrels consist of 7.6 cm diameter polycarbonate tubes generally ranging in length from 0.3 to 0.6 m. During recovery, the pushcoring system was brought to the surface and the core barrels were capped while the end of the core was still in the water to prevent the loss of the cores from the check valve. While holding the core vertically, the bottom core cap was immediately sealed with electrical tape while still being kept vertical. Flourofoam was pushed into the core top so that it rested just above the sediment-water interface, the flourofoam was cut flush with the top of the core barrel and then the top of the core was sealed with a core cap and electrical tape and stored vertically for transport back to the lab.

None of the recovered cores showed any signs of degradation from transportation. The cores were stored in a cold room which is held at a constant temperature of 4 °C. X-radiographs were taken of all cores at an energy level of 64 kV and exposure time of 1.6 mAS with a portable Medison X-ray source and a Varian PaxScan® Amorphous Silicon Digital Imager.

After each core was x-rayed, the entire Harvey layer was extruded. In some cases, each one-centimeter interval was collected, in others, the entire interval was extruded as a single sample. For those for which the sediment was extruded into 1 cm intervals, a subsample of each interval of equivalent volume was combined to make a single Harvey sample and homogenized and subsamples of this were collected for Hg and grain size analyses. For those samples where the entire interval was sampled, the interval was homogenized and subsamples were collected for Hg, grain size distributions, and water content.

2.2. Water content and porosity

Samples (10 g) collected when the cores were sampled and were immediately placed in pre-weighed aluminum tins and kept in an oven at 50 °C for at least 24 h, and then re-weighed to determine water content. The porosity was calculated from the water content by estimating the salt content, using an average sediment density of 2.65 g cm^{-3}.

2.3. Total Mercury analysis

For the analysis of total mercury concentration (HgT) in the sediments, approximately 100 mg of dry and homogenized pulverized sediment samples at 5 cm intervals were analyzed using Direct Mercury Analyzer (DMA-80, Milestone SRL, Italy) which is compliant with U. S. EPA Method 7473 (EPA, 1998). The DMA-80 was calibrated using prepared standard solutions of mercury and the calibration curve was verified with Certified Reference Materials (CRM). In order to ensure precision, reliability, accuracy, and consistency of the sediment samples for the total Hg, three CRMs (MESS-3 Marine sediment (0.091 ± 0.009 mg l^{-1}, National Research Council of Canada), NIST 2702 Inorganics in Marine sediment (0.4474 ± 0.0069 mg l^{-1}, National Institute of Standards and Technology), and PACS-2 Marine sediment (3.04 ± 0.2 mg l^{-1}, National Research Council of Canada)) were used representing a different Hg range. Once the instrument was calibrated with liquid standard solutions, the calibration curve was verified with the three CRMs. Blanks and duplicates were analyzed every 10 samples to ensure accuracy. The results obtained from the CRMs were excellent and in good agreement within the certified range with an average recovery rate for MESS-3 of 97% ± 7% (Mean ± RSD, n = 137), NIST 2702 (96% ± 7% (Mean ± RSD, n = 43), and PACS-2 (97% ± 11% (Mean ± RSD, n = 64).

2.4. Geographic Information System (GIS) map preparations and volume and mass calculations

The maps used in this study were created using various ArcMap Pro 2.5.1 mapping tools. The basemaps were created using elevation data from the United States Geological Survey and bathymetry data (USGS, 2013) from the Texas Parks and Wildlife Department (TPWD, 2013). The development data was retrieved from NOAA (NOAA, 2016). The raw data set was inserted into ArcGIS and was reclassified so that only medium to high development is shown. The shoreline data was retrieved from the Texas Natural Resources Information System (TNRIS, 2014). Contours of the data were generated using the Inverse Distance Weighted (IDW) tool, which assumes that the influence of a variable decreases with distance.

The flood deposit volume was determined based on the contoured data for each sub-bay and converted to mass by assuming a water content of 70% and a sediment density of 2.65 g cm^3, which is the density of quartz. To estimate HgT masses for each sub-bay, an average concentration was used for each sub-bay and the concentration was multiplied by the mass of sediment within the sub-bay.

3. Results

3.1. Comparisons of vibracores and pushcores in San Jacinto Estuary

Bear Lake and Clear Lake are represented by SJRVC-1, which was collected in Clear Lake, 6 river km upstream from the confluence of the San Jacinto River and Buffalo Bayou, and is the only core collected upstream in the SJE upstream of Buffalo Bayou. The Harvey layer in SJRVC-1 was 6.25 cm thick and had a HgT concentration of 30 ng g^{-1}. Burnett Bay had a Harvey thickness of 31.5 cm and a surface HgT concentration of 670 ng g^{-1}.

The pre and post-Harvey Cores 22 were collected at a site within Scott Bay, which is a small, semi-enclosed bay within the SJE in an area where the average Relative Sea Level Rise rate for the past century is estimated to be 2.78 5 cm y^{-1} (Al Mukaimi et al., 2018a). In 2012, pre-Core 22 was collected and subsequently analyzed by Al Mukaimi et al. (2018a, 2018b) for down core concentrations of Hg, x-radiographs were collected as unsplit core x-rays, down core grain size distributions and ^{210}Pb geochronology was performed on the core (Fig. 5). Based on these analyses, it was determined that the average sediment accumulation on this core was 1.5 cm y^{-1}.

In the pre-Harvey Core 22, the x-radiographs and the grain size profiles reveal that the core is consistently composed of 90–98% mud with only 2–10% sand. In pre-Harvey Core 22, there is a prominent Hg spike in concentration of 2374 ng g^{-1} at 76 cm, according to Al Mukaimi et al. (2018b), this corresponds to a depositional event estimated to have happened around 1972. Above this spike, the concentration of Hg sharply decreases and at the surface, the Hg concentration is 162 ng g^{-1}.

In Post-Harvey Core 22, the x-radiograph was taken from a split core and reveals the presence of a 22 cm thick layer at the surface of the core. The base of this new layer is marked by an erosional surface above which is a basal deposit 12 cm thick consisting of shell gravel and sand. The shell layer included intact shells up to 2–3 cm long and coarse

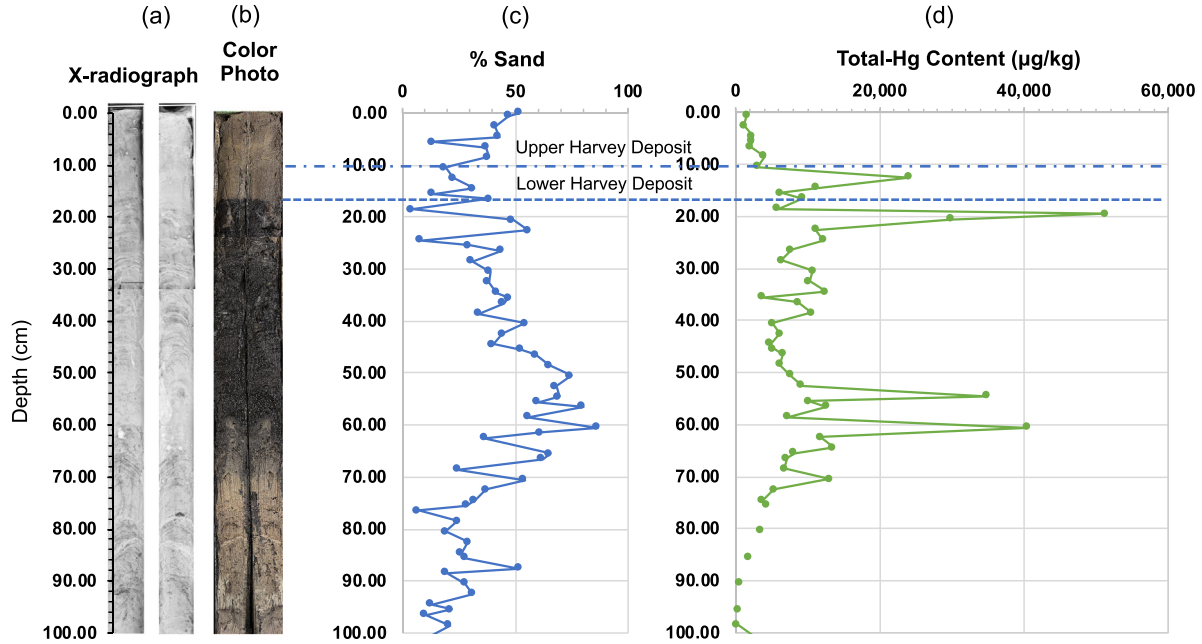

Fig. 6. (a) X-radiograph, (b) color photograph, (c) percent sand content, Total-Hg (HgT) content of Patrick Bayou Core 1. The color photograph (b) shows the Harvey layer as a brown, oxic layer, sitting atop a black, anoxic layer. The x-radiograph (a) reveals that the Harvey layer is generally featureless, suggesting rapid deposition. The percent sand content profile (c) and HgT (d) both reveal that there is a lower, mud dominated averaging 10,000 ng g^{-1}, whereas the upper Harvey layer is sand dominated and has a much lower HgT averaging 2255 ng g^{-1}. (For interpretation of the references to color in this figure legend, the reader is referred to the web version of this article.)

shell fragments. There is a sharp transition at 10 cm in the core, above which there is a layer of well-laminated mud, with sandy laminations, the average sand content of this interval is 25%. This upper 22 cm thick layer found in post-Harvey Core 22 is interpreted as the Harvey layer, with the coarse, basal portion of the flood layer represents bedload transported during the higher flow conditions and the finer upper layer having been deposited during the waning phase of the flood and represents deposition of the suspended load.

The erosional surface within the x-radiograph at the base of the flood layer suggests that there was erosion of the bed during the peak flood discharge conditions. Comparisons of HgT profiles from pre- and post-Harvey Core 22 reveal that at depth, below the flood layer, the HgT profiles correlate well with the 1972 peak HgT spike at 51 cm in the post-Harvey core. The pre-Harvey core collected in 2012 and additional cores collected in 2016 (shown in Hill, 2020) at the Core 22 site all reveal comparable HgT profiles. While the pre-Harvey Core 22 contained no significant or discernable sand layers within the upper 1 m of the core (Al Mukaimi et al., 2018b), aligning the HgT spikes in both cores show that ~48 cm of mud was eroded at the post-Harvey site prior to deposition of the 22 cm thick flood layer. The average concentration of HgT within the muddy portion of the Harvey flood layer was 197 ng g^{-1}.

3.2. Patrick Bayou Core results

Patrick Bayou Core 1 (PBC-1) was collected on May 8, 2019. As noted above, all of the samples were wet sieved to remove sand prior to measuring HgT concentrations, so these concentrations are not significantly skewed due to grain size variabilities. Core photographs (Fig. 6A) reveal that the upper 17 cm of the core contains brown sandy mud and the x-radiograph revealed this layer to be the base of which is delineated by a sharp contact. The upper 17 cm interval appears to consist of two intervals, a basal layer from 10 to 17 cm and a surface layer from 0 to 10 cm. The basal layer has a sand content averaging 22% and it progressively increases upwards from 13.6% at 17 cm to 38% sand at 10 cm and has a HgT concentration averaging 10,762 ng g^{-1}, with a peak HgT concentration of 24,011 ng g^{-1} at 12.5 cm. The x-radiograph reveals no bedding horizons, although there does appear to be a horizontal fabric. In addition, there are a few vertical burrows, suggesting escape burrows and also other vertical sedimentary structures indicative of fluid escape structures, which extend all way to the surface of the core. The fluid escape structures suggest dewatering due to rapid sedimentation, consistent with a storm deposit. The interval from 0 to 10 cm has a higher average sand at 38% with the surface interval having a sand content of 52%, a HgT concentration ranging from 1243 to 4004 ng g^{-1}, with an average HgT of 2255 ng g^{-1}, and generally looks similar to the layer below. It is assumed that the layer from 0 to 17 cm represents the Harvey layer. Directly below the Harvey layer, the HgT concentration is 51,270 ng g^{-1}, the highest concentration found within the entire core, and below this, from 21.5 to 40 cm, the HgT concentrations are generally 10,000 ng g^{-1} or higher. Additionally, from 20 to 60 cm, the core contains black mud, which had a very strong petroleum smell when the core was split and within this interval, the sand content within the core progressively decreases upwards from 69% at 55 cm to 4.2% at 20 cm. The HgT concentration of 51,270 ng g^{-1} at 19.5 cm is over 1000 times background concentrations and is the highest concentration found anywhere else in Galveston Bay, by a factor of 20.

3.3. San Jacinto Estuary Pushcore Harvey layer thickness estimation results

Only the portions of the SJE outside of the dredged and navigable channel are considered in this study. A combination of extremely high vessel traffic, maintenance dredging, and water depths precluded sampling within the ship channels. A total of 6 sites within the SJE were cored to determine deposit thicknesses, each of these sites were within sheltered bays, including Scott, Tabbs, and Burnet Bays, as well as Bear Lake and the upper SJE.

From the x-radiographs, the base of the Harvey layer was determined as well as the thickness of the layer and recorded (Table 1). For each core, the base of the Harvey deposit was easily identified as an anomalous erosional surface with a sand layer sitting atop of it, and above this a high-water content mud deposit (Figs. 5D and 6A). The sand layer was clearly evident as a lighter tone in the x-rays and is an

Table 1
Hurricane Harvey sediment and HgT loads for San Jacinto Estuary and Patrick Bayou.

Sub-Bay	Sediment mass deposited	Mass of HgT deposited	Sediment mass scoured	Mass of HgT scoured
Burnet Bay	7.87×10^5 tons	0.70 tons	1.72×10^6 tons	1.15 tons
Scott/Crystal Bay	1.01×10^6 tons	0.20 tons	2.21×10^6 tons	0.43 tons
Tabbs Bay	3.18×10^6 tons	0.10 tons	8.49×10^6 tons	0.25 tons
Upper San Jacinto Bay	7.52×10^5 tons	0.04 tons	1.64×10^6 tons	0.08 tons
Clear/Bear Lake	1.74×10^6 tons[a]	0.05 tons[a]	2.39×10^6 tons[a]	0.07 tons[a]
Patrick Bayou[a]	2.43×10^4 tons[a]	0.24 tons[a]	1.43×10^5 tons[a]	1.43 tons[a]
Total for San Jacinto Estuary Sub Bays	7.73×10^6 tons	0.96 tons	16.42×10^6 tons	2.0 tons

[a] Not included in total for the San Jacinto Estuary.

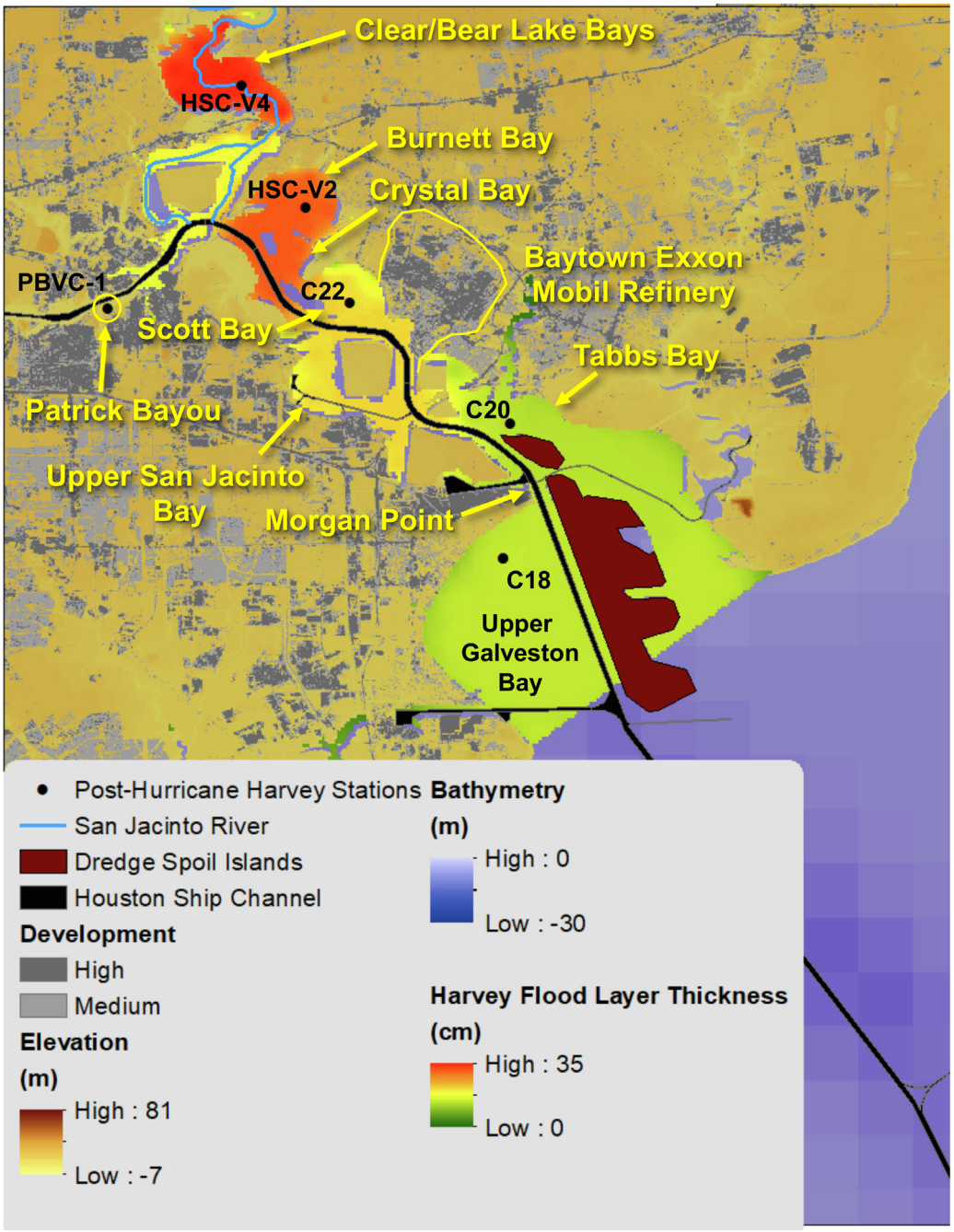

Fig. 7. Isopach map of Hurricane Harvey deposit in the San Jacinto Estuary. This map does not include the thickness of the Harvey deposit within the Houston Navigational Channel but extrapolates deposit thicknesses from the undredged areas across the navigation channel as a minimum thickness estimate. The thickest deposit was found in Core HSC VC-4, which is downstream from the Lake Houston Dam spillway. The next thickest deposit was found in Burnett Bay, where Buffalo Bayou flows into the San Jacinto Estuary. The deposit becomes progressively thinner towards the mouth of the San Jacinto Estuary within upper Galveston Bay.

anomalous feature within these cores as they were all collected in areas where the remainder of the cores are mud dominated. In most cores, there were also shells, many of which were articulated, also sitting atop the erosional surface.

Based on the measurements of the Harvey layer, an isopach map of the thickness of the Harvey deposit was generated for the portion of the SJE investigated, using ArcGIS (Fig. 7). Note, the contours on the map range from 0 to 50 cm, showing the range of cores from those areas outside of the dredged ship channel. For the basis of consideration of the Harvey deposit across the SJE, the dredged Houston Ship channel was ignored and the values from the adjacent areas are extrapolated across the channel areas as a minimum thickness estimate. The Harvey Isopach maps (Fig. 7) show that the thickest deposits were found within the SJE, south of the confluence with Buffalo Bayou, with thicknesses exceeding 50 cm in some places, and also forming a deltaic deposit in Galveston Bay at the mouth of the SJE.

Using ArcGIS, we determined the volume of the entire flood layer within the sub-bays of the SJE to be 9.72×10^6 m^3. Using the density of quartz (2.65 g cm^{-3}) for the sediment density and average water content for the flood deposit (70%), this volume of flood deposit contains a mass of 7.47×10^6 metric tons.

Within the SJE, the analyses of the Scott Bay core document 48 cm of sediment erosion within this bay. We have no other cores where we could effectively estimate the scour depth due to Harvey. However, the other portions of the SJE are generally less sheltered than Scott Bay, suggesting that comparable or greater currents were experienced in these locations. Assuming a scour depth of 48 cm and the same sediment parameters as assumed for estimating the mass of the Harvey deposit, with an area of the sub-bays of the SJE of 43 km^2, it is estimated that 16.4×10^6 tons of sediment was scoured from the SJE from Harvey and that this scoured sediment contained 2 tons of Hg (Table 1).

4. Discussion

4.1. Sources of Hg

According to Al Mukaimi et al. (2018b), Hg is sourced to Galveston Bay through both point-source and non-point sources. Non-point sources include atmospheric fallout from coal-burning and runoff from fertilizer, industrial waste streams from paper mills (e.g. Williams et al., 2015). However, there is one significant point source that has been identified, the wastewater outfalls of Patrick Bayou. Patrick Bayou (Fig. 8) is a 3 km long, sheltered slough that empties into lower Buffalo Bayou and contains seven industrial wastewater outfalls that empty into it. These include two outfalls from Oxyvinyl, (Occidental Chemical Company), as well as outfalls from Shell Oil Company and Lubrizol Corp. refineries. Hg has historically been used as a catalyst in the manufacturing of polyvinyl chloride (PVC; Vallette, 2018) and is a major source of Hg contamination throughout the world (e.g. Ren et al., 2014). PVC is one of the primary product streams of Oxyvinyl (Vallette, 2018).

Patrick Bayou was placed on the US EPA Superfund list for pesticides, polynuclear aromatic hydrocarbons (PAHs), and polychlorinated biphenyls (PCBs), after elevated levels of the contaminants were detected in its sediments in the early to mid-1990s (US EPA, 2017). Wastewater discharges from the outfalls within Patrick were attributed to be the primary sources of these contaminants. In addition, the Texas Natural Resources Conservation Commission (TNRCC), now called the Texas Commission on Environmental Quality (TCEQ), conducted samplings of Patrick Bayou in 2000 and found HgT levels as high as 41,500 ng g^{-1} as well as PCBs as high as 300,000 ng g^{-1} (US EPA, 2017). As noted above, core PB-C1 was collected on May 19, 2019. The two wastewater outfalls from the vinyl chloride processing plant are located 790 and 1100 m upstream for PB-C1. PBC-1 was collected approximately 200 m from the mouth of Patrick Bayou and ~50 m east of a low bridge that blocks vessel access to the remainder of the upstream portion of Patrick Bayou. The HgT from within the Harvey layer had an average concentration of 6122 ng g^{-1} and directly below the Harvey layer, the HgT concentrations were as high as 51,270 ng g^{-1}, indicating a that the core was collected proximal to the source of the Hg.

4.2. Hurricane Harvey Patrick and Buffalo Bayou flooding history and deposition

The Barker and Addicks Reservoirs are located ~75 river km to the west of the confluence of Buffalo Bayou and the SJE. Because of the retention of stormwater in the Barker and Addicks Reservoirs and the prolonged controlled release of these floodwaters, the Harvey flooding

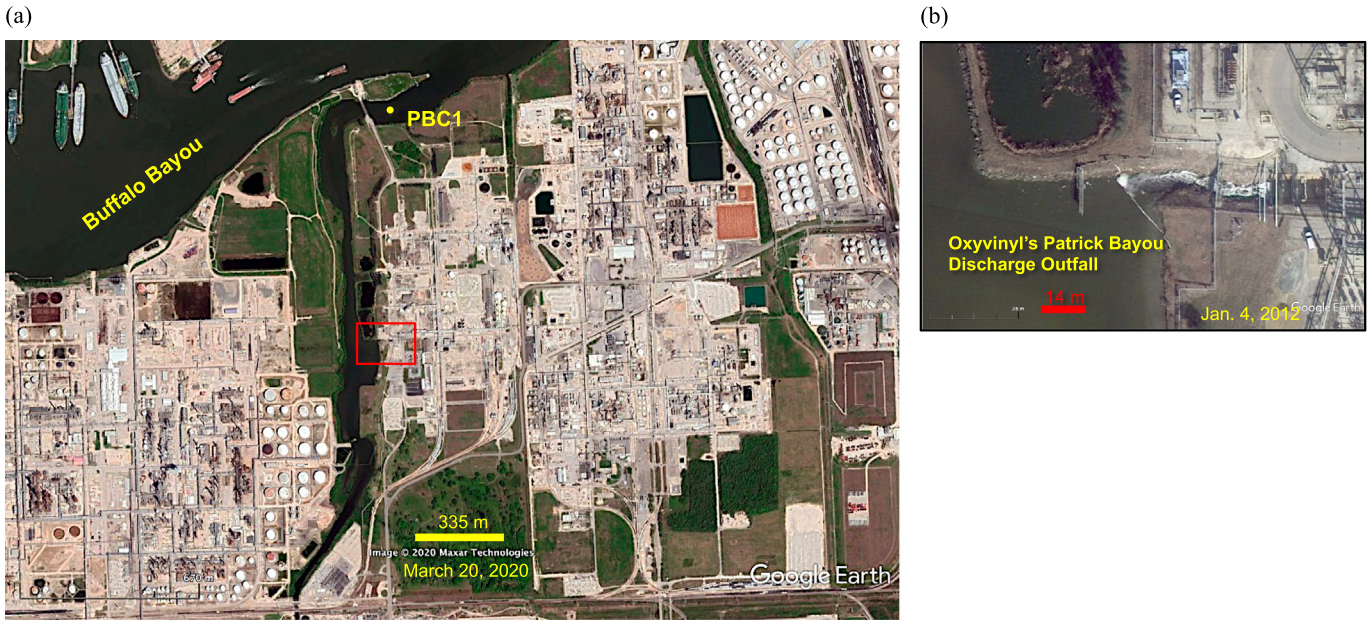

Fig. 8. Patrick Bayou map. A) Basemap from Google Earth March 20, 2020 of Patrick Bayou showing the location of the Oxyvinyl wastewater outfall in Patrick Bayou as well as the location of PBC-1 core location and its proximity to Buffalo Bayou. B) Map inset showing the Oxyvinyl wastewater outfall from the January 4, 2012 Google Earth image.

history of Buffalo Bayou is much different than the flooding histories of the other drainage basins within Galveston Bay. The flooding of Buffalo Bayou during Harvey can be divided into two phases, the first phase occurring during the peak discharge through the beginning of the release of floodwaters from the Barker and Addicks Reservoir. The second phase occurring during the extended-release of Addicks and Barker Reservoir flood water.

During the first phase of the flooding of the San Jacinto River, Brays Bayou, and the Trinity River, between August 23 to September 11, 2017, with peak discharges ending around September 5 or 6, depending on the river. For Buffalo Bayou, the peak discharge of +200 $m^3\ s^{-1}$ lasted for 16 days, from August 27 to September 11, 2017. Within Buffalo Bayou, the flood continued, settling down to a nearly continuous 80 $m^3\ s^{-1}$ during the controlled release, until it finally dropped off on October 13, 2017, for over an additional 32 days. Between Sept. 17 and Oct. 13, 2017, approximately 1.7×10^8 m^3 of floodwaters came from the Barker and Addicks Reservoirs.

During the period of time represented by the falling limb of the hydrographs, Aug. 28-Sept. 11 for the San Jacinto River/Estuary and Sept. 9–19, 2017 for Buffalo Bayou (Fig. 8), sediment deposition would have been occurring. For the SJE, as depicted in core Post-Harvey C-22 (Fig. 5C&D), the initial deposition is a basal deposit consisting of sand and gravel (shell), representing bedload. Above the basal bedload deposit is the upper layer, which is a mud dominated and represents the settling suspended load comprising the upper layer. However, because of the more complex history of the flooding in Buffalo Bayou, the deposit found in Patrick Bayou tells a different story. The 17 cm thick Harvey deposit in PB-C1 can be divided into two layers, a basal layer from 10 to 17 cm, which has a sand content averaging 22% and a HgT concentration averaging 10,762 ng g^{-1}, and a surface layer from 0 to 10 cm, which has an average sand content of 38% and an average HgT concentration of 2255 ng g^{-1}. The muddier basal portion of the Harvey layer in PB-C1 was deposited during the period representing the falling limb of the first flood pulse, prior to the opening of the Barker and Addicks Reservoirs. During this phase of the flood, Patrick Bayou and much of its drainage basin was flooded as well, and during the waning phase of this flood, higher Hg enriched sediment from the upper portion of Patrick Bayou was transported down the bayou and mixed with the Patrick Bayou drainage basin. The upper portion of Harvey flood layer appears to have been deposited during the period of time when the Barker and Addick Reservoir flood waters were released. During this phase of the flood, Buffalo Bayou waters and sediment would have flowed into Patrick Bayou, mixing with Patrick Bayou sediment. During this period, during the flooding of Buffalo Bayou, significant sand deposits were formed within the flood plain upstream of Patrick Bayou and the sediment load delivered during this phase of the flood would have had a significant sand component. The upper Harvey flood layer in the Patrick Bayou core generally has between 8 and 20% more sand than the lower layer and has a HgT averaging 20% of that found in the lower layer. With an average HgT of 2255 ng g^{-1}, it is still 4 to 10 times higher than what is found within the SJE Harvey deposit, suggesting significant mixing with Patrick Bayou derived sediment.

Based solely on the examination of our core, it is unclear whether there was significant erosion within Patrick Bayou during Harvey. However, there is a summary of a report from the Houston-Galveston Area Council (HGAC, 2012) showing results of a core collected upstream of the bridge in Patrick Bayou, directly in front of the outfall, showing a peak HgT concentration at ~130 cm depth. In PB-C1, the peak HgT is just below the base of the Harvey layer. If the sedimentation histories of these two sites are comparable, which seems reasonable, then this would suggest 130 cm of erosion from Patrick Bayou during Harvey. We found 48 cm erosion from within Scott Bay, which was much more sheltered than the PB-C1 site, so it is reasonable to assert that there was at least 1 m of erosion from Patrick Bayou. If we assume a thickness of 1 m, an area of 0.18 km^2, an average concentration of HgT of 10,000 ng g^{-1}, which is likely a conservative estimation, then the total mass of Hg within this one-meter thick layer of eroded sediment would have sourced 1.43 tons of Hg to Galveston Bay during Harvey. In addition, we estimate the HgT mass in the Harvey deposit to be 150 kg of HgT (Table 1), assuming that the flood layer has the same thickness as the PB-C1 core, of 17 cm thick and an average HgT concentration of 10,000 ng g^{-1}.

With the controlled releases from the Barker and Addicks Reservoirs, Buffalo Bayou flooded for 53 days, with a peak discharge (Fig. 9) at the Piney Point USGS Station of 424 $m^3\ s^{-1}$ and discharges of greater than 250 $m^3\ s^{-1}$ for 24 days, from Aug. 17 through Sept. 9. 2017. Pre-flood discharges were around 67 $m^3\ s^{-1}$. The Morgan Point Tidal Gauge reported currents in excess of 2 m s^{-1} for five days, between August 27 and September 1, 2017, and in excess of 3 m s^{-1} for approximately 48 h within this interval (Du et al., 2019a). Much of the water flowing through Morgan Point would have been flowing through Buffalo Bayou and likely comparably high currents were flowing through Buffalo Bayou during this same period, with currents capable of significant erosion of the bed, which mainly consists of soft, easily erodible estuarine mud.

This discharge would have provided ample bottom shear stress to have significantly eroded the bed of Buffalo Bayou. According to the US Army Corps of Engineers, emergency dredging with the Houston Ship Channel above Morgan Point removed 8.8×10^5 m^3 of dredged material between Sept. 4–14, 2017 (pers. comm. with F. Fenner, USACOE), with significantly larger volumes dredged afterward.

4.3. Hg deposits in the San Jacinto Estuary

Analyses of the SJE is focused on the portion of the estuary from the north end of Bear Lake to the mouth of the estuary at Morgan Point, where it empties into Galveston Bay, and does not focus on the open ship channel areas of the estuary. The north end of Bear Lake is located 20 km downstream of the Lake Houston dam. Upstream of Bear Lake, the estuary is sand dominated and generally narrow, following the course of the San Jacinto River.

Core SJRVC-1, with a Harvey Layer thickness of 6.25 cm thick and a HgT concentration of 30 ng g^{-1}, is the only core collected above the confluence with Buffalo Bayou. The relatively thin Harvey thickness suggests that the sediment load delivered from the SJE was likely much lower than from Buffalo Bayou. The HgT concentration approaches background levels and considering the core was collected 6 km upstream of the confluence with Buffalo Bayou, it is reasonable to assume that very little Hg was transported to the lower SJE and Galveston Bay.

Core HSC-V2 was collected from Burnet Bay and the core location is 3.5 km downstream from the confluence of Buffalo Bayou and Patrick Bayou (Fig. 7). Core HSC-V2 had a Harvey layer 29 cm thick and has an average HgT concentration within the Harvey layer of 677 ng g^{-1}, the highest HgT concentration found within the Harvey layer outside of Patrick Bayou (Fig. 4B). The entrance to Burnet Bay is 2 km downstream from the confluence of Buffalo Bayou and the SJE, and is situated such that a significant volume of floodwater mainly from Buffalo Bayou would enter the bay during high discharge conditions but is configured such that the flow from the San Jacinto River would largely be blocked from entering Burnet Bay, so it would receive sediment primarily derived from Buffalo Bayou. In contrast, the location and configuration of Scott Bay (Fig. 7) is such that it likely received sediment both from the San Jacinto River as well as Buffalo Bayou. Analyses of Google Earth images from multiple flood events also show that there is less advection of turbid plumes derived from the San Jacinto River entering Burnet Bay when compared to Scott Bay. There were no pre-Harvey cores from Burnet Bay, so we have used the scour depth from Scott Bay to estimate the scour depth of Burnet Bay, although, given its location, this is likely an underestimation of the scour depth.

Core C-22 in Scott Bay, is located 5 km from the mouth of Buffalo Bayou and 9 km downstream of the mouth of Patrick Bayou. The average HgT concentration within the 22 cm thick Harvey layer in Scott

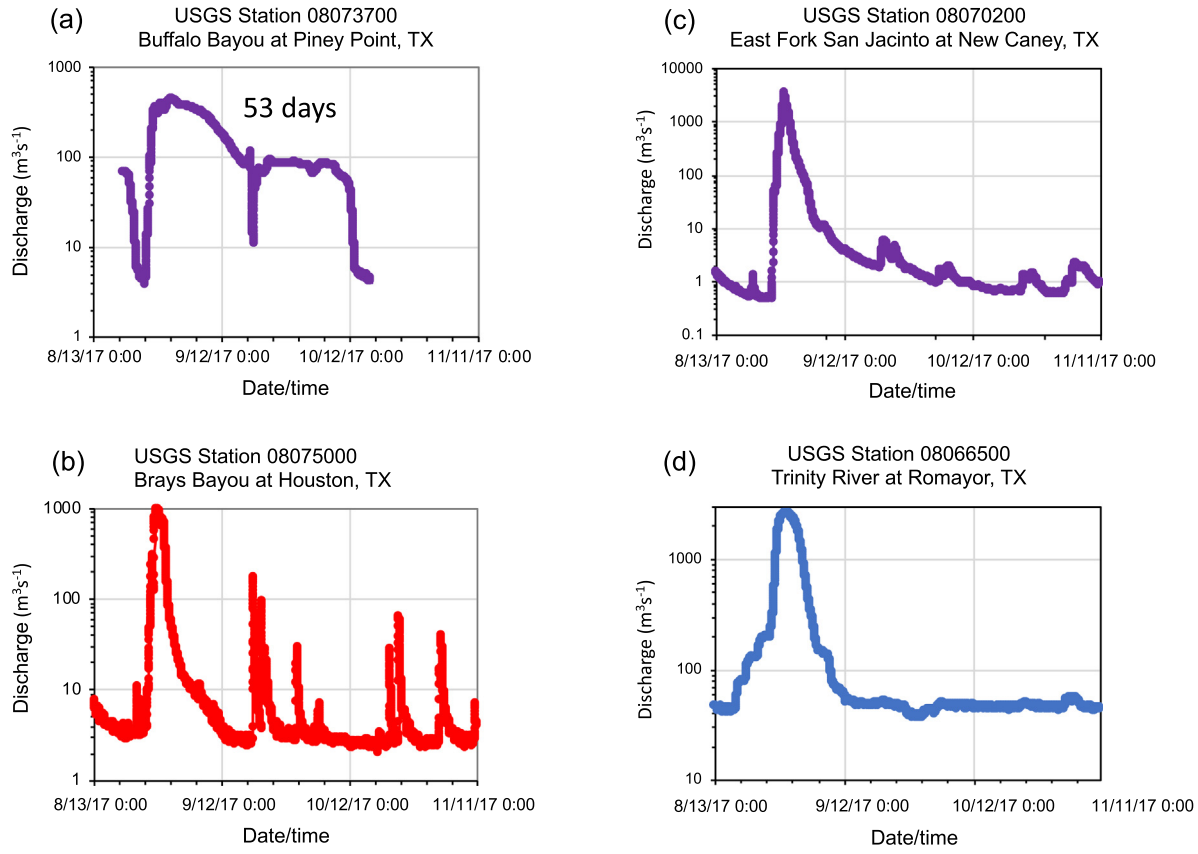

Fig. 9. USGS hydrographs from (a) Buffalo Bayou at Piney Point, (b) Brays Bayou, (c) East Fork of San Jacinto River, and (d) Trinity River at Romayor. Each of these rivers flows into Galveston Bay. Because of the controlled release of floodwaters from the Barker and Addicks Reservoirs (Fig. 3), Buffalo Bayou had two steps in the hydrograph (a), the first step, with higher discharge resulted from the initial phase of the flood, however, a prolonged, nearly flat section of the hydrograph at ~100 $m^3 s^{-1}$ results from the prolong floodwater release, for a total of 53 days of flooding.

Bay is 197 ng g^{-1}. This lower HgT concentration suggests that the further from the source, the lower the HgT concentration, likely due in part because of the mixing of sediment from the San Jacinto River as well as Buffalo Bayou, diluting the high HgT enriched sediment derived from Buffalo Bayou with lower HgT concentration sediment derived from the San Jacinto River.

Downstream of Scott Bay, Upper San Jacinto Bay had only a 4.3 cm thick Harvey deposit. The Upper San Jacinto Bay is an open and exposed section of the river on the western side of the lower SJE (Fig. 7) and would have experienced the full current of the ebbing floodwaters from both the San Jacinto and Buffalo Bayou and had a HgT concentration of 48 ng g^{-1} (Fig. 4B), which is essentially background. Tabbs Bay is located on the eastern side of the lower SJE and is a relatively sheltered embayment, open towards the south to Galveston Bay. C-20 in Tabbs Bay had a 22.25 cm thick Harvey deposit (Fig. 7) and a HgT concentration of 30 ng g^{-1}, the same concentration found in Clear Lake, above Buffalo Bayou (Fig. 4B). The thick deposit likely results from its sheltered location and its very low HgT concentration suggests either that the deposit is largely made up of sediment from the San Jacinto River or from sediment which settled from the flood water derived from the latter half of the flood from Buffalo Bayou when the floodwaters and sediment were derived from the upper Buffalo Bayou basin (Fig. 3).

Hill (2020) used the distribution of two species of benthic foraminifera, *Ammonia beccari* and *Miliamina fusca*, to determine the provenance of sediment within the Harvey flood layer in the SJE and Galveston Bay. *Ammonia beccari* tolerates a wide range of salinity (5 to 35 psu) making it an excellent indicator of brackish conditions (Boonstra et al., 2015; Dissarda et al., 2010; Melis and Covelli, 2013). *Miliamina fusca* typically denotes freshwater and a tolerance to polluted sediment (Eichler et al., 2004; Eichler et al., 2015). Hill (2020) found a moderate abundance of *Ammonia beccari* in the region from Bear/Clear Lake to Tabbs Bay and a high abundance in upper Galveston Bay. In contrast, Hill (2020), overall, found relatively low abundances of *Miliamina fusca* throughout the bay, but found the highest abundances, by a factor of eight in Tabbs Bay and upper Galveston Bay, just below Morgan Point and very low abundances above Tabbs Bay. The higher abundances of *Miliamina fusca* in Tabbs Bay to lower Galveston Bay indicate that the sediment in this area was likely sourced from freshwater source areas, such as those found within the upper drainage basin of Buffalo Bayou and the San Jacinto River. The low abundance of *Miliamina* and moderate abundances of *Ammonia beccari* for the sediment above Tabbs Bay indicate sediment derived from the brackish water perhaps mixed with terrestrial sources.

Fig. 10 summarizes the observations and findings of the sources and dispersal of sediment and Hg in BB, the SJE, and Galveston Bay. The Hg data, taken together with the textural analyses of sediment and the foraminifera data shows that the Harvey flood deposits found in Burnet and Scott Bay were likely sourced from the lower Buffalo Bayou, where salinities are low but still brackish and San Jacinto River upstream of Burnet Bay. The high integrated HgT concentrations suggest that the source area is both Patrick Bayou and the proximal adjoining section of BB (shown in yellow in Fig. 10) and that the Hg load was primarily delivered during the first phase of the flood. The flood layer found in the lower SJE, including Tabbs Bay as well as upper Galveston Bay (brown layer), suggests an upper drainage basin source and was likely delivered primarily during the post-peak discharge (second phase) of the flood, during the release of water from the Addicks and Barker Reservoirs.

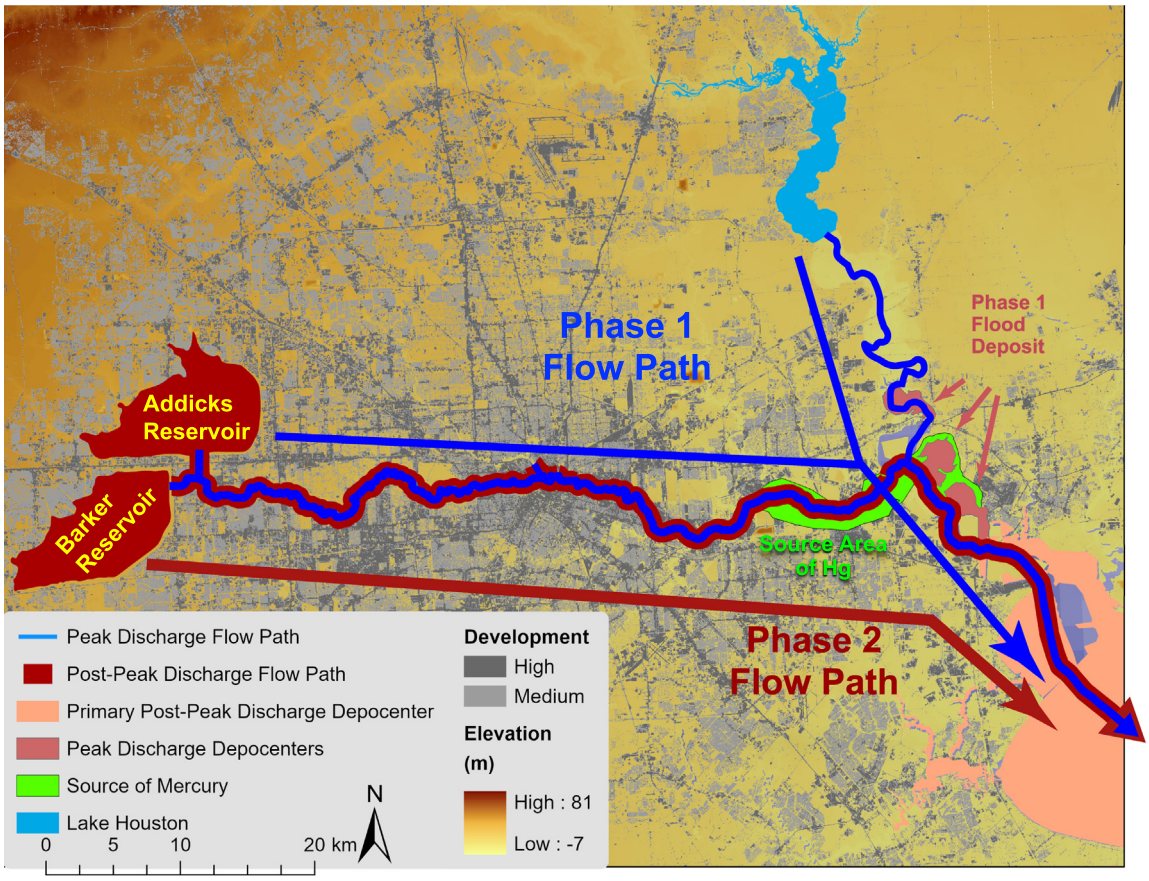

Fig. 10. Conceptual map showing sources and sinks of Hurricane Harvey derived sediment and Hg. During peak discharge, floodwaters (shown in blue) scoured Hg-enriched sediment from lower Buffalo Bayou (BB) and the San Jacinto Estuary (SJE) and sourced a thick deposit of Hg-enriched sediment in Burnet and Scott Bay south of the mouth of BB (shown in red). Additionally, during peak discharge, floodwaters (shown in blue) scoured the SJE, leaving a thick deposit in SJE north of BB. Post peak discharge flooding, including the prolonged release of floodwaters from the Addicks and Barker Reservoirs resulted in the prolonged (44 days) delivery of floodwaters (shown in orange) and basin derived sediment to both the SJE and Galveston Bay (shown in brown). (For interpretation of the references to color in this figure legend, the reader is referred to the web version of this article.)

4.4. HgT, methyl mercury, and enhanced bioavailability

In this study, only HgT was measured, however in marine environments, Hg bioaccumulates as methyl mercury, which is a potent neurotoxin that is among the most widespread contaminants affecting US aquatic ecosystems (Brumbaugh et al., 2001). The anoxic conditions found within estuarine sediment, specifically, under iron, sulfate, methanogenic conditions are where methylmercury is formed (Compeau and Bartha, 1985; Warner et al., 2003; Mason et al., 2006) and more recently it has been found that under these conditions, methylating bacteria are responsible for the rate of methylmercury production and thus bioaccumulation in marine foodwebs (Schartup et al., 2014).

Within the Trinity Bay portion of Galveston Bay, Dellapenna et al. (2006) found the sulfide Redox Potential Discontinuity (RPD) to typically exist within the upper 1–2 cm of the seabed. All of the sediment cores collected in the SJE pre-Harvey and the portions of the post-Harvey cores below the Harvey layer each consisted of black estuarine mud consistent with anoxic sediment. It is reasonable to assume that the RPD resides within the upper few centimeters of the SJE seabed, at least where the substrate is mud dominated, which is generally the case for the areas investigated in this study. This would suggest that nearly the entire sediment column in the SJE is within the zone where methylating bacteria are most active and that the sediment and their porewaters are enriched in methyl mercury proportional to its enrichment in HgT. Consequently, the erosion of these sediments releases elevated amounts of methyl mercury, enhancing its ability to bioaccumulate in the marine food web.

4.5. Potential impacts of the Harvey Storm deposit to the benthic community

In addition to the remobilization, transport, and deposition of legacy contaminants, the massive erosion and deposition of the seabed likely had other impacts on the ecosystem, especially the benthos. The erosion of up to 48 cm of seabed in the SJE is comparable to that which was found in the York River estuary by Dellapenna et al. (1998, 2001, 2003). Schaffner et al. (2001) reported that nearly 50 cm of excavation of sediment in the York River resulted in a loss of all macrobenthic organisms and much of the microbenthic community. Episodic deposition of a thick column of sediment also has a detrimental impact both to the abundance and diversity of benthic communities (Miller et al., 2002; Chou et al., 2004; Naser, 2011).

Thrush et al. (2004) summarized, based on the previous field and laboratory studies, that a critical threshold of episodic deposition of 2 cm in an estuary will quickly create anaerobic conditions within the seabed, resulting in the death of the resident faunal community. The benthic and pelagic coupling within an estuary is central to the nutrient cycling and overall productivity of the system, and an interruption of this coupling resulting from elevated sedimentation rates can have dramatic impacts on the entire ecosystem (Eyre and Ferguson, 2006). Within the lower SJE, there was on average, 22 cm of deposition of new sediment. This suggests the potential for a devastating interruption of the benthic-pelagic coupling of the bay and a significant interruption to the nutrient cycling, at least until the benthic community can ultimately recover. Considering that average sedimentation rates were

already elevated to around 1.5 cm y^{-1} in this system due to elevated land subsidence (Al Mukaimi et al., 2018a), near the 2 cm episodic deposition critical threshold mentioned above (Thrush et al., 2004), it is likely that the benthic community was already stressed. Deposition of 22 cm of sediment in a regime where the sedimentation rate approaches this critical threshold may result in a recovery of the benthos may be much slower than would normally be expected if average sedimentation rates were much lower. It should also be noted that the recovering benthic community will be exposed to elevated levels of a variety of contaminants, including Hg, further exacerbating the situation.

5. Conclusions

The SJE and Buffalo Bayou combined, drain both metropolitan Houston and the Houston Petrochemical complex. Groundwater withdrawal to support both the growing population of Houston as well as the massive petrochemical complex has resulted in 3 m of land subsidence. The accommodation space created this subsidence resulted in the accumulation and archiving of more than 2 m of sediment which contained elevated concentrations of particle-bound and porewater contaminants, including Hg. Industrial wastewater outfalls within Patrick Bayou, located along lower Buffalo Bayou, are the primary source of Hg for the sediments within lower Buffalo Bayou and the SJE, as well as Galveston Bay. Cores from Patrick Bayou reveal HgT concentrations as high as 51,270 ng g^{-1} at a depth of 19.5 cm, which is over 1000 times background concentrations and is the highest concentration found anywhere within Galveston Bay, by a factor of 20.

The extreme rainfall from Harvey delivered 14×10^9 m^3 of freshwater to Galveston Bay and produced record flooding of the Houston bayous and waterways, most of which flowed through Buffalo Bayou and the SJE. The flooding of Buffalo Bayou and the SJE during Harvey can be divided into two phases, the first phase occurred during the peak discharge and the second half occurred during the falling limb of the hydrograph. The entire flood event for the San Jacinto River and other tributaries occurred over a 12–16 day period, however, due to the release of floodwaters from the Barker and Addicks Reservoir, the flood lasted for a total of 53 days for Buffalo Bayou.

Detailed analyses of sediment cores collected within both Patrick Bayou and Scott Bay reveal extensive erosion during the rising flood waters and that the transport of sediment was modulated by the two phases of the flood. Within Scott Bay, Harvey the rising flood waters during the first phase of the flood eroded 48 cm of the sediment, exporting of 16.42×10^6 tons of sediment which contained 2.0 tons of HgT to Galveston Bay. Within Patrick Bayou, it is estimated that 130 cm of sediment was eroded, exporting 1.43×10^5 tons of sediment and 1.43 tons of HgT downstream into the SJE and Galveston Bay. Additionally, overall, in Scott Bay, a 22 cm thick flood layer was deposited and within the SJE, Harvey deposited 7.73×10^6 tons of sediment and 0.96 tons of HgT within the SJE. The basal layer contains shell lag gravel, was likely sourced from the upper SJE and from the lower reach of Buffalo Bayou, during the first phase of the flood. The upper layer is mud dominated, represents the suspended load and was deposited during the second phase of the flood.

Within Patrick Bayou, the basal layer contains extremely elevated HgT concentrations (as high as 24,011 ng g^{-1}) and lower sand content, which indicate that it formed during the first phase of the flood and was sourced primarily from eroded local sediment within the bayou and its drainage basin. The upper layer of the Patrick Bayou Harvey deposit contains a higher sand content and lower HgT. This indicates that this deposit was derived from a combination of upper drainage basin sands derived from the scouring of the river bed mixed with sediment from lower Buffalo Bayou, which contain Hg originally derived primarily from Patrick Bayou.

The Harvey deposit was found to be thickest within the upper SJE above the confluence with Buffalo Bayou within Clear and Bear Lake Bays and just below the confluence of Buffalo Bayou, within Burnett, Crystal, and Scott Bays and thinned southward towards Morgan Point and within the upper Galveston Bay. The Harvey deposit HgT concentrations were found highest within lower Buffalo Bayou and within the same section of the SJE where the Harvey deposit is thickest downstream of the confluence of Buffalo Bayou. The thicker Harvey deposits upstream of the confluence contained background levels of HgT, suggesting that there are no significant sources of Hg coming from upstream of the confluence with Buffalo Bayou. When pre- and post-Harvey HgT distributions are compared, the greatest enrichment is within Burnett Bay at the mouth of Buffalo Bayou. Analyses of foraminifera from cores Scotts Bay as well as from the Harvey deposit from around the SJE indicate the Harvey deposit found within the lowermost SJE and upper reaches of Galveston Bay are enriched in freshwater foraminifera, suggesting that the Harvey deposit found in this area was sourced from the upper drainage basin of Buffalo Bayou. In contrast, the foraminifera found within the Harvey deposit found within Scott, Crystal, and Burnett and surrounding areas were dominated by brackish species. The combined foraminifera HgT distributions strongly suggest that during the initial phase of the flood, sediment from the lower portion of Buffalo Bayou, potentially including Patrick Bayou, were flushed into the semi-sheltered bays of Burnett, Crystal and Scott Bays where they settled proximal to the mouth of Buffalo Bayou, where much of this material was sources during waning half of the first phase of the flood, with a significant component of the deposit comprising bedload material. The second phase of the storm primarily delivered suspended sediment, which was able to be more broadly distributed, hence its greater representation within the lower section of the SJE and upper Galveston Bay.

Elevated land subsidence is a feature of many of the world's urbanized estuaries and deltas and provides a mechanism for the accumulation and archiving of elevated concentration of both particle-bound and porewater contaminants. The conventional wisdom prior to this study was that deeply buried legacy contaminants in estuaries are not of concern because their deeper burial makes them not susceptible to erosion. However, this study shows that intense flooding within estuaries can erode decimeters of sediment, and is in fact, capable of eroding deeply buried legacy contaminants and dispersing tons of these contaminants around the estuarine system.

Within the SJE and Galveston Bay, as well as many of the world's estuaries, Hg is a significant contaminant. Although this study only investigated HgT, Hg bioaccumulates as methyl mercury. Methyl mercury forms within the anoxic conditions found a few centimeters below the surface within estuarine muds. In the context of Hg, it also mobilizes the most toxic forms of Hg, enabling it to be much more bioavailable and enhancing its ability to bioaccumulate in the marine food web. When we consider Harvey and the legacy contaminants archived with the SJE, within Scott Bay, the layer with the highest concentration of HgT was not eroded, but this layer was likely eroded in other parts of the SJE. However, within Scott Bay, this layer is now at least 20 cm shallower than before the storm, making it much more vulnerable to erosion during the next large flood event. When we consider that the frequency of slow-moving tropical cyclones capable of delivering devastating rainfall is increasing, then we can expect an increase in the frequency of extreme flood events that are capable of excavating deeply buried legacy contaminants from the archive of sediment within urbanized estuaries. Consequently, what happened during Harvey is a harbinger of what is to come both for Galveston Bay as well as other urbanized estuaries and deltas around the world.

CRediT authorship contribution statement

Timothy M. Dellapenna: Writing - original draft, Investigation, Formal analysis, Data curation, Conceptualization, Visualization, Methodology, Validation, Resources, Supervision, Writing - review & editing. **Christena Hoelscher:** Visualization, Software. **Lisa Hill:** Investigation, Visualization, Methodology. **Mohammad E. Al Mukaimi:** Writing -

review & editing. **Anthony Knap:** Funding acquisition, Resources, Writing - review & editing.

Declaration of competing interest

The authors declare that they have no known competing financial interests or personal relationships that could have appeared to influence the work reported in this paper.

Acknowledgements

We would like to acknowledge the many undergraduate and graduate students who have helped with both the field and lab phases of this work, including M. Bell, O. Cavazos, J. Lewis, N. Wellbrock, A. Bland, and L. Critides. This work was partially supported by the National Institute of Environmental Health Sciences of the National Institutes of Health under Award P42 ES027704 and by the Texas General Land Office and the National Oceanic and Atmospheric Administration (NOAA) through the Texas Coastal Management Program under Award 19-040-000-B074.

References

Al Mukaimi, M.E., Dellapenna, T.M., Williams, J.R., 2018a. Enhanced land subsidence in Galveston Bay, Texas: interaction between sediment accumulation rates and relative sea level rise. Estuar. Coast. Shelf Sci. 207, 183–193. https://doi.org/10.1016/j.ecss.2018.03.023.

Al Mukaimi, M.E., Kaiser, K., Williams, J.R., Dellapenna, T.M., Louchouarn, P., Santschi, P.H., 2018b. Centennial record of anthropogenic impacts in Galveston Bay: evidence from trace metals (Hg, Pb, Ni, Zn) and lignin oxidation products. Environ. Pollut. 237, 887–899. https://doi.org/10.1016/j.envpol.2018.01.027.

Armstrong, N.E., 1982. Responses of Texas estuaries to freshwater inflows. Estuarine Comparisons. Academic Press, pp. 103–120 https://doi.org/10.1016/B978-0-12-404070-0.50013-2.

Ayuso, R.A., Foley, N.K., Seal II, R.R., Bove, M., Civitillo, D., Cosenza, A., Grezzi, G., 2013. Lead isotope evidence for metal dispersal at the Callahan Cu–Zn–Pb mine: Goose Pond tidal estuary, Maine, USA. J. Geochem. Explor. 126, 1–22. https://doi.org/10.1016/j.gexplo.2012.12.013.

Bank, M.S., 2012. Mercury in the Environment: Pattern and Process. Univ. of California Press.

Bera, G., Camargo, K., Sericano, J.L., Liu, Y., Sweet, S.T., Horney, J., Jun, M., Chiu, W., Rusyn, I., Wade, T.L., Knap, A.H., 2019. Baseline data for distribution of contaminants by natural disasters: results from a residential Houston neighborhood during Hurricane Harvey flooding. Heliyon 5 (11). https://doi.org/10.1016/j.heliyon.2019.e02860 (p.e 02860).

Boonstra, M., Ramos, M., Lammertsma, E., Antoine, P., Hoorn, C., 2015. Marine connections of Amazonia: evidence from foraminifera and dinoflagellate cysts (early to middle Miocene, Colombia/Peru). Palaeogeogr. Palaeoclimatol. Palaeoecol. 417, 176–194. https://doi.org/10.1016/j.palaeo.2014.10.032.

Brumbaugh, W.G., Krabbenhoft, D.P., Helsel, D.R., Wiener, J.G., Echols, K.R., 2001. A national pilot study of mercury contamination of aquatic ecosystems along multiple gradients: bioaccumulation in fish. Biological Science Report 9. https://semspub.epa.gov/work/01/466771.pdf.

Buchman, M., 2008. NOAA screening quick reference tables, NOAA OR&R report 08-1. Office of Response and Restoration Division, National Oceanic and Atmospheric Administration, Seattle , p. 34. https://repository.library.noaa.gov/view/noaa/9327.

Carlin, J.A., Lee, G., Dellapenna, T.M., Laverty, P., 2016. Sediment resuspension by wind, waves, and currents during meteorological frontal passages in a micro-tidal lagoon. Estuar. Coast. Shelf Sci. 172, 24–33. https://doi.org/10.1016/j.ecss.2016.01.029.

Cave, R.R., Andrews, J.E., Jickells, T., Coombes, E.G., 2005. A review of sediment contamination by trace metals in the Humber catchment and estuary, and the implications for future estuary water quality. Estuar. Coast. Shelf Sci. 62 (3), 547–557. https://doi.org/10.1016/j.ecss.2004.09.017.

Chambers, M., Mitchell, A., Fine, A., Mulder, K., Rainville, L., Hackett, D., Smith, D., Dijoseph, P., Kress, M., Mitchell, K.N., Tujague, A., 2018. Port performance freight statistics program: annual report to congress 2017. [Supporting Datasets]. https://www.bts.gov/browse-statistical-products-and-data/port-performance/port-performance-freight-statistics-program.

Chou, L., Yu, J., Loh, T., 2004. Impacts of sedimentation on soft-bottom benthic communities in the southern islands of Singapore. Hydrobiologia 515 (1–3), 91–106. https://doi.org/10.1023/B:HYDR.0000027321.23230.2f.

Ciszewski, D., Grygar, T.M., 2016. A review of flood-related storage and remobilization of heavy metal pollutants in river systems. Water Air Soil Pollut. 227 (7), 239. https://doi.org/10.1007/s11270-016-2934-8.

Compeau, G., Bartha, R., 1985. Sulfate-reducing bacteria: principal methylators of mercury in anoxic estuarine sediment. Appl.Environ.Microbiol. 50 (2), 498–502.

Coplin, L.S., Galloway, D., 1999. Houston-Galveston, Texas. Land Subsidence in the United States: US Geological Survey Circular. vol. 1182 , pp. 35–48. https://www.researchgate.net/profile/Devin_Galloway/publication/284221420_Houston-Galveston_Texas_Managing_coastal_subsidence/links/565867e408ae4988a7b7454f.pdf.

Cutshall, N.H., Larsen, I.L., Nichols, M.M., 1981. Man-made radionuclides confirm rapid burial of kepone in James River sediments. Science 213 (4506), 440–442. https://doi.org/10.1126/science.213.4506.440.

de Souza Machado, A.A., Spencer, K., Kloas, W., Toffolon, M., Zarfl, C., 2016. Metal fate and effects in estuaries: a review and conceptual model for better understanding of toxicity. Sci. Total Environ. 541, 268–281. https://doi.org/10.1016/j.scitotenv.2015.09.045.

Dellapenna, T., Kuehl, S., Schaffner, L., 1998. Sea-bed mixing and particle residence times in biologically and physically dominated estuarine systems: a comparison of lower Chesapeake Bay and the York River subestuary. Estuar. Coast. Shelf Sci. 46 (6), 777–795. https://doi.org/10.1006/ecss.1997.0316.

Dellapenna, T.M., Kuehl, S.A., Pitts, L., 2001. Transient, longitudinal, sedimentary furrows in the York River subestuary, Chesapeake Bay: furrow evolution and effects on seabed mixing and sediment transport. Estuaries 24, 215–227. www.jstor.org/stable/1352946.

Dellapenna, T.M., Kuehl, S.A., Schaffner, L.C., 2003. Ephemeral deposition, seabed mixing and fine-scale strata formation in the York River estuary, Chesapeake Bay. Estuar. Coast. Shelf Sci. 58 (3), 621–643. https://doi.org/10.2307/1352946.

Dellapenna, T.M., Allison, M.A., Gill, G.A., Lehman, R.D., Warnken, K.W., 2006. The impact of shrimp trawling and associated sediment resuspension in mud dominated, shallow estuaries. Estuar. Coast. Shelf Sci. 69 (3–4), 519–530. https://doi.org/10.1016/j.ecss.2006.04.024.

Di Leonardo, R., Tranchida, G., Bellanca, A., Neri, R., Angelone, M., Mazzola, S., 2006. Mercury levels in sediments of Central Mediterranean Sea: a 150 year record from box-cores recovered in the Strait of Sicily. Chemosphere 65 (11), 2366–2376. https://doi.org/10.1016/j.chemosphere.2006.04.076.

Dissarda, D., Nehrke, G., Reichart, G.J., Bijma, J., 2010. The impact of salinity on the Mg/Ca and Sr/Ca ratio in the benthic foraminifera *ammonia tepida*: results from culture experiments. Geochim. Cosmochim. Acta 74 (3), 928–940. https://doi.org/10.1016/j.gca.2009.10.040.

Du, J., Park, K., Dellapenna, T.M., Clay, J.M., 2019a. Dramatic hydrodynamic and sedimentary responses in Galveston Bay and adjacent inner shelf to Hurricane Harvey. Sci. Total Environ. 653, 554–564. https://doi.org/10.1016/j.scitotenv.2018.10.403.

Du, J., Park, K., Dellapenna, T.M., Clay, J.M., 2019b. Corrigendum to "Dramatic hydrodynamic and sedimentary responses in Galveston Bay and adjacent inner shelf to Hurricane Harvey" [Sci. Total Environ. 653 (2019b), 554–564]. Sci. Total Environ. 697, 134219. https://doi.org/10.1016/j.scitotenv.2019.134219.

Eichler, P.P.B., Castelão, G.P., Pimenta, F.M., Eichler, B.B., De Miranda, L.B., Rodrigues, A.R., Pereira, E.R., 2004. Foraminifera and thecamoebians as indicator of hydrodynamic process in a choked coastal lagoon, Laguna estuarine system, SC, Brazil. J. Coast. Res. 39, 1144–1148.

Eichler, P.P.B., Eichler, B.B., Vital, H., 2015. Marine pollution-environmental indicators in marine meiofauna from Brazil. Environmental Indicators, 545–560 https://doi.org/10.1007/978-94-017-9499-2_32 (Springer).

EPA, 1998. Method 7473: Mercury in Solids and Solutions by Thermal Decomposition Amalgamation and Atomic Absorption Spectrophotometry, EPA SW-846. USEPA Office of Research and Development Environmental Monitoring Systems Labratory, Cincinnati.

Eyre, B.D., Ferguson, A.J., 2006. Impact of a flood event on benthic and pelagic coupling in a sub-tropical east Australian estuary (Brunswick). Estuar. Coast. Shelf Sci. 66 (1–2), 111–122. https://doi.org/10.1016/j.ecss.2005.08.008.

He, J., Soden, B.J., 2015. Anthropogenic weakening of the tropical circulation: the relative roles of direct CO2 forcing and sea surface temperature change. J. Clim. 28 (22), 8728–8742. https://doi.org/10.1175/JCLI-D-15-0205.1.

He, J., Winton, M., Vecchi, G., Jia, L., Rugenstein, M., 2017. Transient climate sensitivity depends on base climate ocean circulation. J. Clim. 30 (4), 1493–1504. https://doi.org/10.1175/JCLI-D-16-0581.1.

Held, I.M., Soden, B.J., 2006. Robust responses of the hydrological cycle to global warming. J. Clim. 19 (21), 5686–5699. https://doi.org/10.1175/JCLI3799.1.

HGAC (Houston-Galveston Area Council), 2012. Patrick Bayou Site Status Report Patrick Bayou Superfund Site. http://www.h-gac.com/watershed-based-plans/documents/hsc-ugb/hsc_04-04-2012_Patrick-Bayou-Superfund-Site.pdf.

HGSD, 2008. Houston Galveston Subsidence District- Subsidence: 1906–2000. Available at. http://www.subsidence.org/Assets/PDFDocuments/.

HGSD, 2013. Subsidence and groundwater regulation FAQ's. Available at. http://hgsubsidence.org/frequently-asked-questions/subsidence-groundwater-regulation-faqs/.

Hill, L., 2020. Environmental and Anthropogenic Influences during the 20th Century in Scott Bay. San Jacinto Estuary, Houston, Texas (Unpublished manuscript).

Jelgersma, S., 1996. Land subsidence in coastal lowlands. Sea-Level Rise and Coastal Subsidence. Springer, Dordrecht, pp. 47–62 https://doi.org/10.1007/978-94-015-8719-8_3.

Kennish, M.J., 2002. Environmental threats and environmental future of estuaries. Environ. Conserv. 29 (1), 78–107. https://doi.org/10.1017/S0376892902000061.

Knap, A.H., Rusyn, I., 2016. Environmental exposures due to natural disasters. Rev. Environ. Health 31 (1), 89–92.

Kossin, J.P., 2018. A global slowdown of tropical-cyclone translation speed. Nature 558 (7708), 104–107. https://doi.org/10.1038/s41586-018-0158-3.

Liu, G., Cai, Y., O'Driscoll, N., 2011. Environmental Chemistry and Toxicology of Mercury. John Wiley & Sons.

Macklin, M.G., Hudson-Edwards, K.A., Dawson, E.J., 1997. The significance of pollution from historic metal mining in the Pennine orefields on river sediment contaminant fluxes to the North Sea. Sci. Total Environ. 194, 391–397. https://doi.org/10.1016/S0048-9697(96)05378-8.

Mann, M.E., Rahmstorf, S., Kornhuber, K., Steinman, B.A., Miller, S.K., Coumou, D., 2017. Influence of anthropogenic climate change on planetary wave resonance and extreme weather events. Sci. Rep. 7, 45242. https://doi.org/10.1126/sciadv.aat3272.

Mason, R.P., Kim, E., Cornwell, J., Heyes, D., 2006. An examination of the factors influencing the flux of mercury, methylmercury and other constituents from estuarine sediment. Mar. Chem. 102 (1–2), 96–110. https://doi.org/10.1016/j.marchem.2005.09.021.

Melis, R., Covelli, S., 2013. Distribution and morphological abnormalities of recent foraminifera in the Marano and Grado lagoon (North Adriatic Sea, Italy). Mediterr. Mar. Sci. 14 (2), 432–450. https://doi.org/10.12681/mms.351.

Miller, D.C., Muir, C.L., Hauser, O.A., 2002. Detrimental effects of sedimentation on marine benthos: what can be learned from natural processes and rates? Ecol. Eng. 19 (3), 211–232. https://doi.org/10.1016/S0925-8574(02)00081-2.

Morse, J.W., Presley, B.J., Taylor, R.J., Benoit, G., Santschi, P., 1993. Trace metal chemistry of Galveston Bay: water, sediments and biota. Mar. Environ. Res. 36 (1), 1–37. https://doi.org/10.1016/0141-1136(93)90087-G.

Naser, H.A., 2011. Effects of reclamation on macrobenthic assemblages in the coastline of the Arabian Gulf: a microcosm experimental approach. Mar. Pollut. Bull. 62 (3), 520–524. https://doi.org/10.1016/j.marpolbul.2010.11.032.

NOAA- National Oceanic and Atmospheric Administration, Office for Coastal Management, 2016. 2016 C-CAP Regional Land Cover. Coastal Change Analysis Program (C-CAP) Regional Land Cover. NOAA Office for Coastal Management, Charleston, SC. Accessed June 2020 at. www.coast.noaa.gov/htdata/raster1/landcover/bulkdownload/30m_lc/.

NOAA- National Oceanic and Atmospheric Administration, 2017. NOAA National Centers for Environmental Information, State of the Climate: National Climate Report for Annual 2017. published online January 2018, retrieved on June 11, 2020 from. https://www.ncdc.noaa.gov/sotc/national/201713.

Olsen, C.R., Larsen, I.L., Mulholland, P.J., Von Damm, K.L., Grebmeier, J.M., Schaffner, L.C., Diaz, R.J., Nichols, M.M., 1993. The concept of a equilibrium surface applied to particle sources and contaminant distributions in estuarine sediments. Estuaries 16 (3), 683–696. https://doi.org/10.2307/1352805.

O'Shea, F.T., Cundy, A.B., Spencer, K.L., 2018. The contaminant legacy from historic coastal landfills and their potential as sources of diffuse pollution. Mar. Pollut. Bull. 128, 446–455. https://doi.org/10.1016/j.marpolbul.2017.12.047.

Plumlee, G.S., Morman, S.A., Meeker, G.P., Hoefen, T.M., Hageman, P.L., Wolf, R.E., 2013. The environmental and medical geochemistry of potentially hazardous materials produced by disasters. Treatise on Geochemistry 11, 257–304. http://www.sciencediirect.com/sciience/artiicle/piii/B9780080959757009074.

Ren, W., Duan, L., Zhu, Z., Du, W., An, Z., Xu, L., Zhang, C., Zhuo, Y., Chen, C., 2014. Mercury transformation and distribution across a polyvinyl chloride (PVC) production line in China. Environmental Science & Technology 48 (4), 2321–2327. https://doi.org/10.1021/es404147c.

Rodriguez, A.B., Anderson, J.B., Simms, A.R., 2005. Terrace inundation as an autocyclic mechanism for parasequence formation: Galveston Estuary, Texas, U.S.A. J. Sediment. Res. 75, 608–620. https://doi.org/10.2110/jsr.2005.050.

Rodriguez-Iruretagoiena, A., de Vallejuelo, S.F.O., de Diego, A., de Leão, F.B., de Medeiros, D., Oliveira, M.L., Tafarel, S.R., Arana, G., Madariaga, J.M., Silva, L.F., 2016. The mobilization of hazardous elements after a tropical storm event in a polluted estuary. Sci. Total Environ. 565, 721–729. https://doi.org/10.1016/j.scitotenv.2016.05.024.

Santschi, P.H., Presley, B.J., Wade, T.L., Garcia-Romero, B., Baskaran, M., 2001. Historical contamination of PAHs, PCBs, DDTs, and heavy metals in Mississippi River Delta, Galveston Bay and Tampa Bay sediment cores. Mar. Environ. Res. 52 (1), 51–79. https://doi.org/10.1016/S0141-1136(00)00260-9.

Schaffner, L.C., Dellapenna, T.M., Hinchey, E.K., Friedrichs, C.T., Neubauer, M.T., Smith, M.E., Kuehl, S.A., 2001. Physical energy regimes, seabed dynamics and organism-sediment interactions along an estuarine gradient. Organism-Sediment Interactions 159–179.

Schartup, A.T., Balcom, P.H., Mason, R.P., 2014. Sediment-porewater partitioning, total sulfur, and methylmercury production in estuaries. Environmental Science & Technology 48 (2), 954–960. https://doi.org/10.1021/es403030d.

Schoellhamer, D.H., Mumley, T.E., Leatherbarrow, J.E., 2007. Suspended sediment and sediment-associated contaminants in San Francisco Bay. Environ. Res. 105 (1), 119–131. https://doi.org/10.1016/j.envres.2007.02.002.

Solis, R.S., Powell, G., 1999. Hydrography, residence times, and physical processes. Biogeochemistry of Gulf of Mexico Estuaries. John Wiley, New York, pp. 29–61.

Swales, A., Williamson, R.B., Van Dam, L.F., Stroud, M.J., McGlone, M.S., 2002. Reconstruction of urban stormwater contamination of an estuary using catchment history and sediment profile dating. Estuaries 25 (1), 43–56. https://doi.org/10.1007/BF02696048.

Syvitski, J.P., Kettner, A.J., Overeem, I., Hutton, E.W., Hannon, M.T., Brakenridge, G.R., Day, J., Vörösmarty, C., Saito, Y., Giosan, L., Nicholls, R.J., 2009. Sinking deltas due to human activities. Nat. Geosci. 2 (10), 681–686. https://doi.org/10.1038/ngeo629.

Tessler, Z.D., Vörösmarty, C.J., Grossberg, M., Gladkova, I., Aizenman, H., Syvitski, J.P.M., Foufoula-Georgiou, E., 2015. Profiling risk and sustainability in coastal deltas of the world. Science 349 (6248), 638–643. https://doi.org/10.1126/science.aab3574.

Thrush, S., Hewitt, J., Cummings, V., Ellis, J., Hatton, C., Lohrer, A., Norkko, A., 2004. Muddy waters: elevating sediment input to coastal and estuarine habitats. Front. Ecol. Environ. 2 (6), 299–306. https://doi.org/10.1890/1540-9295(2004)002[0299:MWESIT]2.0.CO;2.

TNRIS - Texas Natural Resources Information System, 2014. Texas Rivers, Streams, and Waterbodies, 2014-02-01. Retrieved on 2020-06-16 from. https://tnris.org.

TPWD - Texas Parks and Wildlife Department, 2013. GIS Maps and Spatial Data: Coastal Bathymetry, 2013-02-01. Retrieved on 2020-06-15 from. https://tpwd.texas.gov/gis/gis-main.

Turner, J.N., Brewer, P.A., Macklin, M.G., 2008. Fluvial-controlled metal and As mobilisation, dispersal and storage in the Río Guadiamar, SW Spain and its implications for long-term contaminant fluxes to the Doñana wetlands. Sci. Total Environ. 394 (1), 144–161. https://doi.org/10.1016/j.scitotenv.2007.12.021.

Uncles, R.J., Stephens, J.A., Woodrow, T.Y., 1988. Seasonal cycling of estuarine sediment and contaminant transport. Estuaries 11 (2), 108. https://doi.org/10.2307/1351998.

US EPA -United States Environmental Protection Agency, 2017. Patrick Bayou Site Profile. Retrieved on 2020- 03-20 from. https://cumulis.epa.gov/supercpad/SiteProfiles/index.cfm?fuseaction=second.Cleanup&id=0605329#bkground.

USGS - United States Geological Survey, 2013. National Elevation Dataset, 2013-01-01. Retrieved on 2020-06-15 from. https://catalog.data.gov/dataset/usgs-national-elevation-dataset-ned.

Vallette, J., 2018. Chlorine and building materials: a global inventory of production technologies, market, and pollution, phase 1: Africa, the Americas and Europe. HBN Know Better Healthy Building Network, Washington D.Chttps://healthybuilding.net/reports/18-chlorine-building-materials-project-phase-1-africa-the-americas-and-europe.

Vecchi, G.A., Soden, B.J., 2007. Global warming and the weakening of the tropical circulation. J. Clim. 20 (17), 4316–4340. https://doi.org/10.1175/JCLI4258.1.

Vecchi, G.A., Soden, B.J., Wittenberg, A.T., Held, I.M., Leetmaa, A., Harrison, M.J., 2006. Weakening of tropical Pacific atmospheric circulation due to anthropogenic forcing. Nature 441 (7089), 73–76. https://doi.org/10.1038/nature04744.

Walsh, K.J., McBride, J.L., Klotzbach, P.J., Balachandran, S., Camargo, S.J., Holland, G., Knutson, T.R., Kossin, J.P., Lee, T.C., Sobel, A., Sugi, M., 2016. Tropical cyclones and climate change. Wiley Interdiscip. Rev. Clim. Chang. 7 (1), 65–89. https://doi.org/10.1002/wcc.371.

Ward, G.H., 1980. Hydrography and circulation processes of gulf estuaries. Estuarine and Wetland Processes. Springer, pp. 183–215 https://doi.org/10.1007/978-1-4757-5177-2_7.

Warner, K.A., Roden, E.E., Bonzongo, J., 2003. Microbial mercury transformation in anoxic freshwater sediments under iron-reducing and other electron-accepting conditions. Environmental Science & Technology 37 (10), 2159–2165. https://doi.org/10.1021/es0262939.

Williams, J., Dellapenna, T., Louchouarn, P., Lee, G., 2015. Historical reconstruction of anthropogenic mercury input from sedimentary records: Yeongsan estuary, South Korea. Estuar. Coast. Shelf Sci. 167, 436–446. https://doi.org/10.1016/j.ecss.2015.10.021.

Hurricane Harvey Delivered a Massive Load of Mercury Rich Sediment to Galveston Bay, Texas

Timothy M. Dellapenna[ab*], Lisa Hill[a], Christena Hoelscher[b], Lindsay Critides[a], Victoria Bartlett[a], Mason Bell[a], Mohammad E. Al Mukaimi[c], Jaibi Du[d], Kyeong Park[ab], and Anthony H. Knap[e]

[a]Department of Marine and Coastal Environmental Science, Texas A&M University at Galveston
[b]Department of Oceanography, Texas A&M University
[c]Department of Marine Science, University of Kuwait
[d]Woods Hole Oceanographic Institute
[e]Geochemical and Environmental Research Group (GERG), Texas A&M University

1. Abstract

Hurricane Harvey (Harvey), a slow-moving storm, struck the Texas coast as a Category 4 hurricane. Over the course of 46 days, the floodwaters of Harvey delivered $14x10^9$ m^3 of freshwater to Galveston Bay. This resulted in record flooding of all of the tributaries that flow into Galveston Bay, including Buffalo Bayou, which drains all of the bayous and waterways that drain Metropolitan Houston and flows into the San Jacinto Estuary (SJE). Harvey deposited a total of $1.49x10^6$ tons of sediment and 6.93 tons of Hg to the Galveston Bay system (including the SJE) which is equivalent to 27 years of average annual sediment load to the bay. Elevated land subsidence within lower Buffalo Bayou and the SJE resulted in the archiving of extremely elevated concentrations of HgT resulting from this historical release of Hg from industrial wastewater outfalls located within Patrick Bayou. Floodwaters from Harvey resulted in the erosion of $16.4x10^6$ tons of sediment and at least 2 tons of Hg from the SJE, and 1.43 tons of HgT from Patrick Bayou. It is believed that the remaining 2.15 tons of Hg found within Galveston Bay was sourced from the sediments within lower Buffalo Bayou. The initial discharge of floodwater and sediment during peak discharge rapidly exited Galveston Bay and was dispersed within the Gulf of Mexico. The amount of sediment and Hg dispersed in the Gulf of Mexico due to Harvey has yet to be investigated. The prolonged flooding due to the slow release of floodwaters trapped within the Barker and Addicks Reservoirs resulted in prolonged hydraulic trapping of both floodwaters and floodwater derived suspended sediment within Trinity and upper Galveston Bay as well as, to a lesser extent, within East Galveston Bay. The Hg associated with these sediments resulted in this sediment load resulted in the broad dispersal of Harvey derived Hg throughout Galveston Bay. With the increase in slow-moving storms and the archiving of legacy contaminants within urbanized estuaries, especially where there is elevated land subsidence suggests that the impact and dispersal of legacy contaminants within Galveston Bay by Harvey is a harbinger of things to come to other, urbanized estuaries throughout the world.

1. Abbreviations

HgT- Total Mercury
PDP- Peak Discharge Phase
PPDP- Post Peak Discharge Phase
SJE- San Jacinto Estuary

2. Introduction

Hurricane Harvey (Harvey) struck the Texas coast between 25-27 August 2017, making landfall as a Category 4 hurricane, and delivered between 76.2 and 127 cm of rain to the Houston Metropolitan area (Fig. 1) and the drainage basin of Galveston Bay (NOAA, 2017). Although the initial flooding from most tributaries lasted less than two weeks, the Barker and Addicks Reservoirs on the west side of Houston (Fig. 2) threatened to flood communities built inside of the reservoir, so a controlled release of retained stormwater resulted in a 53-day flood of Buffalo Bayou. In total, Harvey delivered $14x10^9$ m^3 of freshwater to Galveston Bay, a volume equivalent to 3.7 times the volume of the entire bay (Du et al., 2019a,b). This record rainfall resulted in unprecedented flooding of Houston bayous and waterways, all of which drained into the San Jacinto Estuary (SJE). The main tributaries of the SJE are Buffalo Bayou and the San Jacinto River and the SJE empties into Galveston Bay at Morgan Point (Fig. 2). The lower Buffalo Bayou and lower SJE contain the intensely industrialized Houston Petrochemical complex and the Port of Houston. Dellapenna et al. (2020) found floodwaters of the SJE seabed during Harvey eroded an estimated that $16.4x10^6$ tons of sediment and at least 2 tons of Hg were scoured and transported into Galveston Bay. Within Scott Bay, they found that the upper 48 cm of seabed was eroded during the Harvey flood. They also found that at least an additional 1.43 tons of

HgT was eroded from Patrick Bayou during the peak of the floodwater discharge. The flood also deposited $3x10^6$ tons of sediment, including 22 cm thick sediment flood layer in Scott Bay and 0.96 tons of HgT was deposited within the SJE, mostly sourced from Buffalo Bayou (Dellapenna et al., 2020). The primary source of HgT is attributed to the wastewater outfalls contained with Patrick Bayou, a small slough located 4.3 km upstream from the confluence of Buffalo Bayou and the SJE, where an oxyvinyls plant has historically released Hg in their wastewater stream (Vallette, 2018).

Mercury (Hg) is one of the most detrimental global aquatic contaminants (Bank, 2012; Liu et al., 2011). In marine environments, Hg bioaccumulates as methyl mercury, contaminates seafood, and thus poses a human health hazard (Di Leonardo et al., 2006). There are likely numerous sources of Hg within the Galveston Bay drainage basin, including atmospheric outfall from coal combustion, effluent from wastewater treatment, agricultural runoff, and various industrial runoffs (Al Mukaimi et al., 2018b). However, historically, the greatest source of Hg within the drainage basin is industrial wastewater runoff from Patrick Bayou, a small tributary of Buffalo Bayou, with a water surface area of 0.18 km^2, located 4 km upstream from the confluence of Buffalo Bayou and the SJE (Dellapenna et al., 2020). Patrick Bayou is a US Environmental Protection Agency (EPA) Superfund Site for Polyaromatic Hydrocarbons (PAHs), Polychlorinated Biphenyls (PCBs), Dioxins, Hg, and several other industrial contaminants (US EPA, 2017). Industrial wastewater discharge into PB from a Chloralkali plant located within Patrick Bayou is listed by the EPA as the likely source of the contamination (US EPA, 2017). A core collected 200 m from the mouth of Patrick Bayou had HgT concentrations of 51,270 ng g^{-1} at a depth of 19.5 cm (2 cm below the Harvey erosional surface) is over 1,000 times background concentrations and is the highest concentration found anywhere else in Galveston Bay, by a factor of 20 (Dellapenna et al., 2020).

Al Mukaimi et al. (2018A) investigating the historical input of Total Mercury (HgT) into Galveston Bay. In this study, they found that surface HgT concentrations vary widely from site to site, around the bay, ranging from between 6 - 162 ng g^{-1}, with an average of 50.0 ng g^{-1}, generally following the previously reported range of 10 - 280 ng g^{-1} (Morse et al. 1993; Santschi et al. 2001), with the highest concentrations of surface HgT within the SJE, with elevated concentrations within Clear Lake and the portion of upper Galveston Bay proximal to the mouth of Clear Lake, and also within Trinity Bay down-stream of the mouth of the Trinity River, suggesting both Clear Lake and the Trinity River as additional sources of Hg. In areas distal from these sources, including East and West Galveston Bay, T-H ranged between 15 to 48 ng g^{-1}, approach background concentrations. Mukaimi also documented that background concentrations of HgT, in deeper sections of the core, likely deposited during the pre-Industrial period of the bay, ranged range from 8-20 ng g^{-1} (Al Mukaimi et al., 2018b). NOAA considers levels of 4-51 ng g^{-1} as background conditions (Buchman, 2008).

Harvey was a slow-moving tropical cyclone. The amount of precipitation a tropical cyclone delivers is inversely proportional to the translational speed of the storm (Kossin, 2018), thus, slower-moving storms deliver more precipitation than fast-moving storms, having the potential to deliver substantially greater volumes of floodwaters. Since 1949, globally, there has been a 10% decrease in the translation speed of storms (Kossin, 2018). With an increase in anthropogenically enhanced climate change, there is also a trend towards an increase in persistent weather extremes (Mann et al., 2017), an increase in the frequency and intensity of tropical cyclones (Held and Soden, 2006; He and Soden, 2015; Vecchi and Soden, 2007; Vecchi et al., 2006, and He et al., 2017), and, with an increase in global temperature, there is also an anticipated increase in the amount of rain associated with tropical cyclones (Kossin et al., 2018; Walsh et al., 2016). These slow-moving storms can cause catastrophic flooding, as was the case with Harvey (2017) and more recently Hurricane Florence (2018), which struck Wilmington, NC. When this intense precipitation falls within the watersheds of urbanized/industrialized estuaries, the associated floods increase the risk of erosion and dispersal of legacy contaminated sediments (e.g. Santschi et al., 2001). Many of the world's urbanized estuaries and

deltas are experiencing elevated rates of subsidence (Jelgersma, 1996; Syvitski et al., 2009; Tessler et al., 2015; Al Mukaimi et al., 2018a), which can lead to the archiving of legacy contaminants in their sediments (Uncles et al., 1988; Olson et al., 1993; Mitra et al., 1999; Kennish, 2002; Swales et al., 2002). When these subsiding, urbanized/industrialized estuary subjected to slow moving storms with high rainfall, there is a greater potential that the sediment and associated contaminants will be eroded in the upper reaches of the estuaries, where currents are stronger, and dispersed.

The impact of Harvey provides the opportunity to investigate what happens when a heavily industrialized estuary, which has undergone significant land subsidence and which sediment contains an archived of legacy contaminants, is hit by a major flood event associated with a slow-moving hurricane. Dellapenna et al. (2020) investigated the how the flooding associated with Harvey eroded and transported massive amounts of mercury contaminated sediment within Buffalo Bayou, Patrick Bayou, and the SJE. This paper is a continuation of this work and investigates how the sediment and HgT transported from the SJE, as well as the other tributaries of Galveston Bay (Galveston, Trinity, and East Galveston Bay as well as Clear Lake) were dispersed and trapped within the bay.

3. Material and methods

3.1. *Study Area*

Buffalo Bayou flows 75 km from the Barker and Addicks reservoirs through the heart of metropolitan Houston before emptying into the SJE, which then flows into Galveston Bay (Fig. 2). Houston is the fifth-largest metropolitan area (population of 7 million) and is the fourth-largest city in the US. Houston hosts the second-largest petrochemical complex in the world (Morse et al., 1993; Santschi et al., 2001). The Port of Houston is the second-largest seaport in the U.S. in terms of total shipping tonnage (Chambers et al., 2018).

Galveston Bay is a typical shallow bar-built estuary, with the 3.25 km wide Bolivar Roads Inlet separating Galveston Island and Bolivar Peninsula (Figure 2). The entire Galveston Bay system is the second-largest natural semi-enclosed subtropical estuarine system in the Gulf of Mexico and the seventh-largest in the United States, with a surface area of 1554 km^2, mean depth of 2.46 m, and has a volume of 3.8 billion m^3 (Du et al., 2019a,b,c). The Galveston Bay system is composed of five major sub-bays: Upper and Lower Galveston Bay, Trinity Bay, West and East Galveston Bays (Fig. 2). Galveston is micro-tidal, with a 0.5 – 0.7 m tidal range (Armstrong, 1982), and is considered to be meteorologically dominated, given its small tides, shallow depths, and high susceptibility to wind forces (Solis and Powell, 1999; Ward Jr, 1980), with cold fronts driving much of the sediment resuspension and transport (Carlin et al., 2016). In addition, Clear Lake and Taylor Lake are minor sub-bays with an average water depth of 2 m (Fig. 2). The bay receives annual mean river discharge of 350 $m^3 s^{-1}$ from three major rivers, including Trinity River (mean discharge 271 $m^3 s^{-1}$ in 1988-2017), San Jacinto River (mean discharge 65 $m^3 s^{-1}$ in 2006-2017), and Buffalo Bayou (mean discharge 14 $m^3 s^{-1}$ in 2000-2017; Du et al., 2019a). Water exchange with the coastal ocean is limited, with a mean turn overtime of 30-60 days depending on the river discharge as well as wind condition (Solis and Powell, 1999; Rayson et al., 2016). Galveston Bay is a nursing habitat for multiple valuable fisheries, including white and brown shrimp (Stunz et al., 2010), and provides approximately 14% of the US wild catch of oysters (Haby et al., 2009).

A large amount of groundwater has been withdrawn to support the expanding population of metropolitan Houston and the growing petrochemical complexes has resulted in as much as 3 m of land subsidence across much of the greater Houston area including the upper Galveston Bay and the SJE since 1900 (Coplin and Galloway, 1999; HGSD, 2013). Al Mukaimi et al. (2018a) addressed the question of whether sedimentation has kept pace with subsidence and found that within the lower SJE, the average sedimentation was at half of this rate, averaging 1.5 cm yr^{-1}, about half of the subsidence

rate. The elevated subsidence within the lower SJE resulted in the elevated preservation of legacy contaminants, including Hg, Pb, Ni, and Zn to depths greater than 1 m (Al Mukaimi et al., 2018b).

3.2. *Data collection and core processing*

A total of 56 sites across Galveston Bay for this study, with SJE, upper Galveston Bay, Clear Lake and Trinity Bay cores collected between Oct. 13 and Dec. 4, 2017 and lower Galveston Bay, East Galveston Bay and Dickinson Bayou cores collected on May 15, 2018. All pushcores were collected using a repurposed Benthos® checkvalve pushcoring head, which was attached to an aluminum conduit with stainless steel hose-clamps and electrical tape. The conduit was in 1.5 m long sections that screwed together, with a maximum length of 5 m. The removable core barrels consist of 7.6 cm diameter polycarbonate tubes generally ranging in length from 0.3-0.6 m. During recovery, the pushcoring system was brought to the surface and the core barrels were capped while the end of the core was still in the water to prevent the loss of the cores from the check valve. While holding the core vertically, the bottom core cap was immediately sealed with electrical tape while still being kept vertical. Flourofoam was pushed into the core top so that it rested just above the sediment-water interface, the flourofoam was cut flush with the top of the core barrel and then the top of the core was sealed with a core cap and electrical tape and stored vertically for transport back to the lab. None of the recovered cores showed any signs of degradation from transportation. Boxcores were collected within the Houston Ship Channel, and subcores were extracted from the boxcore using the same polycarbonate subcores, and flourofoam was inserted into the top of core as described above and the bottom of the subcore was capped and taped. All of the cores were stored in a cold room which is held at a constant temperature of 4^{o}C. X-radiographs were taken of all cores at an energy level of 64 kV and exposure time of 1.6 mAS with a portable Medison X-ray source and a Varian PaxScan® Amorphous Silicon Digital Imager.

After each core was x-rayed, the entire Harvey layer was extruded. In some cases, each on centimeter interval was collected, in others, the entire interval was extruded as a single sample. For those for which the sediment was extruded into 1 cm intervals, a subsample of each interval of equivalent volume was combined to make a single Harvey sample and homogenized and subsamples of this were collected for Hg and grain size analyses. For those samples where the entire interval was sampled, the interval was homogenized and subsamples were collected for Hg, grain size distributions, and water content. From the x-radiographs, the base of the Harvey was determined (described below) as well as the thickness of the layer and recorded (Table 1-Supplement).

3.3. *Total mercury analysis*

For the analysis of total mercury concentration (HgT) in the sediments, approximately 100 mg of dry and homogenized pulverized sediment samples at 5 cm intervals were analyzed using Direct Mercury Analyzer (DMA-80, Milestone srl, Italy) which is compliant with U. S. EPA Method 7473 (EPA, 1998). The DMA-80 was calibrated using prepared standard solutions of mercury and the calibration curve was verified with Certified Reference Materials (CRMs). In order to ensure precision, reliability, accuracy, and consistency of the sediment samples for the total Hg, three CRMs including MESS-3 marine sediment (0.091±0.009 ppm, National Research Council of Canada), NIST 2702 Inorganics in marine sediment (0.4474±0.0069 ppm, National Institute of Standards and Technology), and PACS-2 marine sediment (3.04±0.2 ppm, National Research Council of Canada) were used to represent a different Hg range. Once the instrument was calibrated with liquid standard solutions, the calibration curve was verified with the three CRMs. Blanks and duplicates were analyzed every 10 samples to ensure accuracy. The results obtained from the CRMs were excellent and in good agreement within the certified range with an average recovery rate of 97±7% (Mean ± RSD, n = 137) for MESS-2, 96±7% (n = 43) for NIST 2702, and 97±11% (n = 64) for PACS-2.

3.4. *Map preparations using Geographic Information System (GIS)*

The maps used in this study were created using various ArcMap Pro 2.5.1 mapping tools. The basemaps were created using elevation data from the United States Geological Survey and bathymetry data (USGS, 2013) from the Texas Parks and Wildlife Department (TPWD, 2013). The development data was retrieved from NOAA (NOAA, 2016). The raw data set was inserted into ArcGIS and was reclassified so that only medium to high development is shown. The shoreline data was retrieved from the Texas Natural Resources Information System (TNRIS, 2014). Contours of the data were generated using the Inverse Distance Weighted (IDW) tool, which assumes that the influence of a variable decreases with distance. The flood deposit volume was determined based on the contoured data for each sub-bay and converted to mass by assuming a water content of 70% and a sediment density of 2.65 g cm^3, which is the density of quartz. To estimate HgT masses for each sub-bay, an average concentration was used for each sub-bay and the concentration was multiplied by the mass of sediment within the sub-bay.

4. Results

4.1. *Harvey layer thickness*

A total of 56 sites across Galveston Bay, Trinity Bay, East Galveston Bay, the SJE, Clear Lake, and Dickinson Bayou were sampled using a pushcorer in the areas not occupied by dredged channels (Fig. 4b). An x-radiograph was taken of each core. From the x-radiographs, the base of the Harvey was determined as well as the thickness of the layer and recorded (Table 1-Supplement). For most cores, the base of the Harvey deposit was easily identified as an anomalous erosional surface with a sand layer sitting atop of it, and above this a high-water content mud deposit (Fig. 6). The sand layer was evident as a lighter tone in the x-rays and is an anomalous feature within these cores as they were all collected in areas where the remainder of the cores are mud dominated. In many cores, there were also shells, many of which were articulated, also sitting atop the erosional surface.

Although our focus in this study was primarily outside of the dredged channel, we did collect box cores within the channel in December 2017. Despite the maximum depth of 60 cm of the box core, most of the box cores could not penetrate the entire Harvey flood deposit, indicating that the flood layer was thicker than 60 cm in these locations.

The contours on the map range from 0-47 cm, showing the range of cores from those areas outside of the dredge ship channel. The Houston Ship Channel is a 80 km long navigational channel that extends from the mouth Galveston Bay to the lower reach of Buffalo Bayou, it is 160 m wide and 14 m deep. For the basis of consideration of the Harvey deposit across Galveston Bay, the dredged Houston Ship channel was ignored as it only represents approximately 0.5% of surface area of the entire bay.

The Harvey Isopach maps (Fig. 6) show that the thickest deposits were found within the SJE south of the confluence with Buffalo Bayou, with thicknesses exceeding 50 cm. Thicker deposits were also found in Galveston Bay at the mouth of the SJE and Clear Lake with a maximum thickness of 22 cm. The Harvey deposit is thicker in upper Trinity Bay and along the southeastern side of Trinity Bay, with thicknesses averaging 20 cm. The thickest Harvey deposit south of the SJE is found along the 8 km long Texas City Dike where there is a maximum thickness of 37 cm.

Using ArcGIS, we determined the volume of the entire flood layer to be 1.88×10^8 m^3. Using the density of quartz (2.65 g cm^{-3}) for the sediment density and an average water content for the flood deposit (70%), this volume of flood layer is equivalent to a mass of 149.65×10^6 metric tons. Table 1 provides a break-down of the mass of the flood deposit per sub-bay. Note that there are nearly

equivalent masses of Harvey deposits within Upper Galveston Bay, Trinity Bay, and Lower Galveston Bay.

The Trinity River provides about 77% of the freshwater input to Galveston Bay (Du et al., 2019a) with an average sediment load of 4.23×10^6 metric tons (Dellapenna et al., 2006). With the assumption of the remaining 23% of the freshwater discharge coming in with the same sediment concentration, we can estimate 5.49×10^6 metric tons for the average annual sediment load into Galveston Bay. A comparison of this average annual sediment load to the sediment load during Harvey indicates that the amount of sediment delivered to the bay during Harvey is equivalent to 27.2 years of average annual sediment load to the bay.

4.2. Estimating HgT mass and fluxes into Galveston Bay

As noted above, each of the Harvey HgT samples were collected and analyzed as an integrated sample, representing the average integrated concentration of HgT for the Harvey deposit for the specified sample location. The two highest HgT integrated concentrations were found in the SJE; Core HSC VC2 had a Harvey integrated deposit HgT concentration of 669 ng g^{-1} within Burnett Bay, 2.8 km from the mouth of Buffalo Bayou, and Post Harvey Core 22 had a HgT integrated concentration of 80 ng g^{-1}. Using the HgT integrated concentrations from all of the pushcores, a HgT integrated concentration map (Fig. 4b) was generated using ArcGIS, following the same protocols as the other contoured maps in this paper. However, the contours ranges from 0-60 ng g^{-1} to reflect the variations found within Galveston Bay. If the total range of HgT integrated concentrations were used, the variations in HgT integrated concentrations for Galveston Bay in the map would not be evident, as the entire variations would fall within only a few contour intervals. The Harvey deposit HgT integrated concentration in Fig. 4b shows that within Galveston Bay, south of the SJE, that the highest HgT Harvey integrated concentrations are found within Trinity Bay and upper Galveston Bay. These are also the areas where the highest HgT surface concentrations were found pre-Harvey (Fig. 4a). The lowest HgT integrated concentrations were found in lower Galveston Bay and East Galveston Bay, also where the pre-Harvey HgT surface concentrations were the lowest.

The Harvey HgT difference map (Fig. 4c) shows that within the Harvey deposit, there is an enrichment in HgT within much of the SJE, centered around the confluence of the SJE and Buffalo Bayou, much of upper Galveston Bay, the lower half of Trinity Bay, as well as the area just north of the Texas City Dike in lower Galveston Bay and also eastern East Galveston Bay. The Harvey HgT difference map (Fig. 4C) shows net depletion of HgT in the upper reaches of Trinity Bay, much of Clear Lake, Dickinson Bayou, Moses Lake, and mid-Galveston Bay, south of Redfish Reef.

5. Discussion

5.1. Hurricane Harvey sediment dispersal in the SJE

The flooding of the SJE and Galveston Bay can be divided into two phases (Fig. 3), with the first phase being the peak discharge of Buffalo Bayou, the San Jacinto and Trinity Rivers, and Clear Creek, hereinafter referred to as Peak Discharge Phase (PDP), and the second phase being the cintunued discharge from Buffalo Bayou due to the prolonged release of floodwaters from the Barker and Addicks Reservoirs, hereinafter referred to as the Post-Peak Discharge Phase (Post-PDP). The PDP of flooding occurred between August 23 to September 11, 2017, with peak discharges ending around September 5 or 6, depending on the rivers. For Buffalo Bayou, the peak discharge of 200 m^3 s^{-1} lasted for 16 days, from August 27 to September 11, 2017. For the Post-PDP, within Buffalo Bayou, the flood continued, settling down to a nearly continuous 80 m^3 s^{-1} during the controlled release, until it finally dropped off on October 13, 2017, for an additional 32 days. Between September 17 to October 13, 2017, approximately $1.7x10^8$ m^3 of floodwaters came from the Barker and Addicks Reservoirs.

During the PDP, the Morgan Point tidal gauge (location shown in Fig. 2) reported currents in excess of 2 m s^{-1} for five days, between August 27 and September 1, 2017, and in excess of 3 m s^{-1} for approximately 48 hours within this interval (Du et al., 2019a). The bay bottom along lower Buffalo Bayou and the SJE consists primarily of soft, easily erodible estuarine mud and all the water flowing through Morgan Point flowed through Buffalo Bayou and the SJE during the PDP, with currents capable of significant erosion of the bed. Within Scott Bay, Dellapenna et al. (2020) found that there was 48 cm of soft estuarine mud eroded, and in total, they estimated that Harvey scoured 16.42 $x10^6$ tons of sediment from the SJE. This sediment was transported to Galveston Bay, and Modis satellite imagery (Modis image) shows a significant sediment plume extending into the Gulf of Mexico from Galveston Bay through the Bolivar Roads inlet. According to Dellapenna et al. (2020), during the period of time represented by the falling limb of the hydrographs, Aug. 28-Sept. 11 (PDP) for the San Jacinto River/Estuary and Sept. 9-19, 2017 for Buffalo Bayou, the sediment derived from the San Jacinto River settled out, with the largest deposit found north of the confluence with Buffalo Bayou. For the SJE, below the confluence with Buffalo Bayou, the initial deposition is a basal deposit consisting of sand and gravel (shell), representing bedload, ~10 cm thick. Above the basal bedload deposit is the 12 cm thick upper layer, which is mud dominated and represents the settled suspended load.

In total, Harvey deposited 7.73$x10^6$ tons in the SJE. Using HgT data, in combination with the textural analyses of sediment and the foraminifera data (Hill, 2020), Dellapenna et al., (2020) found strong evidence that the Harvey flood deposits found in Burnet and Scott Bay were likely sourced from lower Buffalo Bayou, where salinities are low but still brackish and San Jacinto River upstream of Burnet Bay. Considering the high HgT concentrations, this suggests a source proximal to Patrick Bayou and was likely delivered during the waning of the PDP. The flood layer found in the lower SJE, including Tabbs Bay (Fig. 6b) suggests an upper drainage basin source and was likely delivered primarily during the Post-PDP of the flood, during the release of water from the Addicks and Barker Reservoirs.

5.2. *Hurricane Harvey Sediment Dispersal in Galveston Bay*

Not counting the Harvey deposit in the SJE, Harvey deposited 133.03$x10^6$ tons of sediment in Galveston Bay, with nearly equal amounts deposited in upper Galveston Bay, Trinity Bay, and Lower Galveston Bay (Table 1). Within Galveston Bay, the thickest Harvey deposits are found where the SJE empties into Galveston Bay, on the north side of the Texas City Dike, at the mouth of Clear Lake, and within the middle of Trinity Bay. The deposits at the mouths of the SJE and Clear Lake result from the reduction in currents as the sediment plumes entered Galveston Bay. The thicker Harvey deposit within Trinity Bay likely results from a hydrodynamic trapping of floodwaters, explained in more detail below.

The thickest deposit, at 37 cm, is found north of the Texas City Dike, and this deposit was noted in the field notes as having a notably high sand content. The Texas City Dike extends southeastward from the southwestern shore of Galveston Bay 8.5 km into Galveston Bay. Between the southern end of the dike and the northern tip of Pelican Island, there is a 1.3 km opening between Galveston Bay and West Bay. The Texas City Dike was originally constructed in 1915 to block sediment from entering the Texas City Channel, which is the entrance channel to the Port of Texas City (Moore Memorial Public Library, 2017). The Texas City Dike separates Galveston Bay from West Galveston Bay and also, along with Pelican Island, which blocked the transport of the Harvey flood pulse from entering West Bay. The Texas City Dike deposit also lies within the Bolivar Roads flood tidal delta. A rapid response survey of the Bolivar Roads inlet revealed no Harvey deposition (W. Sager, person. comm.), which is not surprising as this is where the currents would have been strongest as the floodwaters exited Galveston Bay.

5.3. *Flood pulse timing and hydrodynamic trapping of floodwaters in Trinity Bay*

Du et al. (2020) used a Lagrangian particle-tracking method coupled with a 3D hydrodynamic model for Galveston Bay and the shelf of the northern Gulf of Mexico to examine the retention, pathway, and fate of released particles (pollutants) both during the PDP as well as the Post-PDP (Fig. 7). In this modeling simulation, the particles are considered to be neutrally buoyant with no specified mass, which would imply that they are simulating the transport of clay fraction of suspended sediment. Du et al. (2020) defines a new parameter, the Local Exposure Time (LET) to quantitatively evaluate the spatially varying susceptibility within the bay and on the shelf, with a longer LET indicating regions that are more susceptible to the pollutant. They compared particle released from the petrochemical facilities along the Buffalo Bayou and San Jacinto River at two different time periods of during (August 26–30, PDP) and after (September 3-7, Post-PDP) the storm (Fig. 3). They also ran a simulation in which particles were released at the mouth of the Trinity River, i.e., where the Trinity River empties into Galveston Bay.

Du et al. (2020) found that for particles released within the SJE during the PDP (Fig. 7a), that 90% of the particles were flushed from the bay within 2 days, with a maximum LET of 0.3 h along the longitudinal axis of Galveston Bay, roughly along the Houston Ship Channel, and generally 0.1 h or less for areas away from the longitudinal axis of the bay. They also found that during the PDP, there was no tidal (i.e. back and forth) movement. After exiting the bay, due to the strong seaward momentum, the particles moved as far as 50 km offshore. They found that for the particles released within the SJE during the Post-PDP (Fig. 7b), there was a median transit period of 60-90 days, a LET generally between 2-3 h, and that the particles tended to move primarily into Trinity and, to a lesser extent, into East Galveston Bay and that particles stayed within these bays for a longer time. With the longer residence times within these bays, presumably, particles settle out of the water column, a factor not considered in the modeling exercise. The particles became trapped in Trinity and East Galveston Bay due to the small tidal range and slow water renewal in Trinity Bay. Hydrodynamic modeling of Galveston Bay (Du et al., 2019c; Du and Park, 2019) found a negligible tidal signal and a two-month period for salinity recovery. Du et al. (2020) also modeled the release of particles from various locations and found that when particles were released from the mouth of the Trinity River, at the head of Trinity Bay (Fig. 7c), that the particles had their longest residence times along the southeastern shore of Trinity Bay. When we compare the particle trace map to the isopach map of the Harvey flood deposit within Trinity Bay (Fig. 7c and 10f), we see that the flood deposit is thickest along the middle and eastern side of the bay and correlates fairly well with the areas with the highest LET. It would appear that this results from a combination of discharge of sediment from the Trinity River and the entrainment and trapping of sediment from the SJE into Trinity Bay.

5.4. *Sources of Hg*

According to Al Mukaimi et al., (2018), Hg is sourced to Galveston Bay through both point-sources and non-point sources. Non-point sources include atmospheric fallout from coal-burning and runoff from fertilizer, industrial waste streams from paper mills. However, as Dellapenna et al. (2020) documented, the wastewater treatment outfalls of Patrick Bayou have been the primary source HgT for both the SJE and for much of Galveston Bay. In addition, Patrick Bayou has also been a secondary source, being the source of legacy HgT within the sediment that was eroded from both Buffalo Bayou and the SJE. As noted above, Dellapenna et al. (2020) reported that 2 tons of HgT were scoured from the SJE, and 1.43 tons of HgT were scoured from Patrick Bayou during Harvey. As noted above, there was a total of 6.93 tons of HgT contained within the Harvey deposit across Galveston Bay, including the SJE and Patrick Bayou. If we assume that the 6.93 tons of HgT in Galveston Bay was almost entirely sourced from the combined legacy contaminants contained within the scoured sediments from

SJE, Patrick Bayou and Buffalo Bayou, then this means that at least 3.5 tons of HgT was sourced from legacy contaminants, which were contained within eroded Buffalo Bayou sediment. Given the extremely elevated concentrations of HgT found near the mouth of Patrick Bayou, this is a reasonable assertion.

5.5. Distribution of Hg in Galveston Bay

Within Galveston Bay, the highest post-Harvey integrated HgT concentrations are within Trinity Bay and upper Galveston Bay, north of Eagle and Smith Points. As noted above, Table 2 shows that within upper Galveston Bay there was a 57.9% increase in HgT and a 122.2% increase in East Galveston Bay. Although the Harvey integrated HgT maps (Fig. 4c) show a high concentration of HgT in some aprts of Trinity Bay, on average, there was actually a net decrease in the concentration of 8.6% and also a decrease of 21.7% in Clear Lake. Not much is known about the historical sources of HgT in Clear Lake and its sub-bays. The elevated HgT concentration observed in the HgT difference map (Fig. 4c) along with the deposit north of the Texas City Dike most likely results from the elevated overall trapping of sediment from this area.

When we consider the distribution of post-Harvey HgT within Galveston Bay (Fig. 4b) in the context of the particle release model results, it should be noted that Hg is a particle-bound contaminant primarily partitioned to the clay fraction due to the higher surface area to volume ratio of clays. When we compare the LET map for particle releases for the Post-PDP (Fig. 7b), we see that the sediment with the highest integrated HgT concentrations correlates well with the portions of the bay with the longest LET. This strongly suggests hydraulic trapping of the Harvey suspended load within the upper bay as the primary control on the distribution of the integrated post-Harvey HgT within Trinity and Upper Galveston Bay. Although the overall integrated HgT concentrations in East Galveston Bay is quite low, the HgT difference map (Fig. 4c) shows an enrichment of HgT, also explained by hydraulic entrainment and trapping of Harvey suspended sediment within East Galveston Bay.

Figure 7 is an idealized map showing the generalized pathways of particles that were released at different times and from different locations during the Harvey flood. The solid blue lines show the pathways of particles released during the PDP, showing that the flooding of Buffalo Bayou during this phase occurred primarily below the Barker and Addicks Reservoirs, but extended across all of urban Houston. In addition, during this phase, there was extensive flooding within the other tributaries shown. In general, because the flows were so strong and also unidirectional, the majority of the particles were transported from their respective tributaries into the bay and then advected offshore. The yellow-toned area within the lowermost Buffalo Bayou and parts of the SJE depicts the source areas of HgT and are the areas where, during the rising phase of the PDP, the bay bottom was scoured from the high currents, transporting the HgT enriched sediment into Galveston Bay. The red-toned areas depict those areas that received elevated deposition during the early phase of the falling limb of the hydrograph during the Post-PDP. During the Post-PDP, particles flowed into the bay, as shown in orange, and the eddies depicted by the orange lines in Trinity and are meant to depict the hydraulic trapping of particles due to the small tidal range and slow water renewal. The darker brown tone in the Trinity and upper Galveston Bay are meant to depict the greater deposition of both sediment and higher concentrations of HgT, which was primarily the result of the greater hydraulic trapping in these areas. The lighter brown tone in lower Galveston Bay and East Galveston Bay are meant to depict lower deposition of sediment and HgT in these areas.

The pre- and post-Harvey integrated HgT concentration maps (Fig. 4a,b) are very similar. As this study demonstrates, a single storm can have sediment yield comparable to years, if not decades, of average fluvial sediment yield, resulting in the scouring and delivery of legacy contaminants within the bay and tributary bottoms. It is likely that previous storms, such as Tropical Storm Allison (June 4-20, 2001), which was the previously largest flooding event for Houston, also had floodwaters and

suspended sediment hydraulically trapped within Trinity Bay for a prolonged period of time. This may well explain the elevated integrated HgT concentrations within Trinity Bay pre-Harvey.

5.6. Potential Impacts of the Harvey storm deposit to the benthic community

In addition to the remobilization, transport, and deposition of legacy contaminants, the massive deposition of sediment in Galveston Bay likely had other negative impacts on the ecosystem, especially the benthos. Episodic deposition of a thick column of sediment has been documented to have a detrimental impact both to the abundance and diversity of benthic communities (Miller et al., 2002; Chou et al., 2004; Naser, 2011). The erosion of nearly 0.5 m of sediment coupled with deposition of decimeters of sediment in the SJE (Dellapenna et al., 2020) is comparable to that found in the York River estuary (Dellapenna et al., 1998, 2001, 2003; Schaffner et al., 2001) where massive deposition (coupled with erosion) resulted loss of all macrobenthic organisms and much of the microbenthic community. Thrush et al. (2004) summarized, based on the previous field and laboratory studies, that a critical threshold of episodic deposition of 2 cm in an estuary will quickly create anaerobic conditions within the seabed, resulting in the death of the resident faunal community. The benthic and pelagic coupling within an estuary is central to the nutrient cycling and overall productivity of the system, and an interruption of this coupling resulting from elevated sedimentation rates can have dramatic impacts on the entire ecosystem (Eyre and Ferguson, 2006).

The average Harvey layer thickness across Galveston Bay was 14 cm (Table 1), with thicker deposits found in portions of the SJE, Patrick Bayou, Trinity Bay and lower Galveston Bay (Fig. 6). All of these deposit thicknesses exceed the 2 cm threshold of Thrush et al. (2004) and suggest that the conditions were right to have a significant impact on the benthos. Although there were numerous studies on the impact of Harvey on the water quality (Steichen et al., 2020), the zooplankton communities (Topor et al., 2020), the phytoplankton communities (D'Sa, 2019), and on the water column microbial communities (Steichen et al., 2020; Bacosa et al., 2020), to-date, nothing has been published on its impact on the benthic community or the benthic pelagic coupling. Harvey also had an impact on the oyster harvest in the bay. Wild oyster harvest in Galveston Bay averages $43 million in revenue annually (Ropicki et al., 2018) and provides 14% of the U.S wild catch of oysters (Haby et al., 2009). The long residence time of freshwater in the bay resulted in 50-100% mortality in East Galveston Bay and mortality rates ranging from 8 -90% in both lower and upper Galveston Bay (Thyng et al., 2020 and personal communication with Christine Jenson, Texas Parks and Wildlife Department). In addition, it was speculated that a reef in Trinity Bay experienced 28% mortality, in part by sediment smothering. It should also be noted that the recovering benthic and epibenthic communities within both the SJE and Galveston Bay will be exposed to elevated levels of a variety of contaminants, including Hg, potentially further exacerbating their recoveries and health.

6. Conclusions

With the increase in slow-moving storms and the archiving of legacy contaminants within urbanized estuaries, especially where there is elevated land subsidence suggests that the impact and dispersal of legacy contaminants within Galveston Bay by Hurricane Harvey is a harbinger of things to come to other, urbanized estuaries throughout the world.

Within Galveston Bay, as well as many of the world's estuaries, Hg is a significant contaminant. Although this study only investigated HgT, Hg bioaccumulates as methyl mercury. Methyl mercury forms within the anoxic conditions found a few centimeters below the surface within estuarine muds. In the context of Hg, it also mobilizes the most toxic forms of Hg, enabling it to be much more bioavailable and enhancing its ability to bioaccumulate in the marine food web. When we consider Harvey and the legacy contaminants archived within the sediments of Patrick Bayou, lower Buffalo Bayou and the lower SJE, the sediment containing Hg were buried within anoxic sediment,

suggesting that much of the Hg was in the form of methyl mercury. This study documents that 6.93 tons of Hg was deposited within the Galveston Bay system from Harvey, however, during the first phase of the flood, much of the flood waters were exported from the bay. The first phase was also when most of the initial erosion of the legacy contaminants, including Hg occurred, and as the modeling study by Du et al. (2020) indicates, there was a two-day residence time of flood waters within the bay. This indicates that there was likely a significant sediment and Hg load exported from the bay during this phase and that much of this Hg was in the form of methyl mercury.

The erosion of nearly 0.5 m of sediment within the SJE and likely comparable erosion with the lower Buffalo Bayou, coupled with the deposition of decimeters of sediment across much of the Galveston Bay system likely had a devastating impact to the benthic community, potentially interrupting the benthic pelagic coupling within the bay. The prolonged residence time of freshwater in the bay had a devastating impact on the bay's oysters and other shell and finfish. The additional delivery of methyl mercury enriched suspended sediment along with the flood waters only added to the environmental impact of Harvey. When we consider that the frequency of slow-moving tropical cyclones capable of delivering devastating rainfall is increasing (Pfahl et al., 2017; Hall and Kossin, 2019), then we can expect an increase in the frequency of extreme flood events that are capable of excavating deeply buried legacy contaminants from the archive of sediment within urbanized estuaries. Consequently, what happened during Harvey is a harbinger of what is to come both for Galveston Bay as well as other urbanized estuaries and deltas around the world.

7. Acknowledgements

We would like to acknowledge the many undergraduate and graduate students who have helped with both the field and lab phases of this work, including M. Bell, O. Cavazos, J. Lewis, N. Wellbrock, A. Bland, and L. Critides. This work was partially supported by the National Institute of Environmental Health Sciences of the National Institutes of Health under Award P42ES027704 and by the Texas General Land Office and the National Oceanic and Atmospheric Administration (NOAA) through the Texas Coastal Management Program under Award 19-040-000-B074.

8. References

Al Mukaimi, M.E., Dellapenna, T.M., and Williams, J.R., 2018a. Enhanced land subsidence in Galveston Bay, Texas: Interaction between sediment accumulation rates and relative sea level rise. *Estuarine, Coastal and Shelf Science*, *207*, 183-193. https://doi.org/10.1016/j.ecss.2018.03.023

Al Mukaimi, M.E., Kaiser, K., Williams, J.R., Dellapenna, T.M., Louchouarn, P., and Santschi, P.H., 2018b. Centennial record of anthropogenic impacts in Galveston Bay: Evidence from trace metals (Hg, Pb, Ni, Zn) and lignin oxidation products. *Environmental Pollution*, *237*, 887-899. https://doi.org/10.1016/j.envpol.2018.01.027

Armstrong, N.E., 1982. Responses of Texas estuaries to freshwater inflows. In *Estuarine Comparisons* (Kennedy, V.S., ed.), Academic Press, pp. 103-120. https://doi.org/10.1016/B978-0-12-404070-0.50013-2

Bacosa, H.P., Steichen, J., Kamalanathan, M., Windham, R., Lubguban, A., Labonté, J.M., Kaiser, K., Hala, D., Santschi, P.H., and Quigg, A., 2020. Polycyclic aromatic hydrocarbons (PAHs) and putative PAH-degrading bacteria in Galveston Bay, TX (USA), following Hurricane Harvey

(2017). *Environmental Science and Pollution Research International*, 27(28), 34987-34999. https://doi.org/10.1007/s11356-020-09754-5

Bank, M.S., 2012. Mercury in the environment: Pattern and process. *International Journal of Environmental Studies*, 69(5), 863-864. https://doi.org/10.1080/00207233.2012.704679

Buchman, M.F., 2008. NOAA Screening Quick Reference Tables. NOAA OR&R Report 08-1, Office of Response and Restoration Division, National Oceanic and Atmospheric Administration, Seattle, WA, 34 p. https://repository.library.noaa.gov/view/noaa/9327

Carlin, J. A., Lee, G., Dellapenna, T. M., and Laverty, P., 2016. Sediment resuspension by wind, waves, and currents during meteorological frontal passages in a micro-tidal lagoon. *Estuarine, Coastal and Shelf Science, 172*, 24-33. https://doi.org/10.1016/j.ecss.2016.01.029

Chambers, M., Mitchell, A., Fine, A., Mulder, K., Rainville, L., Hackett, D., Smith, D., Dijoseph, P., Kress, M., Mitchell, K.N. and Tujague, A., 2018. Port Performance Freight Statistics Program: Annual Report to Congress 2017 [Supporting Datasets]. https://www.bts.gov/browse-statistical-products-and-data/port-performance/port-performance-freight-statistics-program

Chou, L., Yu, J., & Loh, T., 2004. Impacts of sedimentation on soft-bottom benthic communities in the southern islands of Singapore. *Hydrobiologia, 515*(1-3), 91-106. https://doi.org/10.1023/B:HYDR.0000027321.23230.2f

Coplin, L. S., & Galloway, D., 1999. Houston-Galveston, Texas: Managing coastal substance. In *Land Subsidence in the United States: US Geological Survey Circular 1182*, p. 35-48. https://www.researchgate.net/profile/Devin_Galloway/publication/284221420_Houston-Galveston_Texas_Managing_coastal_subsidence/links/565867e408ae4988a7b7454f.pdf

Dellapenna, T., Kuehl, S., & Schaffner, L. (1998). Sea-bed mixing and particle residence times in biologically and physically dominated estuarine systems: A comparison of lower Chesapeake Bay and the York River subestuary. *Estuarine, Coastal and Shelf Science, 46*(6), 777-795. https://doi.org/10.1006/ecss.1997.0316

Dellapenna, T.M., Kuehl, S.A., and Pitts, L. (2001) Transient, longitudinal, sedimentary furrows in the York River subestuary, Chesapeake Bay: furrow evolution and effects on seabed mixing and sediment transport. *Estuaries*, 24, 215-227. www.jstor.org/stable/1352946

Dellapenna, T.M., Kuehl, S.A. and Schaffner, L.C., 2003. Ephemeral deposition, seabed mixing and fine-scale strata formation in the York River estuary, Chesapeake Bay. *Estuarine, Coastal and Shelf Science*, *58*(3), 621-643. https://doi.org/10.2307/1352946

Dellapenna, T. M., Allison, M. A., Gill, G. A., Lehman, R. D., & Warnken, K. W. (2006). The impact of shrimp trawling and associated sediment resuspension in mud dominated, shallow estuaries. *Estuarine, Coastal and Shelf Science, 69*(3-4), 519-530. https:// doi:10.1016/j.ecss.2006.04.024

Dellapenna, T. M., Hoelscher, C. E., Hill, L., Al Mukaimi, M.E., Knap, A., 2020. How tropical cyclone flooding caused erosion and dispersal of mercury-contaminated sediment in an urban estuary: The

impact of Hurricane Harvey on Buffalo Bayou and the San Jacinto Estuary, Galveston Bay, USA. *Science of the Total Environment*, *748*, 141226. https://doi.org/10.1016/j.scitotenv.2020.141226

Di Leonardo, R., Tranchida, G., Bellanca, A., Neri, R., Angelone, M., & Mazzola, S. (2006). Mercury levels in sediments of Central Mediterranean Sea: A 150 year record from box-cores recovered in the Strait of Sicily. *Chemosphere, 65*(11), 2366-2376. https://10.1016/j.chemosphere.2006.04.076

D'Sa, E., 2019. Floodwater impact on Galveston Bay phytoplankton taxonomy, pigment composition and photo-physiological state following Hurricane Harvey from field and ocean color (Sentinel-3A OLCI) observations. *Biogeosciences*, *16*(9), 1975-2001. https://doi-org.srv-proxy1.library.tamu.edu/10.5194/bg-16-1975-2019

Du, J. and Park, K., 2019. Estuarine salinity recovery from an extreme precipitation event: Hurricane Harvey in Galveston Bay. *Science of the Total Environment*, *670*, 1049-1059. https://doi.org/10.1016/j.scitotenv.2019.03.265

Du, J., Park, K., Dellapenna, T.M., Clay, J.M., 2019a. Dramatic hydrodynamic and sedimentary responses in Galveston Bay and adjacent inner shelf to Hurricane Harvey. Sci. Total Environ. 653, 554–564. https://doi.org/10.1016/j.scitotenv.2018.10.403.

Du J., Park K., Dellapenna T.M., Clay J.M., 2019b. Corrigendum to ‘‘Dramatic hydrodynamic and sedimentary responses in Galveston Bay and adjacent inner shelf to Hurricane Harvey” [Sci. Total Environ. 653 (2019), 554–564]. Sci. Total Environ. 697, 134219. https://doi.org/10.1016/j.scitotenv.2019.134219.

Du, J., Park, K., Shen, J., Zhang, Y.J., Yu, X., Ye, F., Wang, Z., Rabalais, N.N., 2019c. A hydrodynamic model for Galveston Bay and the shelf in the northern Gulf of Mexico. Ocean Sci. 15, 951–966. https://doi.org/10.5194/os-15-951-2019.

Du, J., Park, K., Yu, X., Zhang, Y.J. and Ye, F., 2020. Massive pollutants released to Galveston Bay during Hurricane Harvey: Understanding their retention and pathway using Lagrangian numerical simulations. *Science of The Total Environment*, *704*: 135364. https://doi.org/10.1016/j.scitotenv.2019.135364

EPA (1998) Method 7473: Mercury in Solids and Solutions by Thermal Decomposition Amalgamation and Atomic Absorption Spectrophotometry, EPA SW-846. USEPA Office of Research and Development Environmental Monitoring Systems Labratory, Cincinnati.

Eyre, B. D., & Ferguson, A. J. (2006). Impact of a flood event on benthic and pelagic coupling in a sub-tropical east Australian estuary (Brunswick). *Estuarine, Coastal and Shelf Science, 66*(1-2), 111-122. https://doi.org/10.1016/j.ecss.2005.08.008

Haby, M. G., Miget, R. J., & Falconer, L. L. (2009). *Hurricane Damage Sustained by the Oyster Industry and the Oyster Reefs Across the Galveston Bay System with Recovery Recommendations. College Station, TX*. TAMU-SG-09-201.: The Texas A&M University System. 51 pp.

Hall, T.M. and Kossin, J.P., 2019. Hurricane stalling along the North American coast and implications for rainfall. Clim. Atmos. Sci. 2, 17, doi:10.1038/s41612-019-0074-8ence.

He, J. and Soden, B.J., 2015. Anthropogenic weakening of the tropical circulation: The relative roles of direct CO2 forcing and sea surface temperature change. *Journal of Climate*, *28*(22), 8728-8742. https://doi.org/10.1175/JCLI-D-15-0205.1

He, J., Winton, M., Vecchi, G., Jia, L. and Rugenstein, M., 2017. Transient climate sensitivity depends on base climate ocean circulation. *Journal of Climate*, *30*(4), 1493-1504. https://doi.org/10.1175/JCLI-D-16-0581.1

Held, I.M. and Soden, B.J., 2006. Robust responses of the hydrological cycle to global warming. *Journal of Climate*, *19*(21), 5686-5699. https://doi.org/10.1175/JCLI3799.1

HGSD, 2013. Subsidence and groundwater regulation FAQ's. Available at http://hgsubsidence.org/frequently-asked-questions/subsidence-groundwater-regulation-faqs/.

Hill, L. (2020). *Environmental and anthropogenic influences during the 20th century in Scott Bay. San Jacinto Estuary, Houston, Texas.* Unpublished manuscript.

Jelgersma, S., 1996. Land subsidence in coastal lowlands. In *Sea-Level Rise and Coastal Subsidence* (Milliman J.D. and Haq, B.U., eds.), Coastal Systems and Continental Margins, Vol. 2, Springer, Dordrecht, pp. 47-62. https://doi.org/10.1007/978-94-015-8719-8_3

Kennish, M.J., 2002. Environmental threats and environmental future of estuaries. *Environmental Conservation*, *29*(1), 78-107. https://doi.org/10.1017/S0376892902000061

Kossin, J.P., 2018. A global slowdown of tropical-cyclone translation speed. *Nature*, *558*(7708), 104-107. https://doi.org/10.1038/s41586-018-0158-3

Liu, G., Cai, Y., & O'Driscoll, N. (2011). *Environmental chemistry and toxicology of mercury* John Wiley & Sons.

Mann, M.E., Rahmstorf, S., Kornhuber, K., Steinman, B.A., Miller, S.K. and Coumou, D., 2017. Influence of anthropogenic climate change on planetary wave resonance and extreme weather events. *Scientific Reports*, *7*, p.45242. https://10.1126/sciadv.aat3272

Miller, D. C., Muir, C. L., & Hauser, O. A. (2002). Detrimental effects of sedimentation on marine benthos: What can be learned from natural processes and rates? *Ecological Engineering, 19*(3), 211-232. https://doi.org/10.1016/S0925-8574(02)00081-2

Mitra, S., Dellapenna, T., & Dickhut, R. (1999). Polycyclic aromatic hydrocarbon distribution within lower Hudson River estuarine sediments: Physical mixing vs sediment geochemistry. *Estuarine, Coastal and Shelf Science, 49*(3), 311-326. https://doi.org/10.1006/ecss.1999.0502

Moore Memorial Public Library, 2017. www.texascity-library.org/page/history.tc.dike (accessed 04/07/2020).

Morse, J. W., Presley, B. J., Taylor, R. J., Benoit, G., & Santschi, P. (1993). Trace metal chemistry of Galveston Bay: Water, sediments and biota. *Marine Environmental Research, 36*(1), 1-37. https://doi.org/10.1016/0141-1136(93)90087-G

Naser, H. A. (2011). Effects of reclamation on macrobenthic assemblages in the coastline of the Arabian Gulf: A microcosm experimental approach. *Marine Pollution Bulletin, 62*(3), 520-524. https://doi.org/10.1016/j.marpolbul.2010.11.032

NOAA- National Oceanic and Atmospheric Administration, Office for Coastal Management, 2016. "2016 C-CAP Regional Land Cover." Coastal Change Analysis Program (C-CAP) Regional Land Cover. Charleston, SC: NOAA Office for Coastal Management. Accessed June 2020 at www.coast.noaa.gov/htdata/raster1/landcover/bulkdownload/30m_lc/.

NOAA- National Oceanic and Atmospheric Administration, 2017. NOAA National Centers for Environmental Information, State of the Climate: National Climate Report for Annual 2017, published online January 2018, retrieved on June 11, 2020 from https://www.ncdc.noaa.gov/sotc/national/201713

Olsen, C.R., Larsen, I.L., Mulholland, P.J., Von Damm, K.L., Grebmeier, J.M., Schaffner, L.C., Diaz, R.J. and Nichols, M.M., 1993. The concept of a equilibrium surface applied to particle sources and contaminant distributions in estuarine sediments. *Estuaries*, *16*(3), 683-696. https://doi.org/10.2307/1352805

Pfahl, S., O'Gorman, P.A., and Fischer, E.M., 2017. Understanding the regional pattern of projected future changes in extreme precipitation. Nat. Clim. Chang. 7, 423-427.

Rayson, M. D., Gross, E. S., Hetland, R. D., & Fringer, O. B. (2016). Time scales in Galveston Bay: An unsteady estuary. *Journal of Geophysical Research: Oceans*, *121*, 2268–2285. https://doi.org/10.1002/2015JC011181

Ropicki, A., R. Dudensing, and D. Hanselka. 2018. Economic contributions of the Texas oyster fishery. Tech. rep., Texas Sea Grant, TAMU-SG-18-502.

Santschi, P. H., Presley, B. J., Wade, T. L., Garcia-Romero, B., and Baskaran, M. (2001). Historical contamination of PAHs, PCBs, DDTs, and heavy metals in Mississippi River Delta, Galveston Bay and Tampa Bay sediment cores. *Marine Environmental Research, 52*(1), 51-79. https://doi.org/10.1016/S0141-1136(00)00260-9

Schaffner, L. C., Dellapenna, T. M., Hinchey, E. K., Friedrichs, C. T., Neubauer, M. T., Smith, M. E., and Kuehl, S. A. (2001). Physical energy regimes, seabed dynamics and organism-sediment interactions along an estuarine gradient. In: *Organism-Sediment Interactions* (Aller, J.Y. Woodin, S.A., and Aller, R. C., eds.), University of South Carolina Press, Columbia, SC, 159-179.

Solis, R.S. and Powell, G., 1999. Hydrography, mixing characteristics, and residence times of Gulf of Mexico estuaries. In *Biogeochemistry of Gulf of Mexico Estuaries* (Bianchi, T.S., Pennock, J.R., and Twilley, R.R., eds.), John Wiley, NY, pp.29-61.

Steichen, J.L., Labonté, J.M., Windham, R., Hala, D., Kaiser, K., Setta, S., Faulkner, P.C., Bacosa, H., Yan, G., Kamalanathan, M., and Quigg, A., 2020. Microbial, physical, and chemical changes in Galveston Bay following an extreme flooding event, Hurricane Harvey. *Frontiers in Marine Science*, *7*, 186. https://doi.org/10.3389/fmars.2020.00186

Stunz, G. W., Minello, T. J., and Rozas, L. P. (2010). Relative value of oyster reef as habitat for estuarine nekton in Galveston Bay, Texas. *Marine Ecology Progress Series*, 406, 147–159. https://doi.org/10.3354/meps08556

Swales, A., Williamson, R.B., Van Dam, L.F., Stroud, M.J., and McGlone, M.S., 2002. Reconstruction of urban stormwater contamination of an estuary using catchment history and sediment profile dating. *Estuaries*, *25*(1), 43-56. https://doi.org/10.1007/BF02696048

Syvitski, J.P., Kettner, A.J., Overeem, I., Hutton, E.W., Hannon, M.T., Brakenridge, G.R., Day, J., Vörösmarty, C., Saito, Y., Giosan, L., and Nicholls, R.J., 2009. Sinking deltas due to human activities. *Nature Geoscience*, *2*(10), 681-686. https://doi.org/10.1038/ngeo629

Tessler, Z.D., Vörösmarty, C.J., Grossberg, M., Gladkova, I., Aizenman, H., Syvitski, J.P.M., and Foufoula-Georgiou, E., 2015. Profiling risk and sustainability in coastal deltas of the world. *Science*, *349*(6248), 638-643. https://10.1126/science.aab3574

Thrush, S., Hewitt, J., Cummings, V., Ellis, J., Hatton, C., Lohrer, A., and Norkko, A. (2004). Muddy waters: Elevating sediment input to coastal and estuarine habitats. *Frontiers in Ecology and the Environment, 2*(6), 299-306. https://doi.org/10.1890/1540-9295(2004)002[0299:MWESIT]2.0.CO;2

Thyng, K.M., Hetland, R.D., Socolofsky, S.A., Fernando, N., Turner, E.L., and Schoenbaechler, C., 2020. Hurricane Harvey caused unprecedented freshwater inflow to Galveston Bay. *Estuaries and Coasts*. https://doi.org/10.1007/s12237-020-00800-6

TNRIS - Texas Natural Resources Information System. 2014. Texas Rivers, Streams, and Waterbodies, 2014-02-01. Retrieved on 2020-06-16 from: https://tnris.org

Topor, Z.M., Robinson, K.L., and Turcu, A., 2020. Investigating seasonal succession patterns in mesozooplankton community structure following Hurricane Harvey. *Frontiers in Marine Science*, 7, 462. https://doi.org/10.3389/fmars.2020.00462

TPWD - Texas Parks and Wildlife Department, 2013. GIS Maps and Spatial Data: Coastal Bathymetry, 2013-02-01. Retrieved on 2020-06-15 from: https://tpwd.texas.gov/gis/gis-main

Uncles, R.J., Stephens, J.A. and Woodrow, T.Y., 1988. Seasonal cycling of estuarine sediment and contaminant transport. *Estuaries*, *11*(2), 108-116. https://doi.org/10.2307/1351998

US EPA -United States Environmental Protection Agency, 2017. Patrick Bayou Site Profile. Retrieved on 2020- 03-20 from: https://cumulis.epa.gov/supercpad/SiteProfiles/index.cfm?fuseaction=second.Cleanup&id=0605329#bkground

USGS - United States Geological Survey, 2013. National Elevation Dataset, 2013-01-01. Retrieved on 2020-06-15 from: https://catalog.data.gov/dataset/usgs-national-elevation-dataset-ned

Vallette, J. (2018). *Chlorine and building materials: A global inventory of production technologies, market, and pollution, phase 1: Africa, the Americas and Europe*. Washington D.C.: HBN Know Better Healthy Building Network. https://healthybuilding.net/reports/18-chlorine-building-materials-project-phase-1-africa-the-americas-and-europe

Vecchi, G.A., Soden, B.J., Wittenberg, A.T., Held, I.M., Leetmaa, A., and Harrison, M.J., 2006. Weakening of tropical Pacific atmospheric circulation due to anthropogenic forcing. *Nature*, *441*(7089), 73-76. https://doi.org/10.1038/nature04744

Vecchi, G.A. and Soden, B.J., 2007. Global warming and the weakening of the tropical circulation. *Journal of Climate*, *20*(17), 4316-4340. https://doi.org/10.1175/JCLI4258.1

Walsh, K.J., McBride, J.L., Klotzbach, P.J., Balachandran, S., Camargo, S.J., Holland, G., Knutson, T.R., Kossin, J.P., Lee, T.C., Sobel, A., and Sugi, M., 2016. Tropical cyclones and climate change. *Wiley Interdisciplinary Reviews: Climate Change*, *7*(1), 65-89. https://doi.org/10.1002/wcc.371

Ward, G. H. (1980). Hydrography and circulation processes of gulf estuaries. In: *Estuarine and Wetland Processes* (Hamilton, P. and Macdonald, K.B., eds), Marine Science, Vol. 11, Springer, Boston, MA, pp. 183-215. https://doi.org/10.1007/978-1-4757-5177-2_7

Table 1. Hurricane Harvey sediment and HgT loads to Galveston Bay

Sub-Bay	Sediment Mass (tons)	% of Total Harvey Sediment Mass Deposited	Sediment Thickness (cm)	Mass of HgT (tons)
Patrick Bayou-scoured*	2.43×10^4	-	-130	1.43
Patrick Bayou-deposited*	1.43×10^5	-	+17	0.24
San Jacinto Estuary-scoured+	16.42×10^6	-	-48	2.0
San Jacinto Estuary-deposited*	7.73×10^6	5.02%	+9	1.08
Clear Lake System	0.75×10^6	0.50%	+6	0.03
Upper Galveston Bay	47.78×10^6	31.92%	+14	1.89
Trinity Bay	47.40×10^6	31.72%	+14	1.87
Lower Galveston Bay	46.10×10^6	30.85%	+14	1.82
Total Deposited	149.45×10^6	100.00%		6.93

*From Dellapenna et al. (2020)

Table 2. The per sub-bay average pre-Harvey surface and post-Harvey HgT integrated concentrations, the difference between the two, and the percent change. In addition, the Pre-Harvey HgT surface concentration GIS layer was subtracted from the Post-Harvey integrated concentration GIS layer to generate the Difference between Pre-Harvey surface and Post-Harvey Integrated HgT Concentrations map (HgT Difference Map; Fig. 4C). Table 2 shows average changes between sub-bays and the HgT Difference Map shows the variability of change across the mapped region. The data range shown in the HgT Difference Map (Fig. 4C) ranges from +30 to -30 ng g^{-1} but as Table 2 indicates, the entire data ranges from +535 ng g^{-1} in Burnett Bay to -34 in northeastern Trinity Bay. This range of data was selected to allow for visualization of the data found within Galveston Bay. If the total range was used, the details within Galveston Bay would not be evident.

Sub Bay	Pre-Harvey Surface HgT conc. (ng g^{-1})	Post-Harvey HgT Integrated conc. (ng g^{-1})	Net Change (ng g^{-1})	%Change
San Jacinto Bay				
Burnett Bay	135	670	535	396.30%
Scott Bay	135	197	62	45.93%
Lower SJE Bay	30	48	18	60.00%
Tabbs Bay	13.5	30	16.5	122.22%
Galveston Bay				
Upper Galv. Bay	19	30	11	57.89%
Trinity Bay	49.25	45	-4.25	-8.63%
Lower Galv. Bay	19	20	1	5.26%
East Galveston Bay	9	20	11	122.22%
Taylor Lake	31.2	35	3.8	12.18%
Clear Lake	46	36	-10	-21.74%

9. Figure Captions

Figure 1. Hurricane Harvey Rainfall for Metropolitan Houston and eastern Texas. (a) Accumulated precipitation during Hurricane Harvey between August 21 and 31, 2017 and (b) daily precipitation averaged over Galveston Bay (30 weather stations). In (a), the 6-hourly track (all times in UTC) of Hurricane Harvey, based on data from National Hurricane Center (https://www.nhc.noaa.gov), is shown with circles. Precipitation data in (b) are based on daily records extracted from the Global Historical Climatology Network (https://www.ncdc.noaa.gov). (from Du et al., 2019a)

Figure 2. Base map of the study area showing the location of the Addicks and Barker Reservoirs and the location of major tributaries affected by Hurricane Harvey, as well as the location of other prominent geographic features mentioned in the paper.

Figure 3. USGS hydrographs from (a) Buffalo Bayou at Piney Point, (b) Clear Creek near Friendswood, (c) East Fork of San Jacinto River at New Caney, and (d) Trinity River at Romayor. Each of these rivers flows into Galveston Bay. Because of the controlled release of floodwaters from the Barker and Addicks Reservoirs (Fig. 1), Buffalo Bayou gauge (a) shows two-step changes in discharge over a total of 53 days of flooding, with initial higher discharge resulted from the initial phase of the flood followed by a prolonged, nearly flat discharge (~100 m^3 s^{-1}) from the prolong floodwater release. All other gauges show a single peak discharge of a much shorter duration.

Figure 4. Integrated surface sediment total-Hg (HgT) maps for Galveston Bay. (a) Pre-Harvey condition based on data from Al Mukiami et al. (2018a). (b) Post-Harvey condition from this study's data. (c) difference between pre- and post-Harvey conditions. Note that the map scale only goes up to 60 ng g^{-1} although the surface sediment in the SJE has HgT concentration as high as 670 ng g^{-1}.

Figure 5. (a) Core locations in the Mud Lake portion of Clear Lake and (b) x-radiographs of three cores. The base of each x-radiograph shows the finely laminated mud with few obvious sedimentary features other than bivalve shells. The base of the Harvey layer in each x-radiograph is marked by an erosional surface, which was formed during the peak flow phase of the flood. Above this is a lighter-toned sediment layer or series of layers representing the deposition of bedload sands and gravel. Note that (b) shows articulated bivalves. The fact that the bivalve remains articulated but was deposited in a shell lag deposit suggest that there was minimal transport. Above the lighter tone sandy layer is a darker tone deposit representing the deposition of the fine-grained suspended sediment load as the flood flow was weakened.

Figure 6. Isopach map of Harvey layer thickness in Galveston Bay. The thickest deposits were found within Clear/Bear Lake Bays, Scott and Burnett Bays, all within the San Jacinto Estuary as well as upstream of the Texas City Dike in southwestern Galveston Bay.

Figure 7. Local exposure time (LET) for particles released from the petrochemical facilities along the Buffalo Bayou and San Jacinto River during (a) August 26–30, 2017 (during storm) and (b) September 3–7, 2017 (after storm), and (c) for particles released during August 26–30, 2017 at the Trinity River mouth (black triangle). For each square region (1 km × 1 km), the LET value is an average over all particles released during the respective 5-day period (6890 particles in total). (a)-(c) are from Du et al., (2020). (d) Post-Harvey integrated surface sediment total-Hg (HgT), (e) Difference in HgT concentrations (post-Harvey – pre-Harvey), and (f) Harvey deposit thickness.

Figure 8. A conceptual map showing sources and sinks of Hurricane Harvey derived sediment and Hg. During peak discharge, floodwaters (shown in blue) scoured Hg-enriched sediment from lower Buffalo Bayou (BB) and the San Jacinto Estuary (SJE) and sourced a thick deposit of Hg-enriched sediment in Burnet and Scott Bay south of the mouth of BB (shown in red). Additionally, during peak discharge, floodwaters (shown in blue) scoured the SJE, leaving a thick deposit in SJE north of BB. Post peak discharge flooding, including the prolonged release of floodwaters from the Addicks and Barker Reservoirs resulted in the prolonged (46 days) delivery of floodwaters (shown in orange) and basin derived sediment to both the SJE and Galveston Bay (shown in brown).

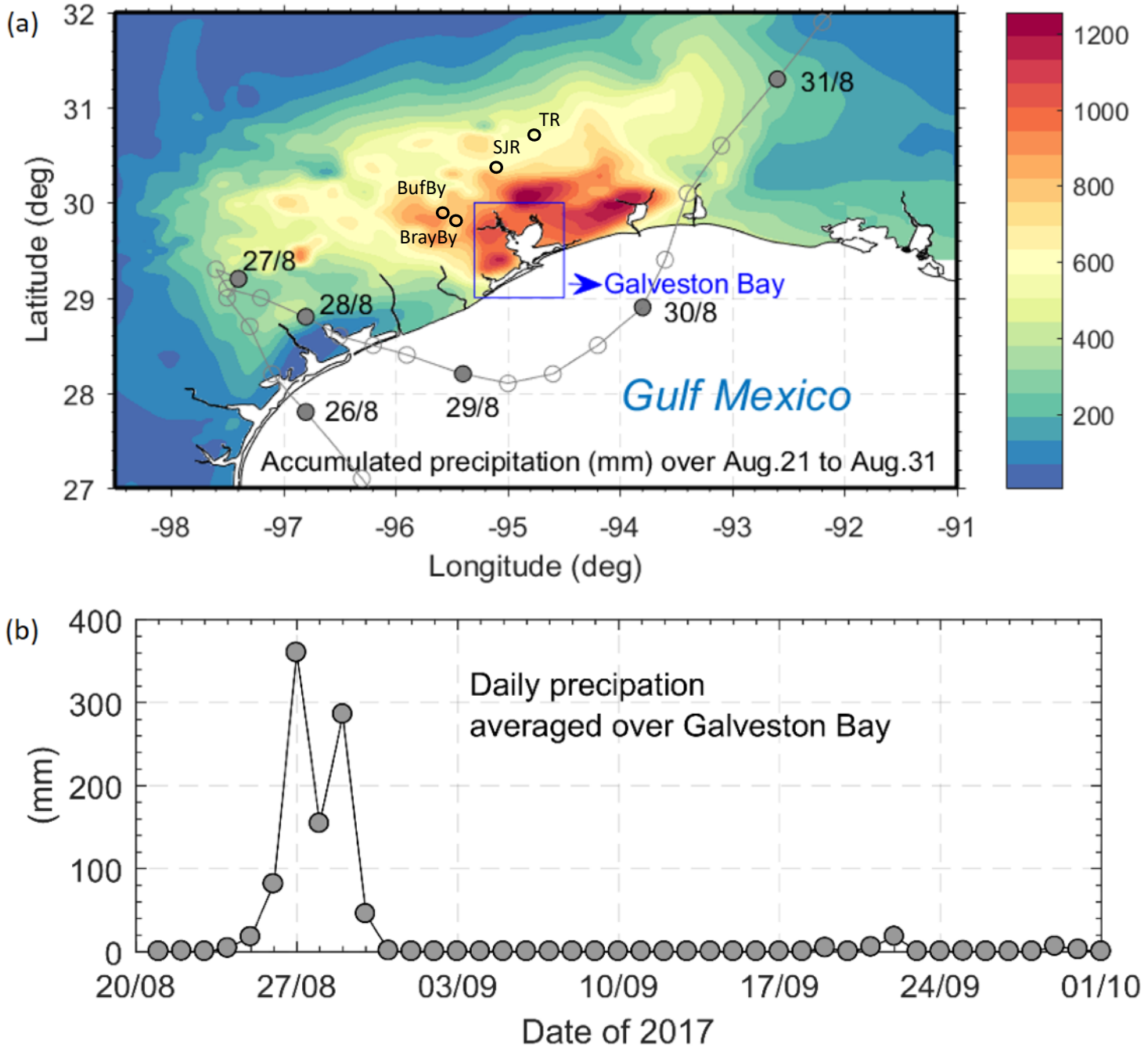
(a)
Latitude (deg)
Longitude (deg)
Accumulated precipitation (mm) over Aug.21 to Aug.31
Gulf Mexico
Galveston Bay
TR
SJR
BufBy
BrayBy
26/8
27/8
28/8
29/8
30/8
31/8
(b)
Daily precipation
averaged over Galveston Bay
(mm)
Date of 2017
20/08
27/08
03/09
10/09
17/09
24/09
01/10

Figure 1

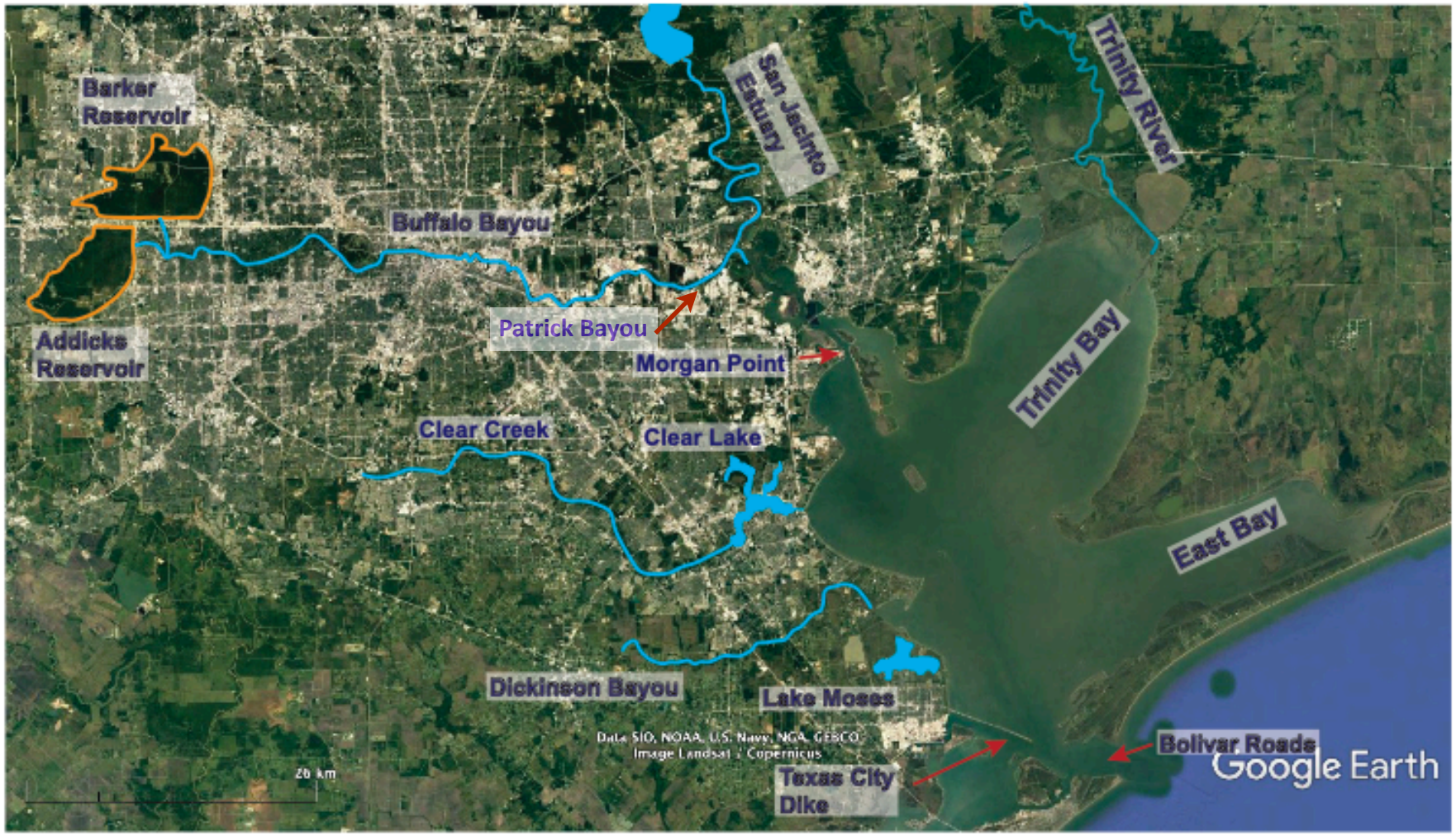
Barker Reservoir
Addicks Reservoir
Buffalo Bayou
San Jacinto Estuary
Trinity River
Patrick Bayou
Morgan Point
Trinity Bay
Clear Creek
Clear Lake
East Bay
Dickinson Bayou
Lake Moses
Bolivar Roads
Texas City Dike
Data SIO, NOAA, U.S. Navy, NGA, GEBCO
Image Landsat / Copernicus
20 km
Google Earth

Figure 2

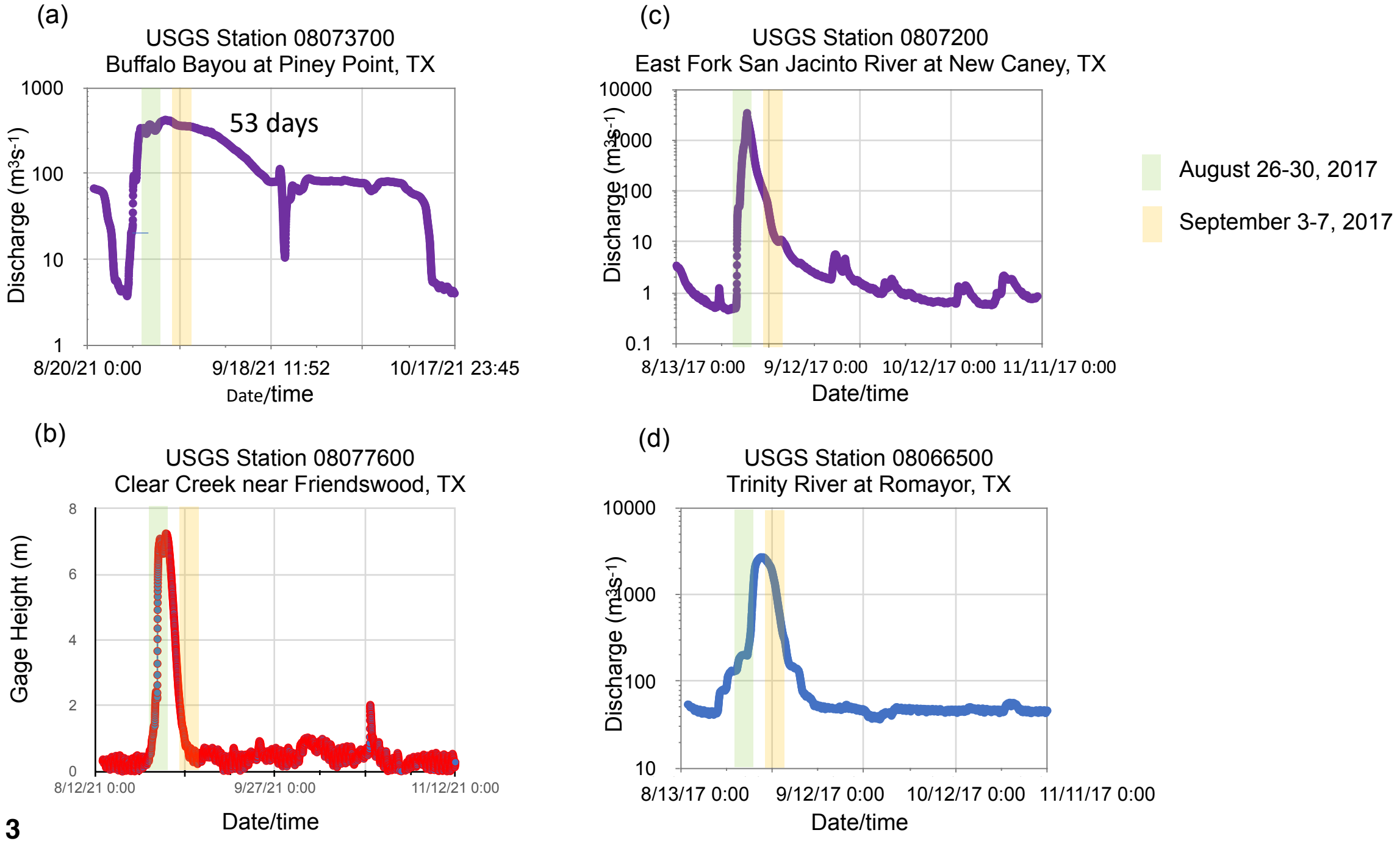
(a)
USGS Station 08073700
Buffalo Bayou at Piney Point, TX
53 days
Discharge (m3s-1)
1000
100
10
1
8/20/21 0:00
9/18/21 11:52
10/17/21 23:45
Date/time
(c)
USGS Station 0807200
East Fork San Jacinto River at New Caney, TX
Discharge (m3s-1)
10000
1000
100
10
1
0.1
8/13/17 0:00
9/12/17 0:00
10/12/17 0:00
11/11/17 0:00
Date/time
August 26-30, 2017
September 3-7, 2017
(b)
USGS Station 08077600
Clear Creek near Friendswood, TX
Gage Height (m)
8
6
4
2
0
8/12/21 0:00
9/27/21 0:00
11/12/21 0:00
Date/time
(d)
USGS Station 08066500
Trinity River at Romayor, TX
Discharge (m3s-1)
10000
1000
100
10
8/13/17 0:00
9/12/17 0:00
10/12/17 0:00
11/11/17 0:00
Date/time

Figure 3

(a)

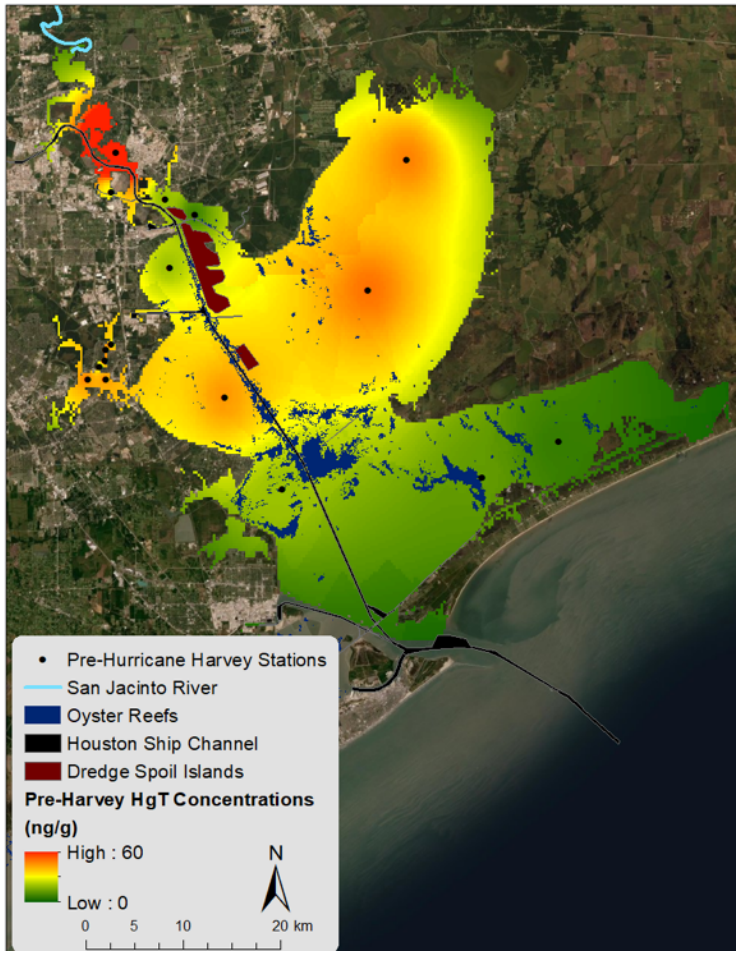
Pre-Hurricane Harvey Stations
San Jacinto River
Oyster Reefs
Houston Ship Channel
Dredge Spoil Islands
Pre-Harvey HgT Concentrations
(ng/g)
High : 60
Low : 0
N
0 5 10 20 km

(b)

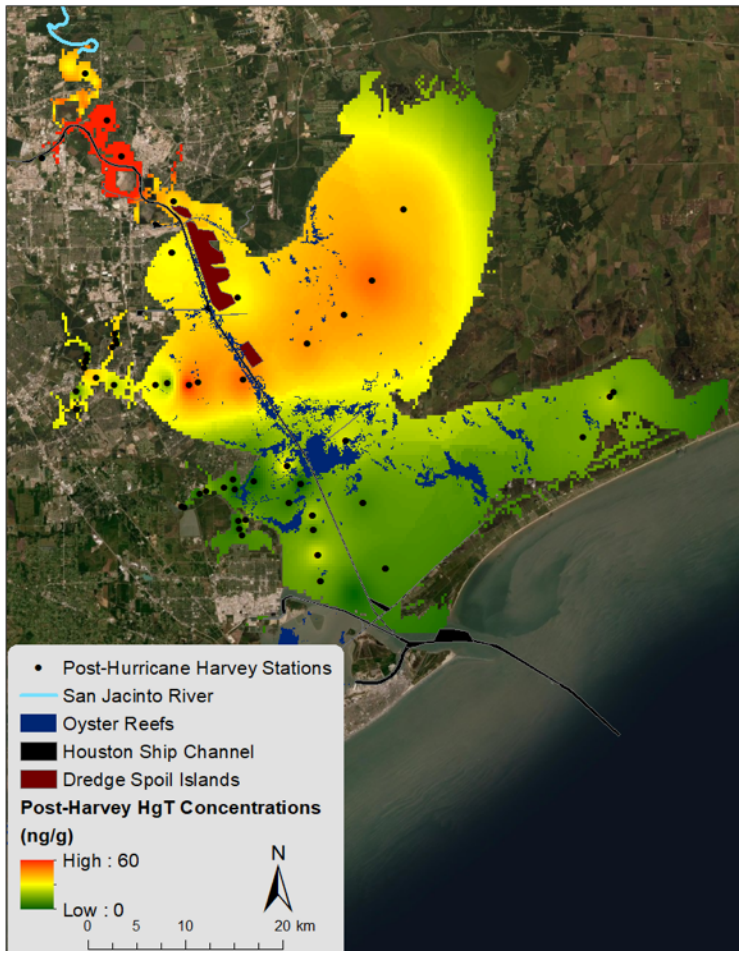
Post-Hurricane Harvey Stations
San Jacinto River
Oyster Reefs
Houston Ship Channel
Dredge Spoil Islands
Post-Harvey HgT Concentrations
(ng/g)
High : 60
Low : 0
N
0 5 10 20 km

(c)

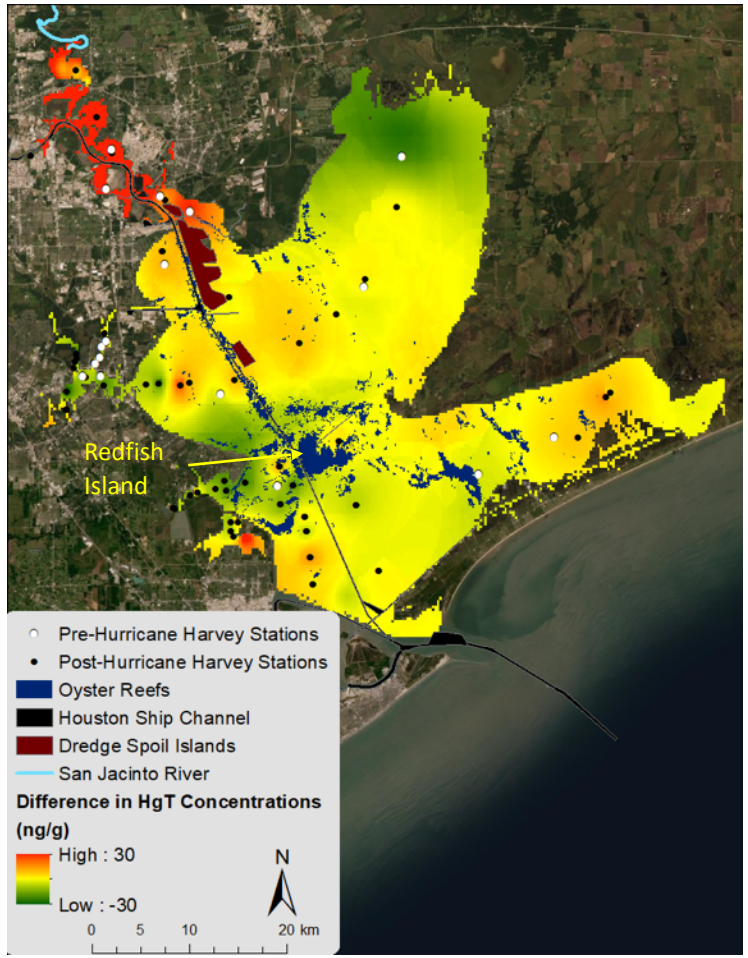
Redfish
Island
Pre-Hurricane Harvey Stations
Post-Hurricane Harvey Stations
Oyster Reefs
Houston Ship Channel
Dredge Spoil Islands
San Jacinto River
Difference in HgT Concentrations
(ng/g)
High : 30
Low : -30
N
0 5 10 20 km

Figure 4

(a)

(b)


Mud Lake
ML-3
ML-2
ML-1
Clear Lake

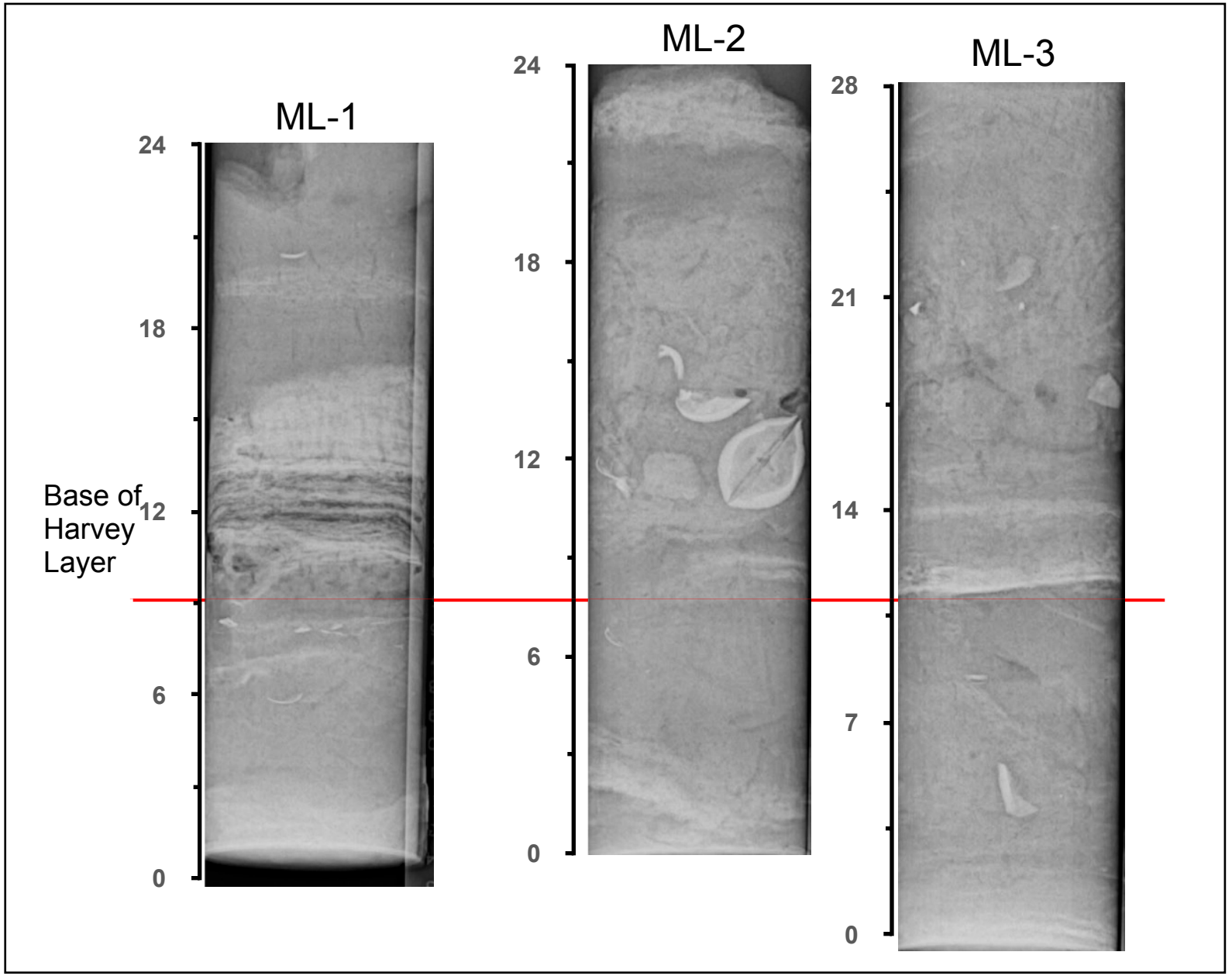
ML-1
ML-2
ML-3
24
18
12
6
0
24
18
12
6
0
28
21
14
7
0
Base of Harvey Layer

Figure 5

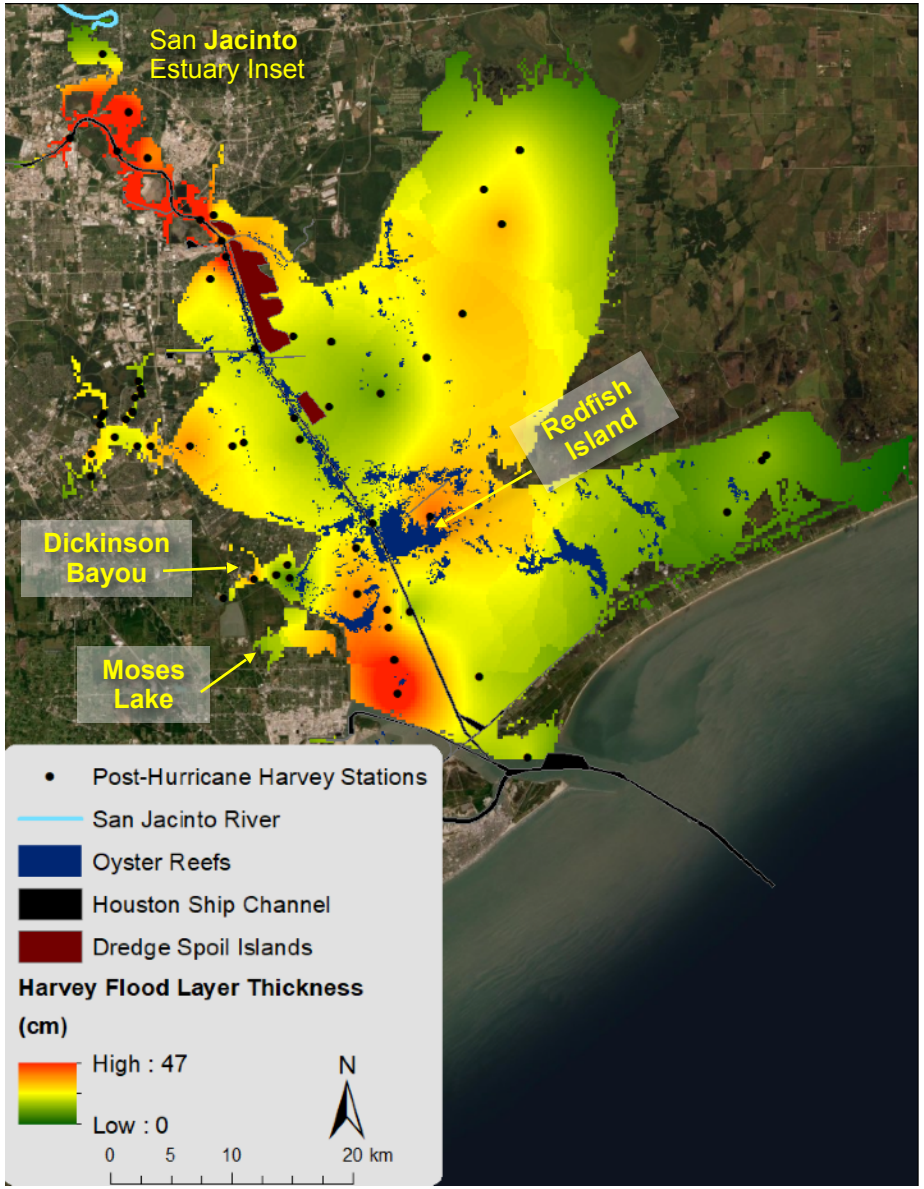
San Jacinto
Estuary Inset
Redfish Island
Dickinson Bayou
Moses Lake
Post-Hurricane Harvey Stations
San Jacinto River
Oyster Reefs
Houston Ship Channel
Dredge Spoil Islands
Harvey Flood Layer Thickness (cm)
High : 47
Low : 0
N
0 5 10 20 km

Figure 6

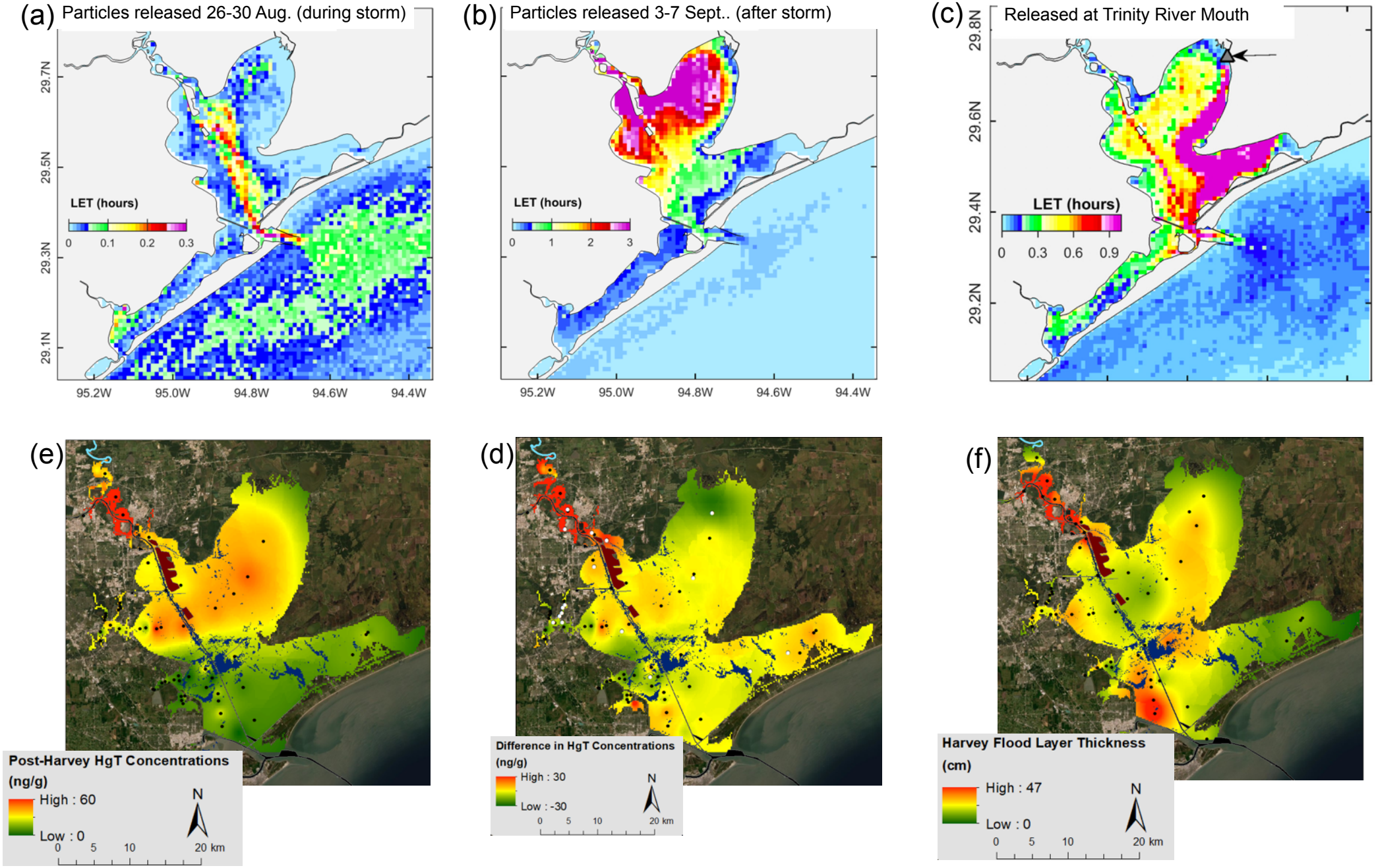
(a) Particles released 26-30 Aug. (during storm)
LET (hours)
0 0.1 0.2 0.3
29.7N
29.5N
29.3N
29.1N
95.2W 95.0W 94.8W 94.6W 94.4W
(b) Particles released 3-7 Sept.. (after storm)
LET (hours)
0 1 2 3
95.2W 95.0W 94.8W 94.6W 94.4W
(c) Released at Trinity River Mouth
LET (hours)
0 0.3 0.6 0.9
29.8N
29.6N
29.4N
29.2N
(e)
Post-Harvey HgT Concentrations (ng/g)
High : 60
Low : 0
0 5 10 20 km
N
(d)
Difference in HgT Concentrations (ng/g)
High : 30
Low : -30
0 5 10 20 km
N
(f)
Harvey Flood Layer Thickness (cm)
High : 47
Low : 0
0 5 10 20 km
N

Figure 7

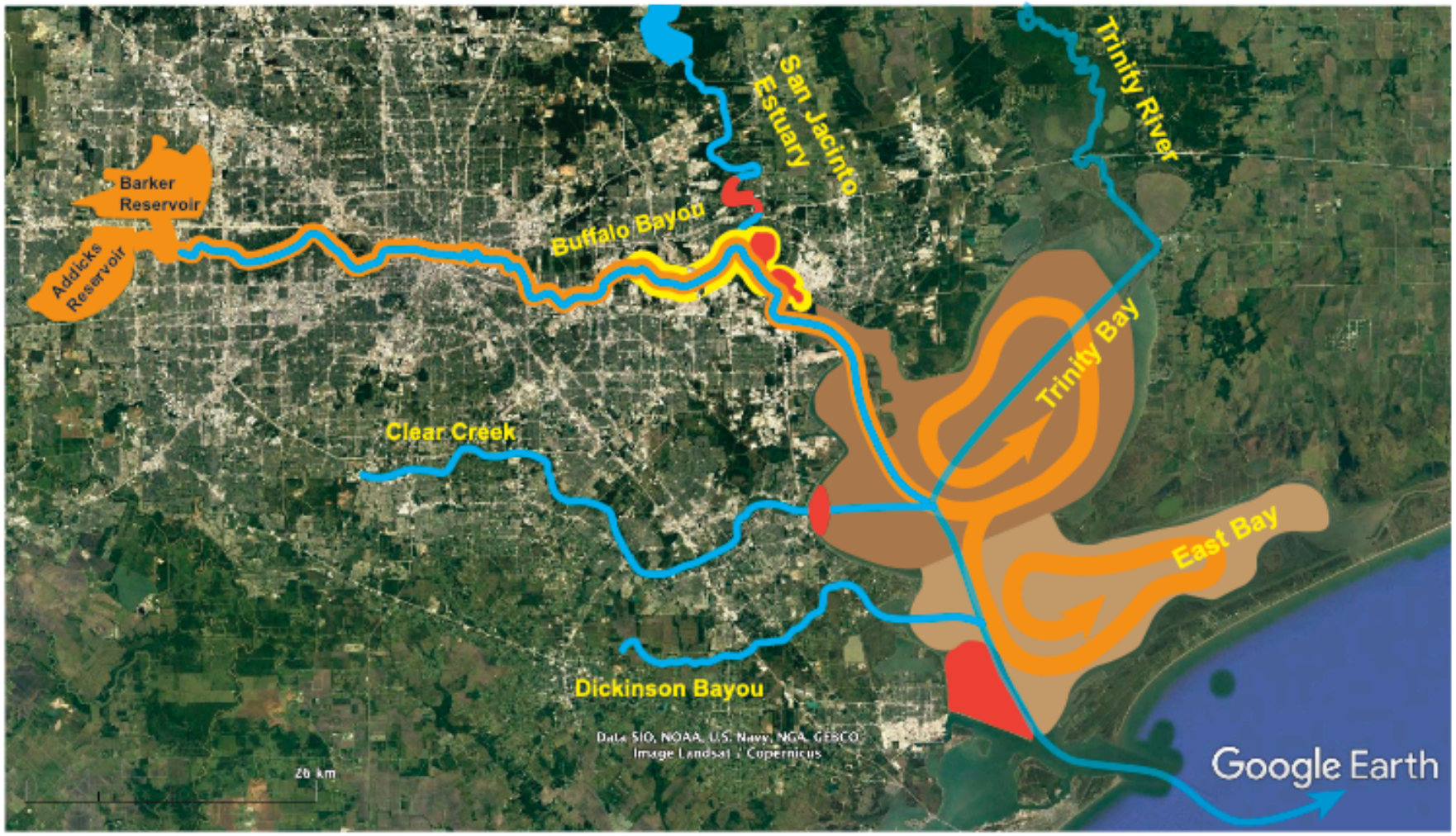
Barker Reservoir
Addicks Reservoir
Buffalo Bayou
San Jacinto Estuary
Trinity River
Trinity Bay
East Bay
Clear Creek
Dickinson Bayou
20 km
Data SIO, NOAA, U.S. Navy, NGA, GEBCO
Image Landsat / Copernicus
Google Earth
Peak Discharge Depocenters
Primary Post-Peak Discharge Depocenter
Secondary Post-Peak Discharge Depocenter
Peak Discharge Flow Path
Post-Peak Discharge Flow Path
Source area for mercury

Figure 8

Title: Polycyclic Aromatic Hydrocarbons in Galveston Bay and the Houston Ship Channel: Post-Hurricane Harvey Baseline Comparison to Historical Data

Alternative Title: Polycyclic Aromatic Hydrocarbon Status in Post-Hurricane Harvey Sediments: Considerations for Environmental Sampling in the Galveston Bay/Houston Ship Channel Region

Authors: Krisa Camargo[1,2], José L. Sericano[2], Sharmilla Bhandari[1], Christena Hoelscher[2,4], Thomas J. McDonald[1,3], Weihsueh A. Chiu[1], Terry L Wade[1,2], Timothy M. Dellapenna[2,4], Yina Liu[2], Anthony H. Knap[1,2].

[1]Texas A&M University College of Veterinary Medicine Interdisciplinary Faculty of Toxicology, College Station TX 77843

[2]Texas A&M University Department of Oceanography, College Station, TX

[3]Texas A&M University School of Public Health College Station, TX 77843

[4]Texas A&M University Department of Marine and Coastal Environmental Science, Galveston, TX 77554

Corresponding Author: Weihsueh A. Chiu

Email: wchiu@cvm.tamu.edu

Address: Texas A&M University Veterinary Integrative Biosciences 4458 TAMU College Station TX 77843

Declaration of Interest: The authors declare no conflicts of interest

CRediT author statement:

Krisa Camargo: Writing-Original Draft preparation, Investigation, Formal analysis, Data curation, Conceptualization, Visualization. José L. Sericano: Methodology, Validation, Resources, Supervision, Writing-Review & Editing. Sharmilla Bhandari: Visualization, Software. Christena Hoelscher: Visualization, Software. Thomas J. McDonald: Conceptualization, Resources, Supervision, Project administration. Weihsueh A. Chiu: Conceptualization, Funding acquisition, Supervision, Validation, Writing-Review & Editing. Terry L Wade: Writing-Reviewing & Editing Resources, Methodology, Validation. Timothy M. Dellapenna: Writing-Reviewing & Editing, Resources, Visualization. Yina Liu: Writing-Review & Editing. Anthony H. Knap: Funding acquisition, Resources, Project administration, Writing-Review & Editing.

Abstract:

Hurricane Harvey led to a broad redistribution of sediment throughout Galveston Bay and the Houston Ship Channel (GB/HSC), but the resulting changes in chemical contaminant distributions have yet to be characterized. To address this question, we collected and analyzed post-Harvey sediment for concentrations of the EPA 16 Priority Pollutant polycyclic aromatic hydrocarbon (PAHs), determining the extent to which the spatial distribution and sourcing of contaminants may have changed in contrast to historical surface sediment data (<5cm) from the National Oceanic Atmospheric Administration (NOAA) available for the years 1996-2011. We found a small, but detectable increase from pre- to post-Harvey in PAH concentrations, with PAH diagnostic sourcing indicating combustion origins. Of the detected PAHs, none exceeded Sediment Quality Guideline values. Overall, we have added to the understanding of PAH spatial trends within the GB/HSC region, and developed a reference PAH baseline to inform future studies.

Funding: This work was supported by the National Institutes of Environmental Health Sciences (NIEHS) Superfund Research Program P42 ES027704 [2017-present]; Texas A&M University Toxicology T32 Training Grant: T32 ES026568 [2016-2018] and the Department of Defense (DOD) Science Mathematics and Research for Transformation (SMART) Program [2019-present].

Keywords (minimum 6 key words): sediments, sediment quality, Galveston Bay, Houston Ship Channel polycyclic aromatic hydrocarbons (PAHs), sediment cores, spatial distribution

Introduction

Hurricane Harvey stalled over Houston, TX in August 2017, where concerns grew about the spread of legacy contaminants within in the Galveston Bay (GB) and the Houston Ship Channel (HSC) region (Al Mukaimi et al., 2018; Hieke et al., 2016; Howell et al., 2011; Jackson et al., 1998; Kennicutt II, 2017; Qian et al., 2001; Santschi et al., 2001; Yeager et al., 2007). The two main freshwater rivers that discharge into GB are the San Jacinto River and Trinity Rivers, with the Bolivar Roads as both the primary tidal inlet as well as serving the entry way for the HSC that extends 80 km into the city of Houston with a maintained depth of 14 m (Programs, 1988; US Army Corps of Engineers (USACE), 2017). The GB estuary is generally flat, with depths ranging from 2-3m, covers about 1500 km^2, and has abundant dredging spoil shoals and oyster reefs (HARC and Galveston Bay Foundation, 2018; Programs, 1988; US Army Corps of Engineers (USACE), 2017). Economically, the HSC is a part of the Port of Houston, which sees over 200 million tons of cargo each year via 9,000 vessels and 200,000 barges and ship channel work provides around 1.2 million jobs (US Army Corps of Engineers (USACE), 2017). The Port of Houston serves a mixture of industries as well as domestic and international businesses (US Army Corps of Engineers (USACE), 2017).

The Galveston Bay Foundation's and HARC's 2017 and 2018 Galveston Bay Report cards grade the overall pollution events and sources as a "C", or in other words "Adequate for Now" (Foundation, 2017; HARC and Galveston Bay Foundation, 2018). Consequently, after strong winds and flooding from Hurricane Harvey, concerns emerged as to contaminant mobilization and consequent redistribution of present contaminants due to documented land subsidence (Al Mukaimi, Dellapenna, et al., 2018; Du et al., 2019; 2020). However, the quantitative impact of Harvey on the distribution of contaminants has not yet been established. Although recognizing there are diverse classes of organic contaminants and heavy metals known to be present in GB/HSC, we selected PAHs for detailed investigation due to their

ubiquitous presence in the environment, their historical detection in local oysters, and previously collected sediments (Al Mukaimi, Kaiser, et al., 2018; Jackson et al., 1998; Qian et al., 2001) and their listing in the Appendix A of 40 CRF Part 423 (EPA (Environmental Protection Agency), 2014). Of the EPA 16 Priority Pollutant PAHs, high molecular weight (HMW) PAHs have ring structures >3 rings, and several of these (e.g. benz[a]anthracene, benzo[a]pyrene, dibenz[a,h]anthracene, and benzo[k]fluoranthene) are considered "reasonably anticipated to be a human carcinogen" (National Toxicology Program, 2011). Our study objectives were to characterize concentrations of the EPA 16 Priority Pollutant PAHs present in post-Harvey sediments and determine whether there was a new baseline, in contrast to historically available PAH concentration data. We also aimed to determine the extent to which PAHs were spatially distributed and the consequent relative sourcing of the PAHs given both the historically available PAH concentration data and post-Harvey data.

Materials & Methods

Data collection and core processing

A total of 32 sediment vibracores and pushcores (Figure 1) were collected on three cruises (October 2017, December 2017, January 2017). Vibracores were collected using an Oztec vibracoring head attached to a 7.6 cm diameter aluminum barrel, with core recovery ranging from 1-4 m. Push cores were collected using a repurposed Benthos® checkvalve pushcoring head, which was attached to an aluminum conduit with stainless steel hose-clamps and electrical tape. The conduit was in 1.5 m long sections that screwed together, with a maximum length of 5m. The removable core barrels consist of 7.6 cm diameter polycarbonate tubes generally ranging in length from 0.3-0.6 m. During recovery, the pushcoring system was brought to the surface and the core barrels were capped while the end of the core was still in the water to prevent the loss of the cores from the check valve. While holding the core vertically, the bottom core cap was immediately sealed with electrical tape while still being kept

vertical. Flourofoam was pushed into the core top so that it rested just above the sediment-water interface, the flourofoam was cut flush with the top of the core barrel and then the top of the core was sealed with a core cap and electrical tape and stored vertically for transport back to the lab. Box cores were collected using a GOMEX style boxcorer. For each box core, a 15.24 cm diameter sub-core as collected and sub-sectioned into 1 cm thick slices using an extruder. In addition, a 7.6 cm diameter polycarbonate sub-core was collected for x-radiography. All cores were stored in a cold room which is held at a constant temperature of 4°C.

Subsequent surface samples (< 5cm depth) were collected in 8oz combusted glass jars with Teflon cap liners and were subsequently stored at -20°C until further processing and analysis. As sample collection occurred after Hurricane Harvey, these sites were selected in the same regional areas as sample collected in prior sediment sampling programs (Al Mukaimi, Dellapenna, et al., 2018; Al Mukaimi, Kaiser, et al., 2018).

In addition to the sediment collected in 2017, organic data in sediment from the National Oceanic & Atmospheric Administration (NOAA) and the National Centers for Coastal Ocean Science (NCCOS) were downloaded in their original text file format and then converted to an Excel spreadsheet. The NOAA data platform Data Integration Visualization Exploration and Reporting (DIVER) Explorer: Southeast (National Oceanic & Atmospheric Administration (NOAA), 2020-a) provided sediment data from 1997-2011, while the NCCOS's National Status and Trends More Data website supplied 1996 sediment data from Galveston Bay (National Oceanic & Atmospheric Administration (NOAA), 2017-b).

Sample Preparation and Analysis

Surface sediment samples were stored at -20°C until further processing and analysis. NOAA National Status and Trends (NS&T) Methods were followed for trace organic analysis in sediments. All sediments were freeze-dried and solvent extracted with methylene chlorine using

a Dionex 200 Automated Solvent Extractor (ASE). Prior to the solvent extraction, deuterated polycyclic aromatic hydrocarbons were added for quantification (d8-naphthalene, d10-acenaphthene, d10-phenanthrene, d12-chrysene, and d12-perylene, Absolute Std 98 + % pure). For QA/QC, duplicate samples, matrix spike samples, and a standard reference material (NIST SRM 1944) were run and analyzed with the sample sets. An average method detection limit (MDL) was 0.38 ng·g-1 d.w for 20 g of sediment with a range from 0.14-0.84 ng·g-1 d.w. Analytes detected below the MDL were included as a part of the total PAH concentrations.

PAHs were isolated from other organics via silica-alumina column chromatography (silica: Aldrich Grade 923 100-200 mesh; alumina: Aldrich, basic, Brockman I 150 mesh). Sulfur present in the sediments was removed with activated copper (Baker 20 to 30 mesh) that was added to the top of each silica-alumina column and a 1:1 mixture of pentane and methylene chloride (200 ml, Burdick and Jackson GC2 grade) was used for column elution. For the quantification of 18 parent and their corresponding alkyl homolog PAHs, gas chromatography and mass spectrometry detection was used (Agilent Technologies model 5890N-MSD) in selected ion mode (SIM). Standard solutions were injected at five different concentrations to calibrate the GC/MS where deuterated aromatic compounds served as internal standards (d10-Fluorene and d12-Benzo(a)pyrene). Injections were made in splitless mode and the fused silica capillary column used was 30 m x 0.25 mm i.d., DB-5MS (0.25 μm film) with the oven temperature heating at a rate of 12°min-1 from 60°C to 300°C. Concentrations reported are in ng/g on a dry weight basis (ng·g-1 d.w.) where analytes were identified based on confirmation ions and the retention time of the PAH quantification ion compared to certified standards. The 16 PAHs listed as priority pollutants (Appendix A of 40 CFR, Part 423-126) as well as low molecular weight (LMW) PAHs consisting of 2-3 ring PAHs, high molecular weight (HMW) PAHs consisting of 4-5 ring PAHs, and total PAHs consisting of all 16 Parent Priority Pollutant PAHs are reported in ng·g-1 d.w.

Statistical Analysis

All data collected were log-normalized as raw data concentrations were highly variable for each dataset. Data analysis was carried out using GraphPad Prism version 8.4.1. Historical data collected for years include 1996, 1997, 2007, 2010, and 2011 compared to the 2017 data we collected, and analyzed using one-way ANOVA followed by a trend test. Based on the ANOVA results, and because the comparisons of interest is pre- versus post-Harvey an unpaired t-test was conducted for the years 1996-2011 vs 2017 for 2-3 Ring PAHs, 4-5 Ring PAHs, and 6-Ring PAHs.

Galveston Bay can also be divided into several large sub-bay regions that include East Bay, West Bay, Upper GB, Lower GB, Trinity Bay and additional small sub-bays (Nichol, 2010); each varying in depth with a maximum of around 4 m (Programs, 1988). The following general location regions were used for the double-plot ratios in PAH relative sourcing: Upper HSC (comprised of samples taken above Morgan's Point), Mid-Ship Channel (samples within Clear Lake, Trinity Bay and Below Morgan's Point), and Lower Bay (samples below Smith's Point to Galveston Island). To understand the general sourcing for PAH inputs to GB/HSC, the following double-plot ratios were used: Fluo/(Fluo + PY) vs. BaA/(BaA + CHR) and Fluo/(Fluo + PY) vs A/(A + PHE).

For the 2016 sediment cores comparisons between the two sites VC-2 and VC-4, raw concentration data in ng-g-1 d.w were reported for depth comparisons. Comparisons were made at different depths, but because only a single sample was available at each site, no formal statistical analysis was performed.

ArcGIS mapping was performed on log-transformed concentration data for Low Molecular Weight (LMW) PAHs, High Molecular Weight (PAHs), and Total PAHs. This data was then Kriged using ArcGIS default geostatistical method: Kriging/Co-Kriging and the Semi-variogram/Covariance Modeling. To handle coincidental sample points (two or more values for

same locations), mean values were used. For this particular dataset, ordinary kriging type was used, and predication was selected as an output surface type.

Results

PAH Distributions in Sediments

As illustrated in Figures 2a-2d, each PAH category had a similar distribution from 1996-2017, with a minor elevation of each category for 2017. To further understand PAH distributions these categories were explored by year. A one-way ANOVA across all groups indicated significant difference by year (Table 1). Post-hoc pairwise tests indicated that 1996 and 2017 were statistically different, and the trend test were significant with all p-values all <0.0001 for all four PAH categories of (Total PAHs, 2-3 Ring PAHs, 4-5 Ring PAHs, and 6 Ring PAHs). Because our focus is on pre- versus post-Harvey, we then assessed whether all the pre-Harvey data could be grouped together. No differences were evident by one-way ANOVA across all pre-Harvey groups (p values between 0.5 and 0.9). After this re-grouping, we found significant differences pre- and post-Harvey by a two-tailed unpaired t-test (Table 2). Based on these results, the 1996-2011 pre-Harvey data were grouped together for mapping and kriging and compared to the 2017 post-Harvey data (discussed in PAH Distribution Maps section).

The latest pre-Harvey surface sediment data from the NOAA database were from 2011, so to provide additional evidence that Harvey was a likely cause of any changes, we compared PAH concentrations in two available sediment cores in Burnett Bay and south of Bear Lake in the San Jacinto River in 2016 (pre-Harvey) (Figure 3a-b). Sample sizes are too small for statistical analysis, so are only presented qualitatively. Consistent with the surface sediment data above, concentrations in the top 5cm showed increases from 2016 to 2017. From depths between 5 and 15 cm, concentrations increased in one core and decreased in the other. Below 15cm, only one core was available with decreases in all PAH ring structures at 15-20cm and increases at 20-25cm. These results are consistent with prior top sediments which indicated

prior top sediments had been eroded from the HSC (Al Mukaimi, Dellapenna, et al., 2018; Du et al., 2019).

PAH Diagnostic Ratios

We divided the study area into three regionals: 1) Lower Bay (black), 2) Mid-Channel (Red), and 3) Upper HSC (green) (Figure 1). The Lower Bay encompasses samples taken below Smith's Point to Galveston Island, Mid-channel include samples taken within Clear Lake, Trinity Bay, and below Morgan's Point, and finally Upper HSC consists of samples taken above Morgan's Point. Figures 3a-d indicate consistent relative sourcing trends within each of three regions between the years 1996 (Figure 3a,3c) and 2017 (Figure 3b,3d). To distinguish PAH sourcing in the 1996 and 2017 sediments, the following PAH diagnostic ratios were used: A/(A+PHE), BaA/(BaA+CHR), IdP/(IdP + BgP), Flu/(Flu + PY) (Davis et al., 2019; Soliman et al., 2019; Tobiszewski & Namieśnik, 2012; Yunker et al., 2002). Both 1996 and 2017 maintain consistent relative sourcing from combustive sources as the BaA/BaA + CHR values are >0.35 and the corresponding Flu/(Flu + PY) are also >0.4 (Figure 3a, 3b) (Davis et al., 2019; Yunker et al., 2002). This trend is further supported by Figure 3c and 3d as the A/(A + PHE) ratios are all >0.1, indicating a combustive source (Yunker et al., 2002) and the Flu/(Flu + PY) ratios remain above >0.4. The Flu/(Flu + PY) ratios for both 1996 and 2017 are also between 0.4-0.5 suggesting the PAH source is more specifically related to petroleum combustion (Yunker et al., 2002). Then, of the general regions listed earlier, there are a few unique samples in the Upper HSC, whereby their origins are associated with petrogenic sources due to the Flu/(Flu + PY) ratios being <0.4 and the BaA/(BaA + CHR) ratios being between 0.2-0.35 (Yunker et al., 2002). Consequently, given the high volume of maritime traffic and roadway traffic, Figures 3a-d results show categories of sources from the surrounding urban and industrialized environment.

Discussion

Benthic Organism Risk Assessment & Sediment Quality Evaluation

Considering the PAH classifications discussed in prior sections provided relative sourcing origins as well as overview distributional relationships, the associated risks for aquatic ecosystems exposed to these sediments are considered by comparing the effects range-low (ERL) and effects range median (ERM) values to the PAH concentrations quantified in this study (Table 3). This comparison references established screening values in NOAA's Screening Quick Reference Tables (National Oceanic & Atmospheric Administration (NOAA), 2020-c), whereby determining whether this study's PAH concentration values in post-Hurricane Harvey sediments pose a possible risk to benthic organisms. Routine National Sediment Quality surveys are conducted in accordance with Section 503 of the Water Resources Development Act of 1992 (Hou Aixin, DeLaune Ronald D, Tan MeiHuey, Reams Margaret, 2009). However, Sediment Quality Guidelines (SQGs), first applied by NOAA in 1989, serve to generally protect fisheries in addition to aquatic environment surface water quality and health (Kwok et al., 2014). As such the NOAA ERM and ERL values have continued to guide whether corrective actions are required to clean or remove sediments within study areas even though they are limited by varying factors (e.g. temperature, salinity, biota, grain size) unique to aquatic ecosystems (Birch, 2018; Chapman, 2018; Kwok et al., 2014). As a result, these factors can impact environmental exposure to chemicals found in the sediments. For example, GB/HSC is an estuary, which is dynamically changing and has variable benthic conditions (e.g. variable salinity) SQGs are not necessarily translatable to this particular ecosystem as the SQGs were developed for either freshwater or saltwater environments (Chapman, 2002). Typically, SQGs are used in sediment management projects (e.g. disposal and relocation of dredging materials should the dredge materials be deemed harmful to aquatic ecosystems) and a preliminary screening process for assessing chemical levels in sediment (Kwok et al., 2014). For the purposes of this project, the SQGs outlined in Table 3 will provide an initial comparison to determining whether post-Harvey sediments redistributed after the hurricane pose a possible environmental risk to the local benthic ecosystem. Based on Table 3, of the detected PAH

concentrations (reported in ng·g-1 d.w.), both the 1996 and 2017 medians were well below both the ERL and ERM values. However, there were a few individual Post-Harvey values for several PAHs that exceeded the ERL values (e.g. Acenaphthylene, Acenaphthene, Fluorene, Anthracene). As for low molecular weight (LMW), high molecular weight (HMW), and total PAHs, both the 1996 and 2017 sediment data had a site where the ERL values were exceed and the corresponding ERM was nearly met. While the post-Harvey samples do not necessarily require remediation or corrective action, the detected PAH concentrations and the corresponding PAH ranges do suggest PAH analysis at later timeframes and in the same or similar sites would be of interest (Table 3).

PAH Distribution Maps: 1996-2011 vs 2017 Post-Hurricane Harvey

The PAH distribution maps (Figures 5a-f) map three categories of PAH concentrations in logscale: Low Molecular Weight (LMW) PAHs, High Molecular Weight (HMW) PAHs, and Total PAHs. Each of these figures utilize kriging where values were interpolated on a logscale. The pre-Harvey sediments indicate a relatively consistent LMW and HMW pattern (Figures 5a-d), while there is a notable difference in the post-Harvey sediments for LMW and HMW PAH distributions (Figure 5b, 5d). As HMW PAHs (4-6 ring PAHs) predominately originate from combustion sources, one of which is black carbon or soot, these PAHs have been found to predominantly remain in the particulate phase either in the atmosphere (Park et al., 2001) or in sediments (Kanzari et al., 2014; Rabodonirina et al., 2015). Consequently, the HMW PAHs are more likely to sorb and partition to organic matter (Chiou et al., 1998; Rabodonirina et al., 2015; Wang et al., 2001) and not readily biodegrade. As the post-Harvey layer was mostly mud dominant with a sand layer at the base, the likelihood of HMW PAHs to be present in the mud layer is likely due to the present organic matter. Thus, the post-Harvey deposit consists of sediment eroded, primarily from within the HSC/upper bay, which was then transported and dispersed around Galveston Bay (Depllapenna et al. In Review A&B; Du et al., 2019, 2020).

Figure 5d shows this pattern as the HMW PAHs have elevated distributions in the Upper HSC that then decrease towards Galveston Bay and Trinity Bay. However, it is important to note the values shown do not include the confidence intervals. As a result, some of the regions farther from the data point (e.g. coast line of Trinity Bay and Lower Galveston Bay) may have high uncertainties associated with the values due to the limited number of nearby sampling sites.

In relation to the PAH diagnostic ratios, PAH transportation and spatial distribution within the environment is influenced by variable environmental matrices (e.g. grain size, organic matter) and anthropogenic sources such as emission mixing (Davis et al., 2019; Rocha & Palma, 2019; Tobiszewski & Namieśnik, 2012; Yunker et al., 2002). The distribution maps show zones of elevated LMW, HMW, or Total PAHs for both pre- and post-Harvey conditions. For the pre-Harvey conditions, the zones of elevated LMW, HMW, or Total PAHs suggest a petroleum combustive input source as Figure 5a and 5c demonstrate. When the LMW and HMW PAHs are compared for the pre-Harvey maps (Figure 5a,5c) there are two consistent elevated zones; one in the middle of Galveston Bay/near Trinity Bay and the other around inner coastal Galveston Island and I-45. In contrast, the post-Harvey LMW and HMW maps (Figure 5b, 5d) show there are more HMW PAHs present than LMW. This difference could be attributed to the sorption of HMW PAHs to the post-Harvey mud and the tendency of HMW PAHs to not be as readily degraded as petroleum PAHs (Davis et al., 2019; Tobiszewski & Namieśnik, 2012). The total PAHs on the other hand combine the LMW and HMW PAHs to show the overall PAH pattern distribution both in pre- and post-Harvey conditions. Figure 5e shows under pre-Harvey conditions the Upper HSC, Clear Lake, inner Coastal Galveston Island/near I-45, and middle Galveston Bay have elevated PAH distributions. Figure 5f shows under post-Harvey conditions, PAHs started with elevated levels in the Upper HSC and were widely distributed into the rest of Galveston Bay. This suggests the PAHs could partition into the available organic matter being redistributed by the severe rainfall and flooding in the area.

When only the pre-Harvey data is considered (Figures 5a, 5c, 5e), the areas predicted to influence total PAH concentration distribution are within the Upper HSC, portions of Mid-Ship Channel (Clear Lake, central Galveston Bay) and urbanized areas near inner Galveston island. These areas demonstrate elevated HMW PAHs and partially elevated LMW PAHs, thereby indicating a possible point-source or event. Under post-Harvey conditions, the HMW PAHs and Total PAHs (Figures 5d, 5f) followed similar distribution patterns to the pre-Harvey data in that the Upper Ship Channel through Morgan' Point and into Trinity Bay and Lower Galveston Bay demonstrated a notable gradient. Therefore, when comparing PAH classes between pre- and post-Harvey conditions, the HMW PAHs tended to contribute more to the overall Total PAH distributions than LMW. This distribution can likely be explained by the prominent flood period and hydraulic trapping of suspended sediment in the mid bay during the Harvey flood (Dellapenna et al., in review B; Du et al. 2020). However, it is important to note that while the post-Harvey distribution appears dispersed within GB, the sediments sampled after Hurricane Harvey do not necessarily reflect proximal sourcing. In other words, the Harvey deposit illustrated in Figure 5b, 5d, and 5f are showing the sediments redeposited from the San Jacinto Estuary and Buffalo Bayou; two areas within the Upper HSC. Therefore, these maps also suggest several areas of interest for future sampling designs: Upper HSC – Morgan's Point, Morgan's Point to Trinity Bay, Morgan's Point to Lower Galveston Bay. Furthermore, as are a few relevant oyster reefs (e.g. Redfish Oyster Reef and Hannah's Reef) in the last region (Morgan's Point to Lower Galveston Bay), there may be addition interest in monitoring these sediments for oyster exposures and in turn human and animal oyster consumption.

Conclusions

Overall, Hurricane Harvey appeared to result in a small, but detectable, increase in surface sediment PAH concentrations as compared to historical data. This small shift is consistent with studies of Harvey-induced sediment transport and dispersal, which suggest that

the newly deposited sediment was eroded largely from the HSC/upper bay, where contamination is typically greater. Additionally, this study detected a gradient trend in HMW and Total PAHs after Hurricane Harvey in three general regions of interest: Upper HSC, Mid-Channel, and Lower Bay. Overall sourcing patterns indicated combustive sourcing that are likely associated with anthropogenic sources from the highly urbanization within the region. Moreover, sourcing patterns were not noticeably different pre- and post-Harvey. Based on the gradient trend detected in the Post-Harvey samples, the Upper HSC and the area between Morgan's Point and Lower Galveston Bay may be of interest to focus sampling in future studies. However, given the San Jacinto Estuary and Buffalo Bayou sediments were deposited in GB, both the Upper HSC and Galveston Bay will need to be sampled to determine whether the PAH distribution is more similar to pre-Harvey or post-Harvey. Then, even though the PAH concentrations detected were not close to any SQG levels (ERL or ERM), this does not mean future sediment samples from the Upper HSC or other areas in Galveston Bay will consistently reflect this trend; especially since the estuarine environment is dynamic. In light of future hurricane seasons, understanding PAH spatial trends and the potential environmental risks associated with sediments can help develop a working baseline for reference within the Galveston Bay and Houston Ship Channel region.

Acknowledgements

The authors are grateful for financial support by NIEHS Superfund Research Program P42 ES027704, Texas A&M University Toxicology T32 Training Grant: T32 ES026568, and the Department of Defense (DOD) Science Mathematics and Research for Transformation (SMART) Program. We also thank the Geochemical Environmental Research group for their analytical support and guidance provided with these samples (M. Devitt, S. Sweet, L. McDonald).

References

Al Mukaimi, M. E., Dellapenna, T. M., & Williams, J. R. (2018). Enhanced land subsidence in Galveston Bay, Texas: Interaction between sediment accumulation rates and relative sea level rise. *Estuarine, Coastal and Shelf Science*, *207*(February), 183–193. https://doi.org/10.1016/j.ecss.2018.03.023

Al Mukaimi, M. E., Kaiser, K., Williams, J. R., Dellapenna, T. M., Louchouarn, P., & Santschi, P. H. (2018). Centennial record of anthropogenic impacts in Galveston Bay: Evidence from trace metals (Hg, Pb, Ni, Zn) and lignin oxidation products. *Environmental Pollution*, *237*, 887–899. https://doi.org/10.1016/j.envpol.2018.01.027

Birch, G. F. (2018). A review of chemical-based sediment quality assessment methodologies for the marine environment. *Marine Pollution Bulletin*, *133*(November 2017), 218–232. https://doi.org/10.1016/j.marpolbul.2018.05.039

Chapman, P. M. (2002). Integrating toxicology and ecology: Putting the “eco” into ecotoxicology. *Marine Pollution Bulletin*, *44*(1), 7–15. https://doi.org/10.1016/S0025-326X(01)00253-3

Chapman, P. M. (2018). Environmental quality benchmarks—the good, the bad, and the ugly. *Environmental Science and Pollution Research*, *25*(4), 3043–3046. https://doi.org/10.1007/s11356-016-7924-2

Chiou, C. T., Mcgroddy, S. E., & Kile, D. E. (1998). Partition characteristics of polycyclic aromatic hydrocarbons on soils and sediments. *Environmental Science and Technology*, *32*(2), 264–269. https://doi.org/10.1021/es970614c

Davis, E., Walker, T. R., Adams, M., Willis, R., Norris, G. A., & Henry, R. C. (2019). Source apportionment of polycyclic aromatic hydrocarbons (PAHs) in small craft harbor (SCH) surficial sediments in Nova Scotia, Canada. *Science of the Total Environment*, *691*, 528–537. https://doi.org/10.1016/j.scitotenv.2019.07.114

Du, J., Park, K., Dellapenna, T. M., & Clay, J. M. (2019). Dramatic hydrodynamic and sedimentary responses in Galveston Bay and adjacent inner shelf to Hurricane Harvey. *Science of the Total Environment*, *653*, 554–564. https://doi.org/10.1016/j.scitotenv.2018.10.403

EPA (Environmental Protection Agency). (2014). *Appendix A to 40 CFR, Part 423–126 Priority Pollutants*. 653–654. https://www.epa.gov/eg/toxic-and-priority-pollutants-under-clean-water-act

Foundation, H. and G. B. (2017). *Galveston Bay Report Card 2017*.

HARC and Galveston Bay Foundation. (2018). *Galveston Bay Report Card 2018*. WWW.GALVBAYGRADE.ORG

Hieke, A. S. C., Brinkmeyer, R., Yeager, K. M., Schindler, K., Zhang, S., Xu, C., Louchouarn, P., & Santschi, P. H. (2016). Widespread Distribution of Dehalococcoides mccartyi in the Houston Ship Channel and Galveston Bay, Texas, Sediments and the Potential for Reductive Dechlorination of PCDD/F in an Estuarine Environment. *Marine Biotechnology*, *18*(6), 630–644. https://doi.org/10.1007/s10126-016-9723-7

Hou Aixin, DeLaune Ronald D, Tan MeiHuey, Reams Margaret, and L. E. (2009). Toxic Elements in Aquatic Sediments: Distinguishing Natural Variability from Anthropogenic Effects. *Water Air Soil Pollution*, *203*(1), 179–191. https://doi.org/10.1007/s11270-009-

0002-3

Howell, N. L., Rifai, H. S., & Koenig, L. (2011). Comparative distribution, sourcing, and chemical behavior of PCDD/Fs and PCBs in an estuary environment. *Chemosphere*, *83*(6), 873–881. https://doi.org/10.1016/j.chemosphere.2011.02.082

Jackson, T. J., Wade, T. L., Sericano, J. L., Brooks, J. M., Wong, J. M., Garcia-Romero, B., & McDonald, T. J. (1998). Galveston Bay: Temporal changes in the concentrations of trace organic contaminants in national status and trends oysters (1986-1994). *Estuaries*, *21*(4 B), 718–730. https://doi.org/10.2307/1353276

Kanzari, F., Syakti, A. D., Asia, L., Malleret, L., Piram, A., Mille, G., & Doumenq, P. (2014). Distributions and sources of persistent organic pollutants (aliphatic hydrocarbons, PAHs, PCBs and pesticides) in surface sediments of an industrialized urban river (Huveaune), France. *Science of the Total Environment*, *478*, 141–151. https://doi.org/10.1016/j.scitotenv.2014.01.065

Kennicutt II, M. C. (2017). Chapter 4 - SEDIMENT CONTAMINANTS OF THE GULF OF MEXICO. In *Habitats and Biota of the Gulf of Mexico: Before the Deepwater Horizon Oil Spill*. https://doi.org/10.1007/978-1-4939-3447-8

Kwok, K. W. H., Batley, G. E., Wenning, R. J., Zhu, L., Vangheluwe, M., & Lee, S. (2014). Sediment quality guidelines: Challenges and opportunities for improving sediment management. *Environmental Science and Pollution Research*, *21*(1), 17–27. https://doi.org/10.1007/s11356-013-1778-7

National Oceanic & Atmospheric Administration (NOAA). (2020-a). *Data Integration Visualization Exploration and Reporting (DIVER): Southeast*. https://www.diver.orr.noaa.gov/web/guest/diver-explorer?siteid=4&subtitle=Southeast. Last Retrieved: January 2020

National Oceanic & Atmospheric Administration (NOAA). (2017-b). *NOAA's National Status and Trends More Data: Gulf of Mexico - Galvestion Bay Organics - Sediment*. https://cdn.coastalscience.noaa.gov/datasets/nsandt/dataFiles/ba/gulfCoast/GalvestonBay_Organics_Sediment.txt. Last Retrieved: January 2020.

National Oceanic & Atmospheric Administration (NOAA). (2020-c). *NOAA Screening Quick Reference*. 1–34. https://response.restoration.noaa.gov/environmental-restoration/environmental-assessment-tools/squirt-cards.html. Last Retrieved: October 2019.

National Toxicology Program. (2011). *Polycyclic Aromatic Hydrocarbons : 15 Listings*. *205*. https://ntp.niehs.nih.gov/ntp/roc/content/profiles/polycyclicaromatichydrocarbons.pdf

Nichol, M. &. (2010). *Galveston Bay Regional Sediment Management Galveston , Texas Programmatic Sediment*. *M&N Projec*(Document No. 6731-02RP002 Rev: 1). https://www.epa.gov/sites/production/files/2017-04/documents/galveston_odmds_smmp_2016_0.pdf

Park, J. S., Wade, T. L., & Sweet, S. (2001). Atmospheric distribution of polycyclic aromatic hydrocarbons and deposition to Galveston Bay, Texas, USA. *Atmospheric Environment*, *35*(19), 3241–3249. https://doi.org/10.1016/S1352-2310(01)00080-2

Programs, N. E. (1988). *Galveston Bay: issues, resources, status, and management*. *13*.

Qian, Y., Wade, T. L., & Sericano, J. L. (2001). Sources and bioavailability of polynuclear

aromatic hydrocarbons in Galveston Bay, Texas. *Estuaries*, *24*(6 A), 817–827. https://doi.org/10.2307/1353173

Rabodonirina, S., Net, S., Ouddane, B., Merhaby, D., Dumoulin, D., Popescu, T., & Ravelonandro, P. (2015). Distribution of persistent organic pollutants (PAHs, Me-PAHs, PCBs) in dissolved, particulate and sedimentary phases in freshwater systems. *Environmental Pollution*, *206*, 38–48. https://doi.org/10.1016/j.envpol.2015.06.023

Rocha, A. C., & Palma, C. (2019). Source identification of polycyclic aromatic hydrocarbons in soil sediments: Application of different methods. *Science of the Total Environment*, *652*, 1077–1089. https://doi.org/10.1016/j.scitotenv.2018.10.014

Santschi, P. H., Presley, B. J., Wade, T. L., Garcia-Romero, B., & Baskaran, M. (2001). Historical contamination of PAHs, PCBs, DDTs, and heavy metals in Mississippi River Delta, Galveston Bay and Tampa Bay sediment cores. *Marine Environmental Research*, *52*(1), 51–79. https://doi.org/10.1016/S0141-1136(00)00260-9

Soliman, Y. S., Alansari, E. M. A., Sericano, J. L., & Wade, T. L. (2019). Spatio-temporal distribution and sources identifications of polycyclic aromatic hydrocarbons and their alkyl homolog in surface sediments in the central Arabian Gulf. *Science of the Total Environment*, *658*, 787–797. https://doi.org/10.1016/j.scitotenv.2018.12.093

Tobiszewski, M., & Namieśnik, J. (2012). PAH diagnostic ratios for the identification of pollution emission sources. *Environmental Pollution*, *162*, 110–119. https://doi.org/10.1016/j.envpol.2011.10.025

US Army Corps of Engineers (USACE). (2017). *Houston Ship Channel - Expansion Channel Improvement Project*. http://www.swg.usace.army.mil/Missions/Projects/Houston-Ship-Channel-Expansion/

Wang, X. C., Zhang, Y. X., & Chen, R. F. (2001). Distribution and partitioning of polycyclic aromatic hydrocarbons (PAHs) in different size fractions in sediments from Boston Harbor, United States. *Marine Pollution Bulletin*, *42*(11), 1139–1149. https://doi.org/10.1016/S0025-326X(01)00129-1

Yeager, K. M., Santschi, P. H., Rifai, H. S., Suarez, M. P., Brinkmeyer, R., Hung, C. C., Schindler, K. J., Andres, M. J., & Weaver, E. A. (2007). Dioxin chronology and fluxes in sediments of the Houston ship channel, Texas: Influences of non-steady-state sediment transport and total organic carbon. *Environmental Science and Technology*, *41*(15), 5291–5298. https://doi.org/10.1021/es062917p

Yunker, M. B., Macdonald, R. W., Vingarzan, R., Mitchell, H., Goyette, D., & Sylvestre, S. (2002). *PAHs in the Fraser River basin: a critical appraisal of PAH ratios as indicators of PAH source and composition*. *33*, 489–515.

Tables

PAH Category	p-value	R^2
Total PAHs	0.0002	0.1766
2-3 Ring PAHs	<0.0001	0.2042
4-5 Ring PAHs	<0.0001	0.2038
6 Ring PAHs	0.0015	0.0613

Table 1: Summary statistics for the one-way ANOVA analysis between each year of with data collection (1996, 1997, 2007, 2010, 2011, 2017)

PAH Category	p-value (1996-2011 vs 2017)	Difference Between Means (1996-2011 vs 2017)
Total PAHs	0.0003	0.4810±0.1293
2-3 Ring PAHs	0.0016	0.3475±0.1074
4-5 Ring PAHs	<0.0001	0.6134±0.1407
6 Ring PAHs	0.0013	0.4660±1422

Table 2: Summary statistics for the two-tailed unpaired t-test for years 1996-2011 PAH categories listed versus the 2017 PAH data.

	Post-Harvey Median	Post-Harvey IQR	Post-Harvey Range	Post-Harvey Median	Post-Harvey IQR	Post-Harvey Range	ERL	ERM
Naphthalene	3.5	2.5, 5.5	0.5, 18.4	7.445	4.3325, 12.15	2.57, 26.33	160	2100
Acenaphthylene	1.9	0.6, 4.2	0, 26.6	3.985	2.2675, 8.065	0.71, 26.09	16	500
Acenaphthene	0.8	0.5, 1.4	0.2, 34.9	3.47	1.8825, 8.0125	0.59, 60.99	44	640
Fluorene	1.1	0.5, 2	0.2, 34.5	5.52	2.5225, 11.0925	1.39, 94.84	19	540
Phenanthrene	3.3	1.7, 6.8	0.2, 501.5	14.395	6.8625, 25.53	3.2, 142.67	240	1500
Anthracene	2.2	0.9, 6	0.1, 228.3	5.68	3.46, 1.5575	1.12, 138.25	85.3	1100
Fluoranthene	8.3	3.1, 18.3	0.1, 1473	33.07	12.6825, 72.7075	4.7, 462.63	600	5100
Pyrene	9.5	3.9, 25.3	0.2, 1502.7	39.13	14.68, 83.67	5.68, 403.6	665	2600
Benzo(a)anthracene	4.3	1.4, 10	0.1, 676.4	15.87	8.085, 35.495	1.83, 192.94	261	1600
Chrysene	5.7	2.1, 12.2	0.1, 711.6	20.42	9.9825, 59.445	2.45, 319.09	384	2800
Benzo(b)fluoranthene	8.5	3.1, 18.8	0.1, 800.4	37.165	15.8575, 73.5525	4.37, 538.74	-	-
Benzo(k)fluoranthene	2.3	0.9, 5.1	0, 178.7	8.595	4.5525, 18.01	0.83, 196.21	-	-
Benzo(a)pyrene	6.6	2.6, 16	0.1, 684.4	17.525	9.485, 32.6925	2.05, 244.5	430	1600
Perylene	6.8	3, 16.2	0.2, 187.2	77.12	41.5, 161.9525	14.88, 347.93	-	-
Indeno(1,2,3-c,d)pyrene	4.2	1.6, 12.1	0.1, 291.5	11.805	5.12, 27.135	0.91, 334.89	-	-
Dibenzo(a,h)anthracene	1.2	0.5, 2.9	0, 66.1	2.165	1.2475, 4.1125	0, 40.17	63.4	260
Benzo(g,h,i)perylene	5.5	2.3, 16.7	0.1, 289.5	20.395	10.49, 49.1425	2.39, 333.32	-	-
2-Methylnaphthalene	2	1, 3.2	0.2, 11	4.37	2.5475, 9.605	1.13, 21.26	70	670
Total LMW PAHs	29.8	12.3, 67.2	2.6, 2035.5	81.32	38.9925, 184.55	16.92, 746.48	552	3160
Total HMW PAHs	51.4	19.5, 117.1	1.8, 5712	271.1	128.9975, 547.655	63.6, 2787.82	1700	9600
Total PAHs	89.2	35.8, 214.1	5, 8040.2	366.365	168.905, 779.885	80.52, 3384.41	4022	44792

Table 3: Modified NOAA SQuiRT Chart with individual PAHs, HMW PAHs, LMW PAHs, and Total PAHs listed in the first column; corresponding SQuiRT Chart for the effects range-low (ERL) and effects range median (ERM) values and study PAH values analyzed in this study are summarized here.

Figure Captions

Figure 1: Base map of all sample sites for sediment data from 1996-2011 (NOAA) and 2017 (post-Harvey). The 1996 data comprised of 72 sample sites, the 1997-2011 data comprised of 6 monitoring sites, and the post-Harvey data comprised of 32 sampling sites.

Figure 2a: Boxplots for PAHs (a: Total, b: 2-3 Ring, c: 4-5 Ring, d: 6 Ring) for 1996-2017. Black boxplots signify the NOAA 1996-2011 data, while the blue boxplot signifies the 2017 post-Harvey data.

Figure 3: Comparison of sediment core PAH distributions (2-3 Ring, 4-5 Ring, and 6 Ring) collected pre-Harvey in 2016 (SB1 and SB2) and post-Harvey in 2017 (VC2 and VC4). Panel a cores were collected south of Bear Lake in the San Jacinto River, panel b cores were collected in Burnett Bay. Due to the small sample size, a qualitative comparison is made between each of pair of cores based on depth.

Figure 4: Double Ratio sourcing plots comparing 1996 NOAA data (a, c) and post-Harvey data (b, d). Panels a and b show BaA/(BaA+CHR) vs. Fluo/(Fluo+PY); panels c and d show A/A(PHE) vs. Fluo/(Fluo+PY). The blue up-triangles show sites from the Upper HSC; purple squares show sites from the mid-channel (between Morgan's point to the beginning of Lower Galveston Bay; black down-triangles show sites from the Lower Bay to the entry point at Bolivar Peninsula.

Figure 5: Geospatial distribution maps of kriged concentrations of PAHs pre-Harvey (a, c, e) and post-Harvey (b, d, and f) sediments. Each pair of maps compares different PAH categories (a and b: Low Molecular Weight; c and d: High Molecular Weight; e and f: Total). Shown on land are developed areas (evident in the Upper Houston Ship Channel and Houston, TX as well as near Texas City, TX) and land elevation (low throughout the region, with higher elevations above the San Jacinto River).

Figures

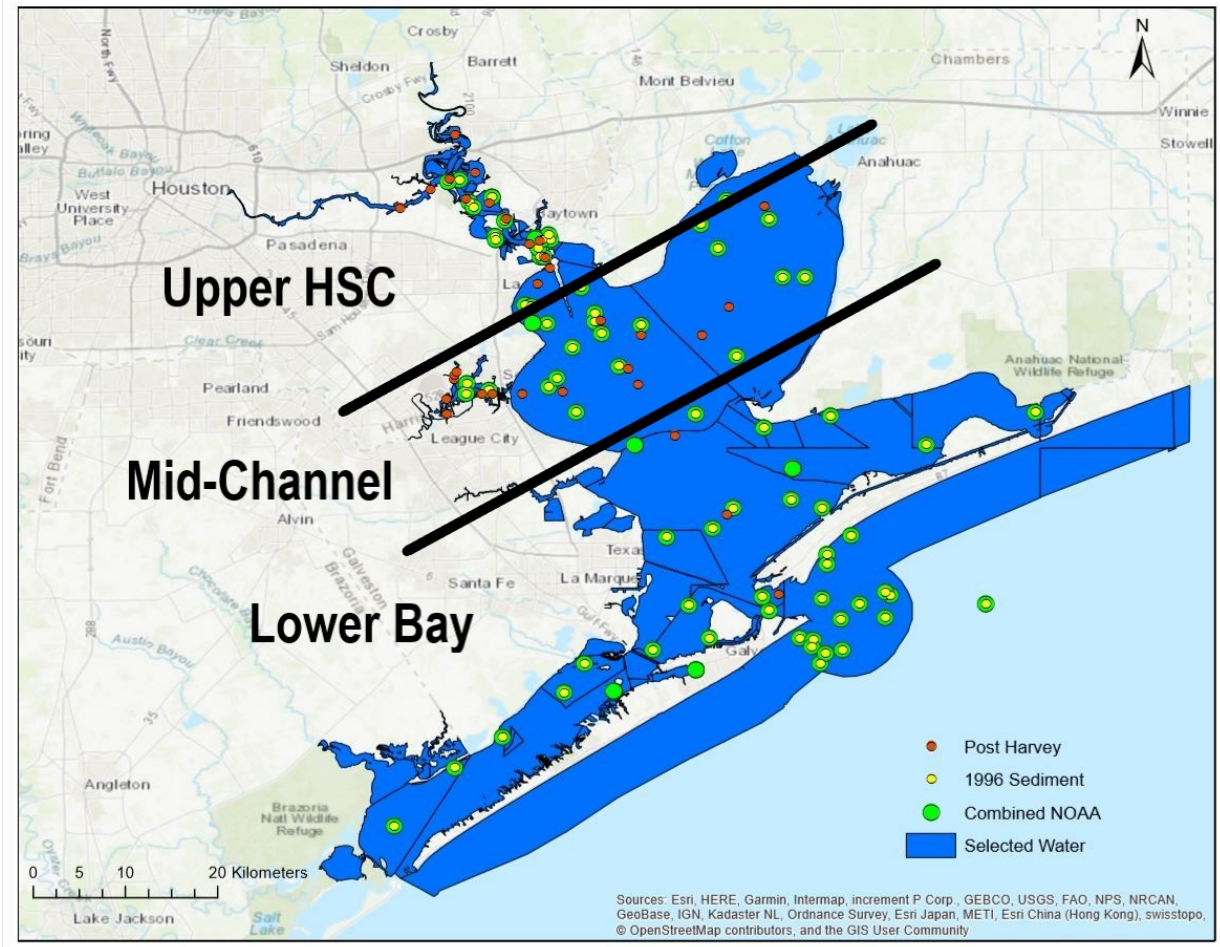

Figure 1: Base map of all sample sites for sediment data from 1996-2011 (NOAA) and 2017 (post-Harvey). The 1996 data comprised of 72 sample sites, the 1997-2011 data comprised of 6 monitoring sites, and the post-Harvey data comprised of 32 sampling sites.

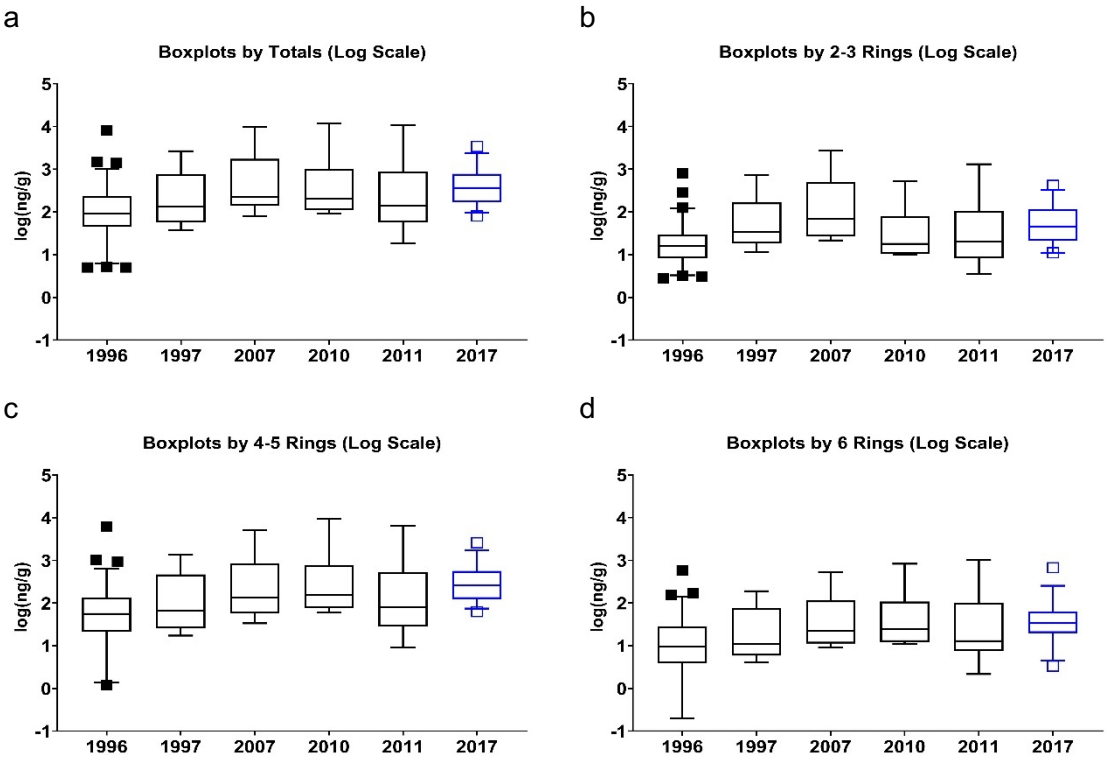

Figure 2: Boxplots for PAHs (a: Total, b: 2-3 Ring, c: 4-5 Ring, d: 6 Ring) for 1996-2017. Black boxplots signify the NOAA 1996-2011 data, while the blue boxplot signifies the 2017 post-Harvey data.

a

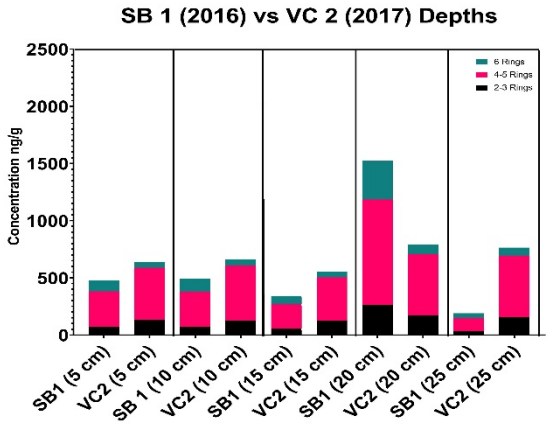

b

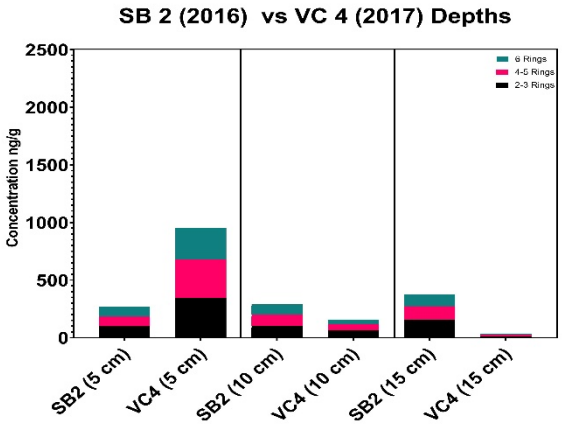

Figure 3: Comparison of sediment core PAH distributions (2-3 Ring, 4-5 Ring, and 6 Ring) collected pre-Harvey in 2016 (SB1 and SB2) and post-Harvey in 2017 (VC2 and VC4). Panel a cores were collected south of Bear Lake in the San Jacinto River, panel b cores were collected in Burnett Bay. Due to the small sample size, a qualitative comparison is made between each of pair of cores based on depth.

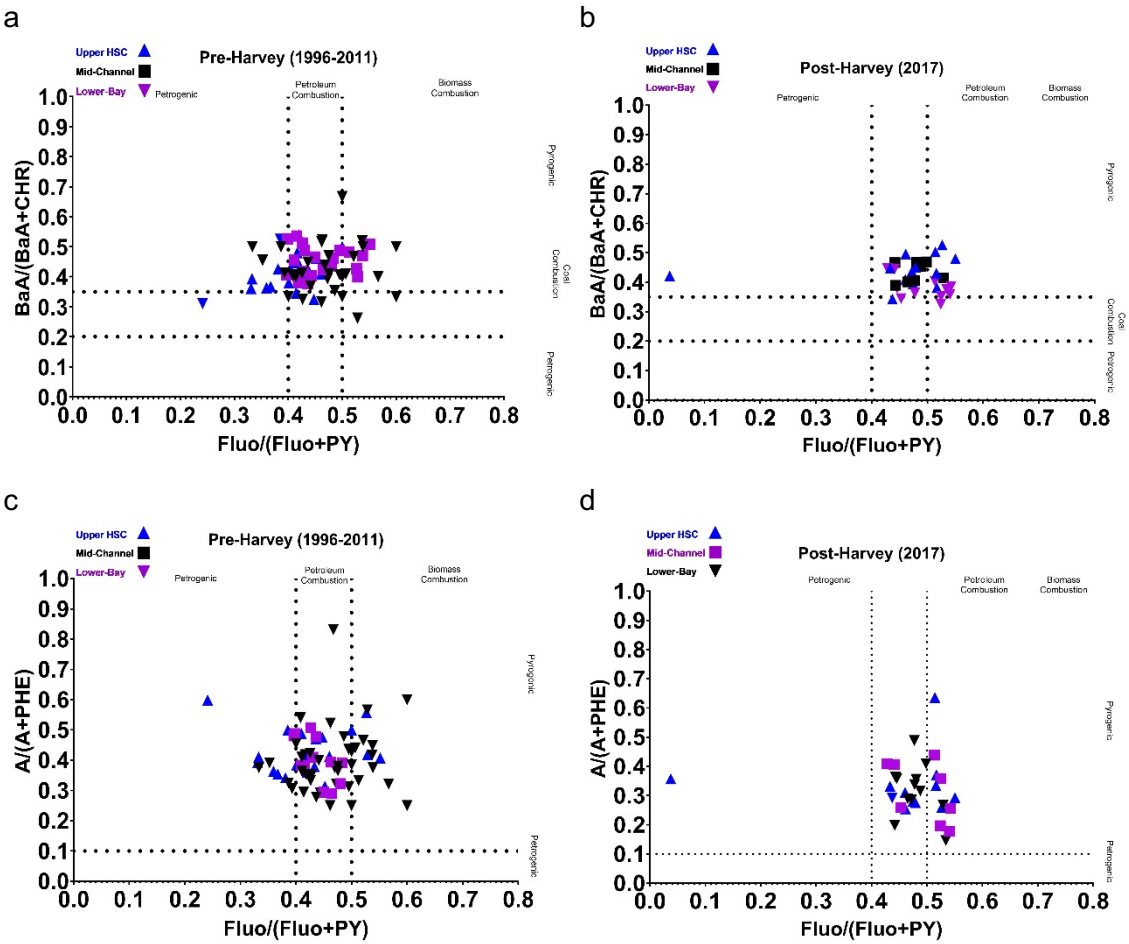

Figure 4: Double Ratio sourcing plots comparing 1996 NOAA data (a, c) and post-Harvey data (b, d). Panels a and b show BaA/(BaA+CHR) vs. Fluo/(Fluo+PY); panels c and d show A/A(PHE) vs. Fluo/(Fluo+PY). The blue up-triangles show sites from the Upper HSC; purple squares show sites from the mid-channel (between Morgan's point to the beginning of Lower Galveston Bay; black down-triangles show sites from the Lower Bay to the entry point at Bolivar Peninsula.

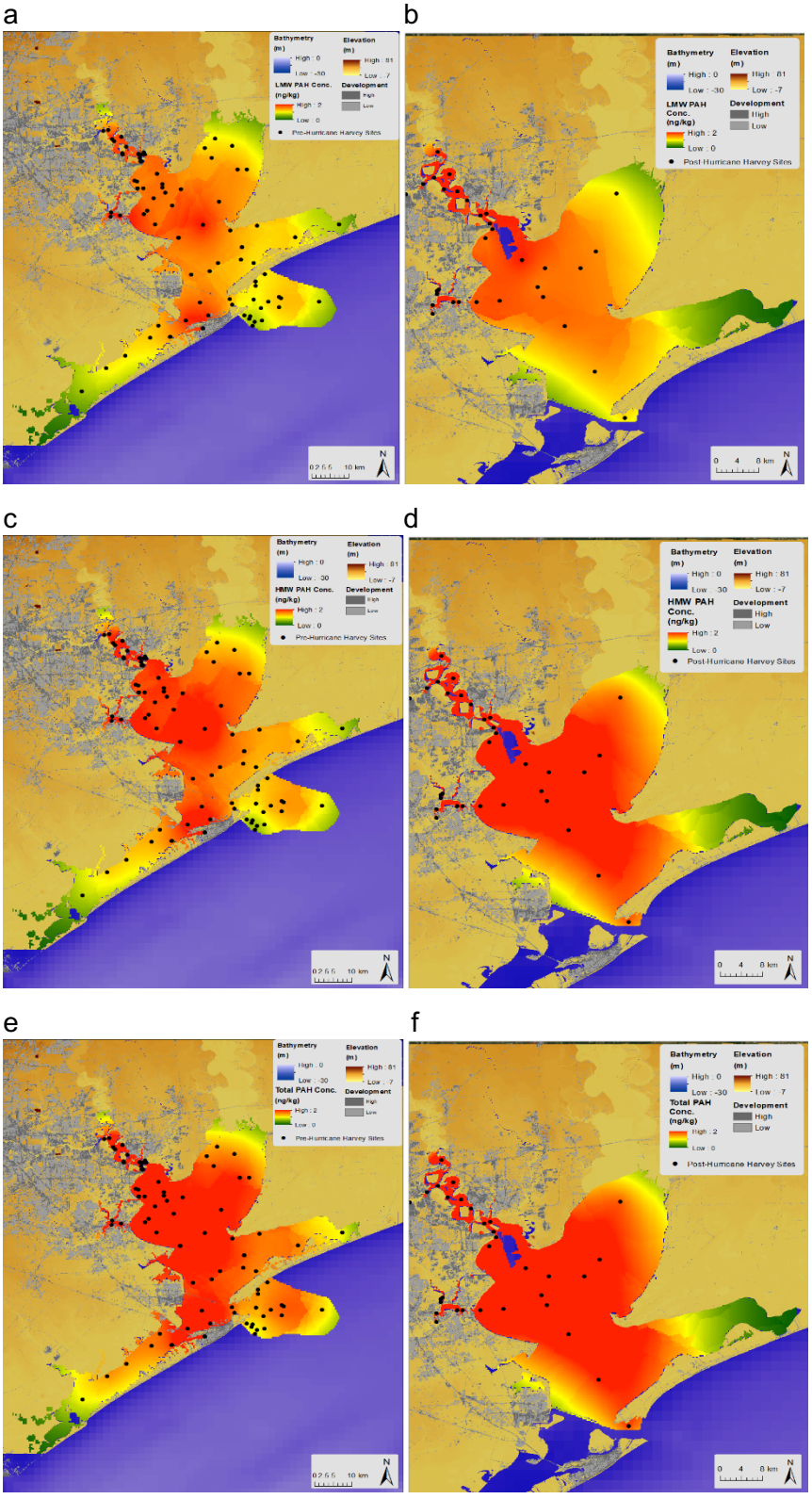

Figure 5: Geospatial distribution maps of kriged concentrations of PAHs pre-Harvey (a, c, e) and post-Harvey (b, d, and f) sediments. Each pair of maps compares different PAH categories (a and b: Low Molecular Weight; c and d: High Molecular Weight; e and f: Total). Shown on land are developed areas (evident in the Upper Houston Ship Channel and Houston, TX as well as near Texas City, TX) and land elevation (low throughout the region, with higher elevations above the San Jacinto River).

Cold Front Sediment Resuspension, Age, and Residence times of suspended sediment using $^{7}Be/^{210}Pb_{xs}$ Ratio in Galveston Bay

Nicole Schmid[ab], Timothy M. Dellapenna[ab], and Kyeong Park[ab]

[a]Department of Marine and Coastal Environmental Science, Texas A&M University at Galveston

[b]Department of Oceanography, Texas A&M University

Abstract

The winds associated with the passage of meteorological fronts (cold fronts) cause waves that induce sediment remobilization/resuspension, especially in shallow estuaries such as Galveston Bay. The passage of cold fronts, collectively, over time, generate more sediment resuspension than most hurricanes and tropical storms, on an annual to decadal basis. With a warming climate, the intensity of all meteorological events is beginning to have even greater impacts on these productive ecosystems. To better understand the effects that the passage of cold fronts have on resuspending sediment, water samples were collected during frontal passages at two locations in Galveston Bay. One in the upper portion of the bay (Kemah, TX) and another closer to the mouth of the bay (Texas A&M University Boast Basin). Additionally, a Conductivity, Temperature, Depth (CTD) data logger and sensor equipped with an Optical Backscatter (OBS) turbidity measuring sensors was deployed in Trinity Bay to collect data during both frontal passages and calm water conditions. By collecting precipitation, water samples in both the upper and lower bay, and measuring the ratio of $^{7}Be/^{210}Pb$ in these samples; we can quantify the residence times of total suspended sediment (TSS) in upper and lower Galveston Bay. We found that, in general, that the age/residence time of the sediment are younger/shorter in the Upper Bay and older/longer towards the mouth of Galveston Bay. Additionally, with stronger winds and the rain that generally accompanies cold fronts, TSS concentrations are higher in upper Galveston Bay versus closer to the mouth. This is because there is more of an abundance of clay dominated mud in upper Galveston Bay and closer to the mouth the bay sediment consists of coarser mud (higher silt content, with sand); allowing for deposition to occur at a faster rate in the lower bay, where muds are coarser and have a higher fall velocity than then finer muds found within the upper bay.

1. Introduction

1.1 NGOM Estuaries

Galveston Bay is a shallow bay and, provides nursing habitat for multiple valuable fisheries, including white and brown shrimp (Stunz et al., 2010) and provides approximately 14% of the US wild catch of oysters (Haby et al., 2009). A key process in shallow estuaries is the frequency of sediment resuspension. An increased amount of sediment resuspension and deposition in an estuary may cause smothering of benthic aquatic organisms and the clogging of water intakes (Winterwept & VanKersteren, 2004). Additionally, sediment resuspension causes the redistribution of biogeochemical constituents, as well as contaminants and organic matter (Dellapenna et al., 2006, Dellapenna et al., 2020). Sediment remobilization/resuspension plays a role in many estuarine processes; especially the cycling of nutrients and pollutants in and out of an estuary (Baskaran & Santschi, 1993). Point source and nonpoint source discharges of pollutants (i.e. trace metals and hydrocarbons) can have significant environmental impacts in an estuary (e.g. Dellapenna et al., 2006; 2020). These constituents can be stored in the sediment during periods of sediment deposition and are resuspended during wind-induced wave resuspension, in addition to any other resuspension events (Dellapenna et al., 2006). Particle reactive contaminants generally move slowly through an estuarine system, transported through the abundant cycles of deposition and resuspension during hydrological stages (tides, etc.) (Saari et al., 2010).

Wind plays an important role in determining water level in many shallow-water, microtidal coastal plain estuaries, including Galveston Bay (Cox et al., 2002). Surface gravity waves are the primary mechanisms driving sediment resuspension in shallow, microtidal estuaries (Booth et al., 2000). South-east prevailing winds tend to generate wave fetch that results in increased water-column mixing and erosion (Ward Jr, 1980). Wind-induced currents and wave resuspension are important sources of energy for sediment transport within an ecosystem and can be dominant in shallow, microtidal estuaries, affecting a large portion, if not all of the water column (Booth et al., 2000). High concentrations of total suspended sediment are most often associated with meteorologically driven events, especially winter cold fronts in Northern Gulf of Mexico estuaries (Perez et al., 2000).

Based on findings in Walker and Hammack (2000), sediment resuspension and transport are maximized during the passage of winter storms over Louisiana estuaries. Throughout a study performed in Fourleague Bay, Louisiana, northerly winds were found to have the greatest wind velocities; and wind direction played an important role in the transport of water and sediment (Perez et al., 2000). The

residence time of suspended sediment in the water column is defined here as the average length of time during which the sediment resides within the bay as suspended sediment. The residence times of suspended sediment in the water column has been found to range from a few days in low-energy estuaries to several weeks in high-energy estuaries (Olsen et al., 1986).

1.2 Cold Fronts

In Galveston Bay, there are on average, 20-30 cold fronts a year that pass, whereas hurricanes and tropical storms impact the bay on average once every 1.5 years, collectively (Walker and Hammack, 2000, Roberts et al., 1987, Byrne, 1975). Overall, cold fronts occur generally between October through April and have a fairly consistent nature in characteristics (Walker and Hammack, 2000, Roberts et al., 1987). The consistent nature of cold fronts begins as a passage defined by a shift from a southerly to northly wind direction that propagates in a clockwise direction (Perez et al., 2000). The nature of cold fronts is thought to be more effective on the coastal environment than tropical storms due to higher occurrence frequency and larger area of coverage along with shifts (Moeller et al., 1993). This is due to the creation of waves caused by the wind shifts that transports fluid mud from one area to another (Kemp, 1986). The larger spatial extend of cold fronts causes them to affect an entire bay. Cold fronts have a greater impact than both hurricanes and tropical storms that tend to affect a smaller spatial area and occur at a lesser frequency (Moeller et al., 1993, Pepper et al., 1999; Roberts et al., 1987). There is a natural variability of wind including the orientation, propagation direction and speed, and strength of winds produced during cold front events that dictates the effect of suspended sediment movement within an estuary (Moeller et al., 1993).

1.3 Sediment Resuspension

Turbidity is a measure of the degree to which water loses its transparency (Hardenbergh, 1938) and is due to both the presence of suspended particles, including sediment, as well as phytoplankton, particulate organic matter and other particulates (MacIntyre & Cullen, 1996; Biggs, 1970). Total suspended sediment (TSS) is the quantification of the mass of sediment that is suspended in the water column. TSS is characterized as being particles that settle too slowly to fall out of suspension during slack water (Sanford and Halka, 1993). Suspended sediment is derived from the erosion, or resuspension and

deposition of sediment at the water-sediment interface (Ha & Park., 2012). TSS concentrations can also vary widely depending upon riverine input, wind forcing's, drainage basin size, depth, area of the bay, sediment composition, and tidal range (Perez et al., 2000). Additionally, Perez et al. 2000 found that total suspended sediment peaks were highly correlated to post-frontal winds.

1.4 Characteristics associated with Cold Fronts

Cold fronts are accompanied by a high variability of wind speed and wind direction that largely affect TSS concentrations and fluxes (Perez et al., 2000). Wind direction and speed have been shown to be the primary factors controlling TSS, sediment transport and circulation (Walker and Hammack, 2000). During these winter storms, wind speed causes the strongest sediment resuspension (Walker and Hammack, 2000). Sanford and Halka (1993), stated that sediment is 2-4 times more erodible shortly after being deposited versus sediments that were deposited for over a year. Booth et al. (2000) state that resuspension events are highest during fall, winter, and early spring due to frequent and intensive cold front events. In relation to cold fronts, winds above 10 m/s can cause resuspension greater than 80% of bottom sediments based on a study performed in Louisiana (Booth et al., 2000). Contaminant transport frequently occurs during storm events, especially if there is heavy precipitation (Du et al., 2020). Water bodies can be heavily impacted by pollution/contaminants from industrial activity, etc. (i.e. heavy metals) (Saari et al., 2010).

Cold fronts are important mechanisms for resuspending/remobilizing sediment in shallow estuaries, such as Galveston Bay (Carlin et al., 2016). Dellapenna et al. (2006) estimated that the sediment resuspension that results from cold fronts have an annual equivalence of 200-270% of the suspended sediment load from Galveston Bay's fluvial source. Sediment resuspension associated with strong cold fronts can reintroduce trace elements and pollutants back into the water column. Thus, increasing the time that these particles are in the water column and adsorbed to sediments (Olsen et al., 1986).

1.5 Isotopes

Short-lived radionuclides can be useful for studying seasonal particle dynamics under different flow regimes (Saari et al., 2010). Short half-lives, for example, 53 days for ^{7}Be and 24 days for for ^{234}Th,

23 years for ^{210}Pb, provide an advantage when considering recent events that cause sediment redistribution (Taylor et al., 2013).

^{7}Be is a cosmogenic radionuclide produced in both the stratosphere and troposphere as a result of cosmic ray spallation of nitrogen and oxygen (Brost et al., 1991). Following atmospheric fallout, ^{7}Be rapidly adsorbs to fine sediment particles (Taylor et al., 2013). ^{7}Be also serves as an indicator of recent sedimentation and transport of surface material on a catchment scale (Taylor et al., 2013). Many studies have demonstrated that deposition of ^{7}Be closely reflects rainfall volume, making it a useful tracer for studying events that relate to rainfall, such as cold fronts (Olsen et al., 1986; Baskaran & Santschi, 1993; Baskaran, Coleman, & Santschi; 1993, Taylor et al., 2013; Evrard et al. ,2015; Taylor et al., 2019). During cold front events when sediment resuspension is high, ^{7}Be within the bed sediment can be recycled back into the water column and interact with newly delivered ^{7}Be (Olsen et al., 1986).

^{210}Pb is a member of the ^{238}U decay chain. When ^{238}U decays in soils, it become ^{226}Ra and then decays into ^{222}Rn. Since radon is a noble gas, it emits from the land into the atmosphere where it decays to ^{210}Pb (atmospheric) (Baskaran, Coleman & Santschi, 1993). ^{210}Pb is released from the atmosphere and delivered from the surface via wet and dry fallout. ^{210}Pb is called $^{210}Pb_{xs}$ once it has adsorbed to particles by the decay of its' parent isotope.

Fallout patterns of ^{7}Be and ^{210}Pb are tightly correlated leading to these nuclides being useful for dependent tracers (Baskaran, Coleman, & Santschi, 1993). The similarities of ^{7}Be and ^{210}Pb as tracers include similar atmospheric deposition and strong adsorption to similar particles; meaning they do not preferentially adsorb to specific particle sizes or compositions. Therefore, using the activity ratio of these two particles is less variable than either isotope individually (Matisoff et al., 2005). Once radionuclides adsorb to sediment particles, they are strongly and nearly irreversibly bound to these particles, making it possible to study the movement and obtain the age of suspended sediment (Taylor et al., 2012). ^{210}Pb and ^{7}Be activities in the water column (dissolved and particulate) have been found to vary with precipitation and river discharge (Baskaran & Swarzenski, 2007; Sommerfield et al., 1999). The measurement of ^{7}Be and ^{210}Pb nuclide activity in sediment quantifies the time that the particles were tagged by the tracers deposited atmospherically (Matisoff et al., 2005). Sediment that has been recently labeled by radionuclides in the water were shown to display a similar ^{7}Be /^{210}Pb activity ratio to the rainfall event (Evrard et al., 2015). The ratio of ^{7}Be /^{210}Pb can also be used to quantify the proportion of resuspended bottom material in the water column (Olsen et al., 1989). Baskaran and Santschi, found that

concentrations of ^{7}Be are quickly diluted into coastal waters and sediment in 1-2 days following rainfall events.

In Galveston Bay, ^{7}Be activity in rainfall has previously been measured to contain 2 Bq[1]/L (Baskaran et al., 1993). Higher percentages of ^{210}Pb have been found to be related to $^{210}Pb_{xs}$[2] that becomes resuspended from bottom sediment (Baskaran & Santschi, 1993). Previous studies have found that over 95% of samples taken in Galveston Bay have $^{7}Be/^{210}Pb$ activity ratios of less than 250 dpm[3]/L (Baskaran, et al., 1993). In Galveston Bay, average concentrations of ^{7}Be and ^{210}Pb were 87,124 and 155 dpm/L and 6.75,6.85, and 11.4 dpm/L, respectively for three years. The inconsistency of seasonal trends in bulk depositional fluxes of ^{7}Be and ^{210}Pb lead to the main influence being based on the amount of precipitation during a specific year (Baskaran, Coleman, & Santschi, 1993).

1.6 Objective of Study

Collecting suspended sediment within the water column to test for TSS during cold fronts, along with instrumental data collection may permit quantification of sediment resuspension during the passage of a frontal system. The two radio-isotopes described above will be applied using the method developed by Matisoff et al., (2005) to find the age of suspended sediment in upper and lower Galveston Bay. The methodology will be explained in further detail in the Methods section below. The data collection for utilization of the method will be performed by collecting water samples in both the upper and lower bay, along with precipitation during the events. The activity of two radioisotopes will then be measured in the samples collected. The age of the sediment should be younger in the Upper Bay and older towards the mouth of Galveston Bay. Additionally, with stronger winds and the rain that generally accompanies cold fronts, TSS concentrations will be significantly higher in upper Galveston Bay versus closer to the mouth. This is because there is more of an abundance of mud in upper Galveston Bay, whereas the lower bay (closer to the mouth) contains a larger abundance of sand/shells as well as silt; allowing for deposition to occur at a faster rate than finer muds due to their respective fall velocities (Figure 1). Understanding physical processes, such as sediment resuspension, allows for proper management strategies to be

[1] Bq: becquerel is the SI derived unit of radioactivity.
[2] $^{210}Pb_{xs}$ is is the atmospherically derived ^{210}Pb from its decay parent isotope ^{226}Ra (Saari *et al.*, 2010).
[3] Dpm: disintegrations per minute

developed to ensure a stable and productive ecosystem for the species that live in the estuary (Walker and Hammack., 2000).

2. Background

Galveston Bay is a shallow, microtidal estuary and is the second largest in Texas, with a surface area of 1600 km^2. The average depth of the bay is 2.1 m and contains a ship channel with dimensions of 150 m in width and 10-15 m deep, oriented along the main axis of the bay (50 km long) (Du & Park, 2019). The exchange of tidal water flows through Bolivar Roads, which is the tidal inlet between Bolivar Peninsula and Galveston Island. An additional tidal inlet exists 47 km to the west and services Christmas Bay and the western half of West Galveston Bay. Average water residence time within Galveston Bay is approximately 40 days (Solis and Powell, 1999). Trinity Bay comprises the northeastern portion of Galveston Bay (Fig. 1), has depths generally ranging between 3-4 meters (Dellapenna et al., 2006) and the Trinity River flows into the head northeastern end of the bay. The Trinity River accounts for approximately 90% of the freshwater input and is the largest sediment source into Galveston Bay (SAGE, 2002, USGS, 2005). Another significant sediment load within the bay is the ongoing maintenance of the Houston Ship Channel. In waters deeper than 1.5m, Trinity Bay bottom sediment is mud dominated (approx. 40% of total bay area) (Dellapenna et al., 2006). Mud is the dominant sediment composition of the majority of the Galveston Bay system (Figure 1).

Adjacent to upper Galveston Bay is Houston, the fourth largest city in the USA. This metropolitan area directly drains into the San Jacinto River and Houston ship channel. Houston is the third largest seaport in the USA in terms of shipping tonnage and has been cited as one of the most polluted water bodies in the USA (EPA, 1980). Further south of Houston is the Houston-Texas City-Galveston area that is highly industrialized, specifically by petroleum, petrochemical, and chemical industries and has been estimated to contain 30-50% of total US chemical production and oil refineries (Santschi et al., 2001). Additionally, Galveston Bay receives over half of the total permitted wastewater discharges for the state of Texas and around 5 km^3 per year of wastewater input (EPA, 1980). Although in recent years, there has been improvement of cleanliness of waterways where nutrients, trace metals, and trace organics do not indicate a greatly polluted system (Santschi et al., 2001).

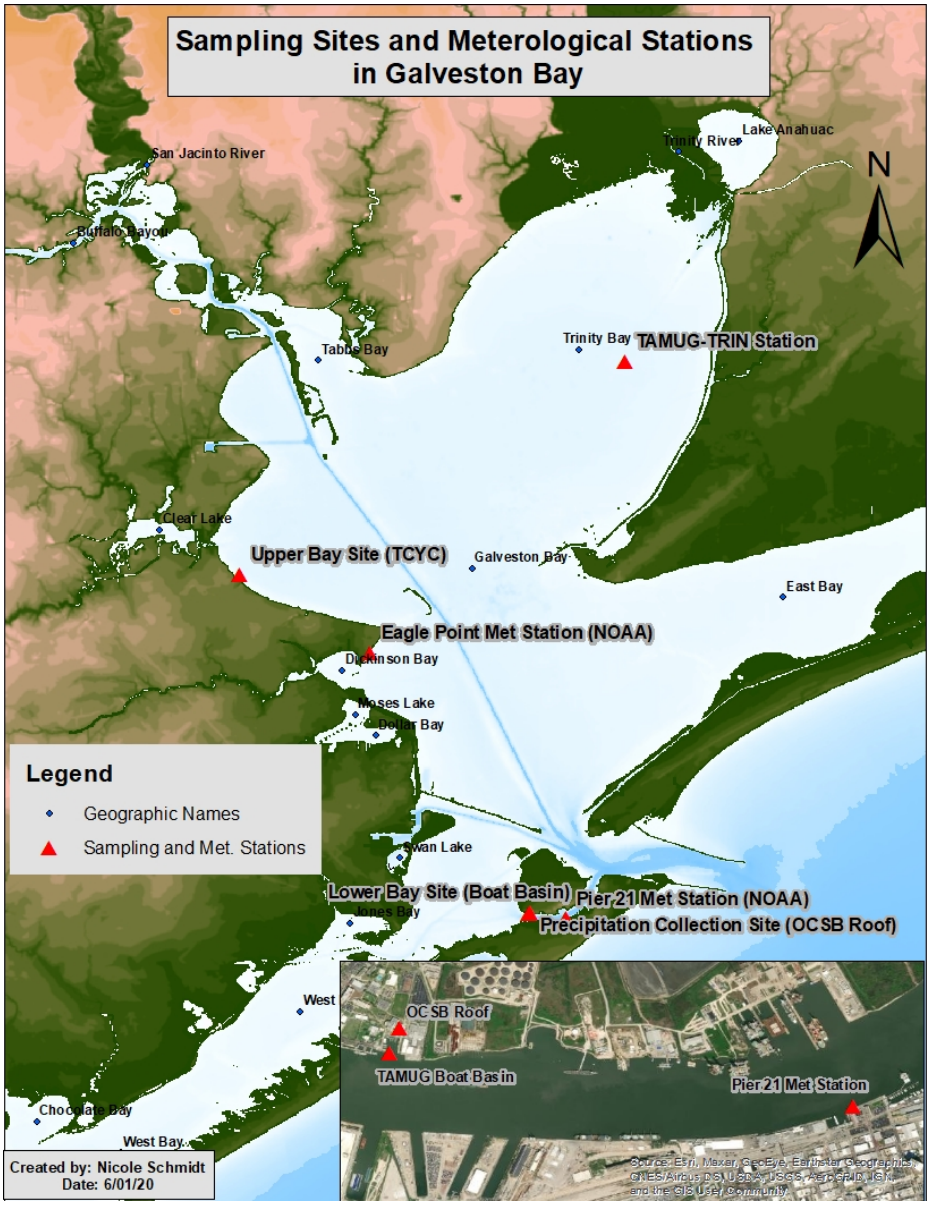

Figure 1: Suspended sediment, CTD deployment, and precipitation data collection sites from September 2019 to February 2020.

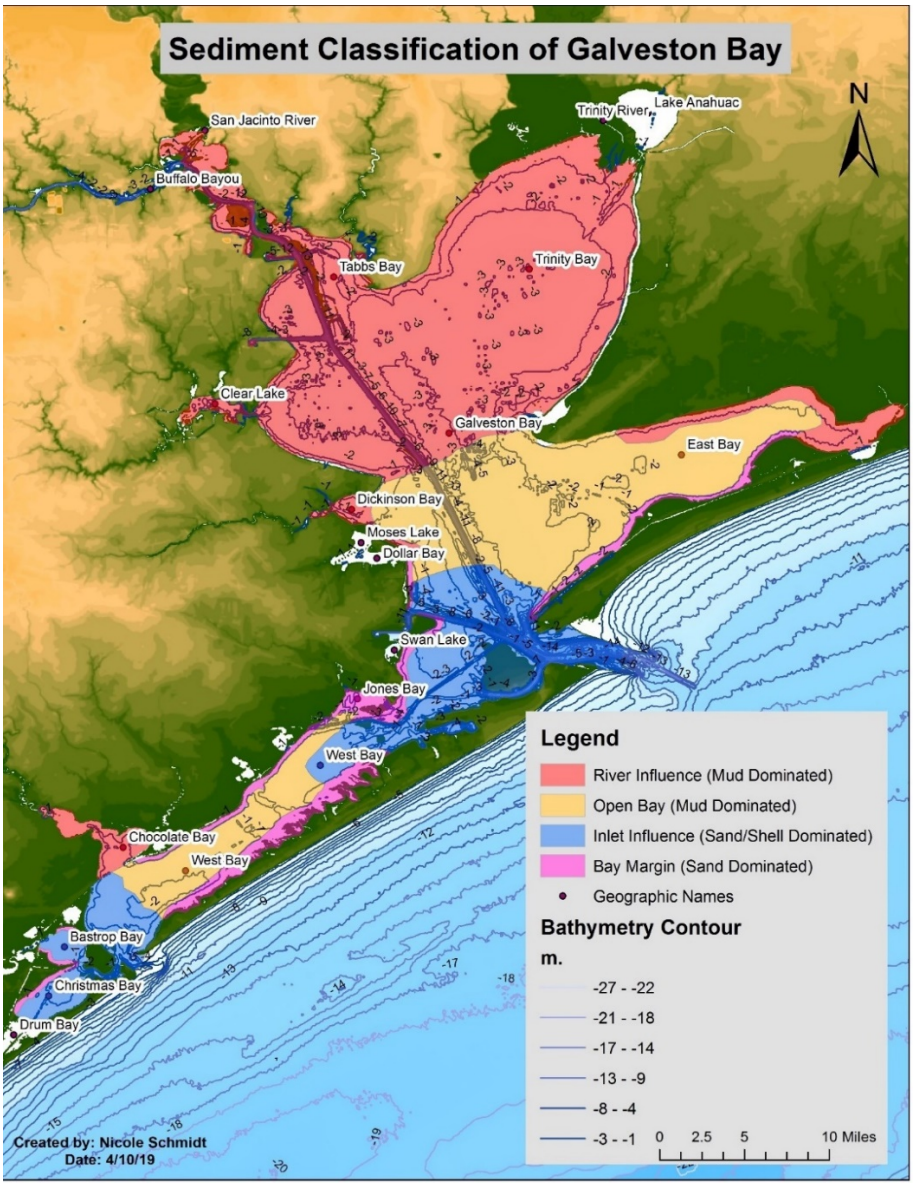

Figure 2: Sediment classification of polygons represented as polygons transcribed from Submerged Lands of Galveston-Houston area physical map. Source: Coastal Geology Lab TAMUG referenced from University of Texas Bureau of Economic Geology: Submerged Lands of Texas, Galveston- Houston Area Plate V. Distribution of Wetlands and Benthic Macroinvertebrates (1985)

Objectives

4.1 Research Questions:

1) What is the residence time of suspended sediment in the Upper Bay and Lower Galveston Bay using the Matisoff Method?
2) Is TSS higher in the Upper Bay versus the Lower Bay?
3) Is TSS higher during ebb or flood tide?
4) Is activity concentration higher in upper Galveston bay versus the lower bay?
5) Stronger winds, higher TSS?
6) Based on one data collection at the boat basin during a Tropical Storm (September 27, 2019), was the TSS higher during this than the TSS measured during cold fronts?

The purpose of this study is to understand the relationship between cold fronts and sediment resuspension. As mentioned above, Dellapenna et al., (2006) found that the passage of cold fronts, on an annual basisl volumetrically resuspends an order of magnitude more sediment than shrimp trawling and is equivalent to 200-270% of annual fluvial sediment input. Most meteorologically driven sediment resuspension occurs during the passage of northern cold fronts which mainly occur during winter months (Henry 1979, Hardy and Henderson, 2003).

By collecting precipitation, water samples in both the upper and lower bay, and measuring the ratio of $^{7}Be/^{210}Pb$ in these samples; we can quantify the residence times of suspended sediment in upper and lower Galveston bay. We hypothesize that the age of the sediment should be younger in the Upper Bay and older towards the mouth of Galveston Bay. Additionally, with stronger winds and the rain that generally accompanies cold fronts, total suspended sediment (TSS) concentrations will be significantly higher in upper Galveston Bay versus closer to the mouth. This is because there is more of an abundance of clay dominated mud in upper Galveston Bay and closer to the mouth contains coarser mud (higher silt content, with sand); allowing for deposition of coarser mud to occur at a faster rate than finer muds.

3. Methods/Data Collection

4.1 *Suspended Sediment Collection*

Figure 3: Texas Corinthians Yacht Club sampling site.

The Texas Corinthians Yacht Club (TCYC) pier located near Kemah, TX, was selected for our sampling location for suspended sediment from the bay. The pier extends 470 m into the bay, with the water depth of 2 m at end of the pier, permitting open water sampling. Water sampling was achieved by attaching a bilge pump to a 4 m long, 3.81 cm diameter aluminum pole, with the bilge pump being mounted 10 cm above the bottom of the pole to prevent penetration into the sediment while still collecting suspended sediment from the bottom. Five samples were collected from October 2019 to February 2020 at Texas Corinthians Yacht Club (TCYC) pier in Kemah, TX and four from September 2019 to February 2020 at the Texas A&M Galveston Boat Basin. Three to Four 20-liter polypropylene carboys were filled at each collection site per collection event.

Following collection, a portion of the samples were homogenized and about 1-2 liters of water were set aside to filter to determine TSS (g L^{-1}). TSS was measured using a Millipore filtration system connected to a vacuum pump filtered through a .45-micron filter. The filter weight and initial volume was recorded along with the post filter weight and volume. These were used to calculate TSS in g L^{-1}. The rest of the water was siphoned and sediment was separated by centrifugation. Once sediment was separated, it was air-dried and ground to a powder in a mortar and pestle, then placed in a test tube for radioisotope analyses. The dried sediment in the test tubes was placed in the germanium gamma well detector and counted for 24 to 36 hours.

Table 1: Wind speed and direction recorded during time of collection at the TAMUG Boat Basin and TCYC.

Boat Basin			
Date	**Time Collected**	**Wind Speed and Gusts (m/s)**	**Wind Direction**
9/27/2019	11:30 AM	N/A	N/A
1/29/2020	3:00 PM	6-7 m/s & 10 m/s gusts	WNW
2/21/2020	4:45 PM	6 m/s & 7.5 m/s gusts	NNE
TCYC			
Date	**Time Collected**	**Wind Speed & Gusts (m/s)**	**Wind Direction**
10/14/2019	11:00 AM - 1:30 PM	N/A	ESE
10/25/2019	1:00 PM - 2:00 PM	7.5 m/s & 13 m/s gusts	NNW
11/12/2019	4:30 PM	8 m/s & 11.5 m/s gusts	N
1/29/2020	1:30 PM	6 m/s	WNW
2/13/2020	2:00 PM -2:45 PM	6 m/s & 8 m/s gusts	N
2/21/2020	3:00 PM	6 m/s & 10 m/s gusts	NNE

4.2 CTD Deployment

An RBR CTD (conductivity, temperature and dept sensor) with two Seapoint optical back-scatter sensors (turbidity) was mounted to a homemade frame (pod) built for deployment in Trinity Bay from January 27, 2020 to February 27, 2020. One sensor was mounted 50 cm above the bed, and the other sensor was mounted 150 cm above the bed (Figure 2). The reasoning for the sensor placements at a specific height relates to the bottom boundary layer (BBL), which is the layer where hydrodynamics

Figure 4: The image on the left is the homemade pod built for deployment in Trinity Bay (right image).

control erosion/deposition of suspended sediment (Ha & Park, 2012). Three 45 kg of dumbbell weights were mounted at the base of the pod to keep it from moving during strong cold front events. Water was collected during deployment and upon retrieval to calibrate the sensors for TSS.

4.3 Turbidity Sensor Calibration

The calibration of the CTD Seapoint turbidity sensors was performed in the lab using sediment and water that was collected on site during deployment of the CTD in Trinity Bay. Prior to running the calibration, the sediment was sieved in order to obtain only the mud (silt and clay) fraction from the sample, which are generally suspended and thus measured during the deployment. The sediment was first filtered through a 250-microns sieve to remove larger shells, etc. and then through a 63-micron sieve to obtain the mud fraction. The leftover sample was centrifuged and evaporated to only contain the mud used for the calibration. The amount of tins and weight of sediment per sample added during the calibration were referenced from Minella et al. (2008), where they used to measure around 10 to 15 samples containing between 0.25 to 2.5 grams of sediment per tin. Similarly, 0.3 to 5.0 grams of sediment were measured into 18 different tins. Around 10 liters of the collected water was poured into a bucket where the calibration took place. The turbidity sensors were attached to a pole and placed in the bucket. A paint stirrer attachment was connected to a drill to allow for continuous homogenization of the bucket. The CTD was set to run on 6Hz profiling to constantly collect data.

Figure 5: Setup for CTD Turbidity Sensor Calibration conducted on 7/22/20.

The drill was inserted to homogenize the water and after this became homogenized, a mud sample was mixed with 1 L of the water from the bucket and mixed back in. After a few minutes, the bucket became equilibrated and around 400-600 mL of the water in the bucket was subsampled for filtering. The steps explained above were repeated 18 times in order to obtain a homogenized subsample after each tin was added. The subsamples were then filtered using the method described in the Suspended Sediment Collection section, above.

4.4 Precipitation Collection

Figure 6: Precipitation jug with attachments mounted on the roof of OCSB located at Texas A&M University at Galveston.

Precipitation was collected on the roof of the Ocean and Coastal Studies building at Texas A&M Galveston Campus (Figure 6). The rain collector was placed on top of OCSB for ease of deployment when rain events occured in Galveston. This location was chosen under the assumption that rainfall is relatively similar throughout Galveston Bay. Based on regular cold front patterns, they generally extend at over the entire area of the bay, making the deployment at OCSB in Galveston a reasonable location for use of the Matisoff method. Activity measurements of ^{210}Pb and ^{7}Be from rain water is necessary to perform the Matisoff method, to determine the "initial" age of the two radio-isotopes for each frontal passage event.

The water was collected using a 20-liter jug with a large funnel attached to the opening along with a 2-liter bucket of water next to it for more collection. Additionally, a rain gauge was attached to the container that held the jug. This was deployed before each rain event from January 2020 to February 2020. Following collection, the containers were acidified with HCl that had a pH of 1-3 and were then transferred to a 2-4-liter container. One to two days prior to acidification of the sample; iron hydroxide was added to the sample to separate the nuclides/particles from the water and was left overnight (2 mL $Fe(OH)_2/L$). Ammonium was slowly added to form aggregates and allowed to settle until it was possible to siphon as much excess water as possible. The rest of the sample was centrifuged to separate more water from the aggregates. Once the sample was combined into one falcon tube, 2 mL of 1M HCl was added to the tube and poured into a test tube. An additional 2 mL of 1M HCl was added to the falcon tube to collect the remainder of the sample. The sample was then transferred to the germanium gamma well

326 detector and counted for 24-36 hours. These isotopes were not measured as a ratio, but as individual
327 isotopes.

328 *Table 2: Rain gauge measurements and amount of precipitation recovered from TAMUG OCSB Roof.*

Date	Rain Gauge (mm)	Precipitation Recovered (L)
1/29/2020	2	0.3
2/13/2020	32	2.5
2/21/2020	2	0.25

329

330 Due to low activity ratios of ^{210}Pb in two precipitation samples (1/29/2020 & 2/21/2020), the hotblock
331 acid digestion method was used. The two water samples were weighed and placed into a hotblock
332 container (Figure 7). While the hotblock was being preheated, 0.25 mL of ^{209}Po tracer was added,
333 followed by 15 mL HNO_3 and 15 mL HCl. The sample heated in the hotblock at 165^{o}C for 30 minutes.
334 To prepare the silver planchet for the Alpha counter, 50 mL of diluted HCl and 5 mL ascorbic acid were
335 added and the set to stir for approximately 24 hours. After the 24 hours, the silver planchet is removed
336 and cleaned with acetone and deionized water and set to count in the Alpha counter for 24-48 hours. ^{210}Pb
337 was then calculated from the activity of ^{209}Po and ^{210}Po.

338

339 *Figure 7: Hotblock used for acid digestion method for low ^{210}Pb activity samples*

340 ***4.5 Suspended Sediment Residence Time Method (Matisoff et al., 2005)***

341 Listed below are the assumptions due to ^{7}Be/^{210}Pb$_{xs}$ chronometer. These assumptions allow for
342 uniformity during deposition and following adsorption onto particles. First, it is assumed that dry fallout
343 flux can be included with wet fallout where both are delivered during precipitation events. Where the

precipitation events generate suspended sediment (for this specific study, cold fronts). Secondly, both isotopes are assumed to be delivered to atmosphere in a constant proportion, disregarding season, latitude, or proximity to ocean. This second assumption separates the highly variable nature of atmospheric flux of each isotope separately. Third, following atmospheric fallout, both isotopes are assumed to rapidly adsorb to particulate matter and remain on the particles during further transport until collection. The fourth assumption states that both isotopes are not differentially adsorbed onto organics or partitioned differently. Lastly, by considering the ratio of ^{7}Be and ^{210}Pb, makes it possible to eliminate differences along flow path that is caused by particle grain size and mineralogical variations and because both isotopes have similar adsorption behavior.

With the assumptions given above, decreases in $^{7}Be/^{210}Pb_{xs}$ ratio can be caused by 2 end-member cases. Matisoff *et al*. (2005) reached the conclusion that these two radionuclides are the best indicator of suspended sediment age because of characteristics that make them act the same when deposited into the given environment. For the first case it is possible to calculate if the ratio for precipitation is known. For

$$A = (^{7}Be)_{sample}$$
$$A_o = (^{7}Be)_{source}$$
$$B = (^{210}Pb_{xs})_{sample}$$
$$B_o = (^{210}Pb_{xs})_{source}$$

the second case, 'New' sediment is defined as the sediment particles that have a $^{7}Be/^{210}Pb_{xs}$ ratio equal to precipitation. This means that sediment particle age is the time since the ^{7}Be isotope tag was delivered to sediment particles. In the second case, $^{7}Be/^{210}Pb_{xs}$ ratio in suspended sediment can decrease by the addition of ^{7}Be -deficient sediment from bottom sediment erosion or entrainment of old (^{7}Be -depleted) bottom sediment.

$$A = (^{7}Be)_{sample}$$
$$A_o = (^{7}Be)_{source}$$
$$B = (^{210}Pb_{xs})_{sample}$$
$$B_o = (^{210}Pb_{xs})_{source}$$

1) First Case:

364 a. Activities of ^{7}Be & ^{210}Pb in sediment are given by

$$A = A_o \, e^{-(\lambda_{^{7}Be} t)}$$
$$B = B_o \, e^{-(\lambda_{^{210}Pb} t)}$$

365

366 b. $^{7}Be/^{210}Pb_{xs}$ ratio in suspended sed. Sample is given by ratio A/B

$$\frac{A}{B} = \frac{A_o}{B_o} e^{-(\lambda_{^{7}Be} - \lambda_{^{210}Pb})t}$$

367

368 c. Age of sediment given by

$$t = \frac{-1}{(\lambda_{^{7}Be} - \lambda_{^{210}Pb})} \ln\left(\frac{A}{B}\right) + \frac{1}{(\lambda_{^{7}Be} - \lambda_{^{210}Pb})} \ln\left(\frac{A_o}{B_o}\right)$$

369

370 **2)** Second Case: the percentage "new" sediment in suspension is directly proportional to the
371 $^{7}Be/^{210}Pb_{xs}$ ratio

$$\%\ \text{'new' sediment} = 100 \times (A/B)/(A_o/B_o)$$

372

373 a. Percentage new sediment can also be determined from the age of sediment:

$$\%\ \text{'new' sediment} = 100 \times \exp\,[-(\lambda_{^{7}Be} - \lambda_{^{210}Pb})t]$$

374

375 b. T is the age of sediment calculated in the same way as the first case.

376

377

4. Results & Discussion

5.1 TSS Results

Table 3: Water sample collection data from TAMUG Boat Basin and Texas Corinthians Yacht Club.

Boat Basin					
Date	**Time Collected**	**Tidal Phase**	**Wind Speed & Gusts (m/s)**	**Wind Direction**	**Average TSS (g/L)**
9/27/2019	11:30 AM	ebb	10 m/s	N/A	17.5
1/29/2020	3:00 PM	flood	6-7 m/s & 10 m/s gusts	WNW	15.6
2/21/2020	4:45 PM	flood	6 m/s & 7.5 m/s gusts	NNE	11.1
TCYC					
Date	**Time Collected**	**Tidal Phase**	**Wind Speed & Gusts (ms^{-1})**	**Wind Direction**	**Average TSS (g/L)**
10/14/2019	11:00 AM - 1:30 PM	ebb	12.5 **ms^{-1}**	ESE	49.4
10/25/2019	1:00 PM - 2:00 PM	flood	7.5 **ms^{-1}** & 13 **ms^{-1}** gusts	NNW	25.5
11/12/2019	4:30 PM	flood	8 **ms^{-1}** & 11.5 **ms^{-1}** gusts	N	16.8
1/29/2020	1:30 PM	flood	6 **ms^{-1}**	WNW	20.6
2/13/2020	2:00 PM -2:45 PM	ebb	6 **ms^{-1}** & 8 **ms^{-1}** gusts	N	12.2
2/21/2020	3:00 PM	flood	6 **ms^{-1}** & 10 **ms^{-1}** gusts	NNE	11.3

The first few water collection deployments were conducted on September 27th 2019 at the TAMUG Boat Basin. Collections during October 14th and 21st, and November 11th of 2019 were at TCYC. All of this data was filtered to collect TSS (g L^{-1}) of the water. The sediment from the last three samples were separated from the water by centrifugation and placed in test tubes to be sent to Carol Wilson of the Department of Geology and Geophysics at LSU to be counted on a gamma detector.

Unfortunately, precipitation data was not collected; therefore, the Matisoff method of suspended sediment age estimation cannot be tested with these deployments. Another round of water collection sampling was conducted on January 29th and February 21st of 2020, where samples were collected at both the TAMUG Boat Basin and TCYC. Water collection was also conducted on February 13th 2020, but only at TCYC. TSS data was processed by filtering approximately 1 L of homogenized water collected at each site for each deployment and is presented in Table 3. This data was also filtered to find TSS and the remaining water was centrifuged to separate the sediment to be counted on the gamma detector.

TSS concentrations varies among the samples and is largely dependent on wind speed and gusts. Wind direction also influences the resuspension of bottom sediments during cold fronts. Six out of the 9 samples were collected during flood tide, whereas, the other three were collected during ebb tide. There was only one ebb tide sample for the lower bay site, which was also collected during a cold front. Comparing ebb tide versus flood tide in the upper bay site; ebb tide had higher TSS concentration with a north wind (2/13/2020 vs. 2/21/2020). Looking at the upper bay and the lower bay with corresponding wind speeds, TSS concentrations were observed to be higher during ebb tide. Comparing these two, TSS concentration was highest at TCYC with an ebb tide. When comparing wind speed/gusts and locations (upper bay vs. lower bay), TSS concentration was generally higher at TCYC. This was observed for the last measured cold front event (2/21/2020). This can be attributed to the mud-dominated composition of bottom sediment that characterizes upper Galveston Bay. For all samples collected, it is observed that the stronger the wind speed and gusts, the higher the TSS concentration is because the wind causes sediment to be resuspended from the bay bottom. Lastly, comparing the sample collected during a tropical storm (9/27/2019) versus the cold front with a similar wind speed (10/14/2019 & 11/12/2019). The two cold front events have an average TSS concentration of 32.9 gL^{-1}, which was higher than the TSS concentration measured from the tropical storm. The higher TSS concentration measured during cold fronts was likely due to the direction of wind and the size and duration of the tropical storm. As stated above in the introduction, cold fronts cover more area than a tropical storm, creating a larger impact on shallow water estuaries, such as Galveston Bay.

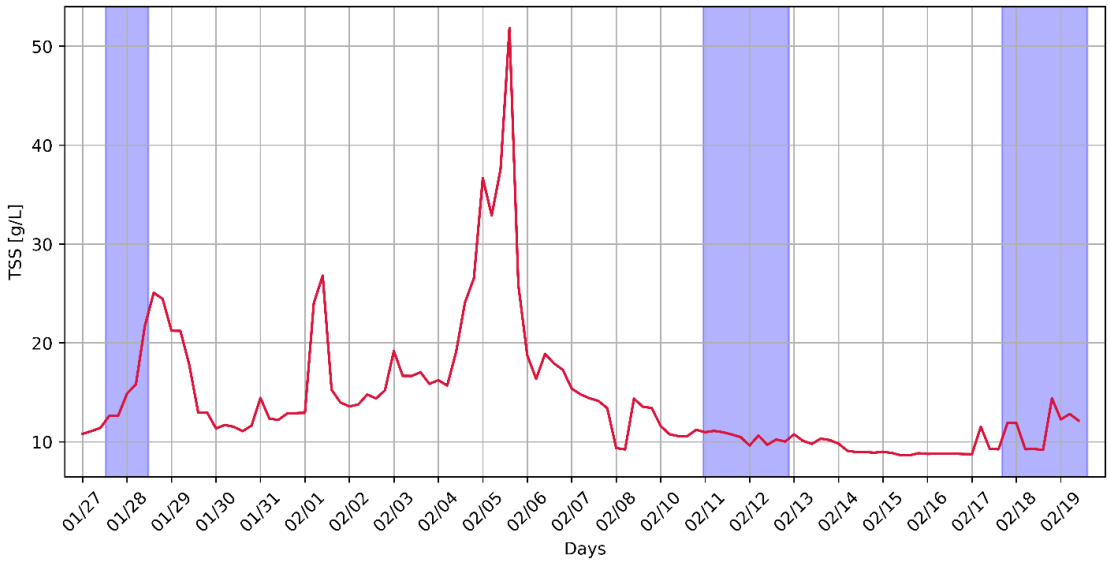

Figure 8: TSS (g/L) from TAMUG-Trin CTD Deployment (9A),

TSS concentrations were also determined from the OBS sensor attached to the CTD during the TRIN pod deploymen January 27 to February 27 in Trinity Bay. TSS concentrations were calculated using the linear equation formula (y = 0.1774x + 8.552) derived from the in-lab CTD turbidity sensor calibration (Figure 8). TSS concentrations throughout the deployment averaged between 8-10 g/L. The TSS concentration spiked following cold front events, aside from the largest peak that occurred 2/5-7/2020. The peak correlates to a winter storm, but there was no rain, therefore precipitation isotope data could not be collected. Following this peak, TSS concentrations do not increase again until 2/18/2020, which matches with the last sampled cold front event (2/18-21/2020).

5.2 Mooring Deployment

Data recorded from the CTD deployment in Trinity Bay was plotted and compared with a NOAA TCOONS station located within Galveston Bay (Eagle Point, TX). At the Eagle Point Station, the sensor height water temperature is measured at 1.3 m below MLLW. The conductivity sensor height is not

Figure 9: NOAA TCOONS Eagle Point, TX meteorological station.

available (Figure 9). This station was chosen because it was within the closest proximity (26.02 km) to the TAMUG-TRIN Pod Station (Figure 1).

Figure 11 displays the CTD data collected during the TRIN Pod deployment. The salinity is lower during every cold front passage, which is likely the result of freshwater added to the bay as a results of the associated rainfall events (Figure 11A). Following the first cold front passage salinity lowers to 10 PSU (practical salinity units) and raises to nearly 14 PSU. Despite the largest rainfall event from January 26-28 (Figure 13 & 14), the salinity does not lower until a few days later. This could be attributed to the rain measurement being in Moses Lake, where it may have taken more time for the majority of the freshwater to flow to the deployment site (Trinity Bay). The lowest salinity follows the rain event on February 13th (Table 2, Figure 13), which, like the first event, lower salinity is measured a couple days following the event. Measured salinity becomes fairly uniform for the remainder of the deployment below 10 PSU. The measured pressure from the CTD fluctuates throughout deployment. Pressure is lower than average during cold fronts. When wind speed increases, pressure decreases (Figure 11B & 11A).

Based on the comparison of the observed temperature from the CTD and NOAA (Eagle Point) found that both instruments follow the same trend where temperature from the CTD tends to be lower (Figure 11E). The decrease in water temperature follows the passage of the cold fronts (1/29-30,2/7-8, 2/13-15, and 2/20). This is similar for measured conductivity, but the CTD measurements tend to be lower than NOAA; and towards the end of deployment, they do not follow a similar trend (Figure 11F). The Eagle Point conductivity sensor measurements slightly increase during each cold front event. The CTD conductivity measurements also increase during these events, aside from the measurements recorded from 1/28-1/30, which were the opposite. The change in the CTD conductivity sensor is likely due to biofouling of the instrument sensor, beginning around 2/08/2020, as discussed in more detail below.

Figure 12A shows wind speed, gusts (m/s) and wind direction (degrees) data taken from NOAA Eagle Point, TX station from the same dates that the CTD was deployed. The figure below (12B) overlays TSS on top of the NOAA wind data. The TSS concentrations spike for the cold front passages of 1/29-30 and 2/7-8, however, the TSS concentrations are very much lower for the cold front passages of 2/13-15, and 2/20 and overall, the TSS concentrations are suppressed for the time series starting on 2/08. When the pod was pulled, it was completely biofouled. The suppressed TSS concentrations from 2/08 to the end of the time series is likely suppressed due to biofouling.

Table 4: Water sample collection data from TAMUG Boat Basin and Texas Corinthians Yacht Club

Date	**TCYC TSS concentration**	**TRIN Pod TSS concentration**	**Percent Difference**
1/29/2020	20.6 gL^{-1}	21 gL^{-1}	2%
2/13/2020	12.2 gL^{-1}	10.7 gL^{-1}	12.2%
2/21/2020	11.3 gL^{-1}	12 gL^{-1}	5.8%

Table 4 shows the TSS concentrations from TCYC and from the TRIN pod site from the same days as well as the percent difference. In each case, the TSS concentrations are generally comparable, with the greatest percent difference being 12.2% for 2/13. However, when comparing TSS concentrations at the TRIN pod site to wind speed, from around 2/08 onward (Fig. 10), the TSS concentrations are greatly suppressed compared to the TSS concentrations during previous high wind events earlier in the time series. As mentioned above, significant biofouling appears to have started on 2/08, suggesting that the only reliable comparison for TSS between TCYC and the TRIN pod location is the 1/29 measurements, where the percent difference is only 2%. This would indicate that TCYC provides a fair estimate of suspended sediment concentrations for upper Galveston Bay, including Trinity Bay.

Figure 10: Wind speed, gusts (m/s) and wind direction (deg) vs. Time obtained from NOAA Eagle Point, TX station (10A), and Wind speed, gusts (m/s) and TSS (g/L) vs. Time (10B).

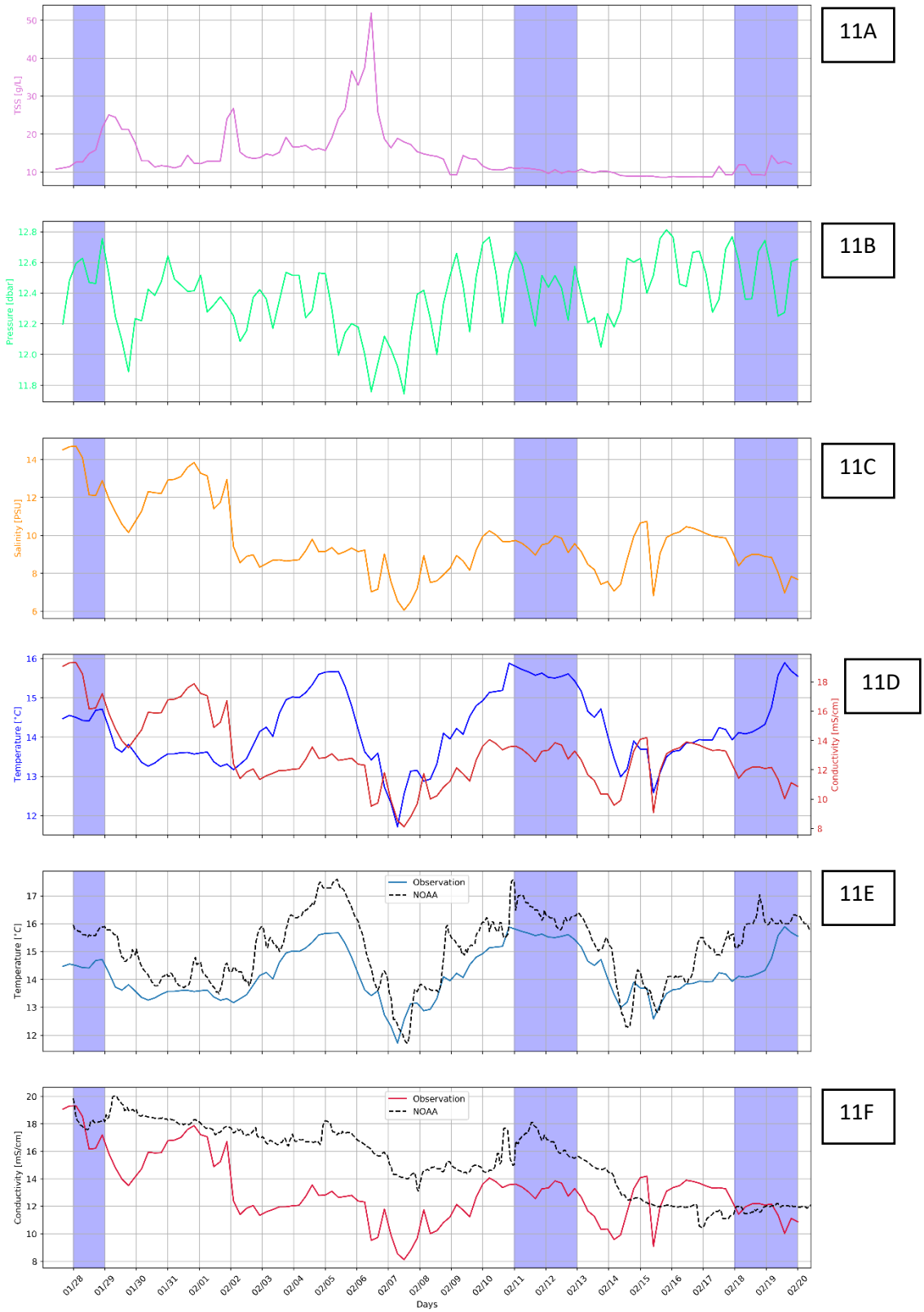

Figure 11: Data measured from the CTD deployed in Trinity Bay (Top to Bottom: TSS (12A), Pressure (12B), Salinity (12C) and Temperature and Conductivity (12D), Observed and NOAA temperature (12E), Observed and NOAA conductivity (12F) vs. Time.

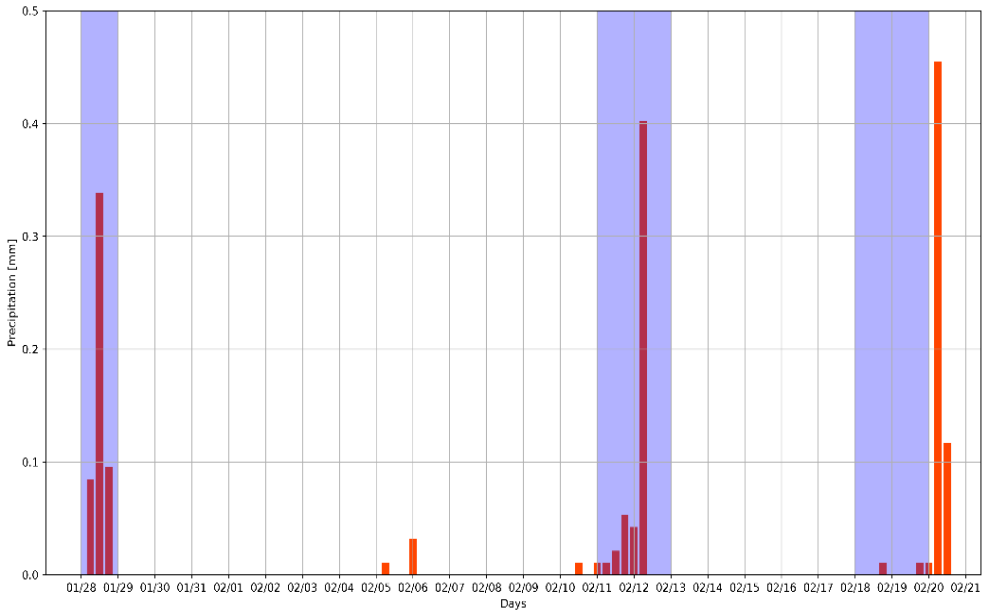

Figure 10: Total precipitation measured from USGS Moses Lake-Galveston Bay station near Texas City, TX for the months of January and February 2020.

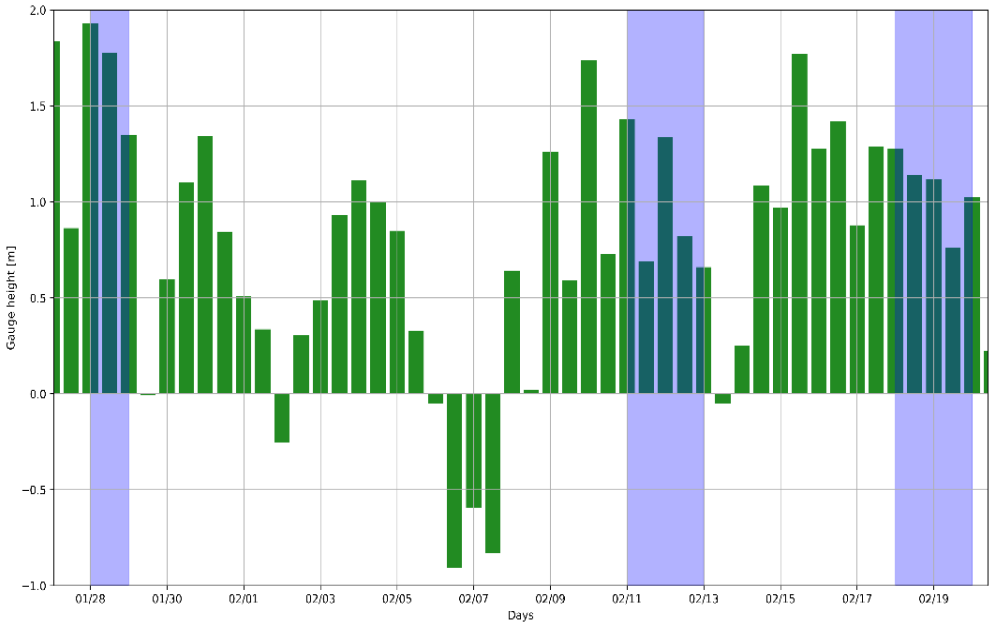

Figure 11: Stream gauge height measured from USGS Clear Creek station near Friendswood, TX for the months of January and February 2020.

5.3 Resident times of TSS

Table 5: ^{210}Pb Activity Concentrations (Bq/kg) of Sediment and Precipitation samples.

	Tide	TCYC	Tide	Boat Basin	Precipitation (OCSB Roof)
Dates		**Activity Concentration (Bq/kg)**		**Activity Concentration (Bq/kg)**	**Activity Concentration (Bq/kg)**
1/29/2020	in	33.654 ± 3.571	in	85.498 ± 9.287	1.378 ± 0.13
2/13/2020	out	66.442 ± 6.354		Not Collected	44.183 ± 5.197
2/21/2020	in	71.916 ± 7.740	in	62.119 ± 6.790	0.554 ± 0.0481

Table 6: ^{7}Be Activity Concentrations (Bq/kg) of Sediment and Precipitation samples.

	Tide	TCYC	Tide	Boat Basin	Precipitation (OCSB Roof)
Dates		**Activity Concentration (Bq/kg)**		**Activity Concentration (Bq/kg)**	**Activity Concentration (Bq/kg)**
1/29/2020	in	97.550 ± 3.397	in	185.474 ± 8.743	38.736 ± 2.312
2/13/2020	out	203.822 ± 5.914		Not Collected	481.894 ± 7.418
2/21/2020	in	116.720 ± 6.550	in	78.883 ± 5.187	63.321 ± 2.531

Activity concentrations of ^{210}Pb and ^{7}Be in Tables 5 and 6 are obtained from the Germanium gamma detector for sediment samples in both TCYC and the TAMUG Boat Basin along with precipitation samples from the OCSB roof. ^{7}Be activity concentrations in all samples are higher than ^{210}Pb. This is attributed to the larger injection of ^{7}Be into the stratosphere, which enhances the stratospheric-tropospheric exchange (Baskaran et al., 1993, Olsen et al., 1985). Another reason for the differences between ^{7}Be and ^{210}Pb fluxes in the spring is linked to the proportions of scavenging from stratiform and convective clouds (Baskaran et al., 1993). The activity concentration of precipitation tends to vary widely between each cold front event. This is due to the fluctuation of rainfall collected between cold front events (Table 2), where the largest amount of rainfall correlates to the highest activity concentration of both ^{7}Be and ^{210}Pb. Activity concentrations within the suspended sediment are higher than precipitation, aside from the samples collected on 2/13/2020.

In relation to tidal phases, it is only possible to compare flood versus ebb tide at TCYC. For both isotopes, activity concentrations are higher during the ebb tide. The ebb tide causes more rain/isotopes to

come into contact with the sampling site since cold fronts generally come from the north. In addition to this observation, it is important to note that there was also the largest volume of rainfall during the cold front (Table 2). The combination of the ebb tidal phase and large volume of rainfall can attribute to a higher activity concentration of both isotopes.

Table 4: $^{7}Be/^{210}Pb_{xs}$ ratios ± standard error calculated from activity concentrations of precipitation, suspended sediment samples with calculated suspended sediment age and percentage new sediment.

	January 29, 2020			February 13, 2020			February 21, 2020		
Source	**$^{7}Be/^{210}Pb_{xs}$**	**Age (d)**	**% New**	**$^{7}Be/^{210}Pb_{xs}$**	**Age (d)**	**% New**	**$^{7}Be/^{210}Pb_{xs}$**	**Age (d)**	**% New**
Upper Bay	4.96 ± .0056	133.77 ± 177.97	17.65 ± 9.95	4.00 ± .762	77.37 ± 6.50	36.68 ± 108.776	2.59 ± .0056	292.17 ± 268.5	2.27 ± 3.08
Lower Bay	28.11 ± .0074	166.91 ± 156.75	11.49 ± 13.12	Not Collected			1.97 ± .0005	313.03 ± 283.22	1.73 ± 2.54

Based on Matisoff et al., (2005), the $^{7}Be/^{210}Pb_{xs}$ ratio is expected to decrease as isotopes travel through a system (Upper Bay to Lower Bay). This is true for the cold front sampled on 2/21/2020, but is much different for the first cold front on 1/29/2020 where the ratio increases by a factor of 4 in the lower bay. Whereas, the age of the sediment does increase closer to the mouth of the Bay, confirming one hypothesis made. In addition to this, Matisoff et al. (2005) states that the percent/fraction of new sediment should decrease as age increases which is seen in Table 6. Unfortunately, a Lower Bay sample was not collected for 2/13/2020. The age of the Upper Bay suspended sediment for second cold front event (2/13/2020) is the lowest compared to the two other events. Additionally, the second storm also has the highest percentage of new sediment added to the water column. This is likely due to the larger volume of precipitation that covered the bay introducing the highest activity concentrations of both isotopes. The differences in these two values may correlate. The low age could be due to more new sediment and isotopes being introduced into the bottom sediment due to the large influx of rainfall. The final storm (2/21/2020) has the smallest isotopes ratio and percent new sediment, which is likely due to the limited rainfall flux during this cold front event. It also has the oldest age in both the upper bay and lower bay and validates Matisoff et al., (2005) expectation mentioned above. The older age in both samples can be linked to older ^{7}Be (measured on 1/29/2020 & 2/13/2020) still being within its half-life. This older sediment is still trapped within the bottom sediment and becomes resuspended from the bottom water and

mixes with new ^{7}Be injected from the rain event. Since there was limited rainfall, the older ^{7}Be overpowers the new. This study validates the use of Matisoff et al., (2005)'s method to determine the age of sediment in Galveston Bay.

5. Conclusion

The residence times/age of suspended sediment increases as suspended sediment moves towards the mouth of the bay. This study validates the use of Matisoff et al., (2005) method to determine the age and transport time of suspended sediment in Galveston Bay. Based on each individual storm, activity concentrations are higher in the lower bay than in the upper bay, aside from the last measured cold front (2/21/2020), which is attributed to the difference between ^{7}Be and ^{210}Pb fluxes in spring. Additionally, in every measured sample, ^{7}Be activity concentrations are higher than ^{210}Pb. In order to fully understand the activity concentrations of ^{7}Be and ^{210}Pb when used to find residence time/age of suspended sediment, additional samples need to be taken during the fall cold front season (October-December).

TSS concentrations are higher in the Upper Bay versus the Lower Bay when winds are stronger than 7 m/s. Otherwise, TSS concentrations are nearly the same when winds are below 7 m/s. This leads to the assumption that stronger winds are attributed to higher TSS concentrations due to more sediment being resuspended from the bottom. This may also, at least in part, be a result of the bay sediment in the Upper Bay having a higher clay content than the sediment within the Lower Bay. Ebb tide has higher TSS concentrations when there is a north wind in the upper bay (2/13/2020 vs. 2/21/2020), likely the result of the addition of tidal current coupled with wind waves and wind driven current imparting greater shear stress to the seabed. For both the Upper Bay and Lower Bay during corresponding wind speeds, TSS concentrations are observed to be higher during ebb tide. This is attributed to the tide bringing more fine sediment from northern parts of the bay to both sites. Comparing these two, TSS concentrations are highest at TCYC with an ebb tide. TSS concentrations are observed to be higher during cold fronts than tropical storms based on the single data measurement collected. This is attributed to the direction of wind, size and duration of storms, where cold fronts affect a larger spatial area, such as the entirety of Galveston Bay.

This study demonstrated the possibility of using ^{210}Pb and ^{7}Be to age date the suspended sediment in various locations within Galveston Bay. This allows for a more thorough understanding of the sediment transport within the bay along with the particle/pollutant residence times. Additionally, TSS data shows that cold fronts accompanied with strong wind speed and a northern wind are significant mechanisms for resuspending/remobilizing sediment in shallow estuaries.

6. Future Plans

In order to further validate the method created by Matisoff et al. (2005), more samples at both sites need to be collected. Also, adding more sites within the upper bay would create a more thorough understanding of suspended sediment in Galveston Bay. Being able to collect more samples during the main cold front occurrences (October-March) and tropical storms/hurricanes will complete the study. The ability to measure TSS concentrations and isotope ratios from the collection of these sample during cold fronts and tropical storms/hurricanes allows for a complete understanding of sediment remobilization during both types of meteorological events.

References

Baskaran, M., Coleman, C., & Santschi, P. (1993). *Atmospheric Depositional Fluxes of 7Be and 210Pb at Galveston and College Station, Texas.*

Baskaran, M., & Santschi, P. (1993). *The role of particles and colloids in the transport of radionuclides in coastal environments of Texas.*

Baskaran, M., & Swarzenski, P. (2007). Seasonal variations on the residence times and partitioning of short-lived radionuclides (234Th, 7Be and 210Pb) and depositional fluxes of 7Be and 210Pb in Tampa Bay, Florida. *Marine Chemistry, 104*(1-2), 27-42.

Booth, J., Miller, R., Mckee, B., & Leathers, R. (2000). *Radio/Infrared/Optical Sensors Branch, 4555 Overlook Ave.* SW.

Carlin, J., Lee, G., Dellapenna, T., & Laverty, P. (2016). Sediment resuspension by wind, waves, and currents during meteorological frontal passages in a micro-tidal lagoon. *Estuarine, Coastal and Shelf Science, 172*, 24-33.

Cox, D., Asce, M., Tissot, P., & Michaud, P. (n.d.). Water Level Observations and Short-Term Predictions Including Meteorological Events for Entrance of Galveston Bay, Texas.

Dellapenna, T., Allison, M., Gill, G., Lehman, R., & Warnken, K. (2006). The impact of shrimp trawling and associated sediment resuspension in mud dominated, shallow estuaries. *Estuarine, Coastal and Shelf Science, 69*(3-4), 519-530.

Dellapenna, T. M., Hoelscher, C. E., Hill, L., Al Mukaimi, M., Knap, A., 2020. How tropical cyclone flooding caused erosion and dispersal of mercury-contaminated sediment in an urban estuary: the impact of Hurricane Harvey on Buffalo Bayou and the San Jacinto Estuary, Galveston Bay, USA. *Science of the Total Environment* (in press). https://doi.org/10.1016/j.scitotenv.2020.141226

Du, J., Park, K., Yu, X., Zhang, Y.J. and Ye, F., 2020. Massive pollutants released to Galveston Bay during Hurricane Harvey: Understanding their retention and pathway using Lagrangian numerical simulations. *Science of The Total Environment*, *704*: 135364. https://doi.org/10.1016/j.scitotenv.2019.135364

Evrard, O., Laceby, J., Huon, S., Lefèvre, I., Sengtaheuanghoung, O., & Ribolzi, O. (2016). Combining multiple fallout radionuclides (137Cs, 7Be, 210Pbxs) to investigate temporal sediment source dynamics in tropical, ephemeral riverine systems. *Journal of Soils and Sediments, 16*(3), 1130-1144.

Ha, H., & Park, K. (2012). High-resolution comparison of sediment dynamics under different forcing conditions in the bottom boundary layer of a shallow, micro-tidal estuary. *Journal of Geophysical Research: Oceans, 117*(6).

Haby, M. G., Miget, R. J., & Falconer, L. L. (2009). *Hurricane Damage Sustained by the Oyster Industry and the Oyster Reefs Across the Galveston Bay System with Recovery Recommendations. College Station, TX.* TAMU-SG-09-201.: The Texas A&M University System. 51 pp.

Mabit, L., & Blake, W. (2019). *Assessing recent soil erosion rates through the use of beryllium-7 (Be-7).* Springer International Publishing.

Matisoff, G., Wilson, C., & Whiting, P. (2005). The 7Be/210PbXS ratio as an indicator of suspended sediment age or fraction new sediment in suspension. *Earth Surface Processes and Landforms, 30*(9), 1191-1201.

Minella, J. P., Merten, G. H., Reichert, J. M., & Clarke, R. T. (2008). Estimating suspended sediment concentrations from turbidity measurements and the calibration problem. *Hydrological Processes: An International Journal*, *22*(12), 1819-1830.

Moeller, C., Huht, O., Robertst, H., Gumley, L., Paul Menzeltt, W., & Abstracti Moeller, A. (1993). *Response of Louisiana Coastal Environments to a Cold Front Passage.*

Olsen, C., Larsen, I., Lowry, P., Cutshall, N., & Nichols, M. (1986). Geochemistry and deposition of 7Be in river-estuarine and coastal waters. *Journal of Geophysical Research, 91*(Cl), 896-908.

Olsen, C., Larsen, I., Lowry, P., Cutshall, N., Todd, J., Wong, G., & Casey, W. (1985). *Atmospheric Fluxes and Marsh-Soil Inventories of 7Be and 2xøpb.*

Perez, B., Day, J., Rouse, L., Shaw, R., & Wang, M. (2000). Influence of Atchafalaya River discharge and winter frontal passage on suspended sediment concentration and flux in Fourleague Bay, Louisiana. *Estuarine, Coastal and Shelf Science, 50*(2), 271-290.

Region, B., Author, U., Walker, N., & Hammack, A. (2000). *Impacts of Winter Storms on Circulation and Sediment Transport: Atchafalaya-Vermilion.*

Residence time. (2020). In *Dictionary.com*. Retrieved July 21, 2020, from https://www.dictionary.com/browse/residence-time

Saari, H., Schmidt, S., Castaing, P., Blanc, G., Sautour, B., Masson, O., & Cochran, J. (2010). The particulate 7Be/210Pbxs and 234Th/210Pbxs activity ratios as tracers for tidal-to-seasonal particle dynamics in the Gironde estuary (France): Implications for the budget of particle-associated contaminants. *Science of the Total Environment, 408*(20), 4784-4794.

Sanford, L., & Halka, J. (1993). *Assessing the paradigm of mutually exclusive erosion and deposition of mud, with examples from upper Chesapeake Bay.*

Stunz, G. W., Minello, T. J., & Rozas, L. P. (2010). Relative value of oyster reef as habitat for estuarine nekton in Galveston Bay, Texas. *Marine Ecology Progress Series*, 406, 147–159. https://doi.org/10.3354/meps08556

Taylor, A., Blake, W., Smith, H., Mabit, L., & Keith-Roach, M. (2013). Assumptions and challenges in the use of fallout beryllium-7 as a soil and sediment tracer in river basins. *Earth-Science Reviews, 126*, 85. Elsevier B.V.

545 Turner, A., & Millward, G. (2002). Suspended particles: Their role in Estuarine biogeochemical cycles. *Estuarine,*
546 *Coastal and Shelf Science, 55*(6), 857-883.

547